UNIVERSIDAD TECNICA
FEDERICO SANTA MARIA

The University of
Nottingham
UNITED KINGDOM · CHINA · MALAYSIA

Energy Storage for Complementary Services in Grid-Tied PV Systems

Nicolás Müller Pollmann

M.Sc.Eng

Thesis submitted to Universidad Técnica Federico Santa María and The University of Nottingham for the degree of Doctor of Philosophy

February 2020

Abstract

The continuous increase in penetration of renewable-based power plants together with the intermittent and variable nature of those natural resources have made grid stability issues a major concern, imposing limitations to higher penetration rates. Energy Storage Systems (ESS) have arise as an enabling technology capable of providing PV/ESS configurations with additional capabilities, as such as ancillary or complementary services.

This work presents a complete analysis of three different complementary services (Maximum Power Ramp Rate limitations, Power Clipping and Peak Shaving). Additionally two different PV/ESS configurations are analysed. For that purpose, three different power converter interfaces between PV and ESS were tested. The results obtained from those tests, showing the performance of the aforementioned complementary services, are presented in this thesis. Moreover, the experimental validation of a PV/ESS, which consists of a full bridge based partial power converter as power interface between PV system and ESS, is also presented in this document.

This document also includes two different ESS sizing strategies, each for an specific complementary service. These sizing strategies rely on a prediction of a year of PV power generation obtained from annual measurements of irradiance and temperature. In both cases, the resulting power prediction is contrasted against a desired power profile.

Keywords

- Complementary services
- Photovoltaic energy
- Energy Storage Systems

Resumen

El continuo incremento de la penetración de sistemas de generación basados en energías renovables junto a la naturaleza intermitente y variable de aquellos recursos naturales han vuelto la estabilidad de la red un tema de gran preocupación, imponiendo limitaciones a mayores tazas de penetración. Los sistemas de almacenamiento de energía (ESS) han surgido como una tecnología habilitadora, capaz de proveer a las configuraciones a las configuraciones PV/ESS de capacidades adicionales, tales como servicios complementarios o adicionales.

Este trabajo presenta un completo análisis de tre diferentes servicios adicionales (Maximum Power Ramp Rate limitations, Power Clipping and Peak Shaving). Adicionalmente, dos distintas configuraciones PV/ESS son analizadas. Para tal propósito tres convertidres de potencia diferentes, operando como interfaz entre el sistema PV y el sistema de almacenamiento de energía, fueron probados. Los resultados obtenidos a pertir de dichas pruebas se encuentran presentados a lo largo de es ta tesis. Además, este documento presenta la validación experimental de una configuración PV/ESS, la cual consiste en un convertidor de potencia parcial basado en convertidores tipo puente completo como interfaz entre los sistemas PV y ESS.

Este documento también incluye dos estrategias distintas de dimensionado de ESS, cada una para un servicio adicional específico. Estas estrategias de dimensionado dependen de la predicción anual de potencia solar, generada a partir de un conjunto anual de mediciones de irradiación y temperatura. En ambos casos la prediicción de potencia resultante es contrastada contra un perfil de potencia deseado.

Palabras Claves

- Servicios adicionales
- Energía Fotovoltáica
- Sistemas de Almacenamiento de Energía

Acknowledgements

The thesis presented in this document was performed as part of a dual degree program between Universidad Técnica Federico Santa María (Chile) and the University of Nottingham (UK). Therefore, the amount of people I wish to thank is not small, I hope not to forget anyone.

I would like to start by thanking my supervisors Dr. Samir Kouro, Prof. Pericle Zanchetta and Prof. Patrick Wheeler, your were of great support during all this process, I really appreciate having the opportunity of working with you. I would also like to acknowledge Christian Rojas and Gonzalo Carrasco for being always happy to share their knowledge, to Diana López and Matías Aguirre for hearing and debating ideas, to Gustavo Bittner for sharing his technical and miscellaneous knowledge, to Rodrigo Lanas for sharing his applied and technical wisdom, to the people in both research groups Powerlab and PEMC for their professional and human quality, to the people gathered in Derby 31 for being our family during our year abroad, to Elizabeth Muga and Bekki Burns for making PhD-life easier, to Madllana, Pati, Ester and Marité for always sharing a bit of happiness. To Karen Eveson for he patience correcting my English. To Bernie, Dani, Maca, Mauro, Chinito, Pau, Papa Bear, Xavi, Bolton, Seba, Mahir and Gustavo, from all my heart, thanks for ALL. You made our year abroad an amazing experience. And finally, special thanks to my wife who is my companion and has been my main support during this long period.

I would also like to thank Comisión Nacional de Investiagación Científica y Tecnológica (CONICYT-PCHA/Doctorado Nacional/2014-21141092) and the Solar Energy Research Center (SERC-Chile, CONICYT/ FONDAP/15110019) and Universidad Técnica Federico Santa María, for the economical support provided during the development of this thesis.

Contents

List of Figures

List of Tables

Acronyms

- 2LVSI: Two Level Voltage Source Inverter.
- AE: Autumnal Equinox.
- BESS: Battery Energy Storage System.
- CAPEX: Capital Expenditure.
- DFT: Discrete Fourier Transform.
- DWT: Discrete Wavelet Transform.
- ESS: Energy Storage System.
- EST: Energy Storage Technology.
- GMPPT: Global Maximum Power Point Tracking.
- GO: Grid Operator.
- IBBC: Isolated Bidirectional Boost Inverter
- ILR: Inverter Loading Ratio.
- LCOE: Levelised Cost Of Energy.
- MPP: Maximum Power Point.
- MPPT: Maximum Power Point Tracking.
- NOCT: Normal Operating Cell Temperature.
- OPEX: Operational Expenditure.
- P&O: Perturb and Observe.
- PCC: Point of Common Coupling.
- PPC: Partial Power Converter.
- PWM: Pulse Width Modulation.
- PV: Photovoltaic.
- RR: Ramp Rate or Maximum Ramp Rate Regulation.
- SC: Supercapacitor.

- SS: Summer Solstice.
- STC: Standard Test Condition.
- VE: Vernal Equinox.
- VOC: Voltage Oriented Control.
- WS: Winter Solstice.

This document corresponds to the Thesis required towards a dual award Ph.D. degree between Universidad Técnica Federico Santa María (Valparaíso, Chile) and the University of Nottingham (Nottingham, UK).

Chapter 1

Introduction

Fossil fuels depletion, CO_2 emissions, greenhouse effect and governmental policies have motivated the development and integration of sustainable energies into electric networks [33]. A worldwide increase of sustainable energy penetration in the electric markets has taken place during recent decades, reaching a 26.2% of the global electric market [1]. Photovoltaic (PV) and Wind Energy conversion systems are at the forefront of sustainable energies, integration into electric networks, showing the highest growth rates in the last few years [34]. Furthermore, installed global PV capacity is nowadays 85% of the total installed wind capacity, in contrast with the 15% it was a decade ago [1]. To illustrate the growth of global PV power, Fig. 1.1 presents the evolution of worldwide installed PV capacity [1].

Grid-connected PV systems can be classified according to their configuration as AC-module

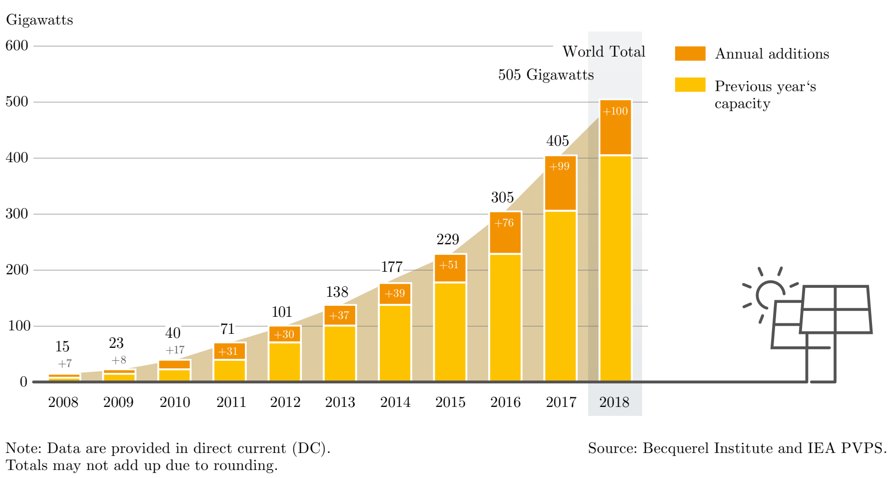

Figure 1.1: Solar PV global capacity and annual additions (2008-2018) [1]

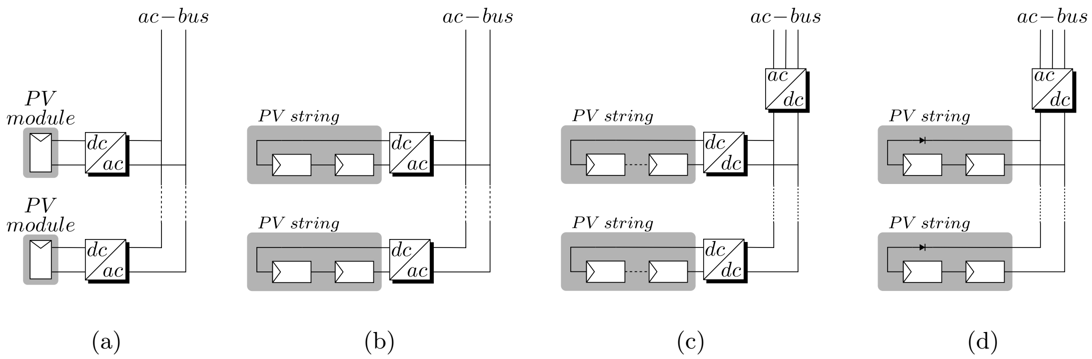

Figure 1.2: PV plant configurations: a) AC-module inverter, b) String inverter, c) Multistring inverter and d) Central inverter.

inverters, string inverters, multistring inverters or central inverters [24, 35]. AC-module inverters, also known as micro-inverters, use a single inverter to connect each PV module to the grid (as shown in Fig. 1.2a). For this reason AC-modules have a power rating close to the Maximum Power Point (MPP) rating of a single PV module ($\leq$ 450 [W] [25]) and provide the best Maximum Power Point Tracking (MPPT) accuracy among all configurations [24]. However, these configurations require an additional dc-dc boosting stage to reach grid-voltage levels, thus having a less efficient power conversion system and being the most expensive alternative in terms of cost per watt [24]. The closest alternative, in terms of power rating to AC-module inverters, are string inverters. These connect an array of series-connected PV modules (PV string) to the grid through a single inverter as shown in Fig. 1.2b. The maximum power rating for this configuration is imposed by the number of PV modules that can be connected in series, due to the string voltage limitation (1,000 [V] [36] or 1,500 [V] [37]). Due to the reduction of power converters, string inverters present a reduction in cost per watt when compared to AC-module inverters. There are a large variety of string inverters including: single conversion stage, double conversion stage, without galvanic isolation, with high frequency transformers and with low frequency transformers, among others. Following up in terms of power rating are multistring inverters which improve their MPPT accuracy, when compared to string inverters, by reducing the length of the PV strings. In this configuration, one or two PV strings are connected to a single dc-dc converter [24, 28]. A single inverter allows connection of the output of several dc-dc converters to the electric grid as shown in Fig. 1.2c. In comparison with string inverters, multistring configurations require more power converters to handle the same amount of power, thus increasing the cost per watt of the configuration. Central Inverters are the configuration with the highest power rating. In this configuration several PV strings are connected in parallel to a single inverter as shown in Fig. 1.2d. This alternative results in the lowest cost

	AC-module inverter	String inverter	Multistring inverter	Central inverter
MPPT efficiency	Highest	Good	High	Lowest
Converter efficiency	Lowest (up to 97.5%)	High (up to 97.8%)	Highest (up to 98.8%)	Highest (up to 98.8%)
Power range	≤ 0.45 [kW]	≤ 30 [kW]	≤ 500 [kW]	≤ 5000 [kW]
Grid connection	1ϕ	1ϕ	1ϕ and 3ϕ	3ϕ
Examples	Enphase IQ7A-72-2-US, – –	Canadian Solar CSI-4KTL1P-GI-FL, SMA Sunny Boy 2.5	Fimer PVI-400.0-TL, Huawei SUN2000-185KTL-H1	Fimer PVS980-58, Siemens SINACON PV1250

Table 1.1: Comparison between PV system configurations [9, 24–29]

per watt and the least efficient alternative in terms of MPP tracking. The main differences among configurations are summarized in Table 1.1.

Efficiency, reduced number of power converters, lower cost per watt, reliability and simplicity make central inverter configurations the best alternatives for large-scale (> 500 [kW]) PV systems [9, 24–28]. For these reasons, the work developed in this thesis has been restricted to PV systems with central inverter configurations.

The continuous increase in participation of PV systems in electric networks, has raised some concerns and challenges related to PV power forecasting, generation-demand matching, grid code compliance, power quality and grid stability [2, 10, 33, 38–41]. Moreover, PV resource intermittency and variability are of special concern in central inverter configurations, where a single MPPT (due to its single inverter) is applied to regulate the power injected to the electric grid.

As a countermeasure against the aforementioned drawbacks, many grid operators (GO) have updated their grid codes, including regulations regarding power quality, frequency and voltage support, voltage ride-through, and other services [3, 42]. These new operating conditions pose restrictions and limit the operation and control of traditional PV inverters, and especially of central inverter configurations, where the single inverter makes them prone to higher power variations, limiting the energy yield and efficiency of the PV system in many cases [16].

Energy Storage Systems (ESS) have been proposed as an alternative for handling variability and intermittency in sustainable sources, allowing them to comply with grid codes and being an enabling technology for complementary services [32, 41, 43], thus opening new routes for revenue.

There are four alternatives when choosing the point of coupling between a PV system and an ESS. A classification of these different PV/ESS configurations, based on the connection point in the PV system, is presented in Fig. 1.3. The mainstream solution for merging ESS into PV systems are grid-side coupling at either the AC-grid side (as shown in 1.4a) [2–8] or at the DC-grid side (as shown in 1.4b) [10–12]. Other alternatives presented in literature consist of connecting

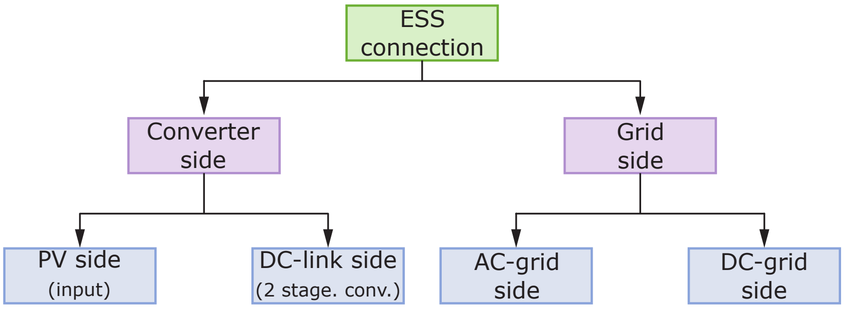

Figure 1.3: Classifications of ESS location in PV/ESS configurations according to the ESS connection point.

the ESS at the power converter side. In these configurations, the most common solution consists of merging the ESS at the dc-link between two power converters in a two-stage configuration (as shown in 1.4c) [2, 3, 13, 14]. Other alternatives consist of connecting the ESS at the input of the PV power converter (as shown in 1.4d) [15].

An additional factor to bear in mind is the additional ESS expenditure (Capital Expenditure or CAPEX), which increases the PV plant total cost per watt (Levelised Cost of Energy or LCOE). Therefore, proper sizing strategies become a fundamental step in PV/ESS integration, increasing the cost-effectiveness of the ESS by performing a trade-off between the associated CAPEX and estimated return. Moreover, an adequate sizing strategy can increase income by allowing the PV plant to increase its energy yield, provide complementary services and decrease fines associated with non-compliance of the grid code (decreasing Operational Expenditures or OPEX). Furthermore, ESS sizing strategies available in literature [23, 40, 44–53] only tackle energy sizing of the energy storage considering power as a limitation imposed by the application. Therefore, neglecting an integral view that includes power dimensioning of the energy storage and power converter, resuls in power oversizing (increased CAPEX) or under-sizing (reduced energy yield).

1.1 Motivation

Two case studies are presented in this section to motivate the research presented in this thesis. The first case corresponds to global MPPT under partial shading conditions in central inverter PV configurations. The second example describes power clipping due to PV array oversizing with respect to the rating of the inverter.

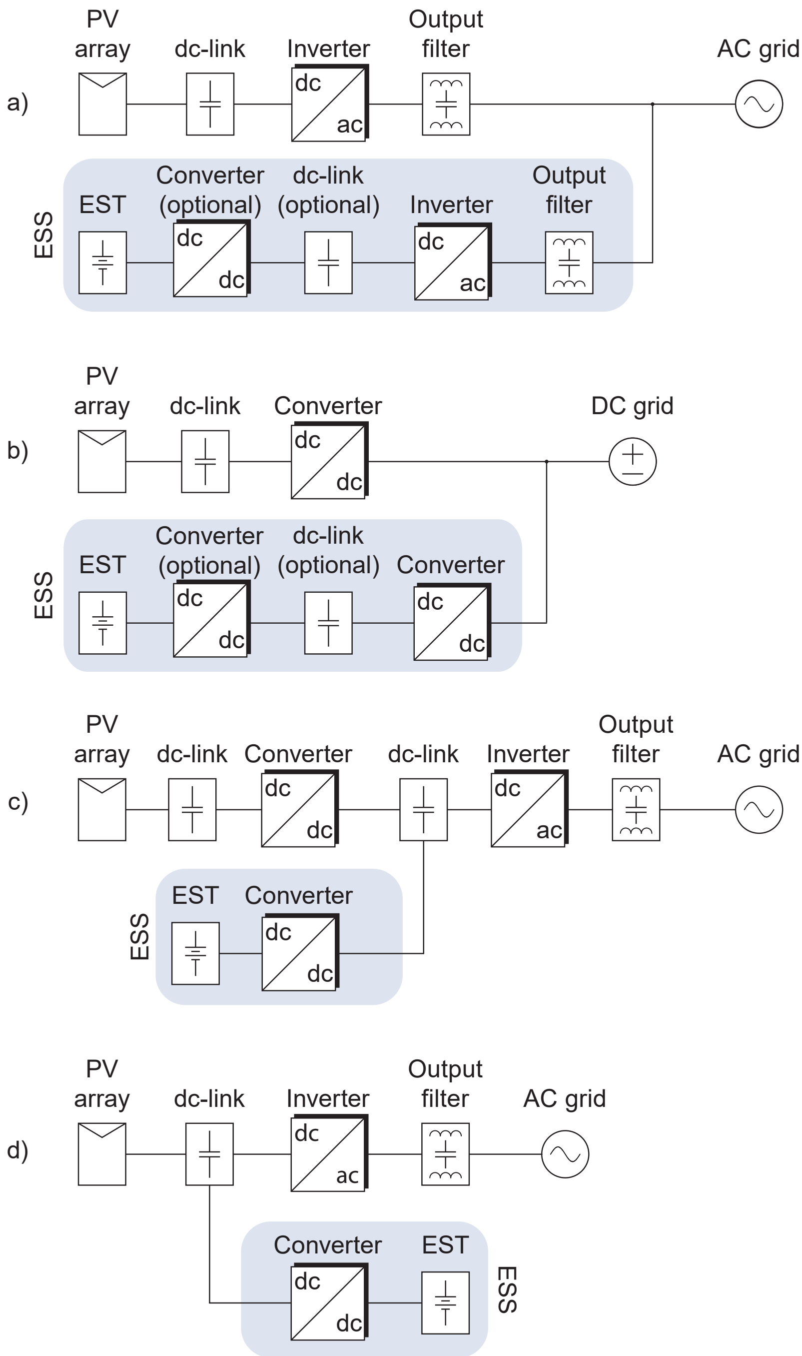

Figure 1.4: PV/ESS configurations: a) AC-grid side connection [2–9], b) DC-grid side connection [10–12], c) DC-link side connection in two-stage PV configurations [2, 3, 13, 14] and d) PV side connection [9, 15]

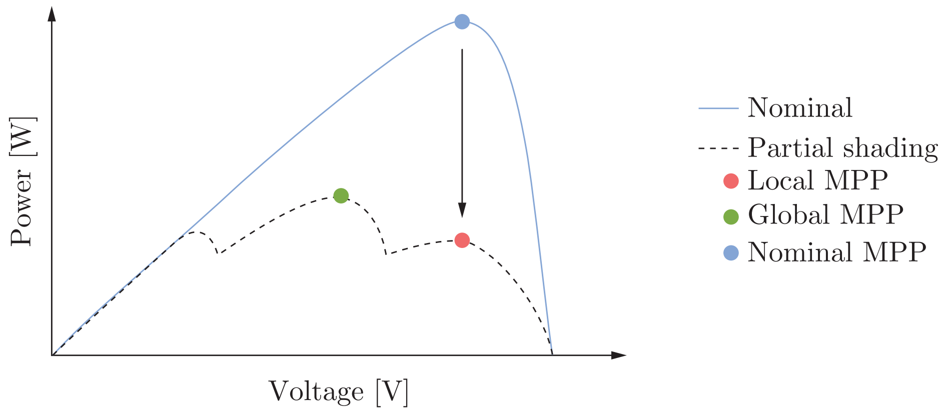

Figure 1.5: Power-voltage characteristic curve of a Central Inverter PV plant under standard test conditions (blue) and under partial shading conditions (black).

1.1.1 Global MPPT in Central Inverter PV Configurations

Central inverter configurations have a single MPPT for each inverter. Under non-uniform conditions, the PV characteristics can present several local maximums as illustrated in Fig. 1.5. In this figure, the power-voltage characteristic of a PV plant operating under Standard Test Conditions (STC) and under partial shading conditions is shown. In order to optimize the produced energy, it is mandatory to implement a MPPT algorithm that is able to track the global maximum. Since classical algorithms such as Perturb and Observe (P&O) may remain in a local maximum, it is necessary to implement dedicated methods. One of the simplest solutions is to perform a scan of the PV characteristic and then start a classical MPPT method around the global Maximum Power Point (MPP) as done in [54–57]. The scanning process can be performed by modifying the PV voltage reference as detailed in [58]. Another solution consists of adding a dedicated external circuit as in [59], where two different circuits operating as variable loads are used for obtaining the power-voltage curve of the PV plant.

One of the main drawbacks of scanning the power-voltage curve is that the system suffers from large power variations during the process, thus reducing its energy yield during the tracking of the global maximum. Recent work on global MPPT algorithms focuses on reducing this aspect. In [60], the global MPP is estimated by the use of distributed PV voltage sensors among the modules of the array. However, this solution results in higher cost and possible failure but avoids too much energy loss due to blind scan. In [61] a scan is performed, but the voltage window search range is restricted to avoid going from open-circuit voltage to short-circuit. In [62], a process which allows reducing the PV array power perturbation steps is proposed. More complex algorithms can also be used to find the global maximum. For example in [63], a Particle Swarm Optimization algorithm is proposed to reach the global MPP.

All of the mentioned PV curve scan methods suffer from wide variations in the array power and these might be prohibited. Indeed, the limitation of maximum PV power variations have been recently included in grid codes [64]. The first country to impose this limitation was Puerto Rico, setting the maximum allowable power variation up to 10% of the nominal power per minute [65]. That limitation comes from the fact that the PV power fluctuation can affect the power quality and reliability of the electric system. Furthermore, power fluctuations shorter than 10 min are typically absorbed by the grid as frequency fluctuations. This issue is of great importance especially in small grids, such as islands with high PV penetration rates, since the smoothing effect from the aggregation of geographically dispersed PV plants is intrinsically limited, therefore justifying those constraints [65, 66]. ESSs can be used to allow the performance of a scanning process to reach the global MPPT, while smoothing power variations at grid side, as shown in [58].

Unlike wind energy farms, which are mostly large in size, PV plants may range from a single module of a few hundred watts (200 W) to large plants having thousands of modules, reaching up to 1 GW [3, 24]. The size of a PV plant is related to the available surface; hence space limits the number of PV modules and the overall power rating. Additionally, there is a large dispersion of PV plant sizes. This motivated the study of the addition of ESS at inverter level, which allows the performance of a tailored modular design, thus proving flexibility and scalability.

1.1.2 Power Clipping in PV Plants

A crucial parameter when designing renewable energy plants is the load factor, also known as capacity factor or plant factor, which corresponds to the ratio between the generated and rated energy of the plant during a certain amount of time. In the UK, PV plants present annual load factors close to 10 % [67], which are calculated considering the rated power of the converter. A common practice is to increase annual plant factor by oversizing the power rating of the PV array, with respect to the converter [68]. The ratio between PV array rated power and the inverter AC rated output power is known as Inverter Loading Ratio (ILR) [69]. In places with high irradiance variability such as the UK, PV array power oversizing can reach as much as 40 % (ILR= 140%), whereas in places with lower irradiance variability, like central Chile, oversizing is closer to 15 % (ILR= 115%). Moreover, the continuous drop on PV module prices have encouraged the increase of ILR in PV plants [68]. Some authors have even proposed ILR oversizing up to 80% (ILR= 180%) [69].

When an oversized PV array reaches the power rating of the converter, the converter loses the capability to increase its current, is therefore unable to reduce the DC-link voltage so loses the

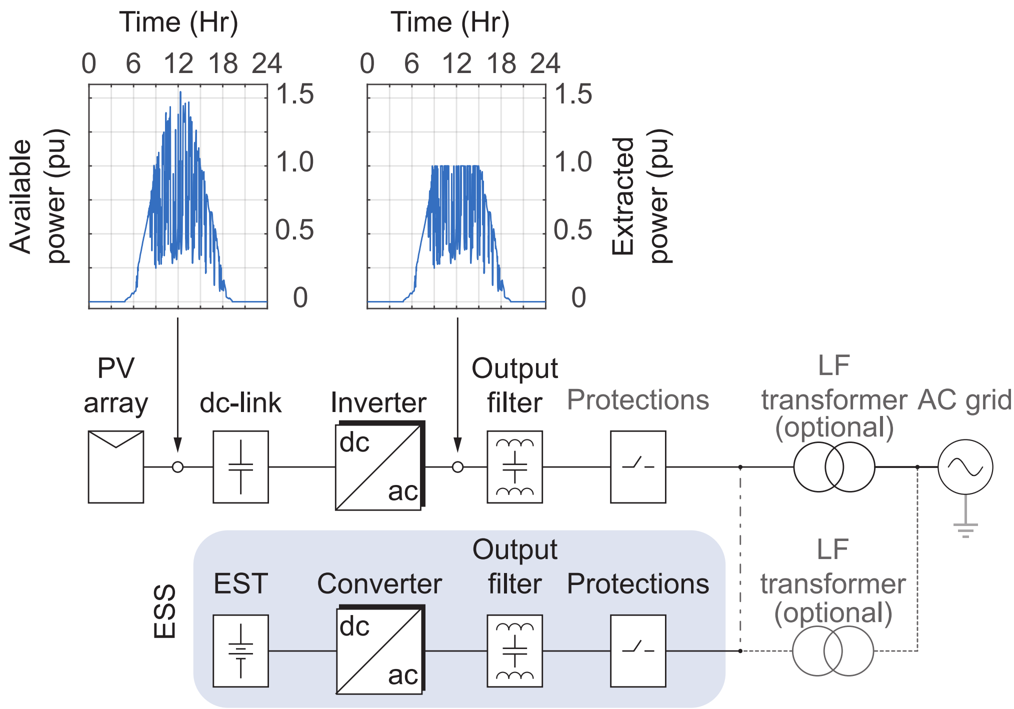

Figure 1.6: Central inverter grid-tied PV plant with additional Battery Energy Storage System (BESS).

capability to track the Maximum Power Point (MPP). This behaviour is called clipping, and it forces the system to waste available PV power. Clipped power is the name assigned to this wasted power. To illustrate this behaviour, Fig. 1.6 presents a grid-tied central inverter PV plant with PV array oversizing, where the available power is truncated at the rating of the inverter (clipped), limiting the extracted power. Both power curves were normalized to the inverter rating.

In electric networks generation-demand matching is achieved managing power generation and consumption along the system, by relying on other generating units connected to the electrical network and/or by adding Energy Storage Systems (ESS). The first solution is not suitable for harnessing clipped power, since it requires the clipped power to be transferred to the electric network through the inverter, which is already operating at its rated power. The latter solution, presents a promising alternative to enhance existing PV plants, enabling the harnessing of the clipped power. This solution has been widely researched as an alternative not only to deal with generation-demand mismatch, but also as a mean for generating units based on sustainable energies to provide additional services, such as load shifting [47], global maximum power point tracking [70], peak-shaving [71], etc. However, PV plants retrofitting by adding ESS to enable clipped power storage, remains an issue. A similar case is presented in [48], where maximum power generation in a PV plant is clipped in order to limit power variation. However, the service presented in [48] corresponds to Power Curtailment where the power limitation is not imposed by the power converter, but rather by the controller. This ESS sizing strategy averages power generation beyond clipping level, hiding power dynamics relevant to the sizing process, therefore providing poorly estimated power and energy sizing. Moreover, this solution is not feasible for power clipping since the ESS is interfaced into the PV system at AC-grid side.

In both study cases, the mainstream commercial solution when retrofitting PV systems, consists of attaching the ESS at the Point of Common Coupling (PCC) of the PV plant, forcing the energy to pass twice through the ESS power converters (storing/releasing energy). Commercial inverters, efficiencies reach up to 98.5%, obtaining round trip efficiency of 97% [9,72]. However, most storage devices that allow modularity and scalability are low DC voltage, hence requiring serialization (stacking) and/or boosting, and transforming DC into AC. On the other hand, Partial Power Converters (PPC) have risen as an alternative to traditional full power dc-dc converters, able to handle the same amount of power as a full power converter, while increasing the power density and efficiency (by up to 99%) [73–75].

Consequently, the research presented in this document focuses on providing a better insight into ESS requirements and design strategy to merge ESS into PV systems with central inverter configurations, and to enable PV/ESS systems to perform complementary services. Therefore, two main topics of research were developed, the first one aimed at obtaining a proper ESS sizing associated with each one of two specific complementary services and the second one oriented at developing a power electronics converter capable of efficiently interfacing the storage and PV.

1.2 Objectives

The main objective of this thesis is to develop an ESS sizing strategy and to propose a power converter interface, in order to retrofit PV plants, enabling them to provide complementary services.

1.2.1 Specific objectives

- To develop an ESS power and energy sizing strategy, that allows to store the excess of energy that would be lost due to PV inverter rating under power clipping conditions due to PV array oversizing.
- To develop an ESS power and energy sizing strategy that allows to comply with ramp rate regulations, while storing the exceeding energy.

- To propose, model and simulate a bidirectional power converter interface, that allows to connect an ESS and a PV plant, while enabling bidirectional power flow control.
- To propose, model and simulate a bidirectional dc-dc power converter interface, that allows to connect an ESS to the PV side (dc-side) of a central inverter PV plant.
- To simulate the proposed PV/ESS configuration, to analyse its use for specific complementary service (ramp-rate regulation, peak shaving and power clipping).
- To build and test an experimental laboratory prototype of a PV/ESS configuration.
- To disseminate the obtained results (conference, journal papers and technical reports).

1.3 Project scope

The work presented in this document is focused on the central PV inverter configuration and does not consider other PV configurations. The main reason being the large number of large-scale PV plants using central PV inverters and the possibility to retrofit these PV plants with ESS. In addition, this topic was of particular interest of a company associated with a technical project related to this thesis.

Due to time limitations only three complementary services were explored along this document (RR Control, Peak Shaving and Power Clipping). Additionally, the economical analysis related to Power Clipping, was not included since it is protected by a non-disclosure agreement with an industrial partner.

1.4 Main contributions

The main contributions of this thesis can be organised in 4 different groups.

- **Estimation of loss of generation:** Two estimations were performed applying real data measured once per minute during a full year. The set of data points used to estimate clipping losses are from a PV plant located in the UK, while the data set used to estimate RR losses comes from a PV plant located in Chile. Each estimation allows calculation of the loss of generation. The first estimation calculates the loss of generation due to power clipping. The second estimation calculates the loss of generation due to complying with different levels of Maximum Power Ramp Rate (RR) regulation (5,10, 15 and 20%). Both estimation methodologies and their application to RR and power clipping correspond to novel contributions of this thesis.

- **ESS sizing strategies:** Two different ESS sizing strategies were developed. The first strategy aims at sizing an ESS capable of recovering the loss of generation caused by power clipping. The second strategy focuses on sizing an ESS that allows smoothing power generation while complying with maximum power RR generation. Both sizing strategies correspond to novel contributions.

- **Bidirectional power converter:** A novel bidirectional partial power converter (PPC), that allows interfacing between an ESS to a PV system at the central inverter PV side (dc-side), is proposed in this thesis. The mathematical model, control design and preliminary validation through simulation are also included in this document. In addition, a reconfigurable PPC based on electromechanical switches that reconfigure the internal connections of a unidirectional PPC converter to provide bidirectional functionality is proposed in this thesis. This topology was preliminary validated through simulation and experimental results.

- **ESS control strategy for Power Clipping:** A novel strategy to handle clipped power storage was developed. The strategy enables to operate at MPP generation despite the power rating limitations of the PV inverter due to clipping. The challenge lies in the fact that the central inverter configuration does not allow the provision of an external MPP reference for retrofitting, thus an adequate control must be implemented to allow the PV inverter to operate around the global MPP. This has been achieved by an algorithm that computes the difference between the rated clipping power and the global MPP to generate the reference current for the ESS. The strategy also takes into account the time constants in the MPPT algorithm of the central inverter (that can not be modified) and the control algorithm of the ESS.

These contributions can be grouped in two main research lines. The first topic corresponds to the development of sizing strategies for Energy Storage Systems (ESS) in Photovoltaic (PV) applications. The second topic corresponds to configurations and power converter interfaces that allow the connection of ESS into PV systems. However, chronologically speaking, the latter topic (configurations and power converters) was developed earlier in the research (as can be seen from the date of the associated publications) due to the initial thesis work plan constrained by funding projects associated to each research stage in the double degree program. For this reason the results and findings of the sizing strategies were not applied in the part of the thesis focused on PV/ESS configurations and power converters.

1.5 Thesis outline

The outline of this document and a brief description of the topics addressed in each chapter are presented below.

- Chapter 2: A brief description of Energy Storage Technologies and a classification and full description of complementary services are presented in this chapter. The latter description includes Ancillary Services for Chilean electrical regulations, Enhanced Grid Code Compliance Services and Supply-Side-Management Services.

- Chapter 3: Three different modelling techniques to estimate PV power generation are presented in this chapter. The models rely on irradiance and temperature measurements to estimate the available PV power at MPP. A comparison of the models with empiric PV generation is also presented. From these results a modelling strategy is selected to estimate the annual PV power generation for two different locations (Chile and the UK). In addition, this chapter presents the results of both annual PV power estimations for the selected locations.

- Chapter 4: This chapter presents the state of the art of ESS sizing strategies to enable PV systems to provide complementary services. Two ESS sizing strategies developed during the thesis are also introduced in this chapter. The first strategy is oriented at complying with maximum ramp rate regulation while providing storage capability and enables the generation of peak-shaved power. The second ESS sizing strategy tackles power clipping due to PV array oversize.

- Chapter 5: State of the art of PV/ESS configurations and ESS power converters are presented in this chapter. Additionally, the circuital diagram and mathematical model of the proposed configurations and topologies are also presented in this chapter. The experimental operation of one of the proposed power converter interfaces, that allows merging of ESS into a central inverter dc-link, is also presented in this chapter. Additionally, this chapter includes the experimental results of the PV/ESS configuration under dynamic tests. The results show the operation of the partial power converter under dynamic and steady state operation, and the operation of the full PV/ESS configuration under dynamic tests.

- Chapter 6: A brief introduction to the state of the art of control strategies for ESS in PV applications is presented in this chapter, followed by a description of four different control strategies oriented to provide three different complementary services, namely Ramp Rate control to perform Global MPPT, peak shaving power and power clipping.

- Chapter 7: This chapter presents the simulation results associated to each one of the PV/ESS configurations presented in chapter 5, applying the control strategies presented in chapter 6.
- Chapter 9: This chapter presents the conclusions of the work performed during development of this thesis. Some proposals for future works are additionally introduced in this chapter.

1.6 List of publications derived from this thesis

1. N. Muller, S. Kouro, H. Renaudineau, and P. Wheeler, "Energy storage system for global maximum power point tracking on central inverter PV plants", in 2016 IEEE 2nd Annu. South. Power Electron. Conf. SPEC 2016, 2016.
2. N. Muller, H. Renaudineau, F. Flores-Bahamonde, S. Kouro, and P. Wheeler, "Ultracapacitor storage enabled global MPPT for photovoltaic central inverters", IEEE Int. Symp. Ind. Electron., pp. 1046-1051, 2017.
3. N. Muller, S. Kouro, P. Zanchetta, and P. Wheeler, "Bidirectional partial power converter interface for energy storage systems to provide peak shaving in grid-tied PV plants", Proc. IEEE Int. Conf. Ind. Technol., vol. 2018-Febru, pp. 892-897, 2018.
4. N. Muller, S. Kouro, P. Zanchetta, P. Wheeler, and A. Marzo, "Wavelet-based ESS sizing strategy to enable power peak-shaving in PV systems", in 2019 IEEE 28th Int. Symp. Ind. Electron., pp. 2458-2463, 2019.
5. N. Müller, S. Kouro, P. Zanchetta, P. Wheeler, G. Bittner, and F. Girardi, "Energy storage sizing strategy for grid-tied PV plants under power clipping limitations", Energies, vol. 12, no. 9, pp. 1-17, 2019.

Chapter 2

Background

2.1 Introduction

The main purpose of this chapter is to familiarise the reader with the concepts related to complementary services and Energy Storage Technologies (ESTs). This chapter also includes the selection of complementary services and ESTs that will be applied in the work presented in this thesis. Additionally, the bidirectional power converter topologies available in literature are presented. For these reasons, this chapter has been divided into three main topics, namely complementary services, ESTs and bidirectional power converters for PV/ESS configurations. The former subject addresses ancillary services in the Chilean electrical regulation, services to support grid code compliance and supply side management services. This section also includes the justification for selecting three complementary services, as relevant applications in central inverter PV configurations with the addition of ESS. The EST subject presents a brief introduction into technologies that enable the storage of electric energy, a comparison between the main aspects of ESTs, and the selection of the best EST candidates to provide the previously selected complementary services. The latter topic presents a literature review of the bidirectional power converter topologies and the selection of different bidirectional power converter topologies to manage the bidirectional power flow.

2.2 Complementary Services

This section addresses complementary services for renewables integration, specifically in PV plants. complementary services are defined in this document as extra services that allow improvement in the response of PV systems to variability, intermittency and perturbations on the electric system and, in general terms, to offer a better quality of energy hence aiming to increase renewables

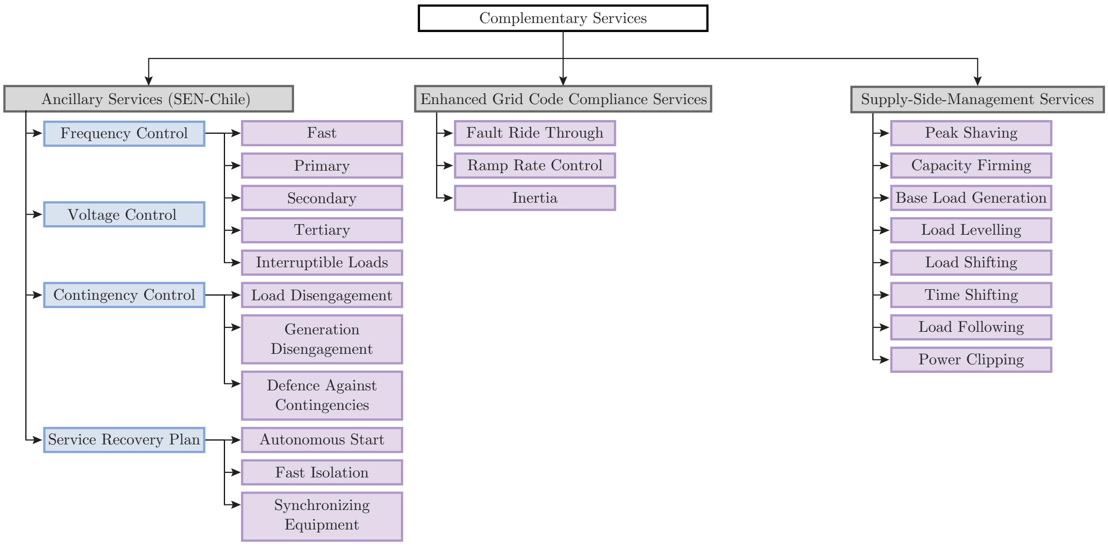

Figure 2.1: Classification of complementary services in PV systems.

integration into the electric markets. complementary services are divided into ancillary services, Enhanced Grid Code Compliance Services and Supply Side Management (SSM) Services. A classification of complementary services is shown in Fig. 2.1. A brief description of each service is given below.

2.2.1 Ancillary Services

According to Energy UK, ancillary services "are services and functions provided to the System Operator (SO) that facilitate and support the continuous flow of electricity so that supply will continually meet demand. The term, ancillary services, is used to refer to a variety of operations beyond generation and transmission that are required to maintain grid stability and security" [76].

Ancillary services are defined locally by each SO, therefore there is no standard definition for which services correspond to ancillary services and which do not. Fig. 2.1, includes a list of ancillary services from the Electrical National System in Chile (SEN, Chile [77]). Ancillary services description for Energy UK (UK) and the Australian Energy Market Operator (AEMO, Australia) can be respectively found in [76, 78].

A brief description of ancillary services in SEN-Chile is given below. The yellow area in Figs. 2.2b, 2.3b, 2.4 and 2.5 indicate a transition period between the beginning and nominal operation of a service. Note that the behaviour within the transition period is not defined.

- **Fast Frequency Control:** Automatic control action that allows for the provision of a fast

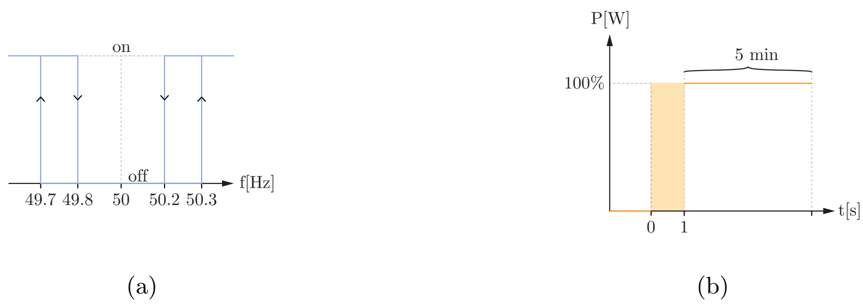

Figure 2.2: Fast Frequency Control: a) Activation and deactivation frequencies and b) Temporal availability requirements.

response to frequency deviations by regulating active power injection to the grid. Facilities must be able to provide, within 1 second, 100% of their compromised reserve (active power). This power support must be available for at least 5 minutes. The reserve must be equal (symmetric) for over and under-frequency regulation. Fig. 2.2 summarises the main aspects of Fast Frequency Control.

- **Primary Frequency Control:** Control actions oriented to hold and correct frequency deviations of the electric system. These actions are triggered automatically by frequency deviations beyond $\pm$ 0.2 [Hz]. Generating plants must be able to provide, within 10 seconds, 100% of their compromised reserve. This power support must be kept for at least 5 minutes. The reserve must be equal for over and under-frequency regulation. Under frequency deviation over $\pm$ 0.2 [Hz] PV (and Wind) farms, are enabled to provide this service, thought they must comply with the following regulations: response reaction must start within 2 seconds. of the detected incident, there is a dead band around 50 [Hz] of $\pm$ 0.2 [Hz], adjustable droop control between 4 to 8%, limited by availability of the primary resource (wind or solar). Fig. 2.2 summarises the main aspects of Primary Frequency Control.

- **Secondary Frequency Control:** Control actions oriented to reinstate the frequency of the system to its nominal value. This control operates in a centralised and automated scheme called Automatic Generation Control (AGC). The compromised reserve must be fully provided (100 %) within 5 minutes and keep full availability for 15 minutes. Fig. 2.4a shows the temporal availability requirements.

- **Tertiary Frequency Control:** Control actions oriented to reinstate the Secondary Frequency Control reserves or incorporate additional reserves to prepare the system to react to contingencies. This control scheme can operate automatically or manually. This service must be active, at

(a) (b)

Figure 2.3: Primary Frequency Control: a) Power reference and b) Temporal availability requirements.

(a) (b)

Figure 2.4: Frequency Control temporal availability requirements: a) Secondary and b) Tertiary.

the most, 5 minutes after its request and can be active for up to 1 hour. The temporal availability requirements are shown in Fig. 2.4b.

- **Interruptible Loads:** Reduction of the load by an individual customer, under request by the SO. The service aims at reducing demand in high-consumption/low-generation periods, performing congestion management or responding to systemic failures. The total of the compromised load must be reduced within 30 minutes of the request and can be held reduced for up to 2 hours. Fig. 2.5 shows the temporal availability requirements are shown in .

- **Voltage Control:** Control actions that allows local regulating of the voltage of the electric system within a range of operation, by injecting reactive power to the electric system. The maximum reactive power that the PV plant is expected to provide is stated in the PQ diagram of PV plants [42, p. 42]. The PQ diagram for PV plants is presented in Fig. 2.6. For PV (and wind) systems there are two voltage control schemes, static and dynamic. Static Voltage Control consists of providing a stationary reactive power previously established externally by the SO. On the other hand, Dynamic Voltage Control corresponds to a local action (the

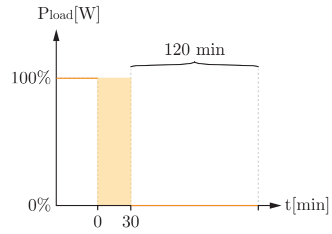

Figure 2.5: Interruptible Load temporal availability requirements.

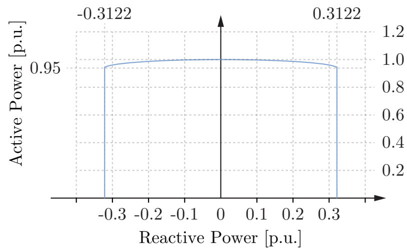

Figure 2.6: PV plant PQ diagram defining maximum active and reactive power generation requirements.

SO does not provide the reference) where the reactive power reference is imposed locally by the plant over its generating units. There are two kinds of Dynamic Voltage Control, fast (response with 1 second) and slow (response within 20 seconds). This service is mandatory for PV utilities with nominal rating over 50 MW.

- **Load Disengage:** Automatic or manual load disengage in order to preserve the security and quality of the service of the electric system. Automatic load disengage is performed due to an under-frequency threshold, a gradient of decreasing frequency, an under-voltage threshold or a direct disengage signals provided by the SO. On the other hand, when the customer falls into hazardous operations (for the safety of the electric system), the SO can request the customer to manually disengage its load.

- **Generation Disengage:** Disengagement or automatic reduction of power injection to the grid, to preserve the safety under abnormal operation of the electric system.

- **Defence Against Contingencies:** A set of automatic actions of corrective control oriented to avoid a partial or total blackout under extreme or critical contingencies.

- **Autonomous Start:** The capability of a generating unit to restart, without requiring an external power supply. This process will allow the energising of electric lines, take the load and synchronise with the electric system. This service is also known as Black Start [79–81].

- **Fast Isolation:** The capability of a generating unit to remain operating in isolated mode, powering only its auxiliary services, after an untimely disengagement from the electric system due to a partial or total blackout.
- **Synchronising Equipment:** The capability provided by certain equipment that allows the synchronising of two areas that have been kept operating independently (isolated from each other).

2.2.2 Enhanced Grid Code Compliance Services

These services are oriented at enabling the system to meet its reliability standards [80].

- **Fault Ride Through:** The capability to remain connected for a certain time during a voltage and/or frequency variation fault [80].
- **Ramp Rate Control:** The maximum allowable power variation per unit of time, usually with respect to 1 minute. Can restrict both positive (increasing) and negative (decreasing) power variations or only positive power variations [16].
- **Inertia:** A function that allows the provision of instantaneous support to drops in the frequency of the electric system [80]. It does not require an abnormal condition to operate.

2.2.3 Supply-Side-Management Services

Supply-Side-Management (SSD) Services reshape the power curve provided by the PV plant to the grid.

- **Peak Shaving:** To store energy in the ESS during low consumption and to release the stored energy during peak consumption [82,83]. Peak shaving is generally related to Demand-Side-Management (DSM), though it might be applied as SSM; in both cases establishing what is considered peak and low consumption is paramount. Fig. 2.7a shows Peak Shaving being performed as SSM for a PV plant.
- **Capacity Firming:** To comply with a previously committed power delivering schedule [84]. Figure 2.7b shows a Capacity Firming schedule, where the committed power and PV plant output power are drawn with a straight and dashed line, respectively. When PV plant power generation is above the committed power, energy is stored in the ESS; on the other hand when energy from the PV plant is lower than the committed power, energy is provided by the ESS.

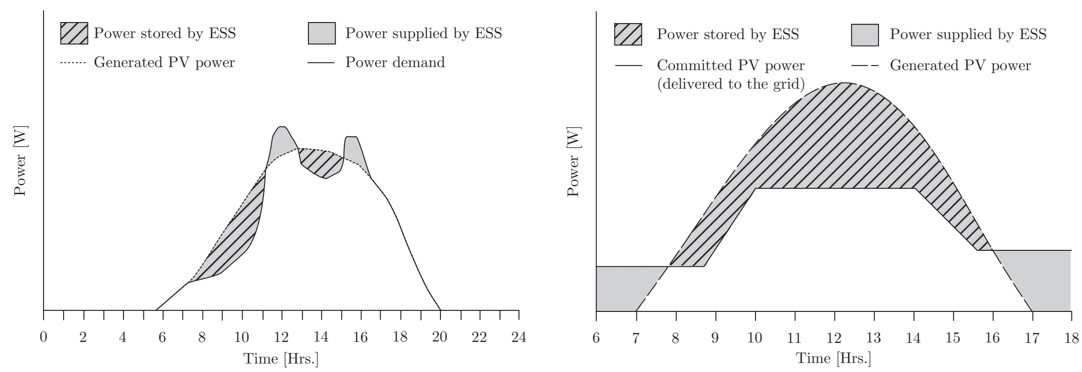

(a) (b)

Figure 2.7: complementary services:(a) Peak Shaving applied at SSM and (b) Capacity Firming.

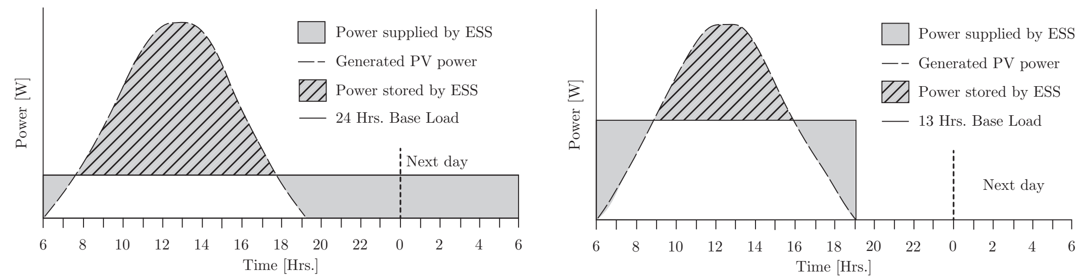

(a) (b)

Figure 2.8: complementary services: (a) 24 hours Base Load generation and (b) 13 hours Base Load generation.

- **Base Load Generation:** To generate constant power by storing/releasing power when generated power is above/below a certain constant reference value [84]. An example of 24 and 13 hours Base Load Generation for a PV plant are displayed in Figs. 2.8a and 2.8b, respectively. This can be considered as a particular case of Capacity Firming.

- **Load Levelling:** To level the power consumption profile during a day by storing/releasing energy when demand is below/above the average of the consumption forecasting [85, 86]. Figure 2.9a shows Load Levelling applied to a PV plant.

- **Load Shifting:** Also known as Energy Shifting, corresponds to the store/release of energy in order to increase profit, generally matching the power demand curve [84]. Figure 2.10a shows an example of Load Shifting daily behaviour.

- **Time Shifting:** To allocate energy for later use by storing all the generated energy when

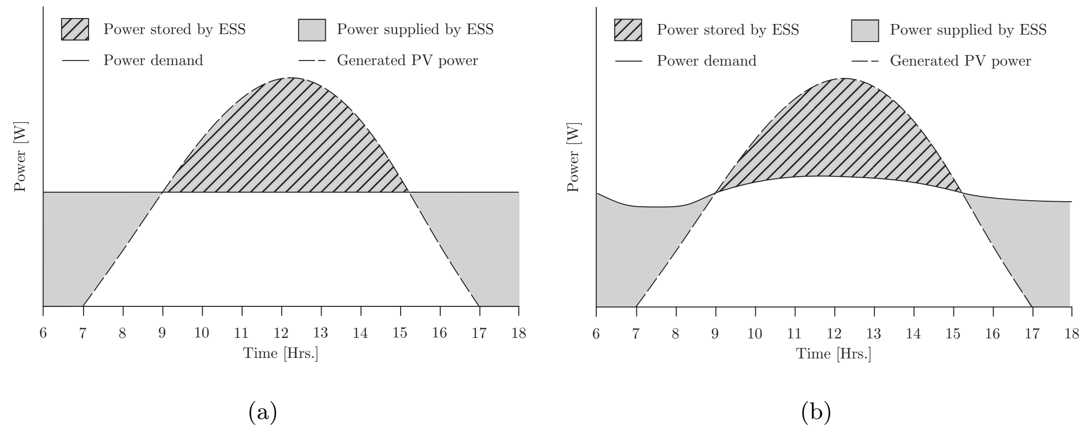

Figure 2.9: complementary services: (a) Load levelling with average consumption reference and (b) Load levelling with modified average consumption reference.

price is lower and and delivering all the stored energy when price is higher. The prediction of the price is calculated by a moving average [87]. Figure 2.10b shows an example of Time Shifting for a PV plant. This can be considered as a particular case of Load Shifting.

- **Load Following:** To regulate power generation as a response to regulating authority (SO) requirements [79, 80]. This action corrects future power mismatches between supply and demand [79,80]. Response time, power variation steep, and maximum and minimum generated power are previously defined [79]. This function is applied during normal operation and reacts slower than primary frequency control (>10[min]) [80].

- **Power Clipping:** To limit the maximum power that can be transferred from the utility to the electric network [16]. This power limitation is imposed by the rating of the inverter, and is associated, in PV systems, with PV plants with ILR>1 [68]. PV power beyond the clipping level can be stored, and later applied to provide (during a limited period) other complementary services (e.g. Frequency Control, Voltage Control, Ramp Rate Control, Inertia).

Note that a similar case to Power Clipping occurs in Power Curtailment, where power is also limited, though this action is performed by control instead of by the rating of the power converter [88]. Power Curtailment is mainly applied for frequency regulation.

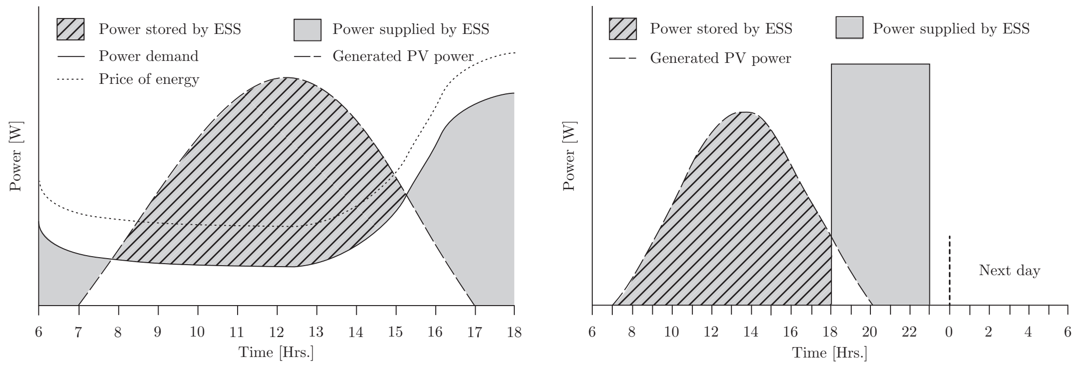

(a) (b)

Figure 2.10: complementary services: (a) Load Shifting and (b) Time Shifting.

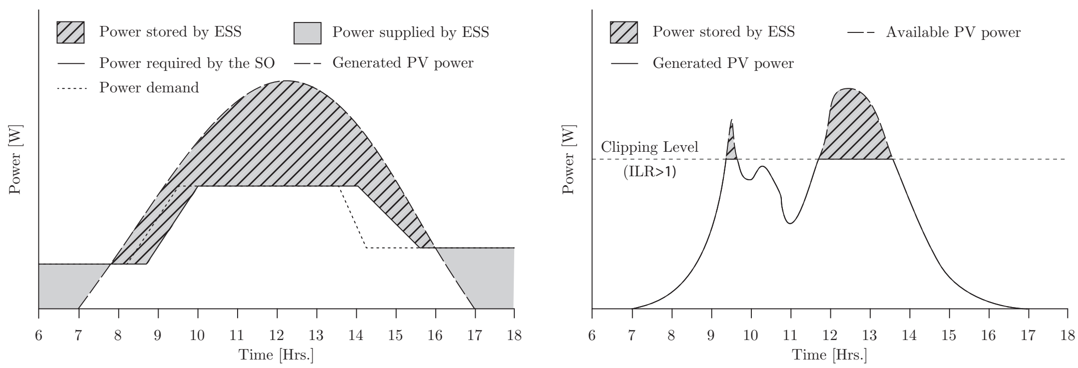

(a) (b)

Figure 2.11: complementary services: (a) Load Following and (b) Power Clipping.

2.2.4 Service Selection

Among all the aforementioned services, three were selected to be implemented in this thesis. The reasons to select each of the services are presented below.

PV array over-sizing (with respect to the PV inverter) has become a common practice in PV systems. This trend has been mostly motivated by the continuous decrease in cost of PV modules. However, the effects in terms of loss of generation and technical challenges associated with the recovery of that loss of generation have not been addressed. For these reasons Power Clipping was selected as one of the services to be analysed and implemented during the development of this thesis. As an additional motivation, Power Clipping in central inverter PV systems was the main topic of an industrial (research) project performed at the University of Nottingham, in which the author of this thesis took part.

Other of the services studied during the thesis is related to the limitation of the maximum output power variations per minute in PV systems. As explained in the previous chapter, power variability is one of the main limitations towards higher penetration of PV plants in the electric markets. Due to the stochastic nature of the ambient variables involved in PV generation, managing maximum power RR restriction is one of the most challenging restrictions for PV systems. In most PV configurations the multiple MPPT algorithms allow the reduction of the overall maximum power RR variations, associated with temperature and irradiance variations. However, the centralized-single-inverter configuration and single MPPT algorithm make central inverter configurations especially prone to high power variations. Moreover, the conventional manner for dealing with positive RR restrictions is to limit power generation. This incurs in a non determined amount of loss of generation, making ramp rate control one of the best alternatives for dealing with RR regulation in PV systems.

The last service considered in this thesis, targets the time displacement between the daily maximum PV power generation (arround midday [16]) and the daily maximum demand consumption (around 18:30 [89, 90]). As PV systems increase their penetration in electric market, displacing the PV power generation to the hours when the energy is needed will become an obligation. A manner of dealing with this future obligation is Peak Shaving, which allows the GO to establish the level of output power the PV system must inject into the grid. Additionally, Peak Shaving is one of the most challenging services among power-displacing Supply-Side-Management services, since the output power reference is not known in advance and is externally provided by the GO. For this reason Peak Shaving was selected as the third service to be implemented in the simulations presented in the thesis.

The last service considered targets the difference between PV power generation and power demand. As PV systems increase their penetration in electric market, matching the variable PV power generation with the demand will become an obligation. A way for dealing with this future necessity is Peak Shaving, which allows the GO to establish the level of output power the PV system must inject into the grid (according to the current power demand). Moreover, Peak Shaving allows managing not only peak power generation (or peak power demand), but also power spikes caused by sudden changes of irradiance (direct irradiance plus refracted irradiance). Additionally, Peak Shaving is one of the most challenging services among Supply-Side-Management services, since the output power reference is not known in advance, it is highly dynamic and is externally provided by the GO. For these reasons Peak Shaving was selected as the third service to be implemented in the simulations presented in the thesis.

Peak Shaving was preferred over Load Following since the faster reaction for provision of the

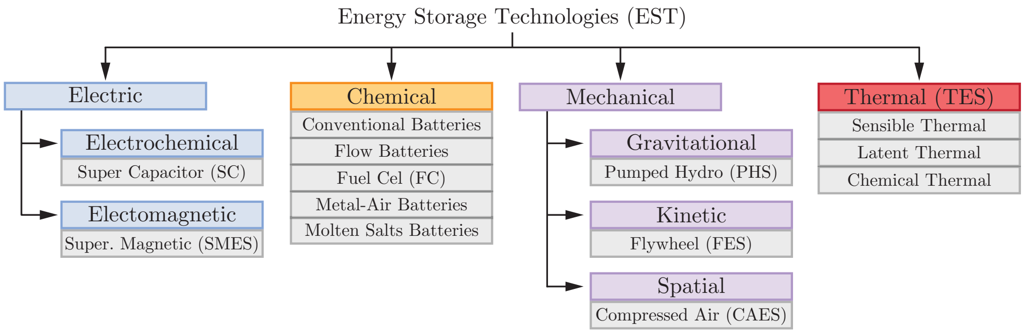

Figure 2.12: Electric energy storage technologies classification [16].

service makes it a better alternative for reducing the effects of power variability and the service is focused at saving (storing) the PV power exceeding the demand curve.

The other SSM services were discarded, since the higher amount of energy associated to each service makes them less economically attractive.

Ancillary services, however important for the correct operation of electric power systems, were not selected among the three services to be implemented during the thesis, since they do not have a direct effect over the mitigation of the drawbacks limiting further PV penetration.

The same criteria applies to Fault Ride Through which targets operation under an abnormal condition.

2.3 Energy Storage Technologies

An ESS consists of an EST and its power converter. This section focuses on ESTs capable of transforming electric energy into another storable form of energy, namely electromagnetic, chemical, mechanical or thermal [91, 92].

2.3.1 Classification

According to the nature of the stored energy, ESTs may be classified as shown in figure 2.12.

A brief description of ESTs, from figure 2.12, is presented below.

Electrochemical

The idea behind Electric ESSs is to stow energy by accumulating electric charge, therefore generating an electric field and a voltage difference between both terminals (electrodes) of the ESS. Capacitors are the only commercially successful and widespread technology to store electric energy. When storing energy, capacitors accumulate electric charge, increasing the voltage between both electrodes. To release energy, capacitors release charge hence reducing their voltage.

In 1978 a new kind of capacitor, named Super-Capacitors (SC), with higher capacity density ($[F/m^3]$) and higher energy density ($[Wh/m^3]$), were developed [91]. SCs rely not only on electric field to store energy, but also on chemical reactions. SCs are also known as Ultra-Capacitors (UC).

Electromagnetic

Electromagnetic Energy Storage, also known as a Magnetic Energy Storage Systems (MESSs), accumulate energy as magnetic field. The principle behind MESS is to store energy by increasing the circulating current through an inductor, hence building up their magnetic field. Current must be kept flowing in order to retain the stored energy. The inverse process allows getting the stored energy back from the inductor [91, 93].

Part of the energy fed to the inductor is dissipated as heat by the internal resistance of the coil. To eliminate such power loss, the inductor can be built with superconducting materials. MESS based on superconducting coils are called Superconducting Magnetic Energy Storage (SMES).

Chemical

Chemical Energy Storage, also known as Electro-Chemical Energy Storage, stores energy by transforming electrical energy into chemical, through electrochemical reactions. Stored energy is released through the inverse process. The broad spectrum of technologies capable of Chemical Energy Storage, may be classified as: Conventional Batteries, Flow Batteries, Fuel Cells, Metal Air Batteries, Molten Salts Batteries and Liquid Metal Batteries. Chemical Energy Storage Technologies are also sub-classified as primary (non-rechargeable) and secondary (rechargeable) batteries. Due to the focus of this thesis only secondary Chemical Energy Storage Technologies will be considered.

The term Battery Energy Storage Systems (BESS) is usually used to refer to a battery pack with or without its power converter.

Gravitational

Gravitational energy corresponds to the potential energy of a body of a given mass stored at a given height. Nowadays, Pumped Hydro Storage (PHS) is the only commercially successful way to store gravitational energy. The idea behind PHS (also named Pumped Hydro, Pumped Storage or Pumped Hydroelectric Storage) is to store large amounts of water at a certain height.

PHSs pump water from a lower level into an upper one, transforming electric energy into gravitational energy. Gravitational energy is transformed back to electric energy when releasing the stored water in the upper level to the lower level, through a set of turbine-generators.

Kinetic

Kinetic energy refers to the energy stored in a body as movement. The movement may be in any of its three forms, rotational, translational or vibrational. Until now only rotational kinetic energy has been usable for energy storage purposes.

Flywheel Energy Storage (FES), also known as Flywheel, is an electro-mechanical system composed by a rotating body merged onto the rotor of an electric machine. The idea is to store electric energy as rotating kinetic energy, therefore the inertia, rotational speed and tensile strength of the body are paramount.

Spatial

The idea is to store a given volume of gas at a given pressure (and temperature), transforming electric energy into potential energy (pressure). The inverse process is obtained when releasing (expanding) the gas.

Since air is the gas being compressed, these systems are called Compressed Air Energy Storage (CAES). There are only two operational CAES plants, Hunfort-Germany (commissioned: 1978) and McIntosh-USA (commissioned: 1991). Two new demonstration facilities, based in Advanced CAES (A-CAES), have been built in the last few years (2015 and 2019) and a third one is due by 2020 [86].

Thermal

Many Thermal Energy applications are heat oriented, using thermal energy directly, without transforming it into another form of energy. In order to stow electric energy, Thermal Energy Storage Systems (TESS) require a thermoelectric generator or a heat engine, to transform electric energy into storable thermal energy and vice versa [94]. TESS, also known as Solar Fuels [92], have evolved into three different kinds of storage technologies: sensible heat storage, latent heat storage and reversible chemical reaction heat storage [94]. Thermal Energy Storage Technologies are usually built of a thermal material, a heat exchanger and a containment system.

2.3.2 Comparisons

Only a handful of ESTs have reached full technical and commercial maturity [94], leaving many ESTs under continuous development and evolution, thus keeping an updated comparison between technologies is a challenging task. Nevertheless, there have been many works contrasting ESTs, some of the latest are [30–32, 95]. The results of those comparisons are summarized in table 2.1, a further comparison including Power Density ([W/m^3]), Energy Density ([Wh/m^3]), Specific Power ([W/kg]), Self Discharge Rate ([% /day]), Cycle Life ([cycles]) and Scale ([MW]) is presented in [30–32, 95].

The most relevant factor when deciding which EST to use is the application, since it provides an insight into the requirements and desired performance. Figure 2.13 [17, 18] shows power ratings and discharge times for different applications and ESTs. From here, it is possible to choose an adequate EST capable of meeting power and discharge time requirements for a given application.

2.3.3 EST selection

The first step towards selecting an EST is knowing the application in which the EST will be implemented. The selected application (Ramp Rate control, Power Clipping and Peak Shaving) sets the power and energy profile that each EST must be able to provide. An example of two different EST sizing strategies (for ramp rate control and power clipping) can be found in chapter 4.

A second step is to decide the criteria which will be applied to select the best performing ESTs. The first criterion selected is modularity/scalability. As stated in the specific objectives of the

Energy Storage Technology	**Power cost (USD/kW)**	**Energy cost (USD/kWh)**	**Round-trip efficiency (%)**	**Lifetime (years)**	**Specific energy (Wh/kg)**	**Maturity**
SC	$100-300$	$300-2,000$	$84-98$	$5-30$	$0.05-15$	Developing
SMES	$200-350$	$1,000-10^4$	$85-98$	$15-30$	$0.5-5$	Demo
LiIon [1]	$1,200-4,000$	$400-2,500$	$75-97$	$5-15$	$120-230$	Commercial
PbA [1]	$175-600$	$150-400$	$63-90$	$5-15$	$30-50$	Mature
NiCd [1]	$500-1,500$	$600-2,400$	$60-75$	$10-20$	$15-55$	Mature
VRB [2]	$600-3,700$	$150-1,000$	$60-90$	$5-20$	$25-35$	Developing
ZBB [2]	$700-2,500$	$100-1,000$	$60-85$	$5-10$	$65-75$	Developing
Hydrogen [3]	$400-2,000$	$1-15$	$20-66$	$5-15$	$600-1,200$	Developing
Metal-Air	$100-250$	$10-160$	$50-65$	>1	$1,000-1,300$	Demo
NaS [4]	$1,000-4,000$	$300-500$	$75-90$	$10-15$	$150-240$	Commercial
ZEBRA [3]	$150-300$	$230-345$	90	$5-15$	$86-140$	Discontinued
PHS	$500-2,000$	$5-100$	$65-87$	$30-60$	$0.5-1.5$	Mature
FES	$100-350$	$1,000-5,000$	$85-95$	$15-20$	$5-80$	Commercial
CAES	$400-1,800$	$2-400$	$41-90$	$20-60$	$30-300$	Developed
Low Temp. [5]	$200-300$	$20-50$	$30-50$	$10-40$	$100-200$	Developing
High Temp. [5]	$200-300$	$30-60$	80	$5-15$	$80-250$	Demo

[1]: conventional battery, [2]: flow battery, [3]: fuel cell, [4]: molten salts batteries and [5]: TES.

Table 2.1: Energy Storage Technologies specifications [30–32]

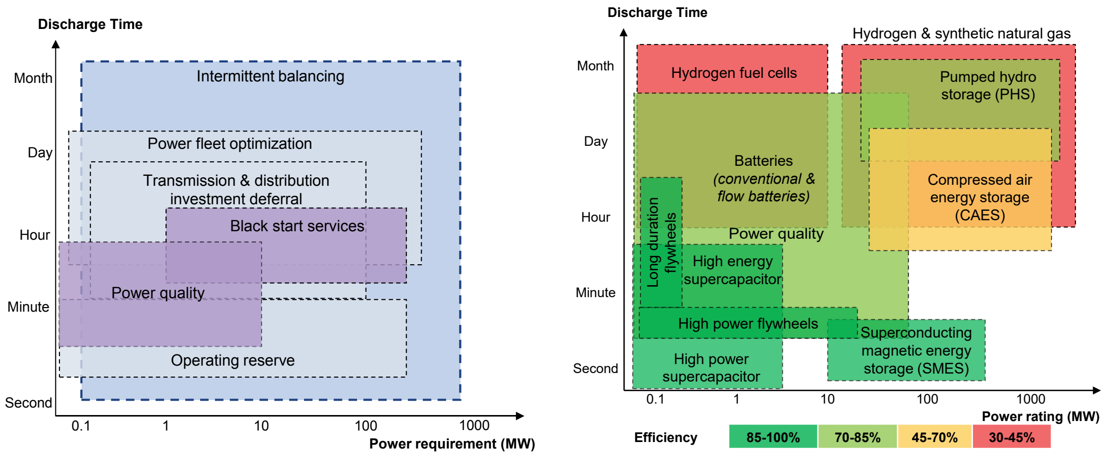

(a) (b)

Figure 2.13: EST applications and ratings [17, 18]: a) Power requirement and discharge time and b) Power capacity and discharge time of ESTs.

thesis, modularity is one of the requirements that must be applied to the PV/ESS system. This criterion discards PHS and CAES, since their way of construction is inherently non-modular nor scalable.

An important part of any complementary service is minimising the energy losses associated to the provision of the service. In this context round-trip efficiency has been selected as the second criterion to be apply in the EST selection process. ESTs having round-trip efficiencies equal or higher than 95% were selected as being possible candidates to provide the aforementioned complementary services.

The third criteria applied was the level of maturity of the EST. The reason for choosing this criterion is that the idea is to propose solutions for the current status of PV power penetration in the electric markets. Thus, ESTs at “Demo” stage were discarded as possible solutions to provide storage capability.

According to these criterion Li-Ion batteries, SCs and FESs were selected as the ESTs capable of providing the selected complementary services and complying with the aforementioned criterion.

On the one hand, applications where power requirements are higher than energy requirements (ramp rate control for global MPPT) SCs offer a less expensive solution. On the other hand, in applications where energy is more relevant as Power Clipping and Peak Shaving, Li-Ion batteries offer a less expensive solution. For these reasons the research presented in this thesis is focused on ESTs based on SCs and Li-Ion batteries.

Note that the current selection could be modified in the near future since most newer ESTs (SCs, Li-Ion batteries, non conventional batteries and FES) are experiencing increases in their lifetime and round-trip efficiency, and decrease of their prices due to new discoveries and improvements in manufacturing technologies.

2.4 Bidirectional power converters for PV/ESS configurations

In order to manage the power flow between an EST and a PV system a converter topology capable of controlling the bidirectional power flow is required. This section presents a literature review of the PV/ESS configurations and the power converters that enable the performance of the aforementioned task. In [10], bidirectional boost converters are applied to merge a Li-Ion battery bank and a SC bank into the common DC bus of a DC micro grid, composed of a PV system, a Wind turbine, a diesel DC generator and a DC load. Three alternatives to interface Li-Ion $LiFePO_4$ or Lead Acid batteries into medium or large scale PV systems at AC-grid side are proposed in [2]. The first alternative proposes a dc-ac configuration formed by several dual-active bridge (DAB) dc-dc converters connected to an Active Neutral Point Clamped (ANPC) converter. The input of each DAB is connected to an independent array of batteries, while the output of all DABs are serialised and connected to the dc-link of the ANPC, thus providing isolation and enabling connection at medium voltage. The second alternative consists of a Cascaded H-Bridge converter. In this topology each H-Bridge handles an independent array of batteries. This alternative allows low-voltage battery arrays to be merged into a medium-voltage grid, through a single power converter. The third proposed alternative consists of an ANPC converter connected to a high voltage battery array. An interleaved bidirectional dc-dc Boost converter and its control are also presented in [2], as an alternative for connecting a 7 kW Li-Ion BESS to the dc-link of a two-stage 5 kW PV system. This last configuration is validated through simulations. In [11] a DC grid composed by a PV plant, a SC bank, a Li-Ion BESS and load is presented. The PV module and Li-Ion BESS are connected to a DC bus through an Isolated Unidirectional dc-dc Boost Converter, while the SC bank is connected to the DC bus through a two-stage DC/DC configuration, where each stage is composed by three interleaved non-isolated bidirectional boost converters. Additionally, an Isolated Bidirectional Ćuk converter is used to directly connect both ESTs (SC bank and Li-Ion battery pack). In [13], two bidirectional boost converters in interleaved connection are used to merge an SC bank into the dc-link of a two-stage PV configuration. In [12], a Li-Ion battery and a fuel cell are connected at the DC-grid side to a PV system. Four interleaved unidirectional boost converters are used to interface the fuel cell, while the Li-Ion battery relies on four interleaved bidirectional boost converters for its connection. A bidirectional boost converter is proposed in [14] as an alternative for merging a battery bank into the dc-link of a two-stage

PV system. In [4], four different power converters are proposed to connect EST into transport or grid applications. The proposed power converters are a bidirectional dc-dc boost converter, a bidirectional dc-dc buck converter, a dc-dc dual active bridge and a dc-ac 2LVSI. In [15], a bidirectional buck converter cascaded to a bidirectional boost converter are proposed to connect a battery into a PV system. The connection is performed at the input of an AC module configuration, parallel to the PV module.

During the development of this thesis the AC-grid side and the PV (input) side configurations were applied to merge ESS into PV systems. Central PV inverters were used to emulate a PV system in both PV/ESS configurations. Commercially available central inverters for PV systems operate at a low voltage level, i.e. PV array voltage (input voltage) < 1.5 [$\mathrm{kV_{dc}}$] and output voltage (AC grid voltage) < 1 [kV] [9, 72]. For this reason, only power converters allowing connection at low voltage were considered, discarding converters operating at medium or high voltage level as the ones proposed in [2] (ANPC and CHB). In addition, most Li-Ion batteries and SCs banks operate at low voltage (≤ 100 [V]), requiring a high voltage gain to reach the voltage level at the PV/ESS merging point. This requirement eliminates bidirectional buck converters and bidirectional boost converters, the first one due to the required voltage elevation and the second one due to the limited voltage gain of boost converters and their low efficiency associated with high voltage gains [96]. Nonetheless, isolated boost converters present a promising alternative, allowing a higher voltage gain than standard boost converters offering, in addition, galvanic isolation between input and output. Moreover, efficiency is a topic of great importance when analysing power systems and even more when analysing ESTs, since their bidirectional power-flow nature incurs in losses during both energy conversion processes (storing and releasing energy). To assess the overall efficiency of ESSs, not only the efficiency of ESTs must be considered, but also the efficiency of the interfacing bidirectional power converter. Partial Power Converters (PPCs) have emerged as a higher efficiency alternative to traditional DC-DC Full Power Converters (FPCs), since only a part of the full system power is processed by the PPC converter, reducing its size and losses compared to FPCs [97]. PPCs have been proposed for a broad variety of unidirectional power flow applications, as such as PV power plants [97–99], long LED arrays [100] and electric vehicle fast charging stations [101]. Despite their advantages, PPCs remain a non-explored alternative in bidirectional power applications.

Due to the aforementioned reasons the IBBC was selected to interface the EST and the PV systems. Additionally, two alternative topologies based on PPCs were developed to allow the connection between EST and PV plant. The circuital diagram and mathematical model of these 3 topologies are available in chapter 5.

2.5 Summary

This chapter introduced the concepts related to complementary services and ESTs. The chapter was separated in to two main sections.

The first section presented a classification of complementary services and a brief definition of each service. Power Clipping, Ramp Rate Control and Peak Shaving were selected as relevant services to be implemented during the thesis. The main reason to select these services was that each of them targets a current drawback, limiting a further penetration of PV systems in electric networks. Specifically, Power Clipping allows to study of how the oversizing of PV modules affect the loss of PV generation, Ramp Rate Control aims at limiting output power variation while storing the exceeding power and Peak Shaving allows managing the differences between PV power generation and power demand.

The second section of this chapter presented a classification and general description of ESTs for electrical applications. This section also included a general comparison between ESTs and the justification for selecting two ESTs as alternatives for providing the selected complementary services (Power Clipping, Ramp Rate control and Peak Shaving). The criterion applied to select the most adequate ESTs were modularity, maturity and round-trip efficiency. The application of the criterion resulted in the selection of Li-Ion batteries, SCs and FESs as possible alternatives. However, economically speaking SCs are a less expensive alternative for power oriented applications such as ramp rate control for Global MPPT. In the case of energy-oriented applications, such as Power Clipping and Peak Shaving, Li-Ion batteries are the less expensive solution. Therefore, the analyses contained in this thesis apply to SCs or Li-Ion batteries.

The third section of this chapter presented a literature review of bidirectional power converters for ESS/PV configurations. Since central inverter PV systems were previously selected to be the focus of the research presented in this document, only bidirectional power converters capable of meeting the technical requirements of commercially available central inverter were considered. In this context, the IBBC and partial power converters were selected as the alternatives to be analysed in the thesis. Note that the IBBC presents advantages in terms of its input-output voltage gain, while PPCs are known for their higher efficiency when compared with conventional full power converters.

Chapter 3

PV model

3.1 Introduction

Power clipping was selected as one of the complementary services to be analysed in this thesis. As stated in the previous chapter, this selection was motivated by an industrial project performed at the University of Nottingham. The objectives of the industrial project were to estimate the loss of generation (in kWh) due to power clipping, to size an ESS capable of storing the power beyond clipping level and to propose a PV/ESS configuration and control strategy that allows retrofitting an existing PV plant while minimising the loss of generation caused by power clipping. The main restriction of the project was that the available data was limited to the solar irradiance, ambient temperature and (clipped) output power of the PV plant. Since the PV plant output power was already clipped, the only alternative for estimating the loss of generation, was to predict the theoretical maximum PV power (non-clipped) through a model of the PV system and subtract this estimation from the real (clipped) PV power.

This chapter focuses on modelling a PV plant to predict the maximum available PV power, under certain irradiance and temperature conditions. The chapter is divided into three main topics. The first topic (section 3.2) states the requirements for the PV model in terms of the inputs and output that can be applied to model the PV plant. This chapter also presents the mainstream PV models available in literature. A description of the three different PV modelling techniques available in literature (sections 3.2.1 to 3.2.3) is also presented in this section. The second main topic is the comparison (section 3.2.4) of the results obtained from each PV model. This comparison, under power clipping scenario, shows novel results and corresponds to new knowledge. Finally, the third topic presents the estimation of annual PV power generation for two locations, based on one of the previous models (sections 3.3 and 3.4).

Note that the technical parameters of the PV modules and measurements of irradiance, temperature and real PV power generation for a full year (with sampling period of 1 minute) were available for the estimation and comparison of PV power generation.

3.2 PV Model Selection

The main restriction to the project was that the data available to be used as inputs of the PV model was limited to the measurements of irradiance, temperature and (clipped) output power of the PV plant. These measurements were taken once per minute during a full year and were available to be used as inputs of the PV model. The PV model has to predict the theoretical maximum PV power. As stated in the introduction, the PV model prediction will be used to: estimate the loss of generation (chapter 4), as the main input to the ESS sizing strategies (chapter 4) and as one of the inputs of the PV/ESS configuration control schemes (chapter 6). This last application will impose a maximum execution time for the PV model (see section 3.2.4).

There are several PV models in literature capable of predicting the theoretical maximum PV power. A classification of the most relevant PV models, capable of predicting the theoretical maximum PV power, is presented in Fig. 3.1.

Circuital models represent the behaviour of the PV system, i.e. I-V (current vs. voltage) and

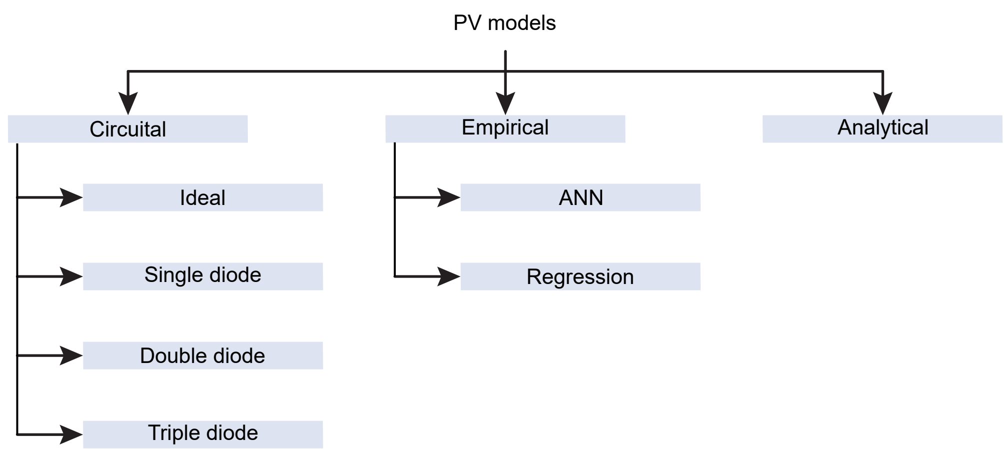

Figure 3.1: Classification of PV module models, for MPP prediction, under irradiance and temperature inputs: circuital [19], empirical [20, 21] and analytical [22].

P-V (power vs voltage) characteristic curves, through an electric circuit. Among circuital models, the single diode model is the most commonly used model, since it presents a good tradeoff between simplicity and accuracy [19, 102]. However, according to [19], the oversimplification of the ideal model (lack of shunt and series resistors), makes it a bad alternative to predict realistic PV power generation. Moreover, when comparing a simulation of a PV system with single and double diode circuital models, the difference between both results is negligible [103]. However, the single diode circuital model is preferred since it is less complex, requires fewer parameters to be identified and the shortest computational time to estimate the output. The same criteria can be applied with respect to the triple diode model, that has even more parameters to be identified, taking a longer computational time to calculate its output.

Empirical models consist of a predefined algebraic model with variable bias and weights. These models depend on a set of known inputs and their corresponding output(s), to minimise the error between the known output (real output) and the predicted output. An optimisation process is applied over the variable bias and weights to minimise the error between the predicted output and the real output. Two empirical models were found in literature, namely regression [20] and Artificial Neural Network (ANN) [104]. A comparison between regression and ANN models, to predict PV power generation, was presented in [20]. The comparison considers data sets from several years, and contrasts the results with empirical measurements. The results show that ANN generates the best prediction of the PV power.

Analytical models, apply a single equation to predict, from irradiance, temperature and datasheet parameters of the PV system, the output power generated by the PV system [22]. In contrast with circuital models and empirical models, analytical models are not required to perform a parameter identification nor the fitting curve process (minimisation of the output error).

Note that the analysis and validation of the PV models available in literature consider power generation without limitations imposed by the inverter. However, power clipping imposes a limitation over the maximum level of power that the PV plant can generate. Thus, limiting the range of useful data for models that require training, that rely on empiric data to fit a curve or that perform parameter identification based on empiric data. The comparison of PV models available in literature [22, 103, 105, 106], to predict the theoretical maximum PV power, consider data sets for the complete range of operation of PV modules, i.e. without power limitations imposed by the inverter (power clipping). For this reason, a novel comparison considering the restrictions in terms of data availability imposed by power clipping, is necessary. The best performing models of each category were selected to be implemented and compared, namely the single diode model (circuital), the ANN (empirical) and the analytical models. A detailed description of each of these methods is given below.

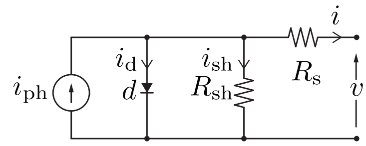

Figure 3.2: Single diode circuital model for PV modules.

3.2.1 Single diode circuital model

An standard single diode circuital model such as the one presented in [107] is shown in Fig. 3.2. Where the parameters and variables i, v, d, R_{s}, R_{sh}, i_{ph}, i_{d} and i_{sh} are respectively the PV module output current in A, PV module output voltage in V, anti-parallel diode, equivalent series resistance in Ω, shunt resistance in Ω, photo-current in A, diode current in A and current through the shunt resistance in A. Applying Kirchhoff's current law to i,

$$i = i_{\mathrm{ph}} - i_{\mathrm{d}} - i_{\mathrm{sh}} \tag{3.1}$$

$$i = i_{\mathrm{ph}} - i_{\mathrm{o}} \left[e^{\left(\dfrac{q \cdot (v + R_{\mathrm{s}} \cdot i)}{n_{\mathrm{s}} \cdot m \cdot k \cdot T_{\mathrm{stc}}} \right)} - 1 \right] - \frac{v + R_{\mathrm{s}} \cdot i}{R_{\mathrm{sh}}} \tag{3.2}$$

where i_{o}, q, n_{s}, m, k and T_{stc} correspond respectively to the reverse saturation current of the anti-parallel diode (d) in A, charge of an electron in C ($q = 1.602 \cdot 10^{-19}$ C), number of PV cells connected in series per PV module, diode quality or ideal factor, boltzmann's constant in J/°K ($K = 1.3806503 \cdot 10^{-23}$ J/°K) and module temperature in °K at Standard Test Condition (STC). The thermal voltage, defined as $v_t = m \cdot k \cdot T_{\mathrm{stc}}/q$, is commonly used to shorten the writing of eq. (3.2).

The parameters to be identified correspond to i_{ph}, i_{o}, m, R_{s} and R_{sh}. Where i_{ph} depends on the module temperature and irradiance, i_{o} only depends on the module temperature, and m, R_{s} and R_{sh} are independent of the temperature and irradiance. A parameter identification procedure was performed according to [107].

Equations (3.3) to (3.8) from [107], account for the irradiance and temperature dependence of the circuital model, where G, G_{stc}, k_{v}, k_{i}, T, T_{stc} and ΔT correspond respectively to the irradiance in W/m^2, irradiance at STC in W/m^2, open circuit voltage linear thermal dependence in %/°K, short circuit current linear thermal dependence in %/°K, module temperature in °K, module temperature at STC in °K and module temperature difference between T and T_{stc} ($T - T_{\mathrm{stc}}$); sub-index $_{\mathrm{stc}}$ indicates variables at STC.

$$v_{\text{oc}}(G) - \ln\left(\frac{i_{\text{ph stc}} \cdot (G/G_{\text{stc}}) \cdot R_{\text{sh}} - v_{\text{oc}}(G)}{i_{\text{o}} \cdot R_{\text{sh}}}\right) \cdot n_{\text{s}} \cdot v_{\text{t}} = 0 \tag{3.3}$$

Eq. (3.3) is numerically solved through Newton-Raphson.

Eqs. (3.4) to (3.7) show the irradiance and/or temperature dependence of the open circuit voltage, short circuit current, reverse saturation current and photo current.

$$v_{oc}(T) = v_{\text{oc stc}} \cdot \left(1 + \frac{k_{\text{v}}}{100} \cdot \Delta T\right) \tag{3.4}$$

$$i_{\text{sc}}(T) = i_{\text{sc stc}} \cdot \left(1 + \frac{k_{\text{i}}}{100} \cdot \Delta T\right) \tag{3.5}$$

$$i_{\text{o}}(T) = \left(i_{\text{sc}}(T) - \frac{v_{\text{oc}}(T) - i_{\text{sc}}(T) \cdot R_{\text{s}}}{R_{\text{sh}}}\right) e^{\left(\frac{-v_{\text{oc}}(T)}{n_{\text{s}} \cdot v_{\text{t}}}\right)} \tag{3.6}$$

$$i_{\text{ph}}(G,T) = \left(i_{\text{o}}(T) \cdot e^{\left(\frac{v_{\text{oc}}(T)}{n_{\text{s}} \cdot v_{\text{t}}}\right)} + \frac{v_{\text{oc}}(T)}{R_{\text{sh}}}\right) \cdot \left(\frac{G}{G_{\text{stc}}}\right) \tag{3.7}$$

Finally, eq. (3.2) is rewritten considering irradiance and thermal dependence. The resulting equation is solved through iterations using the Newton-Raphson numerical method, providing the output current as a function of the irradiance, module temperature and voltage of the PV module.

$$i(G,T) = i_{\text{ph}}(G,T) - i_{\text{o}}(T)\left[e^{\left(\frac{v + R_{\text{s}} \cdot i(G,T)}{n_{\text{s}} \cdot v_{\text{t}}}\right)} - 1\right] - \frac{v + R_{\text{s}} \cdot i(G,T)}{R_{\text{sh}}} \tag{3.8}$$

The numerical resolution of the equations of the circuital model was based on the Newton-Raphson method, although other numerical methods can be implemented instead, as in [102] where the bisection numerical method is applied.

PV plant DC power can be estimated from eq. (3.9), where N_{sp} and N_{ms} correspond to the number of strings in parallel and modules in series per string, scaling consequently a single PV module model to the PV plant rating. The dependence on irradiance, module temperature and voltage is acknowledged through parenthesis notation. Finally, the MPP is obtained through inspection of the P-V curve. This curve is obtained by calculating the output current for several voltage values at a given irradiance and temperature pair.

$$P_{\text{circ}}(G,T,v) = v \cdot i(G,T) \cdot N_{\text{sp}} \cdot N_{\text{ms}} \tag{3.9}$$

$$P_{\text{mpp circ}} = max(P_{\text{circ}}(G, T, v)) \tag{3.10}$$

Additionally, the system of equations presented in this section requires the identification of several parameters (R_{s}, R_{sh}, m). This is achieved through Multi-variable Newton Raphson, applied to a system of equations derived from the data available in the datasheet of the PV module, as shown in [108].

3.2.2 Artificial Neural Network

A three-layered feed-forward Artificial Neural Network (ANN), as the one shown in Fig. 3.3, was generated through MATLAB™ ANN fitting tool. The network is formed by 2 input neurons, 1 hidden layer (with 4 neurons) and one output neuron. The input to the network correspond to irradiance G in W/m^2 and module temperature T in °K measurements, while the output corresponds to DC power ($P_{\text{mpp ann}}$) in W produced by the PV plant. The amount of neurons in the hidden layer was chosen to emulate the amount of PV inverters in the PV plant (4 inverters). Additionally, the ANN model has 3 layers (Input, Hiden, Output), matching most ANN models working with irradiance and temperature inputs [109].

The output z^l_{j} of neuron j in layer l depends on its inputs x^l_{i} ($i \in \{1, \ldots, m\}$), input weights (w^l_{ij}), a bias b^l_{j} and a transfer or activation function $f(\cdot)$ [22], as shown in eq. (3.11). Outputs of neurons in a previous layer correspond to inputs of neurons in the next layer, for the hidden layer ($layer_1$) inputs are provided by the input layer ($layer_0$).

$$z^l_{\text{j}} = f(b^l_{\text{j}} + \sum_{i=1}^{m} w^l_{\text{ij}} \cdot x^l_{\text{i}}) = f(\lambda) \tag{3.11}$$

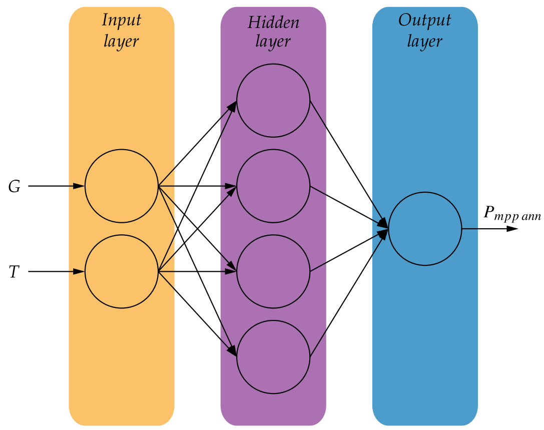

Figure 3.3: Two layer feed-forward ANN diagram for PV plants

A sigmoid transfer functions (*logsig*) was used for neurons in the hidden layer, while a linear transfer function (*purelin*) was applied to the output neuron. These transfer or activation functions ($f(\cdot)$) are defined according to [110], as shown in eq. 3.12.

$$f(\lambda) = \begin{cases} \dfrac{1}{1+e^{-\lambda}} & , \quad \textit{hidden layer neurons} \\ \\ \lambda & , \quad \textit{output layer neuron} \end{cases} \tag{3.12}$$

The training strategy considers a total of 582,174 pairs of input data points (irradiance G in W/m^2 and module temperature T in °K) and 582,174 target points (measured DC power (P_{pv}) in W), using 70%, 15% and 15% ratios respectively for training, validation and testing.

The training procedure consists of adjusting the weights and bias of each neuron in order to minimise the mean squared error between the target (measured DC power P_{pv}) and the ANN output ($P_{\mathrm{mpp\ ann}} = z_1^2$), this optimisation (based in Levenberg-Marquardt method) is carried out by Bayesian Regularization back-propagation [111].

$$P_{\mathrm{mpp\ ann}} = z_1^2(G,T) \tag{3.13}$$

3.2.3 Analytical model

This mathematical model, presented in eq. 3.14, predicts the MPP ($P_{\mathrm{mpp\ eq}}$ in W) as a function of the irradiance (G in W/m^2) and the module temperature (T in °K).

$$P_{\mathrm{mpp\ eq}} = \left(\left[\frac{k_{\mathrm{p}}}{100} \cdot \Delta T + 1 \right] \cdot G \cdot A \cdot \eta \right) \cdot \eta_{\mathrm{mppt}} \cdot N_{\mathrm{ms}} \cdot N_{\mathrm{sp}} \tag{3.14}$$

Where k_{p}, ΔT, A, η, η_{mppt}, N_{ms} and N_{sp} are respectively the temperature coefficient of P_{mpp} in %/°K [112] (or the maximum power correction factor for temperature [22]), the module temperature difference between the module temperature T and the STC module temperature T_{stc} in °K ($\Delta T = T - T_{\mathrm{stc}}$), area covered by PV cells in m^2, STC module efficiency, MPPT efficiency [113], the number of modules in series in each string and number of strings in parallel. A similar alternative was presented in [22] where $A \cdot \eta$ is replaced by $P_{\mathrm{mpp\ stc}}/G_{\mathrm{stc}}$.

3.2.4 Model comparison

This section presents the validation and comparison of the previously presented PV models against real data obtained from a PV plant located in Cambridgeshire, UK.

Three criterion were chosen to select the best fitting PV model, namely the error below the clipping level (measured through 4 error metrics), execution time and percentage error at STC.

The first criterion allows the validation of the models below the clipping level. The second criterion corresponds to the execution time. Since the selected model will be implemented as an input of the control schemes (chapter 6), the execution time becomes a relevant parameter. Additionally, the same control platform that will control the ESS should be capable of estimating the PV power generation. Therefore, an execution time of 100 micro-seconds was chosen as the maximum allowable value. The last criterion considered was the percentage of error at STC. The first criterion allows to validate the model below the clipping level. Thus, an additional criterion is necessary to analyse how adequate the model is beyond the clipping level. According to the manufacturer degradation curve, the PV module has a guaranteed power performance of 95% of its nominal power at STC by the fifth year of operation [112]. The PV plant had five years of operation by the time the data was acquired, thus a maximum error of 5% was selected as the maximum allowable percentage of error at STC.

The first step towards validating the PV models is knowing the power generated by the PV system, thus enabling a straight forward comparison between prediction and real data. Accordingly, Fig. 3.4 shows the annual power generation of the PV system, where measurements were taken every minute. It must be noted that the power rating of the PV array exceeds the power rating of the inverter, hence causing clipping. This is shown in Fig 3.4b, where power is normalised with respect to the PV array rated power (2 MW).

Power measurements from Fig. 3.4 were taken at the DC side of the inverter once per minute during a full year, from the 1st of October 2016 to the 30th of September 2017. Additional information can be obtained by analysing Fig. 3.4 from different angles of view. The analysis of one of the lateral views (Fig. 3.4b), shows an overlapping of all daily DC power generation curves, displaying the power limitation (0.77 [pu]), hereafter power clipping, caused by the oversized PV array reaching the power rating of the inverter. On the other hand, the analysis of figures 3.4c and 3.4d show the seasonal behaviour of PV generation; where year-long dawn, dusk and daily maximum power generation are presented. To simplify the analysis the acronyms SS, VE, WS and AE were added, which correspond respectively to the Summer Solstice, Vernal Equinox, Winter Solstice and Autumnal Equinox in the corresponding hemisphere.

The area covered by the PV plant being analysed allows modelling of the PV system as a low-pass filter of the irradiance [114], where the cut of frequency of the equivalent low-pass filter is greater than 1 minute. Furthermore, PV module temperature behaves as a low-pass filter of the incident irradiance which, depending on the wind speed, has an equivalent time constant of a few minutes [115]. For this reason, uniform irradiance and temperature conditions among PV modules were considered to estimate the PV power generation.

The technical details from the PV plant located in Cambridgeshire and applied to model the

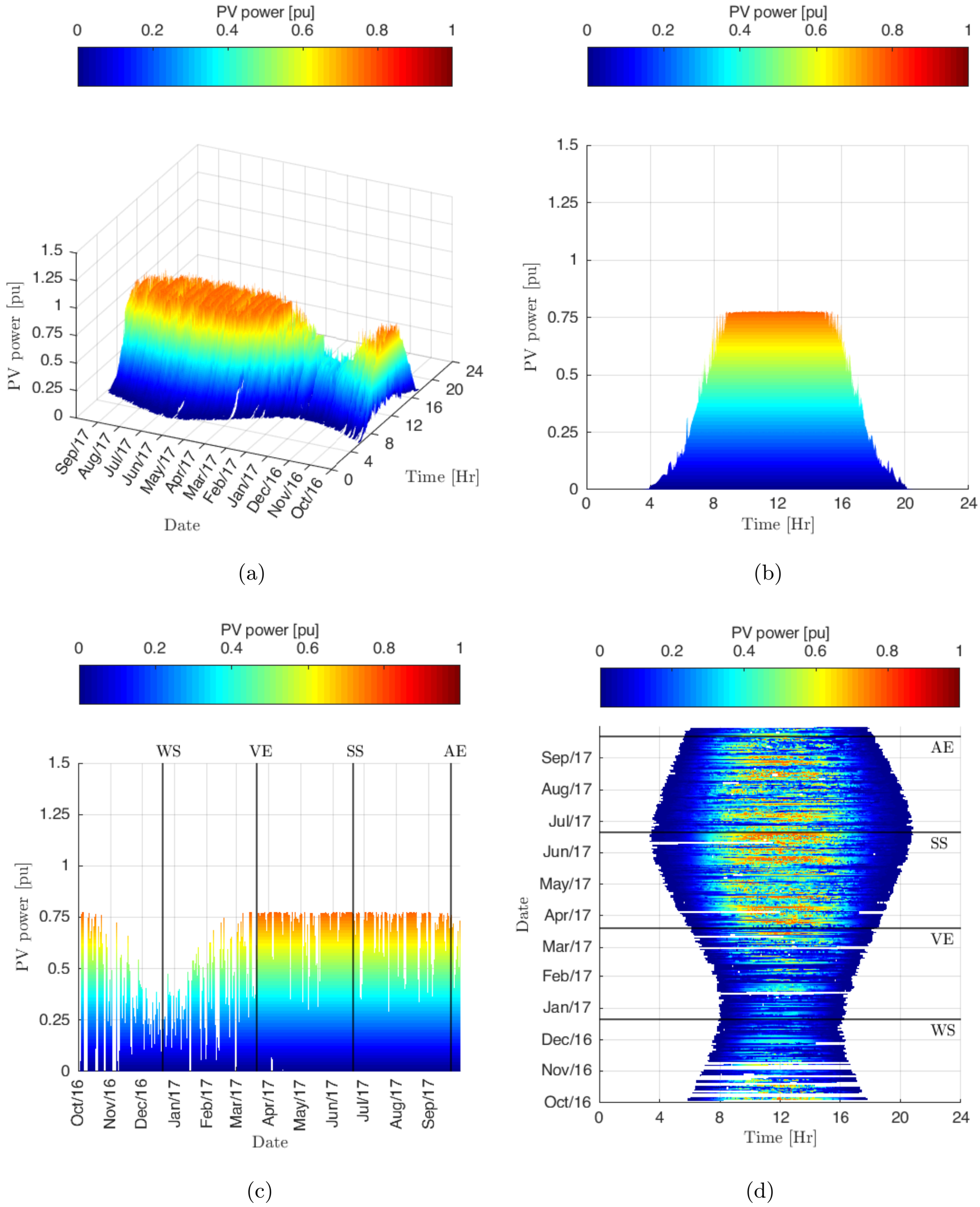

Figure 3.4: Annual PV power generation at the DC side (P_{mpp}) per day and hour: a) per day and per minute power generation, b) overlapping of daily power generation (lateral view of Fig.3.4a), c) daily MPP (lateral view of Fig.3.4a) and d) dawn to dusk power generation (top view of Fig.3.4a).

PV plant are presented in Table 3.1, where the PV modules correspond to the Jinko Solar model JKM260-PP [112]. In order to better illustrate the meaning of the parameters presented in Table

Symbol	Parameter	Value
	PV plant	
$P_{\mathrm{pv\ mpp\ stc}}$	PV array rated power at STC	2 MW
P_{clipping}	Inverter rated power(Clipping level)	1.54 MW
N_{ms}	Number of modules in series	20
N_{sp}	Number of strings in parallel	386
η_{mppt}	MPPT efficiency	98 %
	PV module at STC (1 [kW/m^2], 298.15 [°K])	
$P_{\mathrm{mpp\ stc}}$	Maximum power point	260 W
$V_{\mathrm{mpp\ stc}}$	MPP voltage	31.1 V
$i_{\mathrm{mpp\ stc}}$	MPP current	8.37 A
$V_{\mathrm{oc\ stc}}$	Open circuit voltage	38.1 V
$i_{\mathrm{sc\ stc}}$	Short circuit current	8.98 A
	PV module at NOCT (0.8 [kW/m^2], 318.15 [°K])	
$P_{\mathrm{mpp\ noct}}$	Maximum power point	194 W
$V_{\mathrm{mpp\ noct}}$	MPP voltage	28.3 V
$i_{\mathrm{mpp\ noct}}$	MPP current	6.84 A
$V_{\mathrm{oc\ noct}}$	Open circuit voltage	35.1 V
$i_{\mathrm{sc\ noct}}$	Short circuit current	7.26 A
	PV module general parameters	
k_{i}	Temperature coefficient of i_{sc}	0.06 %/ °K
k_{p}	Temperature coefficient of P_{mpp}	−0.40 %/ °K
k_{v}	Temperature coefficient of v_{oc}	−0.30 %/ °K
A	Area	1.6368 m^2
η	STC efficiency	15.58 %

Table 3.1: PV plant and PV modules parameters: Cambridgeshire.

3.1, a diagram of a generic central inverter PV plant has been included in Fig. 3.5a. This figure also presents qualitative drawings of the characteristic curves (P-V (Fig. 3.5b) and I-V (Fig. 3.5c)) of a PV module.

The PV plant operates under power clipping conditions, thus the power predicted by the models

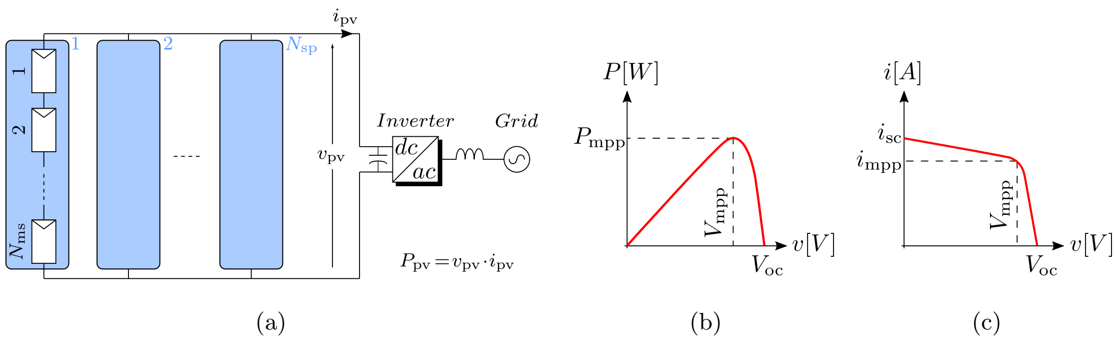

Figure 3.5: PV system diagram and PV module characteristic curves: a) central inverter PV configuration, b) P-V characteristic curve and c) I-V characteristic curve.

must also be clipped (limited) at the DC power rating of the inverter (1.54 MW). The contrast between the predicted PV power and the real PV generation for four different days is displayed in Fig. 3.6. In this figure the irradiance, module temperature, DC power model predictions (clipped) and DC power measurements for the 18th of March 2017, 3rd of June 2017, 10th of August 2017 and 20th of September 2017 are shown. The top plots in figures 3.6a, 3.6b, 3.6c and 3.6d show the daily measurements of the irradiance and temperature of the PV module, while the lower plots show the predicted DC power (clipped) and measured DC power. All three models display an adequate tracking of the measured DC power.

The following error metrics were applied to compare the previously presented PV plant models: Normalised Root Mean Squared Error (NRMSE), Normalised Mean Absolute Error (NMAE), Pearson linear correlation factor (Pearson) and Normalised Root Mean Squared Error Fitness (NRMSEF). Note that the error metrics were applied to the whole year, sampled every minute, and not only on the four days shown in Fig. 3.6.

Equations (3.15) to (3.18) correspond to the mathematical representation of the metrics applied to analyse the error between the DC power measurement (X_{i}) and the clipped DC output power predicted by each model ($\tilde{X}_{\mathrm{i}}$). Variables μ_{X}, $\mu_{\tilde{\mathrm{X}}}$, σ_{X} and $\sigma_{\tilde{\mathrm{X}}}$ in eq. (3.17), correspond respectively to the mean of X_{i} and $\tilde{X}_{\mathrm{i}}$, and the standard deviation of X_{i} and $\tilde{X}_{\mathrm{i}}$. Normalised metrics were measured with respect to the rating of the inverter (clipping power level P_{clip}).

$$NRMSE = \frac{\sqrt{\frac{1}{N} \cdot \sum_{i=1}^{N} (X_{\mathrm{i}} - \tilde{X}_{\mathrm{i}})^2}}{P_{\mathrm{clip}}} \cdot 100 \tag{3.15}$$

$$NMAE = \frac{\frac{1}{N} \cdot \sum_{i=1}^{N} |X_{\mathrm{i}} - \tilde{X}_{\mathrm{i}}|}{P_{\mathrm{clip}}} \cdot 100 \tag{3.16}$$

$$Pearson = \frac{\sum_{i=1}^{N} \left[\left(\frac{X_{\mathrm{i}} - \mu_{\mathrm{X}}}{\sigma_{\mathrm{X}}} \right) \cdot \left(\frac{\tilde{X}_{\mathrm{i}} - \mu_{\tilde{\mathrm{X}}}}{\sigma_{\tilde{\mathrm{X}}}} \right) \right]}{N-1} \cdot 100 \tag{3.17}$$

$$NRMSEF = \left(1 - \frac{||X - \tilde{X}||}{||X - \mu_{\mathrm{X}}||} \right) \cdot 100 \tag{3.18}$$

Table 3.2 summarises the results of the error metrics applied to the models. This results were calculated over a full year of data measurements taken every minute. Note that for the first two error metrics, NRMSE and NMAE, the optimal value is 0%, while in the second pair of error metrics, Pearson and NRMSEF, the optimum is 100%.

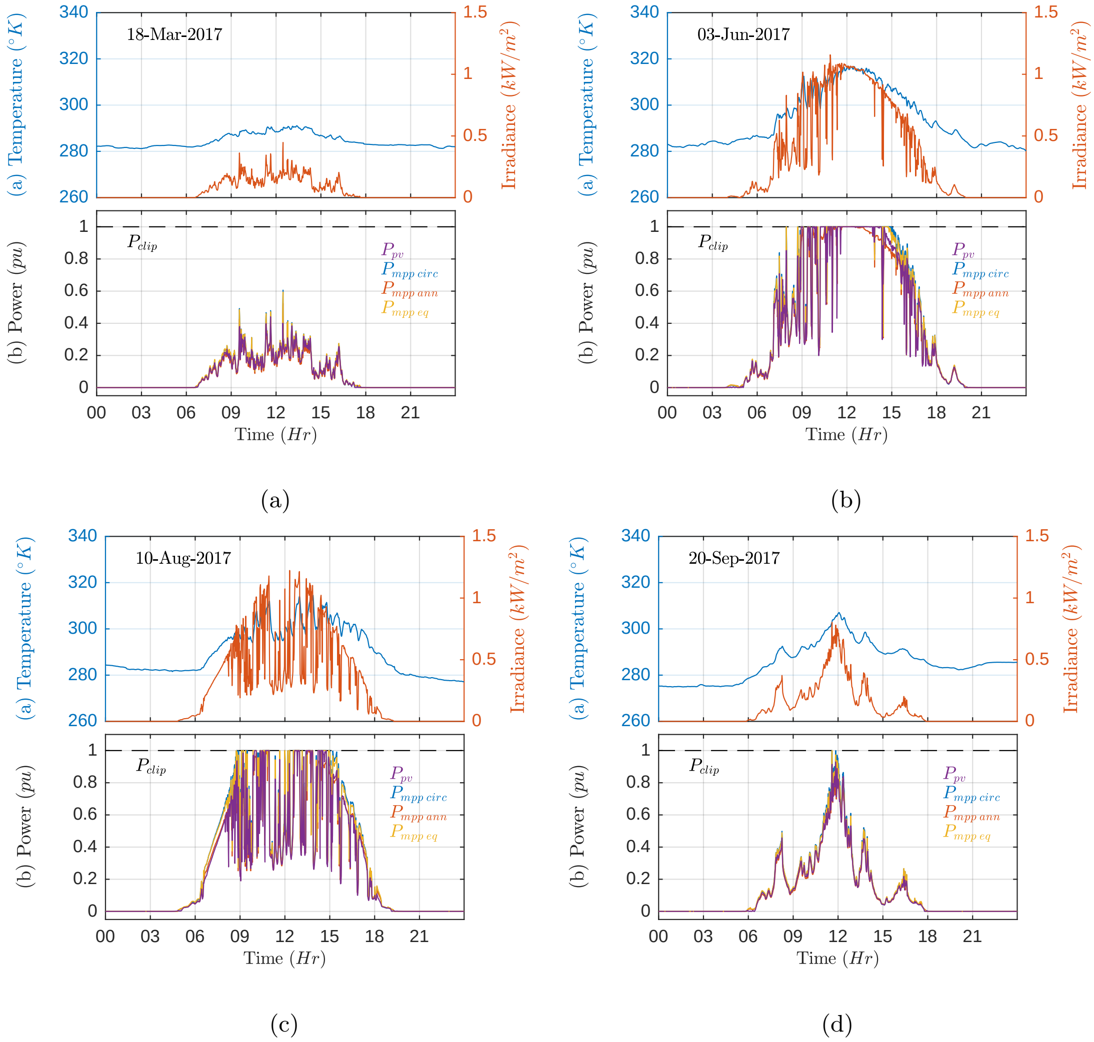

Figure 3.6: Daily analysis of measured DC power versus models, top plot module temperature and irradiance daily measurements, bottom plot clipping level (P_{clip}), measured DC power (P_{pv}), single diode circuital model ($P_{\text{mpp circ}}$), artificial neural network model ($P_{\text{mpp ann}}$) and analytical model ($P_{\text{mpp eq}}$): a) 18-Mar-2017, b) 03-Jun-2017, c) 10-Aug-2017 and d) 20-Sep-2017.

All three models present good matching with the real data below clipping level (low error metrics). However, the circuital model presents the highest error among the three chosen modelling techniques, possibly due to the inherent errors of the numerical resolution method (Newthon-Raphson), generated by selecting an initial solution (starting point of the algorithm), maximum number of iterations and maximum tolerated error; moreover once the full PV curve for a certain irradiance and module temperature is generated, the MPP still needs to be found. ANN shows the lowest error metrics (NRMSE, NMAE, Pearson and NRMSEF), however the training procedure was performed

Parameters	Circuital	ANN	Analytical
NRMSE	4.99 %	3.55 %	4.64 %
NMAE	1.97 %	1.33 %	1.85 %
Pearson	98.87 %	99.06 %	98.91 %
NRMSEF	80.59 %	86.20 %	81.95 %
Percentage Error at STC	0.25 %	-32.60 %	-1.97 %
Execution time	12.68 s	57.47 ms	1.98 μs
Optimisation stage	Yes	Yes	No
Conceptual complexity	Medium	High	Low

Table 3.2: Modelling error metrics

with clipped power (data below clipping level), thus confidence in power predictions beyond the training region is uncertain. This last aspect is underlined by the estimation of the percentage error at STC. For this purpose the theoretical power generation at STC was calculated considering the data sheet parameters and the amount of PV modules. Single diode and analytical models show an error below 5%, thus complying with the percentage-of-error-at-STC criterion. The ANN model presents an error close to 30%. This result (>>5%) shows that the ANN model is not a viable alternative, when the prediction of the ANN model is beyond the training region (i.e. in power clipping scenarios). In terms of execution time, the single diode model surpasses the maximum allowable computational time (100 micro-seconds) by several orders of magnitude, thus not complying with the execution time criterion.

The Analytical model was the only alternative complying with all the criteria and, therefore, was selected as the model to be implemented in the rest of the thesis. Additionally, this model does not need previously processing the data in order to fit the model (train an ANN) or identify the parameters required, as do the other modelling techniques. In terms of simplicity, the Analytical model shows the easiest approach.

The estimation of power generation for two PV plants, one each located in the UK and Chile, based on the selected PV model, are respectively presented in sections 3.3 and 3.4.

3.3 PV power annual generation: Cambridgeshire

The estimation of annual PV generation in a PV plant located in Cambridgeshire (UK), was obtained by applying the previously selected PV model (Analytical Model) over a year of data (irradiance and temperature) sampled every minute. These measurements were acquired through a thermopile pyranometer (Kipp & Zonen - SMP11-V) oriented parallel to the surface of the PV modules) and a thermocouple (PT100) located in the back of PV module. For these reasons no corrections on the angle of incidence or temperature were required.

The PV power estimation, obtained from the application of the data from Cambridgeshire, will be used to estimate the loss of generation due to power clipping (chapter 4), as input of one of the ESS sizing strategies (chapter 4) and as one of the inputs in the control schemes of the PV/ESS configurations (chapter 6).

Fig. 3.7 shows the annual power generation of the PV plant, where PV power generation was normalised with respect to the PV array rating at STC (2 MW). The technical description of the PV plant and PV modules was previously presented in Table 3.1.

3.4 PV power annual generation: Atacama

A year of Global Horizontal Irradiance and temperature measurements, taken from a monitoring station located in the Atacama desert in Chile (-24.0833°, -69.9167°), were used to estimate the power generation of an hypothetical 2 MW PV plant, formed by 447 strings of 20 Jinko JKM60-PP PV modules each [112]. The PV array estimated power at STC has been oversized by 15% with respect to the inverter rated power (2 MW), in accordance with common commercial practices to increase plant factor and correct power reduction caused by temperature. The main parameters of the hypothetical PV plant located in Atacama are presented in table 3.3. Note that the type of PV configuration (central inverter configuration) is the same as the one presented in Fig. 3.5. Moreover, the same PV modules (Jinko JKM260-PP [112]), as in the PV plant located in Cambridgeshire, were considered to model the hypothetical PV plant (see Table 3.1).

The PV power estimation, obtained from the application of the data from Atacama, will be used to estimate the loss of generation due to RR regulation compliance (in chapter 4) and as input of one of the ESS sizing strategies (in chapter 4).

The analytical model presented in section 3.2.3 was applied to estimate the available PV power. Fig. 3.8 shows the estimated annual power generation (P_{mpp}), where the missing area, from 15th to 21st of August 2015 and 26th of August 2015, corresponds to 8 days of data loss.

Symbol	Parameter	Value
	PV plant	
$P_{\text{pv mpp stc}}$	PV array rated power at STC	2.32 MW
P_{inv}	Inverter rated power	2 MW
N_{ms}	Number of modules in series	20
N_{sp}	Number of strings in parallel	447
η_{mppt}	MPPT efficiency	98 %

Table 3.3: PV plant and PV modules parameters: Atacama.

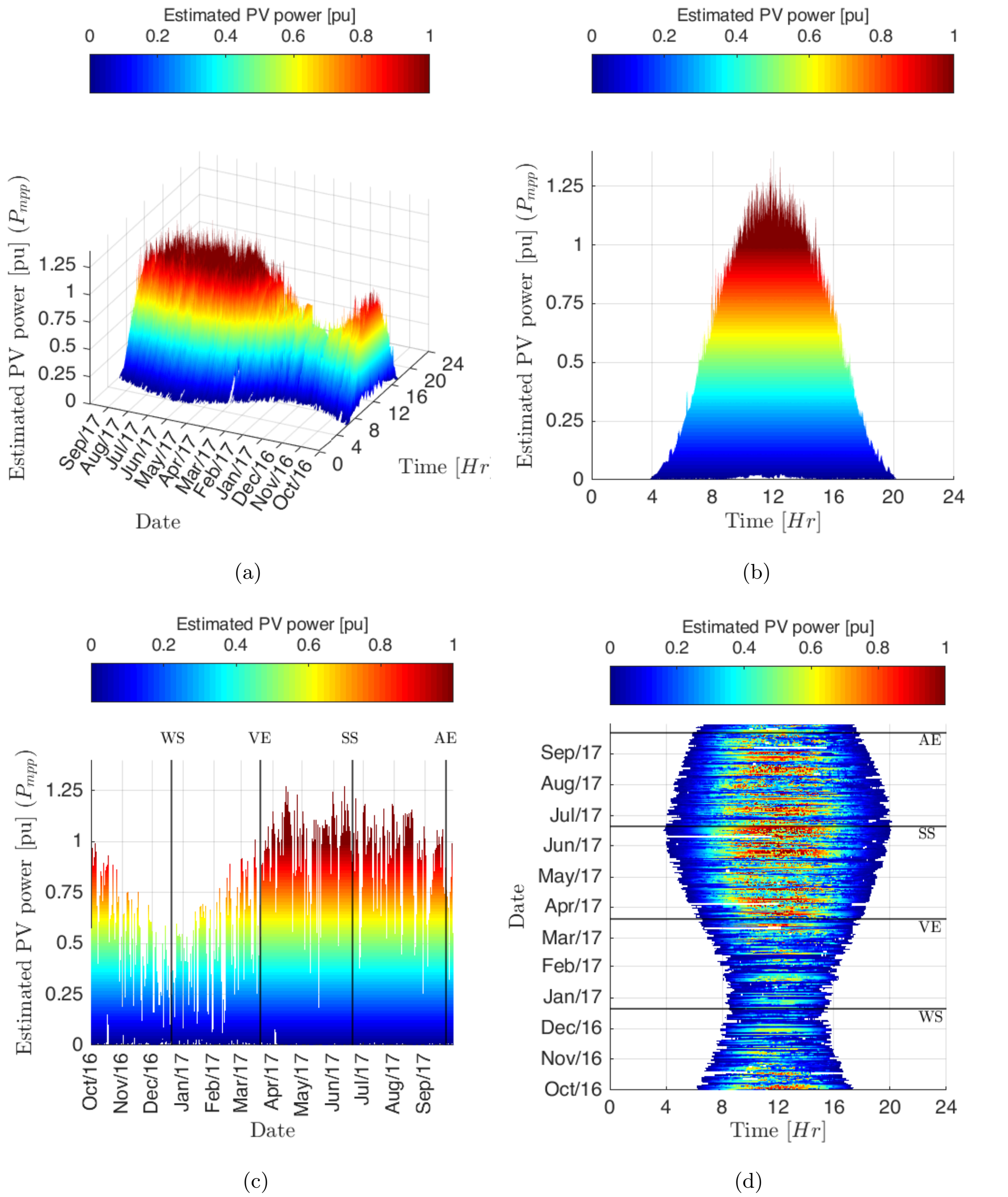

Figure 3.7: Model estimated annual PV power generation at the DC side (P_{mpp}) of the PV plant located in Cambridgeshire: a) per day and per minute power generation, b) overlapping of daily power generation (lateral view of Fig.3.7a), c) daily MPP (lateral view of Fig.3.7a) and d) dawn to dusk power generation (top view of Fig.3.7a).

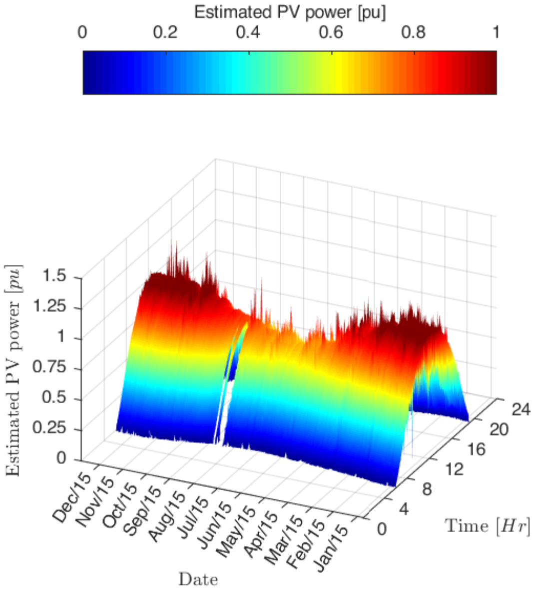

(a)

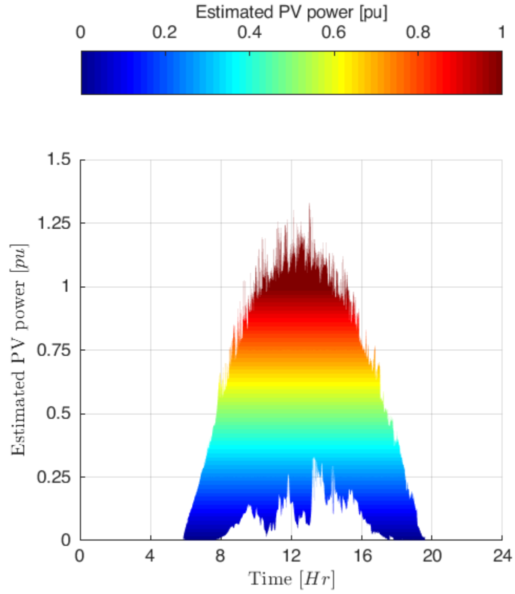

(b)

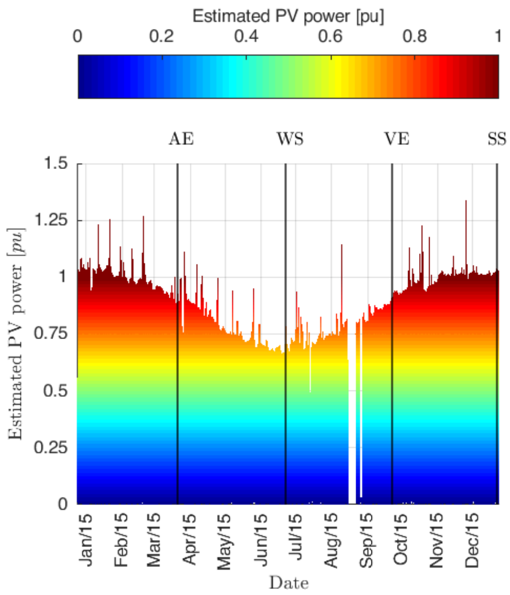

(c)

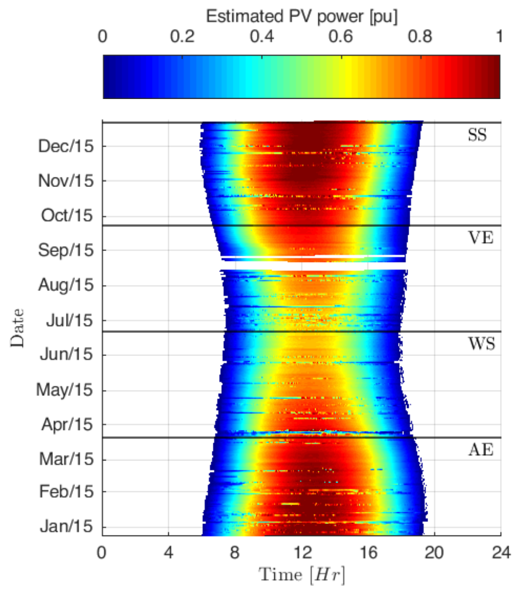

(d)

Figure 3.8: Model estimated annual PV power generation at the DC side (P_{mpp}) of the hypothetical PV plant located in Atacama: a) per day and per minute power generation, b) overlapping of daily power generation (lateral view of Fig.3.8a), c) (lateral view of Fig.3.8a) and d) (top view of Fig.3.8a).

Note that the glitches (spikes) visible in Figs. 3.7b and 3.8b are explained by the scattering and refraction of irradiance caused by the atmosphere and/or clouds [116].

In terms of comparisons, the power generation predicted for Cambridgeshire (Figs. 3.7d and 3.7b) presents a higher variability than the variability predicted in Atacama (Fig. 3.8d and 3.8b). Additionally, the seasonal variation of the length of the days (hours of sunlight) is also higher in Cambridgeshire (Fig. 3.7d) than in Atacama (Fig. 3.8d). Moreover, the amount of time that the PV plant reaches its nominal power is greater in Atacama (Fig. 3.8d). These results show that PV power variability in the UK sets a much more challenging scenario (when compared to Chile) and that ESSs are an enabling technology for smoothing PV power variation and enabling further penetration in the electric market. Moreover, these results also highlight why PV array oversizing is smaller in Chile (15% compared with 40%).

3.5 Summary

This chapter presents a comparison of three different modelling alternatives for modelling a PV plant. Since the data available was restricted to irradiance, temperature and PV power generation under power clipping conditions, the only alternative for predicting the loss of generation caused by power clipping is by modelling the PV plant. However, the modelling alternatives available in literature have only been validated and compared under the complete range of operation of the PV plant, i.e. without power clipping. Thus, their validity for power clipping scenarios was unknown. In order to deal with this limitation the three best performing models (single diode model, ANN and analytical) were selected to be analysed and compared. The criteria selected to choose the best performing model were error below clipping level, execution time and percentage of error at STC. The comparison resulted in the analytical model being the best alternative for estimating the maximum theoretical PV power. This comparison and model validation corresponds to new knowledge.

The best performing model (analytical model) was applied over irradiance and temperature data from two different locations. The first location was Cambridgeshire, UK. The PV power prediction shows high variability (during the day and between days) and, a high seasonal variation of the amount of hours of sunlight. This result suggest that the best application for ESSs will be the support of PV power generation, smoothing its variability. ESSs will become essential equipment in future PV plants close to this particular location, if reducing PV power variability is a goal. Otherwise, higher levels of PV array oversizing with respect to the PV inverter (and higher levels of loss of generation) will be required.

The second location corresponds to Atacama, Chile. The PV power predicted from the available irradiance and temperature measurements, show fewer power variations when compared with Cambridgeshire. The low variability in the resource suggest that PV power generation in Atacama has a better chance for further penetration in the electric markets, when compared to Cambridgeshire. Moreover, this high reliability (low variability) of the resource could allow PV systems close to this location to offer support to the grid (complementary services).

The estimation of the PV power generation for Cambridgeshire will be applied to estimate the loss of generation (kWh), due to power clipping, as an input of one of the ESS sizing strategies and as an input of the PV/ESS configuration control scheme. Meanwhile, the estimation of the PV power generation for Atacama, will be used to estimate the loss of generation due to ramp rate regulation and as input of a second ESS sizing strategy.

Chapter 4

ESS sizing

4.1 Introduction

Power clipping, RR control and peak shaving were selected, in chapter 2, among several complementary services to be analysed and implemented in this thesis. The former two services depend on the variation of the solar resource and rating of the PV plant, while the latter depends on the ratio between generation and demand. Chapter 4 presents two novel ESS sizing strategies, power clipping and RR control services in PV/ESS configurations, both services that depend on the solar resource and rating of the PV plant.

The content of the chapter is divided into four sections, the first section presents the state of the art on ESS sizing strategies for PV systems, the second and third sections present two different ESS sizing strategies developed along the research presented in this thesis. Specifically, the second section presents an ESS sizing strategy for maximum power Ramp Rate (RR) compliance. This section considers a theoretical PV plant located in Atacama (Chile) and the RR regulations from the Chilean grid code. The main input to this ESS sizing strategy is the PV power prediction estimated in chapter 3 (section 3.4). The third section presents an ESS sizing strategy for power clipping in PV plants. This strategy relies on the real data obtained from a PV plant located in Cambridgeshire (UK) and, the predicted maximum theoretical PV power (estimated in chapter 3, section 3.3) to size the ESS. Finally, the fourth section analyses the idle hour operation of the ESS in both cases, i.e. the ESS performing RR control in the (theoretical) PV plant located in Atacama and the ESS performing power clipping support in the PV plant located in Cambridgeshire.

To the best of the author's knowledge, ESS sizing strategies for power clipping have never been addressed in literature. Therefore, the ESS sizing strategy for power clipping applications, presented in section 4.4, is completely novel. Similarly, the ESS sizing strategy for maximum power

RR regulations is also new, however, there are other ESS sizing strategies for this application available in literature. Thus, in order to highlight the advantages of the proposed strategy, it will be compared against one of the strategies available in literature.

4.2 State of the art

Several ESS sizing strategies that allow PV applications to provide Complementary Services have been previously proposed in literature. In [44] and [45] two different ESS sizing strategies to comply with maximum power RR regulations were proposed. The first work proposed an optimal sizing strategy based on power node modelling of the economical dispatch model and the model of the PV power units. The second paper reduces PV power variability by tracking a (low-pass) filtered MPP. The sizing of the battery is obtained from the difference between the filtered MPP and the maximum RR limitation. A sizing strategy to provide support for household PV applications was introduced in [46]. The sizing is calculated through a cost function based on a physical model of the lifetime of the battery. Moreover, real load/PV power profiles and maximum ratings are included to calculate the economic factor of the system. The sizing strategy aims at increasing cost efficiency of the battery additionally required to decrease the electricity bill. A sizing strategy to balance peak and off-peak electricity consumption was presented in [47]. The strategy consists of iterating a simulation considering different sizes of BESS. The simulation uses load and PV generation curves, which were estimated through a probabilistic neural network model. In [48] a sizing strategy for smoothing the power output and storing curtailed power at PV-plant-level is presented. This latter sizing strategy, consists of averaging the PV power beyond a certain power limit (power curtailing level imposed by the GO). A hybrid (battery-supercapacitor) ESS sizing strategy for power curtailment in PV plants is proposed in [117]. This strategy consists of applying multi-objective particle swarm optimisation to solve the hybrid ESS allocation problem, while smoothing PV power injection and complying with the externally-provided power curtailment. In [118], an ESS sizing strategy to comply with a voltage-dependent power curtailment is proposed. The power curtailment level is proportional to the (variable) voltage at the PCC. The ESS sizing strategy consists of selecting the maximum annual difference between PV power generation and the power curtailment level. In [40], the economical advantage of different BESS sizes to provide frequency regulation is presented. The sizing strategy consists of finding, through iteration, the smallest ESS sizing that complies with a set of previously defined rules and achieves frequency regulation within a given range of two performance criteria. An ESS sizing strategy to find the optimal BESS size and location in a distributed power system, including PV generation and BESS, is presented in [49]. The strategy aims at minimizing the ESS size required to perform voltage regulation in the system. The strategy obtains an analytic solution based on the application of the network impedance matrix of the system.

A much wider variety of ESS sizing strategies related to wind power applications can be found in literature . In [50], optimal sizing and reliability analysis of an ESS hybridised with a PV/wind generation system, based on a stochastic framework, is presented. The aim of this sizing strategy is to smooth power generation by performing peak shaving. A sizing strategy to maximize service-hours per BESS unit cost is presented in [51]. The strategy forecasts power generation based on long term historic data and statistical noise. This prediction is then low pass filtered, allowing an ESS power reference curve to be obtained, which is later processed by a cost function obtaining the ESS energy rating. A sizing strategy to minimize penalties caused by not complying with the day-ahead power bidding is presented in [52]. The strategy generates 25 initial ESS power references by subtracting the bid power from 43-hours-power generation forecasts. The initial references are then presented in a histogram, together with a compliance level, which can be used to generate the ESS sizing. A sizing strategy for a hybrid ESS, to comply with maximum power ramp rate regulation, is presented in [53]. For this purpose wind forecast and uncertain load behaviour are subtracted, generating a power reference which is later transformed into frequency-domain by Discrete Fourier Transform (DFT). The result is later separated into low, medium and high frequencies, corresponding to the desired power output, the power reference for BESS and the power reference for SCs, respectively. Another strategy to size an hybrid ESS while complying with maximum power ramp rate is proposed in [23]. Here several historical data sets are filtered by wavelet discrete transform, generating a maximum power ramp rate compliant power curve. An ESS power reference curve is obtained by averaging the differences between all original curves and their filtered version. The result is later filtered selecting high and low frequencies as supercapacitors and BESS power references, respectively.

4.3 ESS sizing strategy for Ramp Rate regulation

As a consequence of the increasing penetration of sustainable resources in the electric markets, many countries have upgraded their grid codes addressing the maximum power Ramp Rate (RR) regulations for renewables, i.e. maximum power variation per unit of time. For example, the grid-code in Hawaii limits RRs to ± 2 or ± 1 MW per minute, depending on the time of day [119]. In Puerto Rico RRs are limited to ± 10% rated power per minute for PV systems [120], while in Australia RRs are limited to ± 16.67% rated power per minute [121]. Other grid codes limit only positive RRs (load taking) as is the case of Ireland and Germany, where 30 MW per minute and 10% rated power per minute are the corresponding positive RR restrictions [23, 119]. The sizing strategy presented in this section is focused on the Chilean RR regulations for PV generation.

Chilean grid code limits positive RRs (load taking) between 0 and 20% of the PV plant nominal power per minute, while negative RRs are not restricted. The instantaneous positive RR level is stated by the GO ("Sistema Electrico Nacional"), according to its requirements, in order to guarantee grid stability of the electric system [122]. Power ramps exceeding RR regulations are not allowed, forcing the system to operate in a non-optimal power point and thus causing non-estimated annual energy losses.

4.3.1 Maximum power ramp rate losses estimation

A first step towards ESS sizing for RR regulations is to assess the annual energy loss caused by complying with different levels of RR regulations. This assessment is based on the PV power generation estimated in section 3.4 (Fig. 3.8).

The procedure to asses the energy losses, consists of limiting the estimated PV power generation increases to 5, 10, 15 and 20% of the nominal power of the PV plant (2 MW). Consequently, the annual energy yield for each case was calculated by integrating the RR limited power. Finally, the annual energy loss was calculated as the difference between the energy yield without RR limitations and the energy yield for each RR limited power.

The analysis of annual energy loss caused by complying with positive power RR limitation is shown in Fig. 4.1, where RR x% corresponds to a maximum power RR of x% per minute of the nominal power of the PV plant. The top plot (Fig. 4.1a)) presents histograms of power exceeding positive RRs of 5, 10, 15 and 20% of the nominal PV plant power (2 MW), while, the bottom plot (Fig. 4.1b)) shows the recoverable annual energy loss as a function of the power loss (power exceeding each RR regulation).

From Fig. 4.1 constantly applying RR regulations of 5%, 10%, 15% or 20% will generate annual energy losses of 43, 20, 11 or 7 MWh, respectively. This corresponds to 0.087%, 0.04%, 0.022% or 0.014% of the annual energy generation, hence annual energy losses caused by RR complying are negligible. Nonetheless, RR regulations must be complied with, by losing or storing the RR % non complying. An RR 10% was selected as limit to be used during the rest of the document, since this presents a good compromise between 0 and 20 %, and it matches other grid-codes RR regulations.

4.3.2 ESS Sizing Strategy

Four of the previously described ESS sizing strategies (section 4.2) address RR regulation, however all of them present relevant concerns that require a solution. For instance, the strategy presented

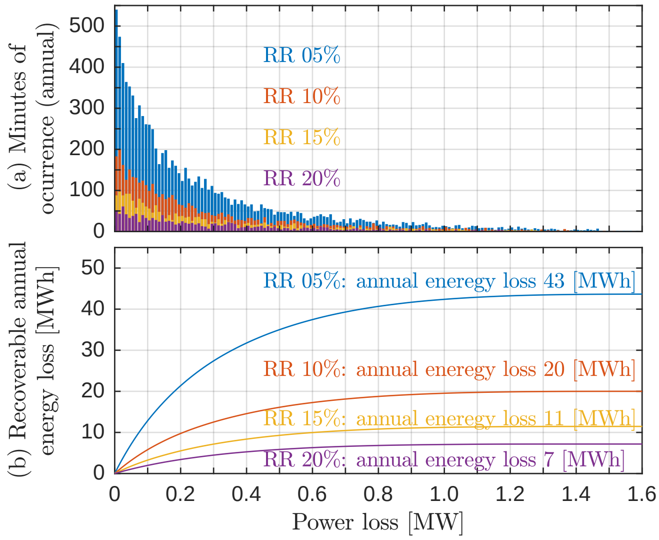

Figure 4.1: Annual energy loss caused by RR regulations: a) Histogram of positive power RR per minute beyond x (RR x%) and b) Recoverable annual energy loss under different RR regulations (RR x%).

in [44] regulates the maximum RR over 5-minutes time frame, despite most RR regulations targeting per minute power variability. Additionally, power sizing only considers the maximum daily power rating, neglecting lower RR behaviour that presents a higher occurrence rate. The strategy presented in [45] tracks a filtered version of the available MPP, thus reducing the energy yield of the PV plant. Moreover, this strategy is based on a single arbitrarily-chosen cloudy day, neglecting inter-day and annual variation and behaviour. The DFT-based ESS sizing strategy presented in [53], decomposes the full signal into periodic sinusoids losing information regarding the time location of frequencies, therefore leading to a wrong sizing of the ESS. The Wavelet ESS sizing strategy in [23] improves frequency location compared to DFT, nonetheless the strategy relies on averaging the results, hence masking some dynamic behaviour of PV power. In consequence, a novel ESS sizing strategy was developed to address the aforementioned drawbacks relating to the existing ESS sizing strategies for RR regulations. The description of this ESS sizing strategy is provided below.

The proposed ESS sizing strategy consists of filtering the estimated PV power (P_{mpp}) (section 3.4) through a Discrete Wavelet Transform (DWT) (see Appendix E), separating the PV power into a peak-shaved RR-10%-compliant power curve (P_{out}) and a non-peak-shaved RR 10% non-compliant power curve (P_{ess}). This latter curve is obtained from the subtraction $P_{\text{mpp}} - P_{\text{out}}$, and corresponds to the power reference to be analysed in the next step of the ESS sizing process. The analysis

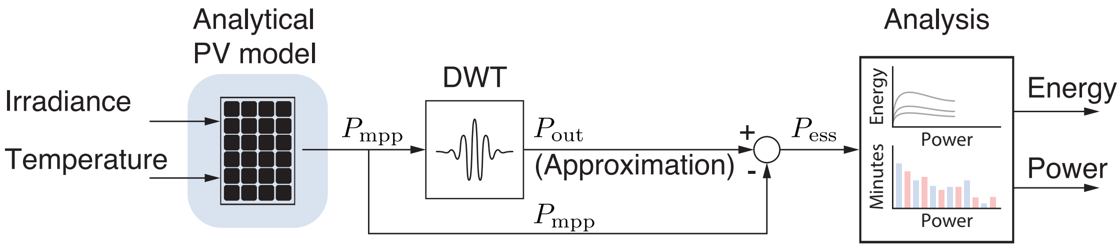

Figure 4.2: ESS sizing strategy for RR regulations.

consists of limiting the resulting bidirectional power reference (P_{ess}) to a certain value ($\tilde{P}_{\mathrm{ess}}$) and then integrating the limited power ($\tilde{P}_{\mathrm{ess}}$) along each day, calculating in this way the daily energy yield of the ESS (E_{made}). This process is iterated for several power ratings, thus generating a curve of the annual maximum accumulated daily energy rating required to fully store the energy which a certain bidirectional power rating is capable of storing. A diagram of the sizing strategy is shown in Fig. 4.2.

The resulting curves from the analysis stage of the ESS sizing strategy are shown in Fig.4.3, were, the maximum annual value of E_{made}, the annual average of E_{made} and annual standard deviation of E_{made} are respectively identified as $\hat{E}_{\mathrm{made}}$, $\overline{E}_{\mathrm{made}}$ and σ_{emade}. Curves depicted in Fig.4.3 correspond to $C_{\mathrm{m}} = \hat{E}_{\mathrm{made}}$, $C_{\mathrm{a3s}} = \overline{E}_{\mathrm{made}} + 3 \cdot \sigma_{\mathrm{emade}}$, $C_{\mathrm{a2s}} = \overline{E}_{\mathrm{made}} + 2 \cdot \sigma_{\mathrm{emade}}$, $C_{\mathrm{a1s}} = \overline{E}_{\mathrm{made}} + 1 \cdot \sigma_{\mathrm{emade}}$ and $C_{\mathrm{a}} = \overline{E}_{\mathrm{made}}$. The bottom plot in Fig.4.3 presents a histogram of positive (store) and negative (release) power. The decrease in E_{made} curves after reaching the maximum is due to limiting the ESS charge to positive values, hence negative power surpassing positive power implies that more power is being drawn from the ESS thus reducing the ESS energy requirements.

Daily ESS charge depletion was assumed during the analysis step, thus starting each day with an "empty" ESS. However, this assumption can be modified according to the selected discharge strategy of the ESS. Note that to perform the filtering process a wavelet transform and decomposition level must be selected. The strategy for choosing both wavelet and the decomposition level is presented in the following section (section 4.3.3).

Finally, the ESS sizing strategy consists in selecting a bi-directional power level and choosing an ESS maximum accumulated daily energy curve from Fig. 4.3. As an example we have selected a bidirectional power rating of 200 kW and selected curve C_{a1s} ($\overline{E}_{\mathrm{made}} + \sigma_{\mathrm{emade}}$) as the compliance criteria, hence ESS energy rating is 50.91 kWh. It must be noted that most ESS power reference (P_{ess}) is concentrated between 0 and 200 kW.

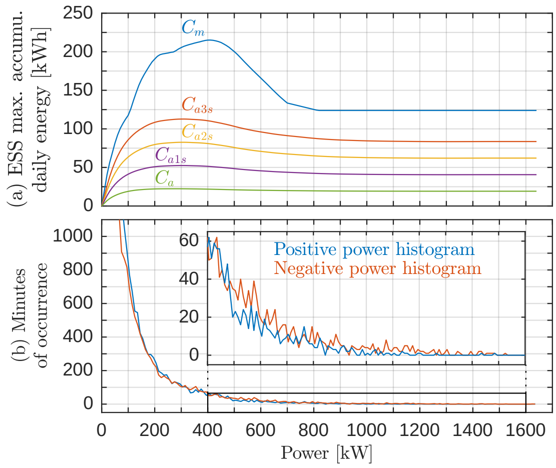

Figure 4.3: ESS power analysis: a) ESS power as function of the daily accumulated energy analysis and b) Histogram of positive ($P_{ess} > 0$, store) and negative ($P_{ess} < 0$, release) power measured per minute during a year.

4.3.3 Wavelet selection

There are several wavelet families capable of filtering the estimated PV power (P_{mpp}) and producing a peak-shaved RR 10% compliant power output, though each wavelet will produce a different ESS requirement. In order to select the best option the filtering capabilities of Wavelets Haar, Daubechies 2 to 10, Symlets 2 to 8 and Coiflets 1 to 5 were compared.

ESS daily depletion was considered since the solar cycle (dawn-dusk) allows the injection of the stored power within a day, reducing energy losses associated with longer storage periods caused by ESS self discharge. Therefore a day-oriented analysis was performed. For this purpose a total of 1440 pairs of irradiance and temperature measurements were taken every day. Since each wavelet level halves (down samples) the number of data samples, only 5 DWT levels are possible without modifying the length of the data set.

As a mean to illustrate the effects of Wavelet filtering, to obtain peak-shaved RR 10% compliant power, Figs. 4.4a and 4.4b show respectively the filtering of P_{mpp} through Wavelets Symlet 2 (decomposition level 5) and Daubechies 8 (decomposition level 4), where the top plots present the wavelet-filtered output power (P_{out}) compared to the estimated PV power (P_{mpp}) and the bottom plots show the required ESS power ($P_{\text{ess}} = P_{\text{mpp}} - P_{\text{out}}$).

A summary of the decomposition level which each wavelet requires to comply with RR 10% is presented in Table 4.1. Note that Haar, Daubechies 2 and Symlets 2 do not comply with RR 10%, despite applying a 5 level decomposition.

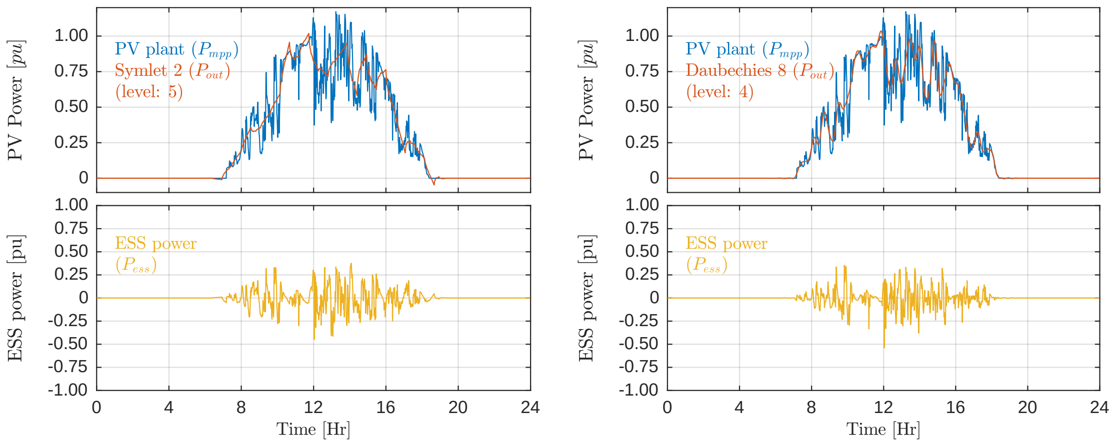

(a) (b)

Figure 4.4: Estimated PV power (P_{mpp}) and wavelet-filtered output power applying Symlet 2 Wavelet (level 5) decomposition (P_{out}) and Required ESS power (P_{ess}) to store/release the power difference between the estimated PV power and the wavelet-filtered output power: a) Symlet 2 level 5 and b) Daubechies 8 level 4

Wavelet	Level	Wavelet	Level
Haar	No compliance	Symlets 2	No compliance
Daubechies 2	No compliance	Symlets 3	4
Daubechies 3	4	Symlets 4	4
Daubechies 4	4	Symlets 5	4
Daubechies 5	4	Symlets 6	4
Daubechies 6	4	Symlets 7	4
Daubechies 7	4	Symlets 8	4
Daubechies 8	4	Coiflets 1	5
Daubechies 9	4	Coiflets 2	4
Daubechies 10	4	Coiflets 3	4
		Coiflets 4	4
		Coiflets 5	4

Table 4.1: Wavelet decomposition level required to comply with RR 10% regulation

Figure 4.5 presents the annual maximum positive and negative RRs obtained by filtering the PV power (P_{mpp}) through the three worst performing wavelets (Haar, Symlet 2 anc Coiflet 1) and the three best performing Wavelets (Daubechies 8, Symlet 6 and Coiflet 2) as a function of the decomposition level (1 to 5).

Therefore, in accordance with the results from Fig. 4.5, Daubechies 8 level 4 was selected as the Wavelet to filter the estimated PV power (P_{mpp}), since it complies with RR 10% and presents even and low positive and negative RRs. Additionally, a lower wavelet decomposition level was

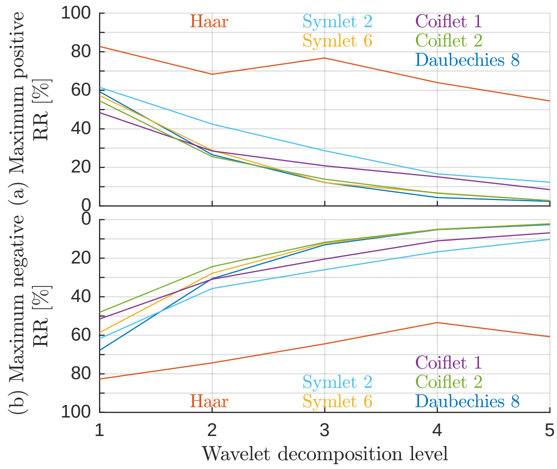

Figure 4.5: Maximum annual RR obtained for each wavelet decomposition level: a) Positive RR and b) negative RR.

preferred, since it requires less computational effort to perform the decomposition.

4.3.4 ESS sizing comparison

This part of the chapter presents a comparison between the proposed ESS sizing strategy for RR regulation and the ESS strategy proposed by Jiang in [23].

The first step will be to apply the ESS sizing strategy from [23] over the PV power data from Atacama. According to [23], the best performing wavelet corresponds to the one with the maximum mean cross correlation between the estimated PV power generation and the approximation obtained from the first level wavelet decomposition. The result from this analysis shows that the best performing wavelet, according to this criterion, was Daubechies 10 (db10). Table 4.2 shows the normalised error between the maximum mean cross correlation (obtained with db10) and the mean cross correlation obtained from other wavelets.

The next step (in [23]) consists of finding the decomposition level that complies with the maximum power RR restriction, i.e. $\pm 10\%$ of the nominal power of the PV plant (0.2 [MW]). This analysis showed that the 4th level db10 (db10-L4) wavelet decomposition complies with this limitation. Finally, the ESS power (P_{ess}) is calculated as the difference between the estimated PV power generation and the low frequency components (approximation) of the 4th level db10 wavelet decomposition. The ESS power sizing is calculated from the mean daily maximum of P_{ess} and corresponds to 406 [kW]. The following step, to size the energy of the ESS, is to calculate the daily cumulative energy ($E_{\text{ess cum}}$). $E_{\text{ess cum}}$ corresponds to the time integral of P_{ess}. Then, the daily energy storage capacity (C_{ess}) is calculated as the difference between the daily maximum and daily minimum of $E_{\mathrm{ess\ cum}}$. The ESS energy sizing is calculated as the mean of C_{ess} and corresponds to 56 [kWh].

In order to compare both ESS sizing strategies the next step is to estimate the loss of generation caused using a different output (power) reference. The method proposed in [23] selected db10-L4 as the best wavelet to filter the PV power generation signal (and comply with RR 10%), while the proposed strategy selected db8 decomposition level 4 (db8-L4). Following the PV power reference proposed in [23] implies a loss of generation of 63.92 [MWh] per year (associated to db10-L4), while the proposed alternative implies a loss of generation of only 53.74 [MWh] per year (associated to db8-L4). Note that both strategies comply with RR 10 [%]. The following step consists of estimating how much of this energy can be recovered by adding an ESS and applying the sizing strategy proposed by each author. Note that a round-trip efficiency of 86.7 [%] was considered in this step.

In order to compare both ESS sizing strategies, the concept of ESS sizing efficiency is introduced. ESS sizing efficiency is defined as the percentage of the annual recoverable energy with respect to the annual loss of generation caused by filtering (through db10-L4 or db8-L4) the PV output power. The strategy proposed by Jiang in [23] has an ESS sizing efficiency of 68.47 [%], however, the strategy proposed by the author does not provide a single power-energy sizing but instead provides a series of curves (shown in Fig. 4.3). A comparison of the ESS sizing efficiency resulting from the strategy proposed by Jiang in [23] and the strategy proposed by the author of this thesis is shown in Fig. 4.6. Additionally, the difference between applying the C_{m}, C_{a3s} or C_{a2s} in terms of ESS sizing efficiency is negligible (Fig. 4.6). However, C_{a2s} shows the smallest ESS energy sizing (for the same ESS power sizing) among C_{m}, C_{a3s} and C_{a2s} (Fig. 4.3). Moreover, the difference in terms of ESS sizing efficiency between C_{a1s} and C_{a2s} is sufficiently small to justify the selection of

Wavelet	Normalised error	Wavelet	Normalised error
Haar	$1.20 \cdot 10^{-4}$	Symlets 2	$3.89 \cdot 10^{-5}$
Daubechies 2	$3.89 \cdot 10^{-5}$	Symlets 3	$2.70 \cdot 10^{-5}$
Daubechies 3	$2.70 \cdot 10^{-5}$	Symlets 4	$2.07 \cdot 10^{-5}$
Daubechies 4	$1.39 \cdot 10^{-5}$	Symlets 5	$9.90 \cdot 10^{-6}$
Daubechies 5	$1.34 \cdot 10^{-5}$	Symlets 6	$1.34 \cdot 10^{-5}$
Daubechies 6	$1.20 \cdot 10^{-5}$	Symlets 7	$1.15 \cdot 10^{-5}$
Daubechies 7	$3.00 \cdot 10^{-6}$	Symlets 8	$9.95 \cdot 10^{-6}$
Daubechies 8	$9.36 \cdot 10^{-6}$	Coiflets 1	$3.63 \cdot 10^{-5}$
Daubechies 9	$5.99 \cdot 10^{-6}$	Coiflets 2	$1.88 \cdot 10^{-5}$
Daubechies 10	0	Coiflets 3	$5.58 \cdot 10^{-6}$
		Coiflets 4	$8.68 \cdot 10^{-6}$
		Coiflets 5	$4.67 \cdot 10^{-7}$

Table 4.2: First level decomposition applying different wavelets: normalised error.

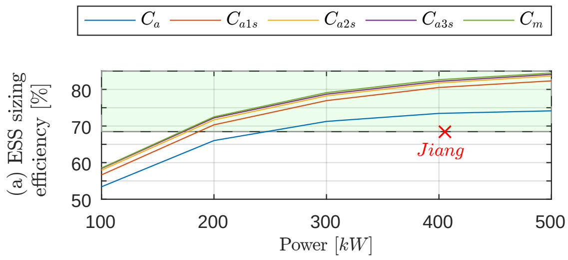

Figure 4.6: ESS sizing comparison: Jiang [23] vs. proposed ESS sizing strategy.

the ESS sizing provided by the curve C_{a1s}.

In order to highlight the ESS sizings that present a better performance than [23], the area where the ESS sizing efficiency is greater than the one obtained by Jiang [23] has been highlighted in green in Fig. 4.6.

Table 4.3 summarizes the ESS sizing in power and energy, the recoverable annual energy, the annual loss of generation and the ESS sizing efficiency for the alternative proposed by Jiang in [23] and several ESS sizings obtained from applying the criterion presented in Fig. 4.3 into the different curves (C_{a}, C_{a1s}, C_{a2s}, C_{a3s} and C_{m}).

In summary, for a similar power rating (400 [kW]) as the one obtained by Jiang [23] (406 [kW]), the proposed ESS sizing strategy allows a higher ESS sizing efficiency to be obtained despite selecting any of the ESS sizing curves presented in Fig. 4.3. This result also shows that from 200 [kW] and above, curves C_{a1s},C_{a2s},C_{a3s} and C_{m} present a better ESS sizing efficiency than the strategy proposed by Jiang. Moreover, Fig. 4.6 also shows that selecting C_{a1s} presents a good trade-off between diminishing ESS energy sizing and increasing ESS sizing efficiency. Note that the maximum possible ESS sizing efficiency is imposed by the round-trip efficiency of the ESS and corresponds to 86.7[%].

4.4 ESS sizing strategy for Power Clipping

The drop in price of PV modules has made PV array oversizing, with respect to the power rating of the inverter, a common practice among new PV systems. An example of this practice was illustrated in section 1.1.2, where the power clipping caused by the PV array oversizing is clearly visible (Fig. 3.4b at 0.77 [pu]). The PV power analysed in section 1.1.2 comes from a real PV plant located in Cambridgeshire, its full description was presented in section 1.1.2 (Table 3.1).

The PV plant being analysed has a 39% of PV array oversizing, which led to a 15.43% of the (annual) plant factor. However, if the PV array oversizing is neglected the resulting plant factor is reduced to 11.11%.

Irradiance, temperature and DC power measurements were the only data available from the PV plant. Since the power limitation applied to the system is imposed by the converter rating, power losses caused by clipping were not known nor accounted for. Therefore, estimating those losses resulted in a mandatory effort to assess clipping effects.

4.4.1 Power Clipping losses

The strategy to estimate annual energy losses caused by clipping, consists of comparing the PV power generation (with power clipping) against the power predicted by the analytical model. PV power generation measured at the DC side of the inverter and PV power estimation based on the analytical model were respectively presented in sections 3.2.4 (Fig. 3.4) and 3.3 (Fig. 3.7).

Clipped power (P_{clipped}) is calculated according to equation (4.1), where P_{mpp} and P_{pv} are respectively the predicted PV power generation from eq. (3.14) and the measured PV power, both in kW. The clipped energy in kWh is estimated according to eq. (4.2), where dt corresponds to

	Power sizing [kW]	Energy Sizing [kWh]	Recoverable annual energy [MWh]	Annual loss of generation [MWh]	ESS sizing Efficiency [%]
Jiang [23]	406	55.46	43.77	63.92	68.47
C_{a}	100	18.99	28.70	53.74	53.40
	200	22.14	35.48	53.74	66.03
	300	22.36	38.30	53.74	71.26
	400	21.87	39.47	53.74	73.45
	500	21.05	39.85	53.74	74.15
C_{a1s}	100	41.28	30.45	53.74	56.66
	200	50.91	37.80	53.74	70.33
	300	52.48	41.35	53.74	76.94
	400	51.44	43.28	53.74	80.53
	500	48.46	44.25	53.74	82.33
C_{a2s}	100	63.57	31.14	53.74	57.94
	200	79.68	38.52	53.74	71.68
	300	82.60	42.05	53.74	78.24
	400	81.00	43.94	53.74	81.76
	500	75.89	44.97	53.74	83.67
C_{a3s}	100	85.86	31.39	53.74	58.41
	200	108.45	38.81	53.74	72.22
	300	112.72	42.29	53.74	78.70
	400	110.56	44.18	53.74	82.21
	500	103.30	45.20	53.74	84.10
C_{m}	100	117.63	31.46	53.74	58.54
	200	190.52	38.97	53.74	72.51
	300	205.43	42.52	53.74	79.13
	400	215.07	44.42	53.74	82.65
	500	200.21	45.39	53.74	84.47

Table 4.3: ESS sizing comparison: Jiang [23] vs. proposed ESS sizing strategy.

the sampling time in min (1 min). The resulting estimated annual energy loss is 33 MWh, which corresponds to 1.22% of the annual energy PV generation.

$$P_{\text{clipped}} = \begin{cases} P_{\text{mpp}} - P_{\text{pv}} & , \quad P_{\text{pv}} > P_{\text{clip}} \\ \\ 0 & , \quad \text{otherwise} \end{cases} \tag{4.1}$$

$$E_{\text{clipped}} = P_{\text{clipped}} \cdot \frac{dt}{60} \tag{4.2}$$

4.4.2 ESS Sizing Strategy

Only one of the ESS sizing strategies presented in section 4.2 tackles power clipping ([48]). Nevertheless, the alternative introduced in [48] presents several concerns. For instance, power beyond the clipping level is averaged, thus masking some power dynamics of the sizing process. Moreover, the analysis is based on a single sunny day, neglecting inter-day variability and seasonal behaviour in PV generation. Additionally, this sizing strategy aims at providing a concentrated solution for a full PV plant, connecting the ESS after the inverter at the PCC. However, clipping is a problem experienced exclusively in PV plants with PV array oversizing (ILR>1), where the restriction (in terms of power) is imposed by the inverter. Therefore, this solution is not a valid option to retrofit existing PV plants and lacks the main advantages derived from oversizing the PV array (increase annual plant factor and decrease LCOE). For these reasons a new ESS sizing strategy capable of handling power clipping was developed and is introduced in this section. Nevertheless, the new solution also requires connecting the ESS to the PV system in a place that allows withdrawal of the clipped power from the system, before the power is clipped by the inverter. In consequence, configuration and control of the ESS will be later addressed in sections 5.2 and 6.4.

A diagram of the full ESS sizing strategy presented in this section is shown in Fig. 4.7. Note that the estimation of the clipped power (P_{clipped}) was previously introduced in eq. (4.1) to estimate the annual energy loss. After obtaining P_{clipped}, the next step consists of analysing, in terms of power and energy, the power loss caused by clipping. For this purpose the ESS is assumed to be depleted at the end of each day. This assumption is based on the daily solar cycle (dawn-dusk), that provides a wide range of hours to inject the stored energy into the grid, thus allowing to decouple inter-day dynamics and reduce ESS energy sizing.

The analysis can be divided into two main parts. A first part addressing the energy analysis presented in Fig. 4.8a and a second part that corresponds to the power analysis presented in

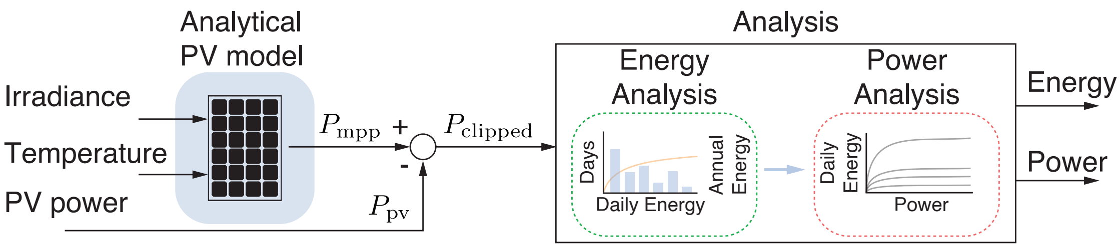

Figure 4.7: ESS sizing strategy for Power Clipping

Fig. 4.8b. The explanation of the analysis procedure is described below, starting with the energy analysis.

The first step consists of estimating the maximum recoverable daily-energy-loss ($\hat{E}_{\text{del}}$), which corresponds to the integral of the clipped power (P_{clip}) along each day, scaled by the efficiency of the PV-ESS-grid system (86.7 %). The resulting daily estimation of $\hat{E}_{\text{del}}$ is then represented through a histogram, as shown in Fig. 4.8a. Two additional curves are included in Fig. 4.8a, the first curve corresponds to the accumulated annual energy loss as a function of the maximum daily-energy-loss (dashed line), while the second curve (continuous line) corresponds to the accumulated recoverable annual energy loss as a function of the maximum recoverable daily-energy-loss ($C_1 : \hat{E}_{\text{del}}$). Both curves were normalized with respect to the annual energy loss (33 MWh).

The next step consists of selecting a recovery ratio, which is calculated as a chosen energy value (E_{rec}) divided by the total annual energy loss (33 MWh). Note that E_{rec} must be lower or equal the the total recoverable annual energy (28.6 MWh). The maximum recoverable daily-energy-loss distribution presented in the histogram can be applied to select an adequate recovery ratio, e.g. 0.8 [pu]. The intersection of the recovery ratio (right-side vertical axis) with the accumulated recoverable annual energy loss curve (continuous line) indicates a value in the horizontal axis, this latter value corresponds to the the initial energy sizing of the ESS, e.g. 0.6 [MWh].

Figure 4.8b shows the power rating analysis, where four ESS power rating design criteria are depicted as a function of the the recoverable-daily-energy-loss. All criteria include a 97 % efficiency of the dc-dc power converter. The criteria C_1 to C_4 correspond respectively to maximum recoverable-daily-energy-loss in MWh ($\hat{E}_{\text{del}}$), average recoverable daily-energy-loss in MWh ($\overline{E}_{\text{del}}$), average plus the standard deviation of recoverable daily-energy-loss in MWh ($\overline{E}_{\text{del}} + \sigma_{\text{Edel}}$) and average plus two times the standard deviation of recoverable daily-energy-loss in MWh ($\overline{E}_{\text{del}} + 2 \cdot \sigma_{\text{Edel}}$). The remaining part of the analysis consists of selecting a ESS power rating design criteria (e.g. C_1), and intersecting the initial energy sizing (left-side vertical axis of Fig. 4.8b) with the curve of the selected criteria, thus obtaining, from the horizontal axis, the ESS power rating (e.g. 0.2 MW). If the initial energy sizing is greater than the maximum value of the selecting criteria,

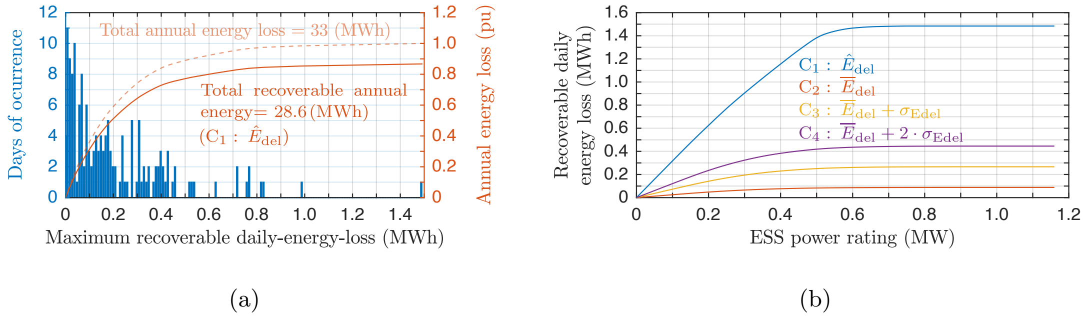

Figure 4.8: PV plant ESS energy and power sizing analysis: a) daily-energy-loss histogram, accumulated annual energy loss and total recoverable annual energy (considering the efficiency of the PV-ESS-grid system) and b) power-limited recoverable daily energy considering the efficiency of the DC/DC power converter

then reduce the recovery ratio until reaching the selected criteria.

As an example, to recover 80% of the annual energy lost due to clipping, an ESS of 600 kWh is required to store the maximum daily-energy-loss of (Fig. 4.8a), which, considering criteria C_1 (from Fig. 4.8b), leads to a power rating of 200 kW.

As stated in section 1, the economical information obtained from the industrial project is protected by an NDA, thus only a general idea of the economical results will be presented. The economical analysis was based on simplex solver method. For this purpose three different brands of commercially available DC/DC power converters (Tame Power, Epic Power, Zekalabs) and battery packs (BYD,LG,Fronius) were considered. The constraints in terms of power and energy applied in the solver correspond to those obtained from the ESS sizing strategy for power clipping. The results showed that the revenue obtained from adding an ESS to store energy from a power clipping application in a PV plant is considerably smaller than the investment. EST (battery) price is by far the most significant cost. However, the sustained reduction of Li-Ion batteries pricing over the last few years and the constant increase of life expectancy makes power clipping a relevant application to bear in mind for the near future.

A similar economical analysis was performed over the data obtained from the RR regulation losses and ESS sizing strategy for RR control. This analysis considered a constant spot price of 37.69 [£/MWh] and the same power converters and battery packs that were applied in the economical analysis for power clipping. Power and energy sizing obtained from the ESS sizing strategy for RR control were used as constraints for the solver. The results show that the cost of the ESS (battery and power converter) is significantly higher than the revenue that could be obtained from avoiding the loss of generation due to RR regulation. Note that the spot price

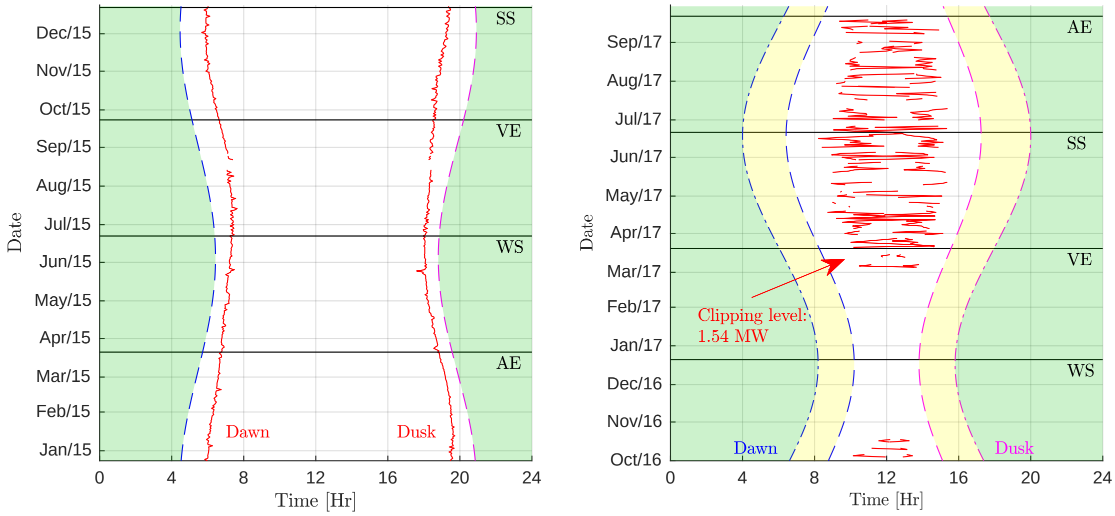

(a) (b)

Figure 4.9: Idle hours of ESS operation (green and yellow) performing complementary services: a) maximum power RR in a theoretical PV plant located in Atacama (Chile), b) power clipping in a real PV plant located in Cambridgeshire (Uk)

considered in the RR limitation analysis was obtained from a PV plant located in Chile.

An alternative for increasing revenue under the current economical situation is to consider performing additional complementary services during the time the ESS will not perform its targeted complementary service. In this context, the next section presents a detailed analysis over idle hours and additional complementary services.

4.5 Idle hours and additional complementary services

Complementary services require an specific event to start providing the service (message from GO, frequency deviation, maximum power RR, reaching of maximum power rating, sunrise, etc.), therefore, risking several hours of idle operation of the ESS. However, in some complementary services, idle operation hours can be predicted, thus, allowing planning ahead and compromising the storage capability to perform other (additional) complementary services. Examples of this behaviour can be observed in both previously analysed cases, maximum power RR regulation and power clipping. The analysis of both cases is presented in this section.

Maximum power RR regulates PV power variation per minute. In consequence its hours of operation are tied to the hours that the PV system can generate power (dawn to dusk). The annual analysis of idle operation hours of an hypothetical ESS, providing RR regulation services in

Atacama (Chile), is shown in Fig. 4.9a. In this figure, the red lines indicate the beginning (Dawn) and end (Dusk) of PV power generation. The green areas show the span when RR regulation is not performed (nightime), thus enabling the ESS to perform other complementary service. The two dashed lines (blue and magenta) in Fig. 4.9a, provide extra time to allow a soft transition (charging/discharging the ESS) from one complementary service to the other.

Power clipping presents a different approach with respect to idle operation of ESS, since idle hours depend on the oversizing of the PV array and the meteorological characteristics of the location. In the case of Cambridgeshire (UK), power clipping presents more idle time operation of the ESS than the idle time that RR regulation (in the same location) will present. This is caused by clipping taking place only during a part of the year and around midday, thus freeing ESS capabilities for other complementary services. This behaviour is shown in Fig. 4.9b, where PV generation reaching clipping level ($P_{\text{pv}} = 1.54$ [MW]) is indicated in red. Two dash-dot lines, blue and magenta, indicate dawn and dusk. And, as in Fig. 4.9a, two dashed lines (blue and magenta) provide extra time to allow a soft transition (charging/discharging the ESS) from one complementary service to another. The green areas indicate time frames when there is no sunlight (no PV generation) and other complementary services can be provided, while, the yellow areas show periods of time when PV power is being generated. However, power clipping services can be performed at nighttime, since, some of these services support power generation being produced by the PV system.

4.6 Summary

Two novel ESS sizing strategies were presented in this chapter. The first strategy tackled maximum power ramp rate for a PV plant located in Atacama Chile. To motivate the addition of ESS, the annual loss of generation for four different levels of RR regulation were estimated. The proposed ESS sizing strategy provides four different curves to size the ESS, among these alternatives C_{a1s} presents the best trade-off between energy sizing and ESS sizing efficiency. A comparison between the proposed ESS sizing strategy and other strategy available in literature was also presented. This contrast shows that the proposed strategy offers a better alternative, reducing the rating of the ESS while increasing the percentage of loss of generation (energy) that can be recovered. The second strategy targeted ESS sizing for power clipping in a PV plant located in Cambridgeshire. To the best knowledge of the author this is the first ESS sizing strategy available in literature that targets power clipping. The annual loss of generation associated with power clipping was also estimated. Both ESS sizing strategies correspond to novel knowledge and provide a power-energy rating criteria to size the ESS. In order to further motivate the addition of ESS into PV systems, the analysis of idle (available) hours, when the selected complementary service will never take place, were also presented. This analysis shows that both services imply a range of hours when the service will never be performed, therefore allowing consideration of that time for the provision of additional complementary services and thus enabling the increase of revenue obtained by the addition of the ESS into the PV configuration.

Chapter 5

Power Converter Topologies for ESS in PV systems

5.1 Introduction

This chapter presents the beginning of the second research topic addressed in the thesis, i.e. bidirectional dc-dc power converters for PV/ESS configurations. Since this part of the thesis was developed earlier in the research, the ESS sizing strategies, presented in the previous chapter, were not available (at that time) and thus were not implemented in the results shown in the following chapters (second part of the thesis).

The selection of the PV/ESS configurations, that will be implemented in the simulations and experimental tests (chapters 7 and 8), is presented in this chapter.

In this chapter the circuit diagram and mathematical model of the bidirectional dc-dcpower converter topologies that have been implemented in the thesis are presented. These power converters correspond to an Isolated Bidirectional Boost Converter (IBBC) and two novel full-bridge based bidirectional Partial Power Converters (PPC). The outcome of this chapter corresponds to the transfer functions of the averaged model of each power converter. These were applied in chapter 6 to design the control loops that were implemented in the simulations and experimental result presented in chapter 7 and 8. Moreover, this chapter also includes the proposal of a (new) unified bidirectional averaged model for the IBBC.

5.2 Selected configurations

The AC-grid-connection and the PV-connection PV/ESS configurations (Fig. 5.1a and Fig. 5.1b) were selected to be implemented during the thesis. The former corresponds to the mainstream solution, when provisioning (enhancing) power plants with energy storage systems [123–125]. The latter configuration, PV/ESS configuration with interconnection at PV array side, was selected since it was the only configuration capable of tackling the loss of generation in power clipping scenarios (a topic previously discussed in chapter 1 section1.1.2). Moreover, the addition of the ESS at inverter level allows a modular design that provides flexibility and scalability.

The following sections present the circuit diagram and mathematical model of the bidirectional dc-dcpower converters applied in the aforementioned PV/ESS configurations. Note that the circuit diagram and mathematical averaged model of the conventional Two Level Voltage Source Inverters (2LVSI), implemented in all the simulations and experimental test of the PV/ESS configurations, can be found in appendix A.

5.3 Isolated Bidirectional Boost Converter

The circuit diagram of an isolated bidirectional boost dc-dc converter (IBBC) is presented in Fig. 5.2. In this circuit diagram v_{in}, L, i_{L}, v_{fm}, i_{p}, i_{s}, v_{p}, v_{s}, n_1, n_2, i_{d}, C_{o}, i_{oc}, i_{o}, v_{o} and s_{x} are the input voltage in [V], inductance of the input filter in [H], current trough the input filter (L) in [A], voltage before the semiconductors in [V], current in the primary winding in [A], current in the secondary winding of the ideal transformer in [A], voltage in the primary winding of the ideal transformer in [V], voltage in the secondary winding of the ideal transformer in [V], number of turns in the primary winding of the transformer, number of turns in the secondary winding of the transformer, current after the right-side full bridge in [A], capacitance of the output capacitor in

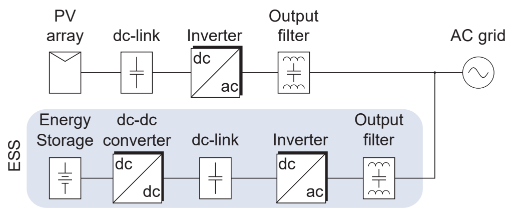

(a)

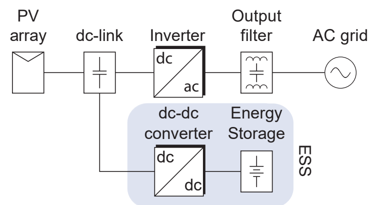

(b)

Figure 5.1: Applied PV/ESS configurations: a) AC-grid-side connection and b) PV-side connection.

[F], current through the output capacitor in [A], output current of the IBBC in [A], output voltage of the IBBC in [V] and triggering signal of the semiconductor x ($x \in \{1, \ldots, 8\}$). The IBBC model presented in this section is based on a simplified model of the transformer, that only includes the ideal transformer. For the IBBC to operate, the output voltage (v_o) of the converter must be greater than the input voltage of the converter (v_in). The mathematical model of the IBBC is presented below.

Equations (5.1) and (5.2) are obtained from applying Kirchhoff laws to the IBBC. In eq. (5.1), R_L corresponds to the resistance of the input filter (L) in [Ω].

$$v_\mathrm{in} - L\frac{di_\mathrm{L}}{dt} - R_\mathrm{L} \cdot i_\mathrm{L} - v_\mathrm{fb} = 0 \tag{5.1}$$

$$C_\mathrm{o}\frac{dv_\mathrm{o}}{dt} = (i_\mathrm{d} - i_\mathrm{o}) \tag{5.2}$$

The IBBC is capable of managing bidirectional power flow, for this reason the analysis of the circuit will be separated into two operating modes with the first one corresponding to the analysis of power flowing from v_in to v_o (boosting). The second operation mode analyses power flowing from v_o to v_in, namely bucking.

5.3.1 Boosting mode model

In this operation mode semiconductors s_5 to s_8 are kept un-triggered, while semiconductors s_1 to s_4 are turned on and off, allowing control of the power flow from v_in to v_o. The allowed combinations of switching states of MOSFETs 1 to 4 (keeping MOSFETs 5 to 8 off) in boosting mode operation are shown in Table 5.1.

Equation (5.3) summarises the content of Table 5.1 regarding v_fb.

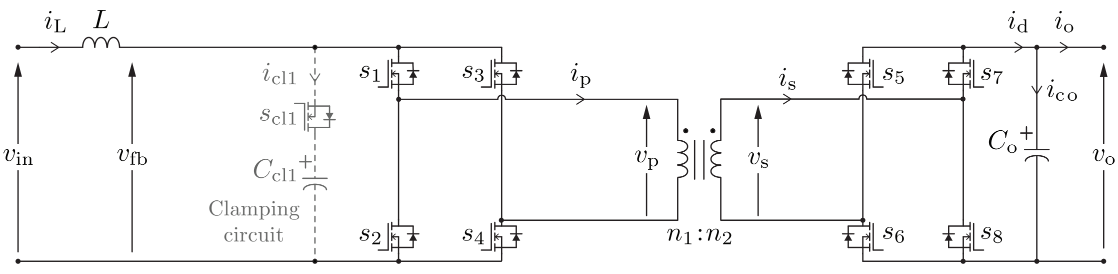

Figure 5.2: Isolated Bidirectional Boost Converter (IBBC) topology.

$$v_{\mathrm{fb}} = \begin{cases} v_{\mathrm{p}} & , if \quad s_1 \cdot \bar{s}_2 \cdot \bar{s}_3 \cdot s_4 = 1 \\ -v_{\mathrm{p}} & , if \quad \bar{s}_1 \cdot s_2 \cdot s_3 \cdot \bar{s}_4 = 1 \\ 0 & , otherwise \end{cases} \tag{5.3}$$

Defining $\Gamma_p = (s_1 \cdot \bar{s}_2 \cdot \bar{s}_3 \cdot s_4 - \bar{s}_1 \cdot s_2 \cdot s_3 \cdot \bar{s}_4)$, eq. (5.1) can be rewritten as,

$$v_{\mathrm{in}} - L\frac{di_{\mathrm{L}}}{dt} - R_{\mathrm{L}} \cdot i_{\mathrm{L}} - \Gamma_p \cdot v_{\mathrm{p}} = 0 \tag{5.4}$$

The relationship between the voltage of the primary winding of the transformer and the output of the converter is shown in eq. (5.5). The additional term Γ, was added to show the effect of having a zero voltage across the primary (and secondary) winding of the transformer over the conductivity of the internal body diodes of the MOSFETs in the secondary-winding-side (s_5 to s_8).

$$v_{\mathrm{p}} = \left(\frac{n_1}{n_2}\right) \cdot \Gamma_p \cdot v_{\mathrm{o}} \tag{5.5}$$

Applying eq. (5.5) into eq. (5.4),

$$v_{\mathrm{in}} - L\frac{di_{\mathrm{L}}}{dt} - R_{\mathrm{L}} \cdot i_{\mathrm{L}} - \Gamma_p^2 \cdot \left(\frac{n_1}{n_2}\right) \cdot v_{\mathrm{o}} = 0 \tag{5.6}$$

Note that $s_{\mathrm{x}} \in \{0,1\}$ (x $\in \{1,2,3,4\}$), thus $\Gamma_p \in \{-1,0,1\}$ and $\Gamma_p^2 \in \{0,1\}$. Transforming the previous model into an averaged model and replacing Γ_p^2 by M in eq. (5.6), gives:

$$v_{\mathrm{in}} - L\frac{di_{\mathrm{L}}}{dt} - R_{\mathrm{L}} \cdot i_{\mathrm{L}} - M_{\mathrm{p}} \cdot \left(\frac{n_1}{n_2}\right) \cdot v_{\mathrm{o}} = 0 \tag{5.7}$$

where M_{p} corresponds to the modulation index.

The expression for i_{L} is obtained by applying the Laplace transform and clearing i_{L} in the previous equation.

$$i_{\mathrm{L}} = \left(\frac{1}{s \cdot L + R_{\mathrm{L}}}\right) \cdot \left(v_{\mathrm{in}} - M_{\mathrm{p}} \cdot \left(\frac{n_1}{n_2}\right) \cdot v_{\mathrm{o}}\right) \tag{5.8}$$

Γ_{p}	s_1	s_2	s_3	s_4	s_5	s_6	s_7	s_8	v_{fb}
1	1	0	0	1	0	0	0	0	v_{p}
-1	0	1	1	0	0	0	0	0	$-v_{\mathrm{p}}$
0	1	1	1	1	0	0	0	0	0

Table 5.1: Allowed switching states of the IBBC in boosting mode

The mathematical model of the output capacitor C_o is obtained from the development of eq. (5.2). The relationship between i_d and i_p is given by,

$$i_\mathrm{d} = \Gamma_p \cdot \left(\frac{n_1}{n_2}\right) \cdot i_\mathrm{p} \tag{5.9}$$

Additionally, i_p is equivalent to:

$$i_\mathrm{p} = \Gamma_p \cdot i_\mathrm{L} \tag{5.10}$$

Hence replacing eqs. (5.10) into eq. (5.9),

$$i_\mathrm{d} = \Gamma_p^2 \cdot \left(\frac{n_1}{n_2}\right) \cdot i_\mathrm{L} \tag{5.11}$$

Transforming eq. (5.11) into its averaged form and replacing Γ_p^2 by M_p,

$$i_\mathrm{d} = M_p \cdot \left(\frac{n_1}{n_2}\right) \cdot i_\mathrm{L} \tag{5.12}$$

Replacing eq. (5.12) into eq. (5.2),

$$C_\mathrm{o}\frac{dv_\mathrm{o}}{dt} = \left(M_\mathrm{p} \cdot \left(\frac{n_1}{n_2}\right) \cdot i_\mathrm{L} - i_\mathrm{o}\right) \tag{5.13}$$

5.3.2 Bucking mode model

In bucking mode power flows from v_o to v_in, thus semiconductors 1 to 4 are kept un-triggered, while semiconductors 5 to 8 are turned on and off, enabling the control on the power flow. The switching states that are allowed in this operation mode are presented in Table 5.2.

Proceeding in the same way as in boosting mode analysis, i.e. defining Γ_s as $\Gamma_s = (s_5 \cdot \bar{s}_6 \cdot \bar{s}_7 \cdot s_8 - \bar{s}_5 \cdot s_6 \cdot s_7 \cdot \bar{s}_8)$.

The relationship between the output voltage (v_o) and v_fb can be found by applying the definition of Γ_s and is presented in eq. (5.14).

Γ_s	s_1	s_2	s_3	s_4	s_5	s_6	s_7	s_8	v_s
1	0	0	0	0	1	0	0	1	v_o
-1	0	0	0	0	0	1	1	0	$-v_\mathrm{o}$
0	0	0	0	0	0	1	0	1	0

Table 5.2: Allowed switching states of the IBBC in bucking mode

$$v_{\mathrm{fb}} = \Gamma_{\mathrm{s}}^2 \cdot \left(\frac{n_1}{n_2}\right) \cdot v_{\mathrm{o}} \tag{5.14}$$

Transforming the model into an averaged model and replacing Γ_{s}^2 by M_{s} and eq. (5.14) into eq. (5.1).

$$v_{\mathrm{in}} - L\frac{di_{\mathrm{L}}}{dt} - R_{\mathrm{L}} \cdot i_{\mathrm{L}} - M_{\mathrm{s}} \cdot \left(\frac{n_1}{n_2}\right) \cdot v_{\mathrm{o}} = 0 \tag{5.15}$$

The relationship between the i_{d} and the current through the inductor L (i_{L}) is presented in eq. (5.16).

$$i_{\mathrm{d}} = \Gamma_{\mathrm{s}}^2 \cdot \left(\frac{n_1}{n_2}\right) \cdot i_{\mathrm{L}} \tag{5.16}$$

Transforming eq. (5.16) into its averaged form (replacing Γ_{s}^2 by M_{s}),

$$i_{\mathrm{d}} = M_{\mathrm{s}} \cdot \left(\frac{n_1}{n_2}\right) \cdot i_{\mathrm{L}} \tag{5.17}$$

Applying eq. (5.17) into eq. (5.2).

$$C_{\mathrm{o}}\frac{dv_{\mathrm{o}}}{dt} = \left(M_s \cdot \left(\frac{n_1}{n_2}\right) \cdot i_{\mathrm{L}} - i_{\mathrm{o}}\right) \tag{5.18}$$

5.3.3 Bidirectional model

The resulting average model for both operation modes are identical, except for the modulation index (M_{p} and M_{s}). However, each modulation index is associated to one operation mode, i.e. when performing in boosting mode $M_{\mathrm{s}} = 0$ while $M_{\mathrm{p}} \in \{0, 1\}$, when performing in bucking mode $M_{\mathrm{p}} = 0$ while $M_{\mathrm{s}} \in \{0, 1\}$. Therefore, the following equation allows the representation of both operation modes through a single set of equations:

$$M = M_{\mathrm{p}} + M_{\mathrm{s}} \tag{5.19}$$

Equations (5.20) to (5.23) are obtained from applying eq. (5.19) into the resulting equations from boosting and bucking mode operation models.

$$\frac{di_{\mathrm{L}}}{dt} = \frac{1}{L} \cdot \left(-R_{\mathrm{L}} \cdot i_{\mathrm{L}} - \left(\frac{n_1}{n_2}\right) \cdot v_{\mathrm{o}} \cdot M + v_{\mathrm{in}}\right) \tag{5.20}$$

$$\frac{dv_{\mathrm{o}}}{dt} = \frac{1}{C_{\mathrm{o}}} \cdot \left(\left(\frac{n_1}{n_2}\right) \cdot i_{\mathrm{L}} \cdot M - i_{\mathrm{o}}\right) \tag{5.21}$$

$$v_{\text{fb}} = \left(\frac{n_1}{n_2}\right) \cdot M \cdot v_{\text{o}} \tag{5.22}$$

$$i_{\text{d}} = \left(\frac{n_1}{n_2}\right) \cdot i_{\text{L}} \cdot M \tag{5.23}$$

Considering M and i_{L} respectively as the input and output of the system, the transfer function between M and i_{L} can be obtained by linearising eq. 5.20 and transforming it into the Laplace domain:

$$G_{i_{\text{L}}M} = \frac{i_{\text{L}}}{M} = \left(\frac{n_1}{n_2}\right) \cdot \left(\frac{-v_{\text{oQ}}}{L \cdot s + R_{\text{L}}}\right) \tag{5.24}$$

The transfer function between the square of the output voltage v_o^2 and the (IBBC) inductor's current i_L can be obtained from the relation between the input power ($i_{\text{L}} \cdot v_{\text{in}}$), power stored in the output capacitor ($C_{\text{o}}(dv_{\text{o}}/dt) \cdot v_{\text{o}}$) and output power ($P_{\text{o}}$). Note that this relation considers that the power losses in the IBBC have been neglected.

$$G_{v_{\text{o}}^2 i_{\text{L}}} = \frac{v_{\text{o}}^2}{i_{\text{L}}} = \frac{v_{\text{in}}}{C_{\text{o}} \cdot s} \tag{5.25}$$

The state space model of the IBBC is available in appendix D.

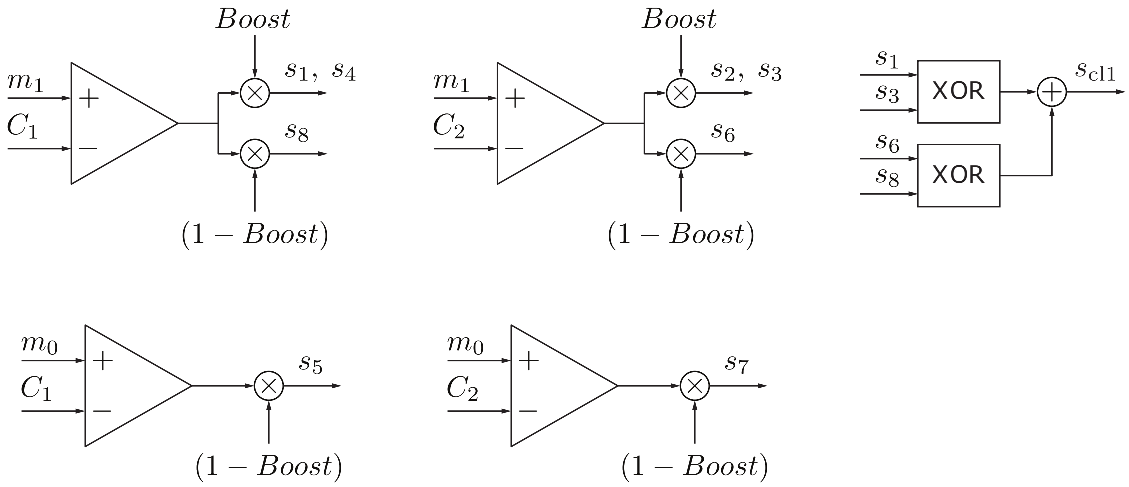

Figure 5.3: Modulation scheme for IBBC under bidirectional power flow: boosting (s_1, s_2, s_3, s_4 and s_{cl1}) and bucking (s_5, s_6, s_7, s_8 and s_{cl1}) mode.

5.3.4 Modulation scheme and resulting waveforms

The modulation index adaptations (m_0 and m_1), presented in eqs. (5.26) and (5.26), allow a symmetrical voltage waveform in the windings of the transformer (v_p and v_s) to be obtained.

$$m_0 = \left(\frac{M}{2}\right) \tag{5.26}$$

$$m_1 = \left(1 - \frac{M}{2}\right) \tag{5.27}$$

A diagram of the implemented modulation scheme is presented in Fig. 5.3, where C_1, C_2, *Boost* corresponds respectively to the Pulse Width Modulation (PWM) carrier 1, PWM carrier 2 (shifted π [rad] respect to C_1) and a control signal, which indicates the power direction. When power flows from v_in to v_o (boosting: $Boost = 1$) or from v_o to v_in (bucking: $Boost = 0$).

The idealised waveforms resulting from applying the previously described modulation scheme to the IBBC, under continuous conduction mode, are presented in Fig. 5.4. The left-side of Fig. 5.4 presents the resulting waveforms of the IBBC operating in boosting mode, while the right-side presents the converter operating in bucking mode.

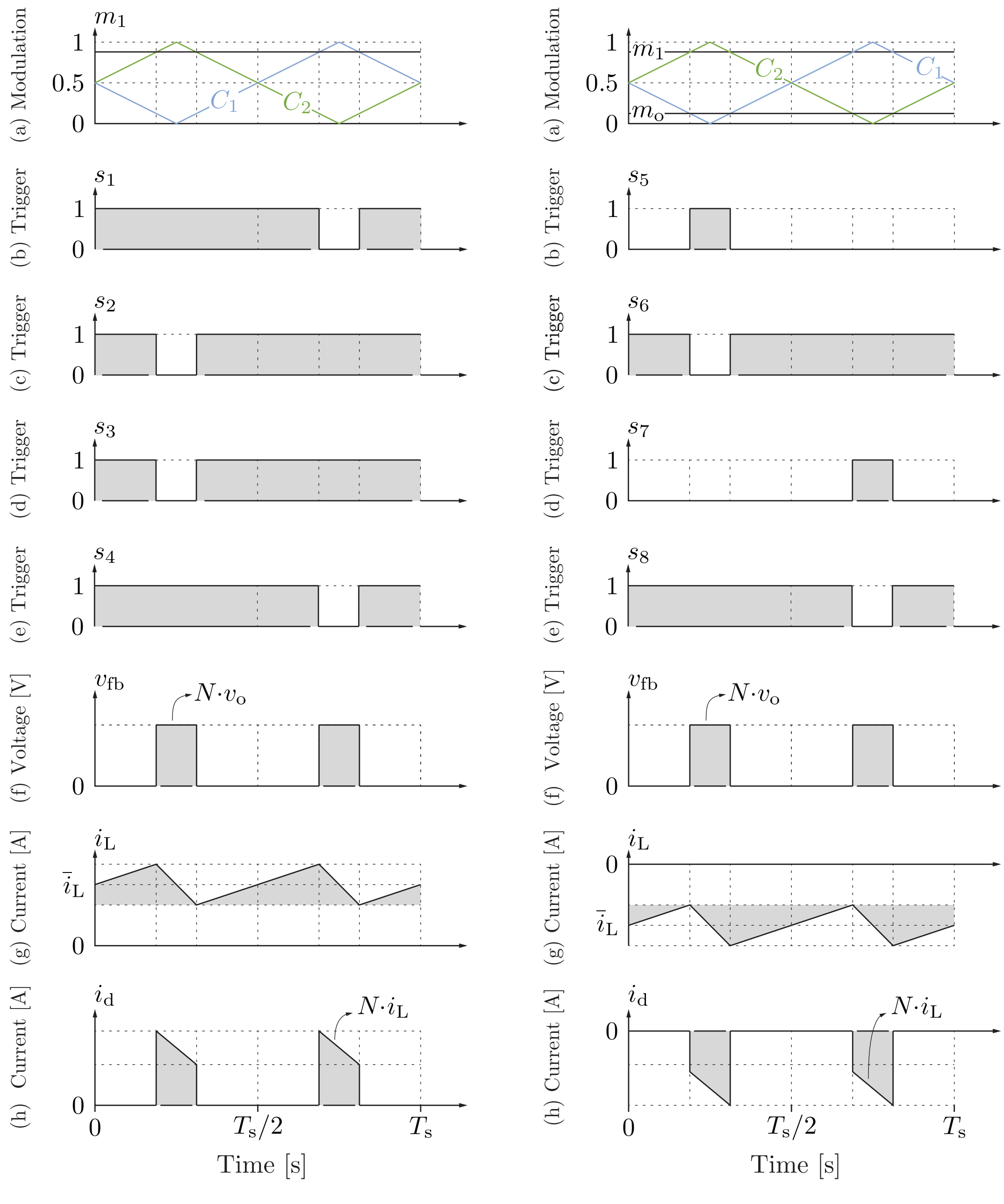

Figure 5.4: Idealized waveforms of a IBBC, operating in boosting (left) and bucking (right) modes: a) modulation index and PWM carriers, b) to e) gate signals, f) voltage across the left-side winding of the transformer and its semiconductors, g) current through the inductor L, h) output current.

5.4 Bidirectional Partial Power Converter - Input Side Inductor

A full-bridge based Partial Power Converter (PPC) with bidirectional power flow capability is shown in Fig. 5.5. The mathematical model of this power converter is presented below. Equations (5.28) to (5.32) are obtained from applying Kirchhoff's laws and the respective element equations to the circuit in Fig. 5.5,

$$v_{\text{in}} + L\frac{di_{\text{L}}}{dt} + R_{\text{L}} \cdot i_{\text{L}} + v_{\text{fbp}} - v_{\text{o}} = 0 \tag{5.28}$$

$$v_{\text{in}} + L\frac{di_{\text{L}}}{dt} + R_{\text{L}} \cdot i_{\text{L}} - v_{\text{fbs}} = 0 \tag{5.29}$$

$$v_{\text{fbs}} + v_{\text{fbp}} - v_{\text{o}} = 0 \tag{5.30}$$

$$i_{\text{L}} - i_{\text{bp}} - i_{\text{ppc}} = 0 \tag{5.31}$$

$$C_{\text{o}}\frac{dv_{\text{o}}}{dt} + \frac{v_{\text{o}}}{R_{\text{o}}} + i_{\text{bp}} - i_{\text{o}} = 0 \tag{5.32}$$

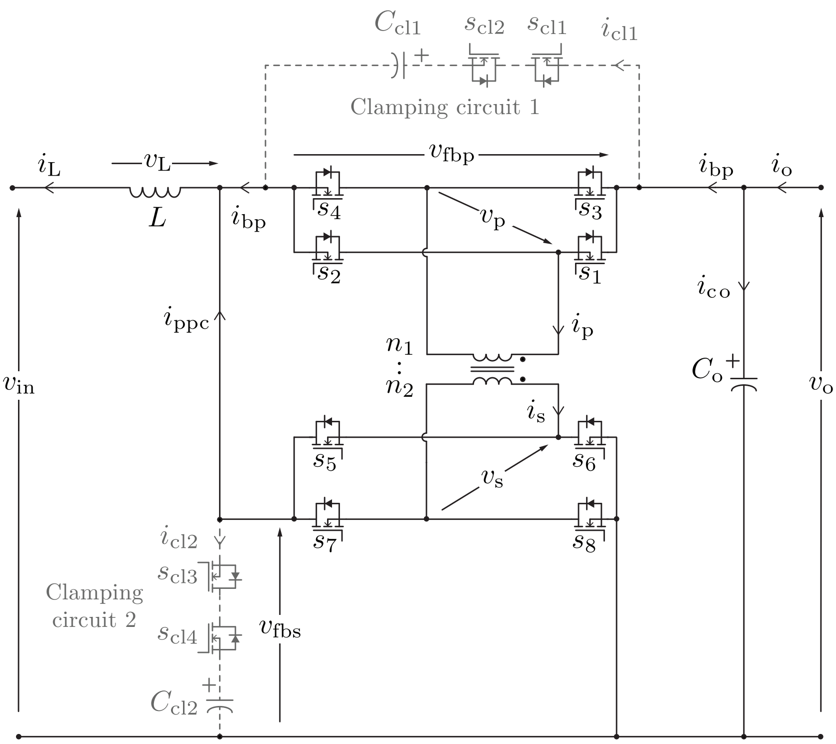

Figure 5.5: Full-bridge based Partial Power Converter topology with an inductor in the input side.

where v_{in}, L, R_{L}, i_{L}, v_{fbp}, v_{fbs}, v_{o}, C_{o}, R_{o}, i_{co}, i_{bp}, i_{ppc} correspond respectively to the voltage in the terminals of the EST in [V], inductance of the input filter (L) in[H], resistance of the inductor L in [Ω], current through the inductor L in [A], voltage across the top winding and its semiconductors in [V], voltage in the bottom winding and its semiconductors in [V], output voltage of the converter in [V], capacitance of the output capacitor in [F], output capacitor self-discharge resistance in [Ω], current through the output capacitor in [A], bypass current in [A] and partial power current in [A]. Note that the following analysis considers that v_{in} is lower than v_{o}.

In order to simplify the modelling of the circuit, its analysis has been separated in two operation modes, namely bucking and boosting. The former corresponds to power flowing from v_{o} to v_{in}, while the latter corresponds to power flowing from v_{in} to v_{o}.

Regarding the clamping circuits, in bucking mode operation Clamping Circuit 1 is enabled ($s_{\mathrm{c2}} = 1$), while Clamping Circuit 2 is disabled ($s_{\mathrm{c4}} = 0$). On the other hand during boosting mode operation Clamping Circuit 1 is disabled ($s_{\mathrm{c2}} = 0$) and Clamping Circuit 2 is enabled ($s_{\mathrm{c4}} = 1$).

5.4.1 Bucking mode model

During bucking operation only the upper MOSFETs (s_1, s_2, s_3 and s_4) are triggered, while the lower semiconductors (s_5, s_6, s_7 and s_8) are kept un-triggered, relying on the internal diode characteristic of the MOSFETs for its conduction. The allowed switching states of the full bridge based PPC in bucking mode are presented in Table 5.3.

Equations (5.33) and (5.34) show the value of the voltages v_{fbp} and v_{fbs} for each switching state.

Γ_{t}	s_1	s_2	s_3	s_4	s_5	s_6	s_7	s_8	v_{fbp}	v_{fbs}
1	1	0	0	1	0	0	0	0	v_{p}	v_{s}
-1	0	1	1	0	0	0	0	0	$-v_{\mathrm{p}}$	$-v_{\mathrm{s}}$
0	0	0	0	0	0	0	0	0	v_{o}	0

Table 5.3: Allowed switching states of the full bridge based PPC in bucking mode.

$$v_{\mathrm{fbp}} = \begin{cases} v_{\mathrm{p}} & , if\ s_1 \cdot \bar{s}_2 \cdot \bar{s}_3 \cdot s_4 = 1 \\ -v_{\mathrm{p}} & , if\ \bar{s}_1 \cdot s_2 \cdot s_3 \cdot \bar{s}_4 = 1 \\ v_{\mathrm{o}} & , otherwise \end{cases} \tag{5.33}$$

$$v_{\mathrm{fbs}} = \begin{cases} \left(\dfrac{n_2}{n_1}\right) \cdot (v_{\mathrm{p}}) & , if\ s_1 \cdot \bar{s}_2 \cdot \bar{s}_3 \cdot s_4 = 1 \\ \left(\dfrac{n_2}{n_1}\right) \cdot (-v_{\mathrm{p}}) & , if\ \bar{s}_1 \cdot s_2 \cdot s_3 \cdot \bar{s}_4 = 1 \\ 0 & , otherwise \end{cases} \tag{5.34}$$

Replacing eqs. (5.33) and (5.34) in eq. (5.30) and rewriting v_{fbp},

$$v_{\mathrm{fbp}} = \begin{cases} \left(\dfrac{n_1}{n_1 + n_2}\right) \cdot v_{\mathrm{o}} & , if\ s_1 \cdot \bar{s}_2 \cdot \bar{s}_3 \cdot s_4 = 1 \\ \left(\dfrac{n_1}{n_1 + n_2}\right) \cdot v_{\mathrm{o}} & , if\ \bar{s}_1 \cdot s_2 \cdot s_3 \cdot \bar{s}_4 = 1 \\ v_{\mathrm{o}} & , otherwise \end{cases} \tag{5.35}$$

Considering eqs. (5.30) and (5.35) and rewriting v_{fbs}

$$v_{\mathrm{fbs}} = \begin{cases} \left(\dfrac{n_2}{n_1 + n_2}\right) \cdot v_{\mathrm{o}} & , if\ s_1 \cdot \bar{s}_2 \cdot \bar{s}_3 \cdot s_4 = 1 \\ \left(\dfrac{n_2}{n_1 + n_2}\right) \cdot v_{\mathrm{o}} & , if\ \bar{s}_1 \cdot s_2 \cdot s_3 \cdot \bar{s}_4 = 1 \\ 0 & , otherwise \end{cases} \tag{5.36}$$

Defining Γ_{t} as,

$$\Gamma_{\mathrm{t}} = s_1 \cdot \bar{s}_2 \cdot \bar{s}_3 \cdot s_4 - \bar{s}_1 \cdot s_2 \cdot s_3 \cdot \bar{s}_4 \tag{5.37}$$

hence, eqs. (5.35) and (5.36) can be rewritten as:

$$v_{\mathrm{fbp}} = \Gamma_{\mathrm{t}}^2 \cdot \left(\frac{n_1}{n_1 + n_2}\right) \cdot v_{\mathrm{o}} + (1 - \Gamma_{\mathrm{t}}^2) \cdot v_{\mathrm{o}} \tag{5.38}$$

$$v_{\mathrm{fbs}} = \Gamma_{\mathrm{t}}^2 \cdot \left(\frac{n_2}{n_1 + n_2}\right) \cdot v_{\mathrm{o}} \tag{5.39}$$

Replacing eq. (5.39) into eq. (5.29),

$$L\frac{di_{\mathrm{L}}}{dt} = -R_{\mathrm{L}} \cdot i_{\mathrm{L}} + \left(\frac{n_2}{n_1 + n_2}\right) \cdot v_{\mathrm{o}} \cdot \Gamma_{\mathrm{t}}^2 - v_{\mathrm{in}} \tag{5.40}$$

Performing a similar analysis to i_{L}, as the analysis performed to v_{fbs}

$$i_{\mathrm{bp}} = \begin{cases} i_{\mathrm{L}} - i_{\mathrm{ppc}} & , if\ s_1 \cdot \bar{s}_2 \cdot \bar{s}_3 \cdot s_4 = 1 \\ i_{\mathrm{L}} - i_{\mathrm{ppc}} & , if\ \bar{s}_1 \cdot s_2 \cdot s_3 \cdot \bar{s}_4 = 1 \\ 0 & , otherwise \end{cases} \tag{5.41}$$

$$i_{\mathrm{ppc}} = \begin{cases} \left(\dfrac{n_1}{n_2}\right) \cdot i_{\mathrm{bp}} & , if\ s_1 \cdot \bar{s}_2 \cdot \bar{s}_3 \cdot s_4 = 1 \\ \left(\dfrac{n_1}{n_2}\right) \cdot i_{\mathrm{bp}} & , if\ \bar{s}_1 \cdot s_2 \cdot s_3 \cdot \bar{s}_4 = 1 \\ i_{\mathrm{L}} & , otherwise \end{cases} \tag{5.42}$$

Replacing eq. (5.42) into eq. (5.41)

$$i_{\mathrm{bp}} = \begin{cases} \left(\dfrac{n_2}{n_1 + n_2}\right) \cdot i_{\mathrm{L}} & , if\ s_1 \cdot \bar{s}_2 \cdot \bar{s}_3 \cdot s_4 = 1 \\ \left(\dfrac{n_2}{n_1 + n_2}\right) \cdot i_{\mathrm{L}} & , if\ \bar{s}_1 \cdot s_2 \cdot s_3 \cdot \bar{s}_4 = 1 \\ 0 & , otherwise \end{cases} \tag{5.43}$$

Considering eqs. (5.41) into eq. (5.43) and rewriting i_{ppc}

$$i_{\mathrm{ppc}} = \begin{cases} \left(\dfrac{n_1}{n_1 + n_2}\right) \cdot i_{\mathrm{L}} & , if\ s_1 \cdot \bar{s}_2 \cdot \bar{s}_3 \cdot s_4 = 1 \\ \left(\dfrac{n_1}{n_1 + n_2}\right) \cdot i_{\mathrm{L}} & , if\ \bar{s}_1 \cdot s_2 \cdot s_3 \cdot \bar{s}_4 = 1 \\ i_{\mathrm{L}} & , otherwise \end{cases} \tag{5.44}$$

Considering eqs. (5.43) and (5.44) the definition of Γ_{t}, i_{bp} and i_{ppc} can be rewritten as

$$i_{\mathrm{bp}} = \left(\frac{n_2}{n_1 + n_2}\right) \cdot i_{\mathrm{L}} \cdot \Gamma_{\mathrm{t}}^2 \tag{5.45}$$

$$i_{\mathrm{ppc}} = \left(\frac{n_1}{n_1 + n_2}\right) \cdot i_{\mathrm{L}} \cdot \Gamma_{\mathrm{t}}^2 + i_{\mathrm{L}} \cdot (1 - \Gamma_{\mathrm{t}}^2) \tag{5.46}$$

Replacing eq. (5.45) into eq. (5.32)

$$C_{\mathrm{o}} \frac{dv_{\mathrm{o}}}{dt} = -\frac{v_{\mathrm{o}}}{R_{\mathrm{o}}} - \left(\frac{n_2}{n_1 + n_2}\right) \cdot i_{\mathrm{L}} \cdot \Gamma_{\mathrm{t}}^2 + i_{\mathrm{o}} \tag{5.47}$$

5.4.2 Boosting mode model

During boosting mode operation power flows from v_{in} towards v_{o}. In order to manage the current flow, semiconductors 5 to 8 (lower bridge) are turned on and off, while semiconductors 1 to 4 (upper bridge) are kept un-triggered. However, current flow in the upper bridge is accomplished through the body diode in MOSFETs 1 to 4. Table 5.4 summarises the switching states allowed during boosting mode operation.

Proceeding in the same form as in the bucking mode operation, v_{fbp} and v_{fbs} can be expressed as

$$v_{\mathrm{fbp}} = \begin{cases} \left(\dfrac{n_1}{n_1+n_2}\right)\cdot v_{\mathrm{o}} & , if\ s_5\cdot\bar{s}_6\cdot\bar{s}_7\cdot s_8 = 1 \\ \left(\dfrac{n_1}{n_1+n_2}\right)\cdot v_{\mathrm{o}} & , if\ \bar{s}_5\cdot s_6\cdot s_7\cdot\bar{s}_8 = 1 \\ v_{\mathrm{o}} & , otherwise \end{cases} \tag{5.48}$$

$$v_{\mathrm{fbs}} = \begin{cases} \left(\dfrac{n_2}{n_1+n_2}\right)\cdot v_{\mathrm{o}} & , if\ s_5\cdot\bar{s}_6\cdot\bar{s}_7\cdot s_8 = 1 \\ \left(\dfrac{n_2}{n_1+n_2}\right)\cdot v_{\mathrm{o}} & , if\ \bar{s}_5\cdot s_6\cdot s_7\cdot\bar{s}_8 = 1 \\ 0 & , otherwise \end{cases} \tag{5.49}$$

Defining Γ_{b} as

$$\Gamma_{\mathrm{b}} = (s_5\cdot\bar{s}_6\cdot\bar{s}_7\cdot s_8 - \bar{s}_5\cdot s_6\cdot s_7\cdot\bar{s}_8) \tag{5.50}$$

then, v_{fbp} and v_{fbs} can expressed as:

$$v_{\mathrm{fbp}} = \Gamma_{\mathrm{b}}^2\cdot\left(\frac{n_1}{n_1+n_2}\right)\cdot v_{\mathrm{o}} + (1-\Gamma_{\mathrm{b}}^2)\cdot v_{\mathrm{o}} \tag{5.51}$$

$$v_{\mathrm{fbs}} = \left(\frac{n_2}{n_1+n_2}\right)\cdot v_{\mathrm{o}}\cdot\Gamma_{\mathrm{b}}^2 \tag{5.52}$$

Replacing eq. (5.52) into eq. (5.29)

$$L\frac{di_{\mathrm{L}}}{dt} = -R_{\mathrm{L}}\cdot i_{\mathrm{L}} + \left(\frac{n_2}{n_1+n_2}\right)\cdot v_{\mathrm{o}}\cdot\Gamma_{\mathrm{b}}^2 - v_{\mathrm{in}} \tag{5.53}$$

Equations (5.54) and (5.55) shows respectively the possible values of i_{bp} and i_{ppc} depending on the state of switches 5 to 8.

Γ_{b}	s_1	s_2	s_3	s_4	s_5	s_6	s_7	s_8	v_{fbp}	v_{fbs}
1	0	0	0	0	1	0	0	1	v_{p}	v_{s}
-1	0	0	0	0	0	1	1	0	$-v_{\mathrm{p}}$	$-v_{\mathrm{s}}$
0	0	0	0	0	1	1	1	1	v_{o}	0

Table 5.4: Allowed switching states of the full bridge based PPC in boosting mode.

$$i_{\mathrm{bp}} = \begin{cases} \left(\dfrac{n_2}{n_1+n_2}\right)\cdot i_{\mathrm{L}} & , if\ s_5\cdot\bar{s}_6\cdot\bar{s}_7\cdot s_8 = 1 \\ \left(\dfrac{n_2}{n_1+n_2}\right)\cdot i_{\mathrm{L}} & , if\ \bar{s}_5\cdot s_6\cdot s_7\cdot\bar{s}_8 = 1 \\ 0 & , otherwise \end{cases} \tag{5.54}$$

$$i_{\mathrm{ppc}} = \begin{cases} \left(\dfrac{n_1}{n_1+n_2}\right)\cdot i_{\mathrm{L}} & , if\ s_5\cdot\bar{s}_6\cdot\bar{s}_7\cdot s_8 = 1 \\ \left(\dfrac{n_1}{n_1+n_2}\right)\cdot i_{\mathrm{L}} & , if\ \bar{s}_5\cdot s_6\cdot s_7\cdot\bar{s}_8 = 1 \\ i_{\mathrm{L}} & , otherwise \end{cases} \tag{5.55}$$

Equations (5.54) and (5.56) can be summarised as:

$$i_{\mathrm{bp}} = \left(\frac{n_2}{n_1+n_2}\right)\cdot i_{\mathrm{L}}\cdot\Gamma_{\mathrm{b}}^2 \tag{5.56}$$

$$i_{\mathrm{ppc}} = \left(\frac{n_1}{n_1+n_2}\right)\cdot i_{\mathrm{L}}\cdot\Gamma_{\mathrm{b}}^2 + i_{\mathrm{L}}\cdot(1-\Gamma_{\mathrm{b}}^2) \tag{5.57}$$

Replacing eq. (5.56) into eq. Eq. (5.32)

$$C_{\mathrm{o}}\frac{dv_{\mathrm{o}}}{dt} = -\frac{v_{\mathrm{o}}}{R_{\mathrm{o}}} - \left(\frac{n_2}{n_1+n_2}\right)\cdot i_{\mathrm{L}}\cdot\Gamma_{\mathrm{b}}^2 + i_{\mathrm{o}} \tag{5.58}$$

5.4.3 Bidirectional model

Only one operation mode can be performed at any given time, therefore when the system is in bucking mode semiconductors 5 to 8 are never triggered (conducting current only through their body diode), thus $\Gamma_{\mathrm{b}} = 0$. On the other hand when the system is operating in boosting mode, semiconductors 1 to 4 are kept un-triggered, hence making Γ_{t} equal to 0.

The bidirectional averaged model formed by the set of eqs. from (5.59) to (5.64) is obtained from averaging and joining both unidirectional models and replacing them in the resulting equations $\Gamma_{\mathrm{t}}^2 + \Gamma_{\mathrm{b}}^2$ by M.

$$L\frac{di_{\mathrm{L}}}{dt} = -R_{\mathrm{L}}\cdot i_{\mathrm{L}} + N_2\cdot v_{\mathrm{o}}\cdot M - v_{\mathrm{in}} \tag{5.59}$$

$$C_{\mathrm{o}}\frac{dv_{\mathrm{o}}}{dt} = -\frac{v_{\mathrm{o}}}{R_{\mathrm{o}}} - N_2\cdot i_{\mathrm{L}}\cdot M + i_{\mathrm{o}} \tag{5.60}$$

$$v_{\mathrm{fbp}} = M\cdot N_1\cdot v_{\mathrm{o}} + (1-M)\cdot v_{\mathrm{o}} \tag{5.61}$$

$$v_{\text{fbs}} = N_2 \cdot v_{\text{o}} \cdot M \tag{5.62}$$

$$i_{\text{bp}} = N_2 \cdot i_{\text{L}} \cdot M \tag{5.63}$$

$$i_{\text{ppc}} = N_1 \cdot i_{\text{L}} \cdot M + i_{\text{L}} \cdot (1 - M) \tag{5.64}$$

Note that to shorten the writing of the previous equations, the following definitions of N_1 and N_2 were applied

$$N_1 = \left(\frac{n_1}{n_1 + n_2} \right) \tag{5.65}$$

$$N_2 = \left(\frac{n_2}{n_1 + n_2} \right) \tag{5.66}$$

Considering M and i_{L} respectively as the input and output of the system, the transfer function between M and i_{L} corresponds to:

$$G_{i_{\text{L}}M} = \frac{i_{\text{L}}}{M} = \left(\frac{N_2 \cdot v_{\text{oQ}}}{s \cdot L + R_{\text{L}}} \right) \tag{5.67}$$

The state space model of the Bidirectional PPC with inductor in the input de is available in appendix D.2.

5.4.4 Modulation scheme and resulting waveforms

The modulation scheme applied to the Full-Bridge based PPC is presented in Fig. 5.6. In this figure m_0, C_1 and C_2 correspond to the adapted modulation index, PWM carrier 1 and PWM carrier 2 (shifted π [rad] respect to C_1). The power flow direction is indicated through the signal *Boost*, where:

$$Boost = \begin{cases} 1 & \text{, if power flows from } v_{\text{in}} \text{ to } v_{\text{o}} \quad \text{(Boosting)} \\ 0 & \text{, if power flows from } v_{\text{o}} \text{ to } v_{\text{in}} \quad \text{(Bucking)} \end{cases} \tag{5.68}$$

The adapted modulation index m_0 is a function of modulation index $M\,(\in [0,1])$ and the signal *Boost* $\in \{0,1\}$, and is calculated through eq. (5.69).

$$m_0 = \left(\frac{M}{2} \right) \cdot (1 - Boost) + \left(1 - \frac{M}{2} \right) \cdot Boost \tag{5.69}$$

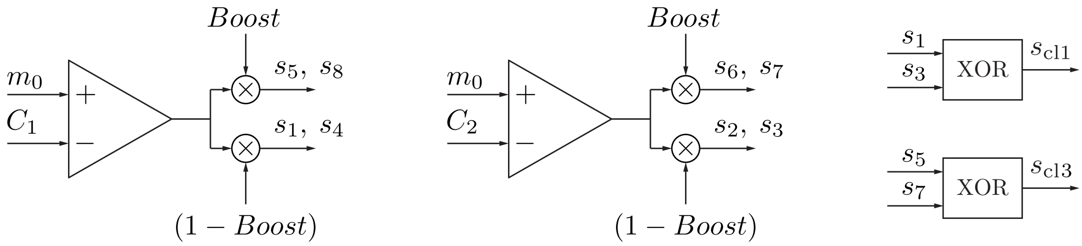

Figure 5.6: Modulation scheme applied to the Full-Bridge based PPC under bidirectional power flow (bucking mode operation $s_{\mathrm{c2}} = 1$ and $s_{\mathrm{c4}} = 0$, boosting mode operation $s_{\mathrm{c2}} = 0$ and $s_{\mathrm{c4}} = 1$).

The resulting waveforms obtained from applying the previously described modulation scheme to the Full-Bridge based PPC are presented in Fig. 5.7. The operation of the converter in bucking mode (power flow from v_{o} to v_{in}) is presented in the left-side plots of Fig. 5.7, while the right-side plots show the operation in boosting mode (power flow from v_{in} to v_{o}).

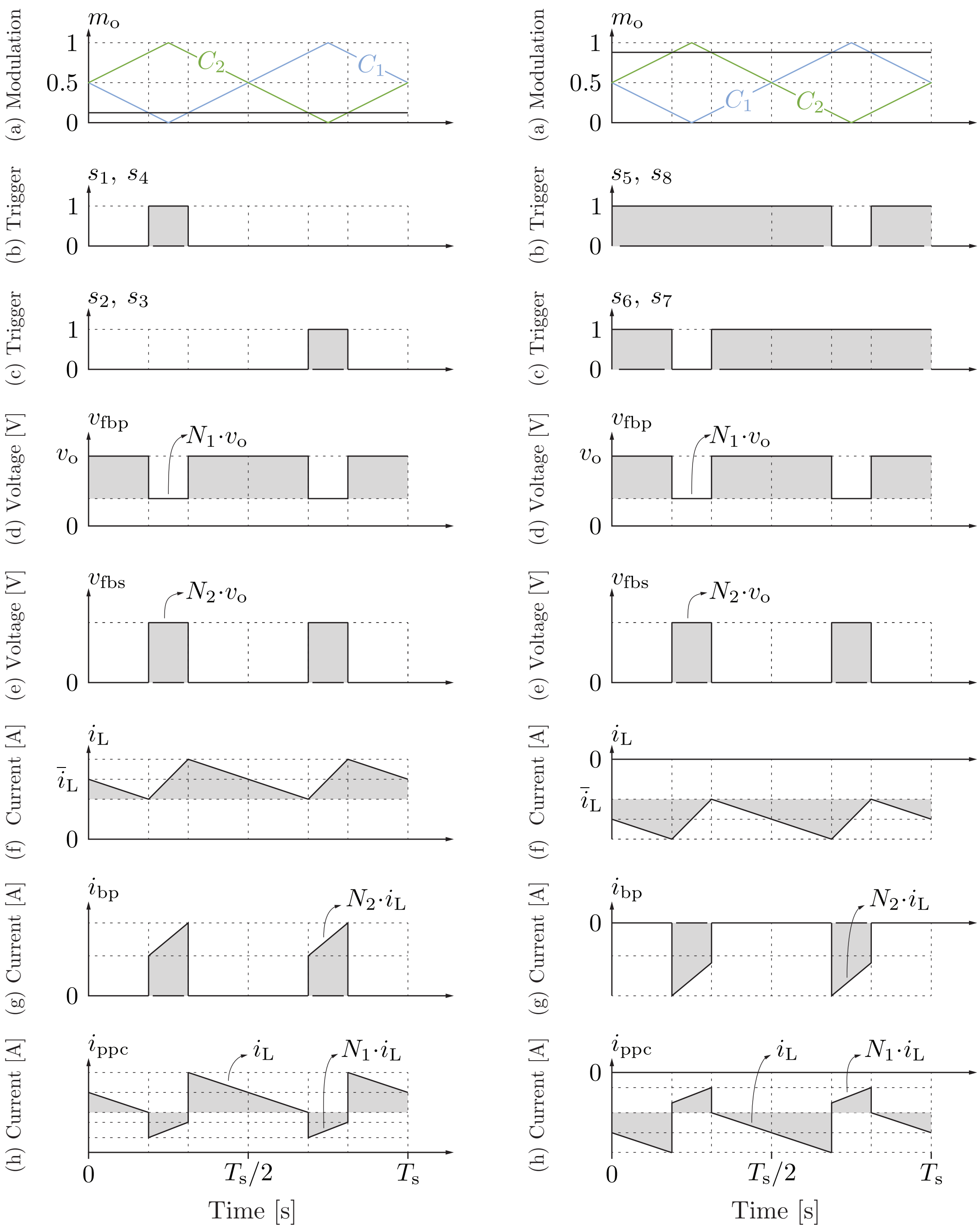

Figure 5.7: Idealized waveforms of a bidirectional PPC, operating in bucking (left) and boosting (right) modes: a) modulation index and PWM carriers, b) gate signals, c) gate signals, d) voltage across the top winding and its semiconductors, e) voltage in the bottom winding and its semiconductors, f) current through the inductor L, g) bypass current, h) partial power current.

5.4.5 Partiality

In order for a power converter to be considered a PPC, the power processed by the converter must be lower than the input power. This relationship is called partial power ratio (k_{pr}) and is mathematically represented by the ratio between the power processed by the PPC (P_{ppc}, input power in a standard full-bridge converter) and its input power (P_{in}) [100]. Therefore, a power converter must comply with $k_{pr} < 1$ to be a PPC. Figure 5.8 shows the relevant variables that allow calculation of the partiality equations. In order to match the partiality definition found in literature [73, 126], the partial voltages for each operation mode (v_{pc1} bucking and v_{pc2} boosting) were added to the simplified circuital diagram shown in Fig. 5.8.

Equation 5.70 shows the partiality ratio for each power flow direction.

$$k_{\mathrm{pr}} = \frac{P_{\mathrm{ppc}}}{P_{\mathrm{in}}} = \begin{cases} \dfrac{v_{\mathrm{pc1}} \cdot i_{\mathrm{bp}}}{v_{\mathrm{o}} \cdot i_{\mathrm{bp}}} & \text{, if power flows from } v_{\mathrm{o}} \text{ to } v_{\mathrm{in}}\ (\textit{Bucking}) \\ \\ \dfrac{v_{\mathrm{pc2}} \cdot (-i_{\mathrm{ppc}})}{v_{\mathrm{in}} \cdot (-i_{\mathrm{L}})} & \text{, if power flows from } v_{\mathrm{in}} \text{ to } v_{\mathrm{o}}\ (\textit{Boosting}) \end{cases} \tag{5.70}$$

Table 5.5 summarises the equations governing the partiality of the proposed bidirectional PPC, for both power flow directions, towards v_{in} (noted by $_{in}$) and towards v_{o} (noted by $_{o}$),

where k_{v} and η correspond respectively to the voltage gain and the efficiency of the PPC.

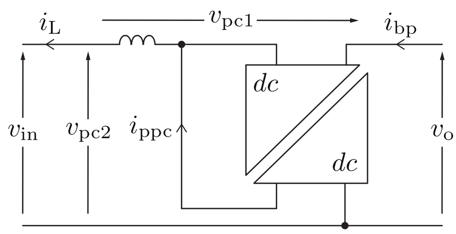

Figure 5.8: Partiality analysis circuit diagram, PPC topology with inductor in the input side.

	Power flow towards v_{in} (bucking)	Power flow towards v_{o} (boosting)
Voltage gain	$k_{\mathrm{v\ in}} = \dfrac{v_{\mathrm{in}}}{v_{\mathrm{o}}}$	$k_{\mathrm{v\ o}} = \dfrac{v_{\mathrm{o}}}{v_{\mathrm{in}}}$
Efficiency	$\eta_{\mathrm{in}} = \dfrac{v_{\mathrm{in}} \cdot i_{\mathrm{L}}}{v_{\mathrm{o}} \cdot i_{\mathrm{bp}}}$	$\eta_{\mathrm{o}} = \dfrac{v_{\mathrm{o}} \cdot i_{\mathrm{bp}}}{v_{\mathrm{in}} \cdot i_{\mathrm{L}}}$
Partiality ratio	$k_{\mathrm{pr\ in}} = 1 - k_{\mathrm{v\ in}}$	$k_{\mathrm{pr\ o}} = 1 - \dfrac{\eta_{\mathrm{o}}}{k_{\mathrm{v\ o}}}$

Table 5.5: Partiality equations, PPC with an inductor in the partial side.

5.5 Bidirectional Partial Power Converter - Partial Side Inductor

A full-bridge based Partial Power Converter (PPC) with an inductor in the partial side and bidirectional power flow capability is shown in Fig. 5.9. Note that the four relays in the topology allow the circuit to be reconfigured, enabling control of the power flow from v_o towards v_in ($s_\mathrm{pf} = 0$, bucking mode operation) or from v_in towards v_o ($s_\mathrm{pf} = 1$, boosting mode operation).

According to PPC classification existing in literature, the operation in bucking mode can be classified as a Step-Down II PPC [73] or a Input Series Output Parallel (ISOP) PPC [127], while the boosting mode operation corresponds to a Step-Up II PPC [73] or a Input Series Output Parallel (ISOP) PPC [127].

Likewise the previous section, an equivalent mathematical model can be derived from the power converter depending on the operation mode, i.e. bucking mode model (power flowing from v_o towards v_in) or boosting mode model (power flowing from v_in towards v_o). Note that the following analyses consider that v_in is lower than v_o.

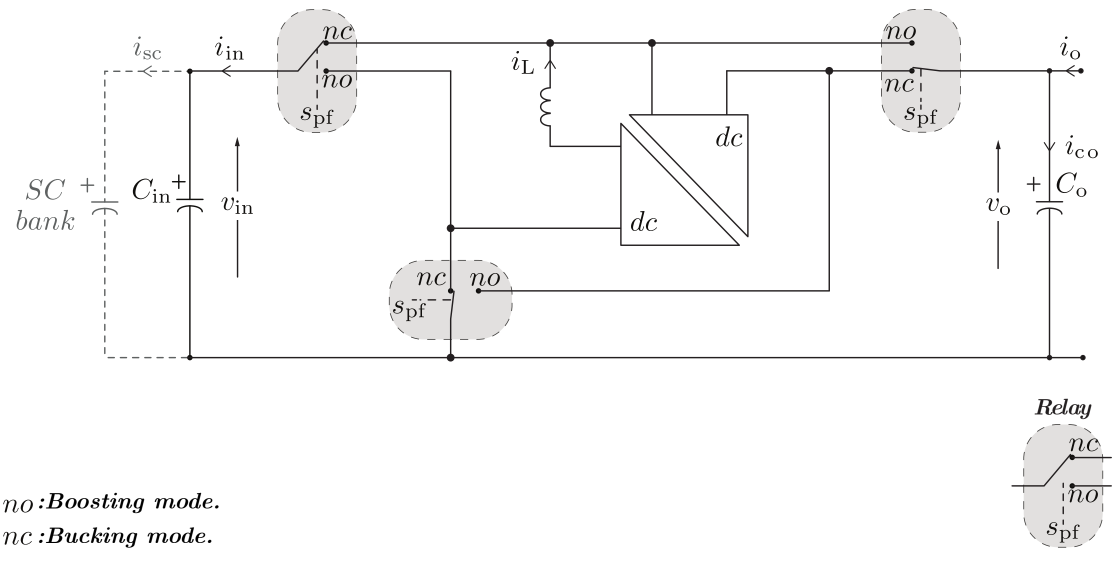

Figure 5.9: Full-bridge based Partial Power Converter topology with an inductor in the partial side, *nc* (normally closed): bucking mode operation and *no* (normally opened): boosting mode operation.

5.5.1 Bucking mode model

Figure 5.10 shows the equivalent circuit obtained from operating the topology (in Fig. 5.9) in bucking mode operation (relay in *nc* position, $s_{\mathrm{pf}} = 0$) where, v_{in}, L, R_{L}, i_{L}, v_{fbp}, v_{fbs}, v_{o}, C_{o}, R_{o}, i_{co}, i_{bp}, i_{in} correspond respectively to the voltage in the terminals of the EST in [V], inductance in the partial side (L) in [H], resistance of the inductor L in [Ω] (not included in Fig.), current through the inductor L in [A], voltage across the MOSFETs and winding of the transformer that has the MOSFET bridge in [V], voltage across the diodes and winding of the transformer that has the diode bridge in [V], output voltage of the converter in [V], capacitance of the output capacitor in [F], output capacitor self-discharge resistance in [Ω] (not included in Fig.), current through the output capacitor in [A], bypass current in [A] and input current in [A].

In terms of PPC taxonomy, this operation mode corresponds to a Step-Down II PPC [73] or an Input Series Output Parellel (ISOP) PPC [127].

The mathematical model of the power converter shown in Fig. 5.10 is presented below. Eqs. (5.71) to (5.75) are obtained from applying Kirchhoff's laws and the respective element equations to the circuit in Fig. 5.10.

$$v_{\mathrm{in}} + v_{\mathrm{fbp}} - v_{\mathrm{o}} = 0 \tag{5.71}$$

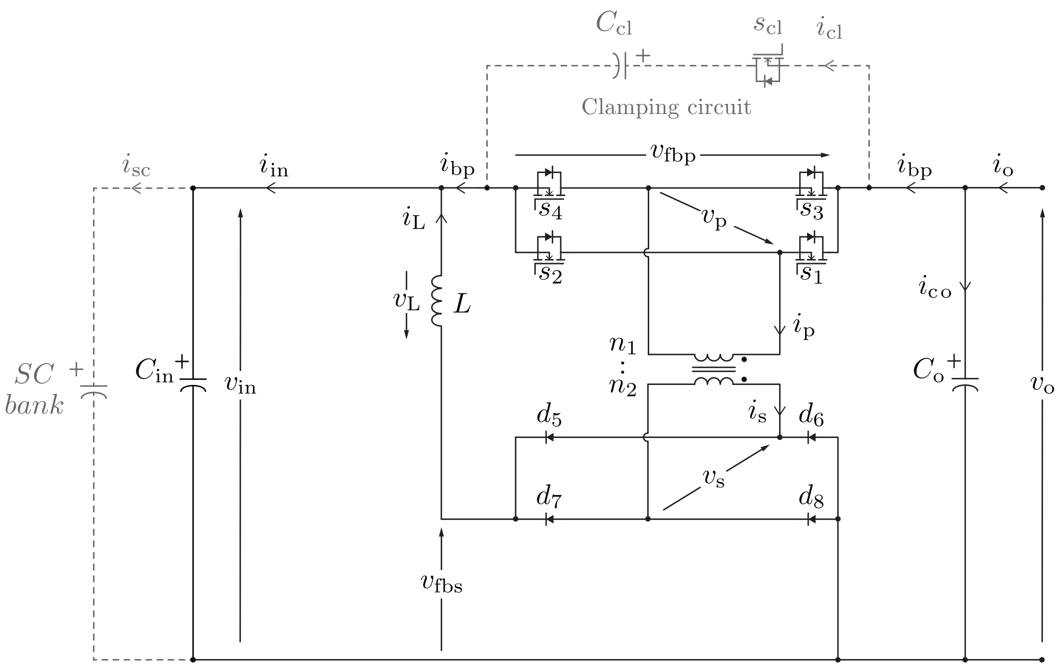

Figure 5.10: Full-bridge based Partial Power Converter topology with an inductor in the partial side ($v_{\mathrm{in}} < v_{\mathrm{o}}$), in bucking mode operation (power flows from v_{o} towards v_{in}).

$$v_{\mathrm{in}} + L\frac{di_{\mathrm{L}}}{dt} + R_{\mathrm{L}} \cdot i_{\mathrm{L}} - v_{\mathrm{fbs}} = 0 \tag{5.72}$$

$$v_{\mathrm{fbs}} + v_{\mathrm{fbp}} - v_{\mathrm{o}} = 0 \tag{5.73}$$

$$i_{\mathrm{in}} - i_{\mathrm{L}} - i_{\mathrm{bp}} = 0 \tag{5.74}$$

$$C_{\mathrm{o}}\frac{dv_{\mathrm{o}}}{dt} + \frac{v_{\mathrm{o}}}{R_{\mathrm{o}}} + i_{\mathrm{bp}} - i_{\mathrm{o}} = 0 \tag{5.75}$$

During bucking mode operation the MOSFETs (s_1, s_2, s_3 and s_4) are triggered, while the diodes (d_5, d_6, d_7 and d_8) rely on its natural conduction characteristic to drive the current. The allowed switching states of the full bridge based PPC in bucking mode operation are presented in Table 5.6.

Equations (5.76) to (5.78) show the value of the voltages v_{fbp}, v_{p} and v_{fbs} for each switching state.

$$v_{\mathrm{fbp}} = v_{\mathrm{o}} - v_{\mathrm{in}} \tag{5.76}$$

$$v_{\mathrm{p}} = \begin{cases} v_{\mathrm{o}} - v_{\mathrm{in}} & , if\ s_1 \cdot \bar{s}_2 \cdot \bar{s}_3 \cdot s_4 = 1 \\ -(v_{\mathrm{o}} - v_{\mathrm{in}}) & , if\ \bar{s}_1 \cdot s_2 \cdot s_3 \cdot \bar{s}_4 = 1 \\ 0 & , otherwise \end{cases} \tag{5.77}$$

$$v_{\mathrm{fbs}} = \begin{cases} \left(\frac{n_2}{n_1}\right) \cdot (v_{\mathrm{p}}) & , if\ s_1 \cdot \bar{s}_2 \cdot \bar{s}_3 \cdot s_4 = 1 \\ \left(\frac{n_2}{n_1}\right) \cdot (-v_{\mathrm{p}}) & , if\ \bar{s}_1 \cdot s_2 \cdot s_3 \cdot \bar{s}_4 = 1 \\ 0 & , otherwise \end{cases} \tag{5.78}$$

Γ_t	s_1	s_2	s_3	s_4	v_{fbp}	v_{p}	v_{fbs}
1	1	0	0	1	$v_{\mathrm{o}} - v_{\mathrm{in}}$	$v_{\mathrm{o}} - v_{\mathrm{in}}$	v_{s}
-1	0	1	1	0	$v_{\mathrm{o}} - v_{\mathrm{in}}$	$-(v_{\mathrm{o}} - v_{\mathrm{in}})$	$-v_{\mathrm{s}}$
0	1	0	1	0	$v_{\mathrm{o}} - v_{\mathrm{in}}$	0	0
0	0	1	0	1	$v_{\mathrm{o}} - v_{\mathrm{in}}$	0	0

Table 5.6: Allowed switching states of the full bridge based PPC in bucking mode operation.

Replacing eq. (5.77) into (5.78) gives

$$v_{\mathrm{fbs}} = \begin{cases} \left(\dfrac{n_2}{n_1}\right) \cdot (v_{\mathrm{o}} - v_{\mathrm{in}}) & , if\ s_1 \cdot \bar{s}_2 \cdot \bar{s}_3 \cdot s_4 = 1 \\ \left(\dfrac{n_2}{n_1}\right) \cdot (v_{\mathrm{o}} - v_{\mathrm{in}}) & , if\ \bar{s}_1 \cdot s_2 \cdot s_3 \cdot \bar{s}_4 = 1 \\ 0 & , otherwise \end{cases} \tag{5.79}$$

In order to simplify the notation, Γ_{t} is defined as

$$\Gamma_{\mathrm{t}} = s_1 \cdot \bar{s}_2 \cdot \bar{s}_3 \cdot s_4 - \bar{s}_1 \cdot s_2 \cdot s_3 \cdot \bar{s}_4 \tag{5.80}$$

hence, eq. (5.79) can be rewritten as:

$$v_{\mathrm{fbs}} = \Gamma_{\mathrm{t}}^2 \cdot \left(\frac{n_2}{n_1}\right) \cdot (v_{\mathrm{o}} - v_{\mathrm{in}}) \tag{5.81}$$

Replacing eq. (5.81) into eq. (5.72),

$$L\frac{di_{\mathrm{L}}}{dt} = -R_{\mathrm{L}} \cdot i_{\mathrm{L}} + \left(\frac{n_2}{n_1}\right) \cdot (v_{\mathrm{o}} - v_{\mathrm{in}}) \cdot \Gamma_{\mathrm{t}}^2 - v_{\mathrm{in}} \tag{5.82}$$

Performing a similar analysis to i_{in} and i_{bp}, as the analysis performed over v_{fbs}

$$i_{\mathrm{in}} = \begin{cases} i_{\mathrm{L}} + i_{\mathrm{bp}} & , if\ s_1 \cdot \bar{s}_2 \cdot \bar{s}_3 \cdot s_4 = 1 \\ i_{\mathrm{L}} + i_{\mathrm{bp}} & , if\ \bar{s}_1 \cdot s_2 \cdot s_3 \cdot \bar{s}_4 = 1 \\ i_{\mathrm{L}} & , otherwise \end{cases} \tag{5.83}$$

$$i_{\mathrm{bp}} = \begin{cases} \left(\dfrac{n_2}{n_1}\right) \cdot i_{\mathrm{L}} & , if\ s_1 \cdot \bar{s}_2 \cdot \bar{s}_3 \cdot s_4 = 1 \\ \left(\dfrac{n_2}{n_1}\right) \cdot i_{\mathrm{L}} & , if\ \bar{s}_1 \cdot s_2 \cdot s_3 \cdot \bar{s}_4 = 1 \\ 0 & , otherwise \end{cases} \tag{5.84}$$

Replacing eq. (5.84) into eq. (5.83) gives

$$i_{\mathrm{in}} = \begin{cases} \left(\dfrac{n_1 + n_2}{n_1}\right) \cdot i_{\mathrm{L}} & , if\ s_1 \cdot \bar{s}_2 \cdot \bar{s}_3 \cdot s_4 = 1 \\ \left(\dfrac{n_1 + n_2}{n_1}\right) \cdot i_{\mathrm{L}} & , if\ \bar{s}_1 \cdot s_2 \cdot s_3 \cdot \bar{s}_4 = 1 \\ i_{\mathrm{L}} & , otherwise \end{cases} \tag{5.85}$$

Equations (5.84) and (5.85) can be rewritten as,

$$i_{\mathrm{bp}} = \left(\frac{n_2}{n_1}\right) \cdot i_{\mathrm{L}} \cdot \Gamma_{\mathrm{t}}^2 \tag{5.86}$$

$$i_{\mathrm{in}} = \left(\frac{n_2}{n_1}\right) \cdot i_{\mathrm{L}} \cdot \Gamma_{\mathrm{t}}^2 + i_{\mathrm{L}} \tag{5.87}$$

On the other hand, the voltage in the output capacitor (C_{o}) can be rewritten by replacing eq. (5.86) into eq. (5.75).

$$C_{\mathrm{o}} \frac{dv_{\mathrm{o}}}{dt} = -\frac{v_{\mathrm{o}}}{R_{\mathrm{o}}} - \left(\frac{n_2}{n_1}\right) \cdot i_{\mathrm{L}} \cdot \Gamma_{\mathrm{t}}^2 + i_{\mathrm{o}} \tag{5.88}$$

Transforming the previous mathematical model into an averaged model and replacing Γ_{t}^2 by M_{t} in eqs. (5.82), (5.88), (5.86) and (5.87) gives:

$$\frac{di_{\mathrm{L}}}{dt} = -\frac{R_{\mathrm{L}}}{L} \cdot i_{\mathrm{L}} + \frac{1}{L} \cdot \left(\frac{n_2}{n_1}\right) \cdot M_{\mathrm{t}} \cdot (v_{\mathrm{o}} - v_{\mathrm{in}}) - \frac{1}{L} \cdot v_{\mathrm{in}} \tag{5.89}$$

$$\frac{dv_{\mathrm{o}}}{dt} = -\frac{1}{R_{\mathrm{o}} \cdot C_{\mathrm{o}}} \cdot v_{\mathrm{o}} - \frac{1}{C_{\mathrm{o}}} \cdot \left(\frac{n_2}{n_1}\right) \cdot M_{\mathrm{t}} \cdot i_{\mathrm{L}} + \frac{1}{C_{\mathrm{o}}} \cdot i_{\mathrm{o}} \tag{5.90}$$

$$i_{\mathrm{bp}} = \left(\frac{n_2}{n_1}\right) \cdot i_{\mathrm{L}} \cdot M_{\mathrm{t}} \tag{5.91}$$

$$i_{\mathrm{in}} = \left(\frac{n_2}{n_1}\right) \cdot i_{\mathrm{L}} \cdot M_{\mathrm{t}} + i_{\mathrm{L}} \tag{5.92}$$

Considering i_{bp} and M_{t} respectively as the output and input of the system. The transfer function between M_{t} and i_{bp} is given by:

$$G_{i_{\mathrm{bp}} M_{\mathrm{t}}} = \frac{i_{\mathrm{bp}}}{M_{\mathrm{t}}} = \frac{2 \cdot (v_{\mathrm{oQ}} - v_{\mathrm{inQ}})}{s \cdot L + R_{\mathrm{L}}} \cdot \left(\frac{n_2}{n_1}\right)^2 \tag{5.93}$$

where the sub-index $_{\mathrm{Q}}$ indicates a variable in the operation point.

5.5.2 Boosting mode model

Figure 5.11 shows the equivalent circuit of the full bridge-based PPC with an inductor in the partial side (presented in Fig. 5.5) in boosting mode operation (relay in *no* position, $s_{\mathrm{pf}} = 1$) where, v_{in}, L, R_{L}, i_{L}, v_{fbp}, v_{fbs}, v_{o}, C_{o}, R_{o}, i_{co}, i_{bp}, i_{in} correspond respectively to the voltage in the terminals of the EST in [V], inductance in the partial side (L) in [H], resistance of the inductor L in [Ω] (not included in Fig.), current through the inductor L in [A], voltage across the MOSFETs and winding of the transformer that has the MOSFET bridge in [V], voltage across the diodes and winding of the transformer that has the diode bridge in [V], output voltage of the converter in [V], capacitance of the output capacitor in [F], output capacitor self-discharge resistance in [Ω] (not included in Fig.), current through the output capacitor in [A], bypass current in [A] and input current in [A].

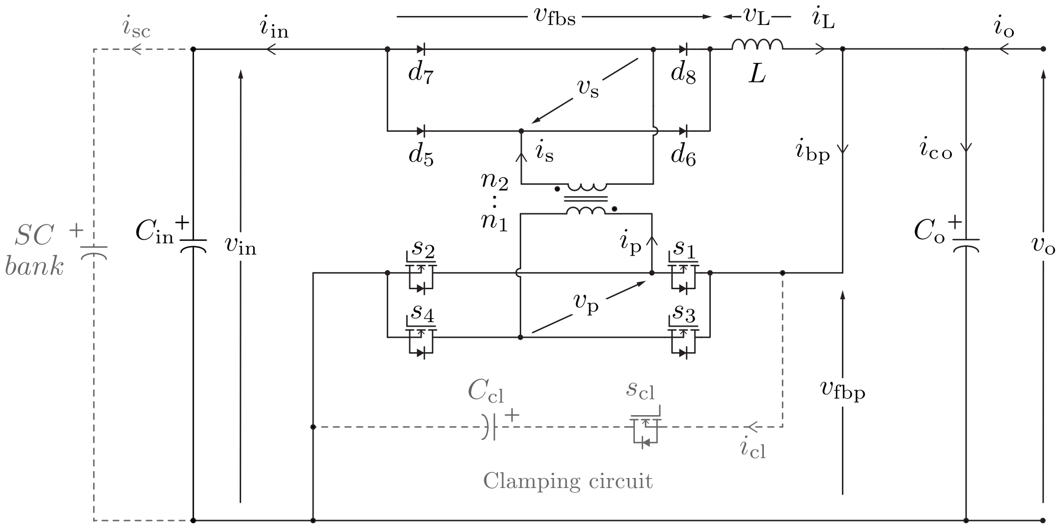

Figure 5.11: Full-bridge based Partial Power Converter topology with inductor in the partial side ($v_{\text{in}} < v_{\text{o}}$), in boosting mode operation (power flows from v_{in} towards v_{o}).

According to the aforementioned PPC taxonomy, this operation mode corresponds to a Step-Up I PPC [73] or a Input Parallel Output Series (IPOS) PPC [127].

The mathematical model of the equivalent power converter is presented below. Equations (5.94) to (5.99) are obtained from applying Kirchhoff's laws and the respective element equations to the circuit in Fig. 5.11.

$$v_{\text{in}} + v_{\text{fbs}} - L\frac{di_{\text{L}}}{dt} - R_{\text{L}} \cdot i_{\text{L}} - v_{\text{o}} = 0 \tag{5.94}$$

$$v_{\text{in}} + v_{\text{fbs}} - L\frac{di_{\text{L}}}{dt} - R_{\text{L}} \cdot i_{\text{L}} - v_{\text{fbp}} = 0 \tag{5.95}$$

$$v_{\text{fbp}} - v_{\text{o}} = 0 \tag{5.96}$$

$$i_{\text{in}} + i_{\text{L}} = 0 \tag{5.97}$$

$$i_{\text{bp}} + i_{\text{co}} - i_{\text{L}} - i_{\text{o}} = 0 \tag{5.98}$$

$$C_o \frac{dv_o}{dt} + \frac{v_o}{R_o} + i_{bp} - i_L - i_o = 0 \tag{5.99}$$

During boosting mode operation the MOSFETs (s_1, s_2, s_3 and s_4) are triggered, while the natural conduction characteristic of the diodes (d_5, d_6, d_7 and d_8) allows the current flow. The allowed switching states of the full bridge based PPC in bucking mode are presented in Table 5.7.

Equations (5.100), (5.101) and (5.102) show the value of the voltages v_p, v_s and v_{fbs} for each switching state.

$$v_p \quad = \quad \begin{cases} v_o & , if\ s_1 \cdot \bar{s}_2 \cdot \bar{s}_3 \cdot s_4 = 1 \\ -v_o & , if\ \bar{s}_1 \cdot s_2 \cdot s_3 \cdot \bar{s}_4 = 1 \\ 0 & , otherwise \end{cases} \tag{5.100}$$

$$v_s \quad = \quad \begin{cases} \left(\frac{n_2}{n_1}\right) \cdot v_o & , if\ s_1 \cdot \bar{s}_2 \cdot \bar{s}_3 \cdot s_4 = 1 \\ -\left(\frac{n_2}{n_1}\right) \cdot v_o & , if\ \bar{s}_1 \cdot s_2 \cdot s_3 \cdot \bar{s}_4 = 1 \\ 0 & , otherwise \end{cases} \tag{5.101}$$

$$v_{fbs} \quad = \quad \begin{cases} \left(\frac{n_2}{n_1}\right) \cdot v_o & , if\ s_1 \cdot \bar{s}_2 \cdot \bar{s}_3 \cdot s_4 = 1 \\ \left(\frac{n_2}{n_1}\right) \cdot v_o & , if\ \bar{s}_1 \cdot s_2 \cdot s_3 \cdot \bar{s}_4 = 1 \\ 0 & , otherwise \end{cases} \tag{5.102}$$

In order to simplify the notation, Γ_b is defined as

$$\Gamma_b = s_1 \cdot \bar{s}_2 \cdot \bar{s}_3 \cdot s_4 - \bar{s}_1 \cdot s_2 \cdot s_3 \cdot \bar{s}_4 \tag{5.103}$$

hence, eqs. (5.100), (5.101) and (5.102) can be rewritten as:

Γ_b	s_1	s_2	s_3	s_4	v_p	v_s	v_{fbs}
1	1	0	0	1	v_o	$(n_2/n_1) \cdot v_o$	$(n_2/n_1) \cdot v_o$
-1	0	1	1	0	$-v_o$	$-(n_2/n_1) \cdot v_o$	$(n_2/n_1) \cdot v_o$
0	1	0	1	0	0	0	0
0	0	1	0	1	0	0	0

Table 5.7: Allowed switching states of the full bridge based PPC in boosting mode operation.

$$v_{\mathrm{p}} = \Gamma_{\mathrm{b}} \cdot v_{\mathrm{o}} \tag{5.104}$$

$$v_{\mathrm{s}} = \Gamma_{\mathrm{b}} \cdot \left(\frac{n_2}{n_1}\right) \cdot v_{\mathrm{o}} \tag{5.105}$$

$$v_{\mathrm{fbs}} = \Gamma_{\mathrm{b}}^2 \cdot \left(\frac{n_2}{n_1}\right) \cdot v_{\mathrm{o}} \tag{5.106}$$

Replacing eq. (5.106) into (5.94) and clearing $L\dfrac{di_{\mathrm{L}}}{dt}$,

$$L\frac{di_{\mathrm{L}}}{dt} = -R_{\mathrm{L}} \cdot i_{\mathrm{L}} + v_{\mathrm{in}} + \left[\Gamma_{\mathrm{b}}^2 \cdot \left(\frac{n_2}{n_1}\right) - 1\right] \cdot v_{\mathrm{o}} \tag{5.107}$$

Performing a similar analysis to i_{bp}, as the analysis performed to v_{p}

$$i_{\mathrm{bp}} \quad = \quad \begin{cases} \left(\dfrac{n_2}{n_1}\right) \cdot i_{\mathrm{L}} & , if\ s_1 \cdot \bar{s}_2 \cdot \bar{s}_3 \cdot s_4 = 1 \\ \left(\dfrac{n_2}{n_1}\right) \cdot i_{\mathrm{L}} & , if\ \bar{s}_1 \cdot s_2 \cdot s_3 \cdot \bar{s}_4 = 1 \\ 0 & , otherwise \end{cases} \tag{5.108}$$

Replacing Γ_{b} in eq. (5.108) gives,

$$i_{\mathrm{bp}} = \Gamma_{\mathrm{b}}^2 \cdot \left(\frac{n_2}{n_1}\right) \cdot i_{\mathrm{L}} \tag{5.109}$$

Evaluating eq. (5.109) into eq. (5.98)

$$i_{\mathrm{co}} = i_{\mathrm{o}} + \left[1 - \Gamma_{\mathrm{b}}^2 \cdot \left(\frac{n_2}{n_1}\right)\right] \cdot i_{\mathrm{L}} \tag{5.110}$$

Finally, the voltage in the output capacitor (C_{o}) can be rewritten by replacing eq. (5.110) into eq. (5.99).

$$C_{\mathrm{o}}\frac{dv_{\mathrm{o}}}{dt} = -\frac{v_{\mathrm{o}}}{R_{\mathrm{o}}} + i_{\mathrm{o}} + \left[1 - \Gamma_{\mathrm{b}}^2 \cdot \left(\frac{n_2}{n_1}\right)\right] \cdot i_{\mathrm{L}} \tag{5.111}$$

The restructuring applied in this topology allows the power flow to be handle in each direction (bucking or boosting), however, this reconfiguration produces a different equivalent circuit, thus requiring a different model each operation mode. The following analyses show the resulting models for each operation mode.

Transforming the previous model (eqs. (5.107), (5.109) and (5.111)) into an averaged model and replacing Γ_{b}^2 by M_{b} gives

$$\frac{di_{\mathrm{L}}}{dt} = -\frac{R_{\mathrm{L}}}{L} \cdot i_{\mathrm{L}} + \frac{1}{L} \cdot \left[\left(\frac{n_2}{n_1} \right) \cdot M_{\mathrm{b}} - 1 \right] \cdot v_{\mathrm{o}} + \frac{1}{L} \cdot v_{\mathrm{in}} \tag{5.112}$$

$$\frac{dv_{\mathrm{o}}}{dt} = -\frac{1}{R_{\mathrm{o}} \cdot C_{\mathrm{o}}} \cdot v_{\mathrm{o}} - \frac{1}{C_{\mathrm{o}}} \cdot \left[\left(\frac{n_2}{n_1} \right) \cdot M_{\mathrm{b}} - 1 \right] \cdot i_{\mathrm{L}} + \frac{1}{C_{\mathrm{o}}} \cdot i_{\mathrm{o}} \tag{5.113}$$

$$i_{\mathrm{bp}} = \left(\frac{n_2}{n_1} \right) \cdot M_{\mathrm{b}} \cdot i_{\mathrm{L}} \tag{5.114}$$

Considering M_{b} and i_{bp} respectively as the input and output of the system. The transfer function between M_{b} and i_{bp} corresponds to:

$$G_{i_{\mathrm{bp}}M_{\mathrm{b}}} = \frac{i_{\mathrm{bp}}}{M_{\mathrm{b}}} = \frac{2 \cdot v_{\mathrm{oQ}}}{s \cdot L + R_{\mathrm{L}}} \left(\frac{n_2}{n_1} \right)^2 \tag{5.115}$$

The state variable model for bucking and boosting modes, for the bidirectional PPC with inductor in the partial side can be found in appendices D.3.1 and D.3.2.

5.5.3 Modulation scheme and resulting waveforms

A single modulation scheme, shown in Fig. 5.12, was applied to the configuration, despite of the operation mode.

The resulting waveforms, for each operation mode (bucking and boosting), are shown in Fig. 5.13

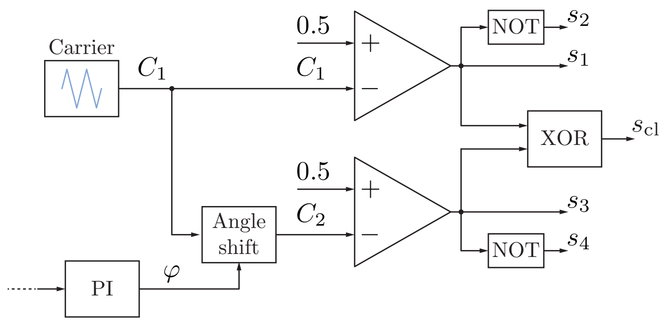

Figure 5.12: Modulation Full-bridge based Partial Power Converter topology with inductor in the partial side: phase shifted carrier.

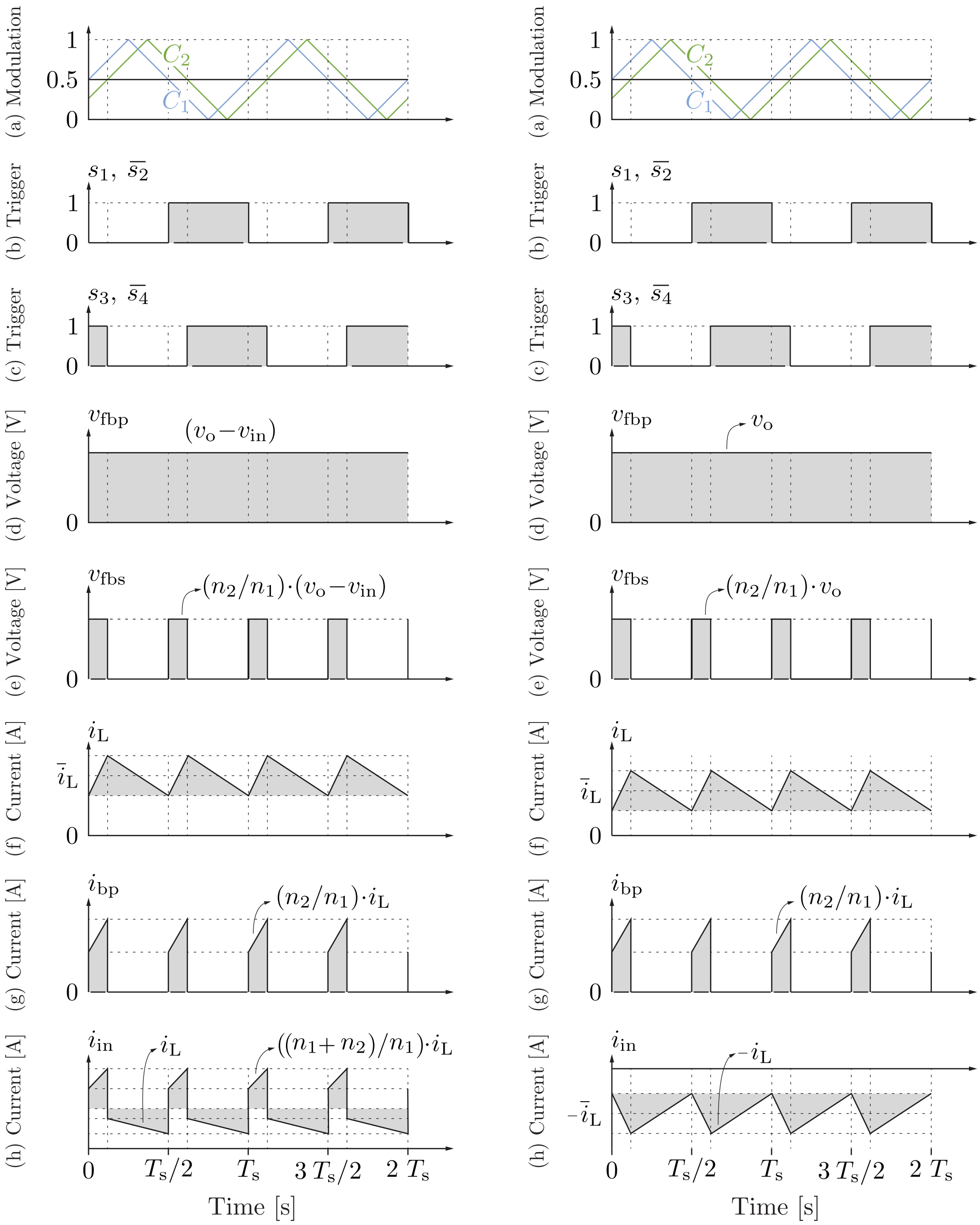

Figure 5.13: Idealized waveforms of a bidirectional PPC, operating in bucking (left) and boosting (right) modes: a) modulation index and PWM carriers, b) gate signals, c) gate signals, d) voltage across the winding with the MOSFETs bridge and its semiconductors, e) voltage in the winding with the diodes bridge and its semiconductors, f) current through the inductor L, g) bypass current, h) partial power current.

5.5.4 Partiality

Figure 5.14 shows a diagram of the PPC topology with an inductor in the partial side.

The same definitions introduced in section 5.4.5 were applied to obtain the partiality equations of the PPC topology with an inductor in the partial side. The resulting partiality equations are presented in table 5.8, where the sub-index $_o$ and $_{in}$ indicate, respectively, the power flow direction from (boosting) and towards (bucking) of the SC bank. Note that k_v and η, in table 5.8, correspond to the voltage gain and the efficiency of the PPC, respectively.

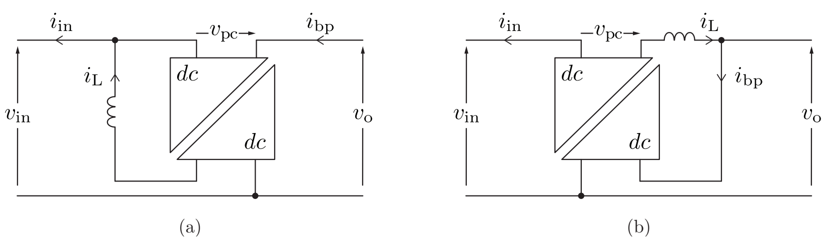

Figure 5.14: Partiality analysis circuit diagram, PPC topology with inductor in the partial side: a) bucking mode operation and b) boosting mode operation.

	Bucking mode operation (Power flow towards v_in)	Boosting mode operation (Power flow towards v_o)
Voltage gain	$k_{\mathrm{v\ in}} = \dfrac{v_\mathrm{in}}{v_\mathrm{o}}$	$k_{\mathrm{v\ o}} = \dfrac{v_\mathrm{o}}{v_\mathrm{in}}$
Efficiency	$\eta_\mathrm{in} = \dfrac{v_\mathrm{in} \cdot i_\mathrm{in}}{v_\mathrm{o} \cdot i_\mathrm{bp}}$	$\eta_\mathrm{o} = \dfrac{v_\mathrm{o} \cdot i_\mathrm{x}}{v_\mathrm{in} \cdot i_\mathrm{in}}$
Partiality ratio	$k_{\mathrm{pr\ in}} = 1 - k_{\mathrm{v\ in}}$	$k_{\mathrm{pr\ o}} = k_{\mathrm{v\ o}} + \eta_\mathrm{o}$

Table 5.8: Partiality equations, PPC with inductor in the partial side.

5.6 Summary

This chapter presented the selection of PV/ESS configurations (AC-grid side and PV side configurations) that will be implemented in the following chapter. The selection was based on the mainstream solution to merge ESS into power plants and the configuration that allowed assessment of the loss of generation presented in power clipping scenarios.

Additionally, this chapter presented three different bidirectional dc-dc converters capable of enabling the connection between an EST and a PV system. The selected dc-dc converter topologies allow connection of arrays of low voltage ESTs (as SCs and batteries) into central inverter PV systems. This chapter also presented the circuit diagram and the mathematical switched model of each bidirectional dc-dc topology. Each one of these models was transformed into its averaged form, which allowed the averaged transfer function between input (actuation) and output of the resulting model to be obtained. These transfer functions will be implemented in the following chapters to design the controllers that will regulate the operation of each power converter in the simulations and experimental results that will be shown in the following chapters.

The dc-dc power converters presented in this chapter correspond to the Isolated Bidirectional Boost Converter (IBBC), full-bridge based Partial Power Converter (PPC) with inductor at input side and full-bridge based Partial Power Converter (PPC) with inductor at partial side. The contributions of this chapter correspond to the proposal of a single (unified) bidirectional model for the IBBC, the proposal of a new PPC converter (PPC with an inductor at the input side) and the analysis and the proposal of a new bidirectional PPC configuration based on two (previously proposed) unidirectional PPCs (PPC with an inductor at the partial side).

Chapter 6

Control Strategies for Complementary Services in PV systems

6.1 Introduction

This chapter presents four control strategies that were implemented over the PV/ESS configurations selected in chapter 5. The objective of these strategies is to allow each PV/ESS configuration to provide a specific complementary service. The selected complementary services correspond to those presented in chapter 2, i.e. maximum power RR regulation, Peak Shaving and Power Clipping.

This chapter also presents the design of the PI controllers implemented in the control scheme of each PV/ESS configuration. These designs were based on the models of the power converters presented in chapter 5 and App. A. The control schemes and PI controller presented in this chapter will be implemented over the simulations presented in chapter 7.

Two PV/ESS configurations were selected in chapter 5, to simulate the provision of the aforementioned complementary services. These configurations correspond to a PV/ESS with an ESS connection at the AC-grid side and a PV/ESS with ESS connection at the PV side. In both configurations the PV system corresponds to a PV array connected to a 2LVSI acting as a central inverter.

Voltage Oriented Control (VOC), Direct Power Control, Virtual Flux Control and Model Predictive Control are the most common control strategies for grid-tied inverters [128]. Due to its simplicity, VOC was selected as the control strategy to regulate the 2LVSI in each PV system of the

PV/ESS configurations. ESSs also require a proper control strategy to manage the stored/released power and to enable the PV/ESS configuration to provide a complementary service. Many control alternatives for PV/ESS have been proposed in literature. In [43], a simulation of model predictive control strategy for a grid-tied PV plant with an energy storage system to minimize economical penalties for not delivering the daily committed amount of energy is proposed. In [13], a non-linear controller, based on flatness property, is used to regulate a PV plant with SC based ESS. The purpose of the controller is to smooth PV power generation in a distributed generation system. The results are experimentally validated. In [12], a Fuzzy logic controller, based on flatness property, is applied to a PV/SC/Fuel-Cell generation system. The operation of the system is experimentally validated. In [129], a Sliding Mode controller is applied to a BESS in a DC micro grid, formed by a PV system, Fuel cell, AC and DC loads. The sliding model controller allows the system to provide voltage support. The results presented in this work are contrasted against conventional cascaded linear PI controllers. However, due to the focus of this thesis, the simplest alternative (linear PI controllers) was applied to provide the required regulation of the ESS in each configuration.

This chapter is divided into three main sections. Each section focuses on a different Complementary Service. Section 6.2 shows two alternatives for performing Global MPPT, while complying with Maximum power RR regulation. A control strategy to generate peak shaved power is presented in section 6.3. Section 6.4 presents a novel control strategy to retrofit a central inverter PV plant, in order to reduce the loss of generation caused by power clipping.

This chapter includes a general control strategy (section 6.5). This strategy comprises the common characteristics of all the other control strategies. This strategy will be applied over a PV/ESS configuration with the ESS connection at the PV side. The simulation results obtained from this analysis (presented in Chapter 7) will be compared with the experimental results presented in chapter 8. The parameters of the PV/ESS configuration and the design of the controllers involved in this strategy are included in this section.

6.2 Maximum power RR regulation

Two configurations were considered as alternatives to allow PV/ESS to provide Global MPPT while complying with the maximum power RR regulation. As explained in chapter 1 (section 1.1.1), under non uniform conditions a central inverter PV configuration may present several maxima. Traditional MPPT strategies do not guarantee finding the global MPP, hence decreasing the energy yield. This section presents two alternatives that allow for the performance of the Global MPPT in a central inverter PV system, while complying with maximum power RR regulation.

The two PV/ESS configurations presented in this section are composed of a PV system formed

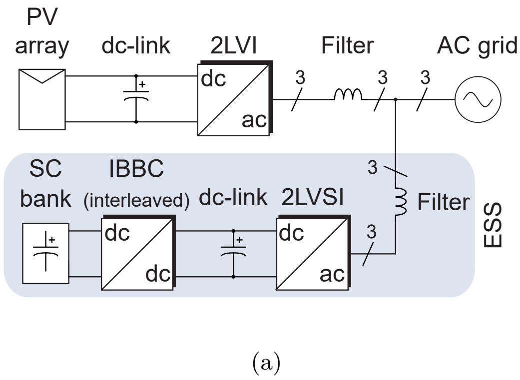

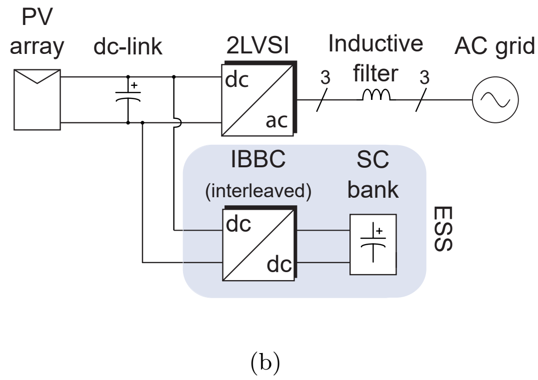

Figure 6.1: PV/ESS configurations for maximum power RR regulation: a) AC-grid-side connection and b) PV-side connection.

by a PV array, a 2LVSI acting as a central inverter and an ESS. The difference between both configurations is the point of connection between the PV system and the ESS. The first PV/ESS configuration, shown in Fig. 6.1a, corresponds to an AC-grid-side-connection configuration, where the ESS is connected to the PV system at AC-grid side. Note that the ESS is composed of an SC bank connected to eight interleaved IBBCs. The output of each IBBCs is connected to a 2LVSI that allows the connection at the AC-grid side. The second PV/ESS configuration, shown in Fig. 6.1b, corresponds to a PV-side-connection configuration. In this configuration the ESS is composed of an SC bank connected to eight interleaved IBBCs. The output of each IBBCs is connected to the dc-link of the 2LVSI of the PV system. In both configurations the 2LVSI acting as a central PV inverter is controlled through traditional VOC, where the external voltage reference is provided by an MPPT algorithm operating in either Global MPPT mode or P&O mode.

Figure 6.2 shows a standard VOC strategy composed by three control loops, i.e. an external and slower loop controlling the dc-link voltage (v_{dc}) and two internal and faster loops controlling the direct (i_{gd}) and quadrature (i_{gq}) currents. The grid currents (i_{ga}, i_{gb} and i_{gc}) and the grid voltages (v_{ga}, v_{gb} and v_{gc}) are transformed into coordinates in the rotational reference frame (direct and quadrature) through Clarke and Park transformations. The Phase Locked Loop (PLL) included in the diagram, allows the orientation of the direct-quadrature rotational frame, hence allowing the control of the active and reactive power injection. Finally, the reference voltages in the inverter (v^*_{ra}, v^*_{rb} and v^*_{rc}) are obtained from the inverse Park and Clarke transformations of the output of the current-loop-PI controllers. These voltages are fed into the PWM modulation block, generating the gate signals.

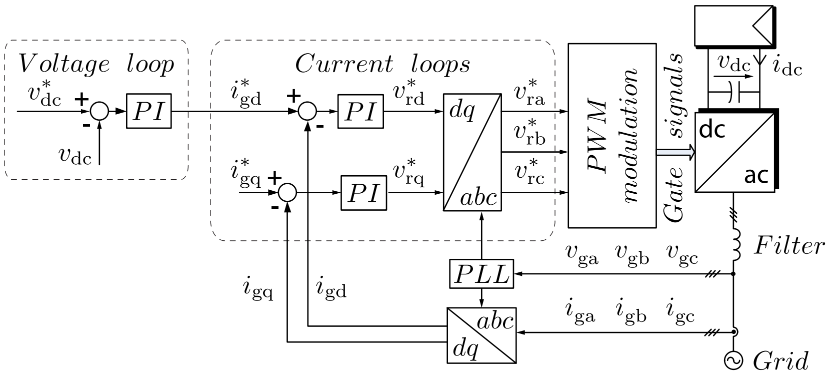

Figure 6.2: Voltage Oriented Control (VOC) scheme applied to a central inverter PV plant.

6.2.1 MPPT operating modes

The Global MPPT consists of scanning the power versus voltage (P_{pv} vs v_{dc}) PV curve. For this purpose the PV plant voltage reference v_{dc} is moved to the minimum voltage within the scanning range ($\check{v}_{\mathrm{dc}}$), and then increased to the maximum voltage in the scanning range ($\hat{v}_{\mathrm{dc}}$), as shown in Fig. 6.3. During the voltage swapping (from $\check{v}_{\mathrm{dc}}$ to $\hat{v}_{\mathrm{dc}}$) the global MPP (P_{mpp}) is found, and the voltage generating the MPP (v_{mpp}) is set as the new reference ($v^*_{\mathrm{dc}} = v_{\mathrm{mpp}}$). Once the dc-link has reached $\hat{v}_{\mathrm{dc}}$, the voltage reference is decreased until it reaches the new voltage reference ($v^*_{\mathrm{dc}} = v_{\mathrm{mpp}}$), the system is then returned to P&O. During Global MPPT mode the voltage reference variation rate is limited, hence reducing the power required from the ESS.

According to [61], the range where the voltage generating the Global MPP can be found, is limited to $[\check{v}_{\mathrm{dc}}, \hat{v}_{\mathrm{dc}}]$ with $\check{v}_{\mathrm{dc}} = P_{\mathrm{mpp\ k\text{-}1}}/i_{\mathrm{sc\ stc}}$ and $\hat{v}_{\mathrm{dc}} = 0.9 \cdot v_{\mathrm{dc\ ocv}}$. It must be noticed that the lower limit ($\check{v}_{\mathrm{dc}}$) is dynamic, while the upper limit ($\hat{v}_{\mathrm{dc}}$) is constant.

When the system is in P&O mode, the dc-link voltage reference (v^*_{dc}) is provided by a standard P&O. The size of the voltage step (Δv), applied in the P&O algorithm, was selected according to

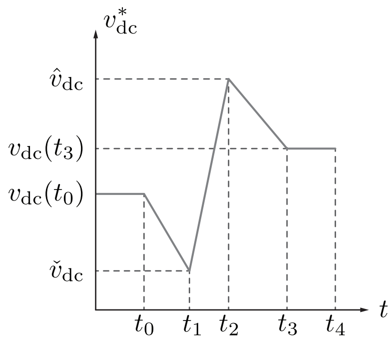

Figure 6.3: Global MPPT voltage reference (v^*_{dc}) scanning.

the criteria reported in [130], i.e. within the range $[0.1\%v_{\mathrm{mpp}}, 2\%v_{\mathrm{mpp}}]$. The selected voltage step value corresponds to 20 [V]. This step size is a good compromise between the MPP tracking speed and a fast and smooth transition between voltage levels. Additionally, this step size allows a clear identification of each one of the P&O steps, while observing the effect of the Global MPPT in a single plot in the results presented in chapter 7.

The transition from Global MPPT mode to P&O mode is time-triggered. Once the dc-link voltage reference (v_{dc}^*) has ended the scanning, reaching the new MPP voltage, the voltage reference is kept constant for one period (the same length as one P&O-MPPT's step). After that time, the MPPT returns to P&O mode. This algorithm allows the P&O MPPT to store the power and voltage measurements from a previous time sample (k-1). This strategy was implemented in both configurations, i.e. AC-grid-side-connection and PV-side-connection.

6.2.2 ESS connection at AC grid side

The first PV/ESS configuration applied is presented in Fig. 6.4, and corresponds to a PV/ESS configuration with ESS connection at the AC grid side. The configuration is formed by two parts, a PV system composed of a PV array and a 2LVSI (PV-2LVSI) as a central inverter. An ESS composed by a dc-ac 2LVSI (SC-2LVSI) is connected to the output of eight IBBCs in an interleaved connection. The input of the IBBCs is merged to an SC-bank. The control diagram of the full PV/ESS is also presented Fig. 6.4. Here the left-side inverter (PV-2LVSI) manages the operation of the PV system, while the right-side converters (SC-2LVSI and IBBC) regulate the operation of the EST (SC bank).

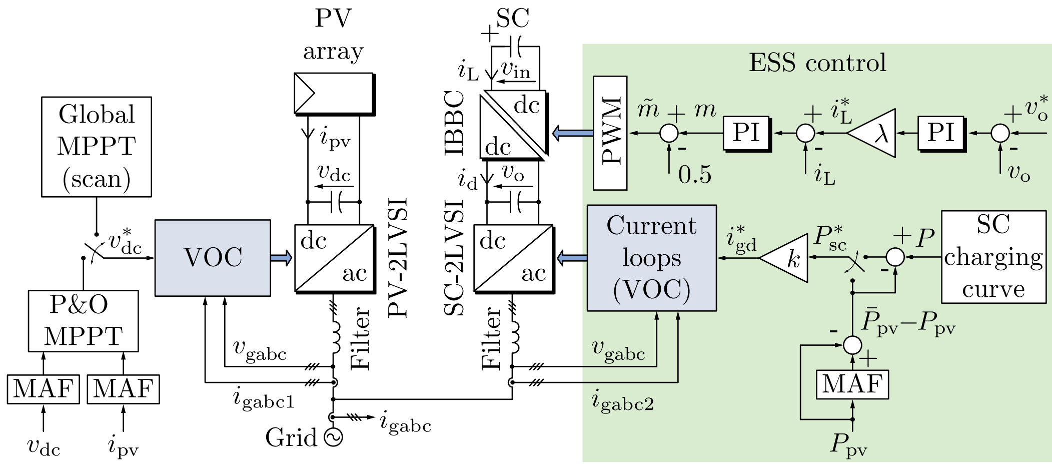

Figure 6.4: Control diagram of a PV/ESS, with ESS connection at AC side, to provide Maximum power RR regulation during Global MPPT.

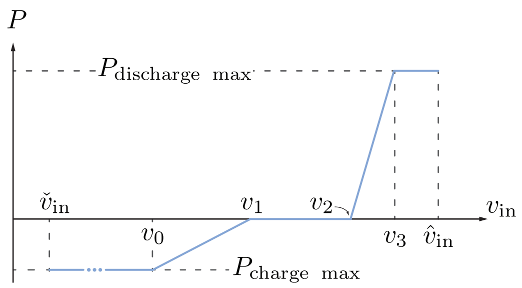

Figure 6.5: SC charging curve power reference applied when MPPT is in P&O mode.

Symbol	Value	Symbol	Value	Symbol	Value
$\check{v}_{\text{in}}$	100 [V]	v_2	310 [V]	$P_{discharge\ max}$	400 [kW]
v_0	280 [V]	v_3	315 [V]	$P_{charge\ max}$	-50 [kW]
v_1	300 [V]	$\hat{v}_{\text{in}}$	320 [V]		

Table 6.1: SC charging curve diagram

The SC-2LVSI is controlled through two current loops, identical to the inner current loops in the PV inverter VOC scheme. As seen in Fig. 6.4, the d-axis current reference (i^*_{gd}) is proportional to a power reference P^*_{sc}, where $k = 2/(3 \cdot v_{\text{gd}})$, and v_{gd} corresponds to the d-axis grid voltage. Conversely the current reference for the quadrature coordinate (i^*_{gq}), regulating the reactive power, is set to zero.

When the PV system is performing in P&O mode, the SC power reference (P^*_{sc}) is calculated as $P - (\bar{P}_{\text{pv}} - P_{\text{pv}})$, where P, $\bar{P}_{\text{pv}}$ and P_{pv} are respectively a power reference provided by the power vs voltage curve (in Fig. 6.5), the average PV power and the instantaneous PV power. This strategy allows the SC bank to charge while keeping its voltage within its operating range (100 - 310 [V]) and diminishing the output power power variations. The parameters applied in the SC charging curve (in Fig. 6.5) are presented in Table 6.1 and were determined empirically.

Note that the acronym MAF, in the control schemes, stands for Moving Average Filter.

During Global MPPT, the SC power reference (P^*_{sc}) is calculated as the difference between the PV plant average power ($\bar{P}_{\text{pv}}$), calculated during the previous P&O period, and the current PV power (P_{pv}).

The control strategy for the IBBCs is shown in the upper-right-side of Fig. 6.4. The external control loop reference (v^*_{o}) is kept constant at 1100 [V] and the output of the external control loop provides the total current reference for all the IBBCs ($8 \cdot i^*_{\text{L}}$). Since each of the interleaved IBBCs handles one eighth of the current of the SC bank, the total current reference is multiplied by 0.125 (λ =0.125). The inner control loop manages the current through all the inductors (L), generating the modulation index (m). Afterwards the modulation index is fitted to generate a symmetric voltage waveform in the transformer. Each IBBC operates with 2 PWM carriers shifted by π [rad]. A phase shifting of $\pi/8$ [rad] is introduced between the sets of PWM carriers to reduce the current and voltage ripples.

The PV/ESS configuration was designed considering the rated values of Canadian Solar CS6X-325P-FG high isolation PV modules (1.5 [kV]) [131], GE Pro-Solar PSC-800 MV-L-QC central solar inverter [132] and Maxwell SC packs model BMOD0006 E160 B02 [133]. The parameters associated with this PV/ESS configuration are presented in Table 6.2. The design of the inductance and capacitance of the power converters involved in this configuration are available in App. B.

The design of the PI controllers was performed according to the procedure described in App. C and applying the continuous-time plants of the power converters presented in chapter 5 and App. A. The discrete PI controllers of the 2LVSI considered a sampling frequency of 5[kHz]. The PI controller of the current (inner) loop (in the VOC scheme) considered a damping ratio of $\xi = 1/\sqrt{2}$ and a cut-off frequency of $f_{\mathrm{bw}} = 500[Hz]$. The dc-link voltage (outer) loop in the VOC scheme, has a damping ratio of $\xi = 1.0$ and a cut-off frequency of $f_{\mathrm{bw}} = 100[Hz]$. The discrete PI controller implemented in the IBBC had a sampling frequency of 50[kHz], a damping ratio of $\xi = 1/\sqrt{2}$ and a cut-off frequency of $f_{\mathrm{bw}} = 1[kHz]$. Table 6.3 summarises the plant's transfer function, continuous controller and distretized controller.

Figures 6.6 and 6.7 show the Bode diagrams, root locus and step response of the dc-link voltage controller (outer, slower) and current (inner,faster) loops of the 2LVSI respectively. The Bode diagrams, root locus and step response of the current and (dc-link) voltage loop controllers of the IBBC are shown in Fig. 6.8 and 6.9 respectively.

PV plant (Under STC)		
Maximum power point	P_{mpp}	735 [kW]
Maximum Power point voltage	$v_{\mathrm{dc\ mpp}}$	1.18 [kV]
Maximum Power point current	$i_{\mathrm{pv\ mpp}}$	622 [A]
Open circuit voltage	$v_{\mathrm{dc\ oc}}$	1.46 [kV]
Short circuit current	$i_{\mathrm{pv\ sc}}$	710 [A]
Modules connected in series	N_{ms}	36
String connected in parallel	N_{sp}	76
2LVSI & Grid		
PV-2LVSI dc-link capacitance	C_{dc}	2050 [μF]
PV-2LVSI dc-link voltage	v_{dc}	0.72-1.3 [kV]
SC-2LVSI dc-link capacitance	C_{o}	2050 [μF]
SC-2LVSI dc-link voltage	v_{o}	1.1 [kV]
Grid voltage (line-line RMS)	$v_{\mathrm{ac\ RMS}}$	440 [V]
Grid phase voltage (peak)	v_{g}	360 [V]
Grid filter inductance	L_{g}	0.05 [mH]
Grid filter resistance	R_{g}	0.167 [mΩ]
Grid frequency	f_{g}	50 [Hz]
2LVSI switching frequency	f_{sw}	5 [kHz]
SC bank & IBBC		
IBBC power	P_{ibbc}	50.0 [kW]
IBBC inductance	L	0.075 [mH]
IBBC inductor's resistance	R_{L}	0.167 [mΩ]
IBBC transformer ratio	$n_1 : n_2$	1:1
IBBC switching frequency	f_{ibbc}	50 [kHz]
Number of interleaved IBBCs	N_{ibbc}	8 [-]
SC bank equivalent capacitance	C_{sc}	2.9 [F]
SC bank maximum voltage	$\hat{v}_{\mathrm{in}}$	310 [V]
SC bank minimum voltage	$\check{v}_{\mathrm{in}}$	100 [V]

Table 6.2: Maximum power RR regulation in a PV/ESS configuration with ESS connection at AC-grid side: configuration parameters.

Converter	Design	Plant	PI controller	
(loop)	details	$(G_{\rm o}(s))$	Continuous-time $(C(s))$	Discrete-time $(C[k])$
2LVSI (Current)	$T_{\rm s} = 0.2$[ms] $f_{\rm bw} = 500$[Hz] $\xi = 1/\sqrt{2}$	$\dfrac{1}{L_{\rm g} \cdot s + R_{\rm g}}$	$\dfrac{0.1079 \cdot s + 116.5}{s}$	$\dfrac{0.1196 \cdot z - 0.09628}{z - 1}$
2LVSI (Voltage)	$T_{\rm s} = 0.2$[ms] $f_{\rm bw} = 100$[Hz] $\xi = 1.0$	$-\dfrac{3}{2} \cdot \dfrac{v_{\rm gd}}{C_{\rm dc} \cdot s}$	$\dfrac{0.001922 \cdot s + 0.2432}{s}$	$\dfrac{0.001946 \cdot z - 0.001897}{z - 1}$
IBBC (Current)	$T_{\rm s} = 0.02$[ms] $f_{\rm bw} = 5$[kHz] $\xi = 1/\sqrt{2}$	$\left(\dfrac{(n_1/n_2) \cdot v_{\rm o}}{L \cdot s + R_{\rm L}}\right)$	$\dfrac{0.001245 \cdot s + 13.44}{s}$	$\dfrac{0.00138 \cdot z - 0.001111}{z - 1}$
IBBC (Voltage)	$T_{\rm s} = 0.02$[ms] $f_{\rm bw} = 100$[Hz] $\xi = 1/\sqrt{2}$	$\dfrac{v_{\rm sc}}{C_{\rm o} \cdot s}$	$\dfrac{0.00885 \cdot s + 1.911}{s}$	$\dfrac{0.00887 \cdot z - 0.008831}{z - 1}$

Table 6.3: PI controllers design for the 2LVSI and IBBC.

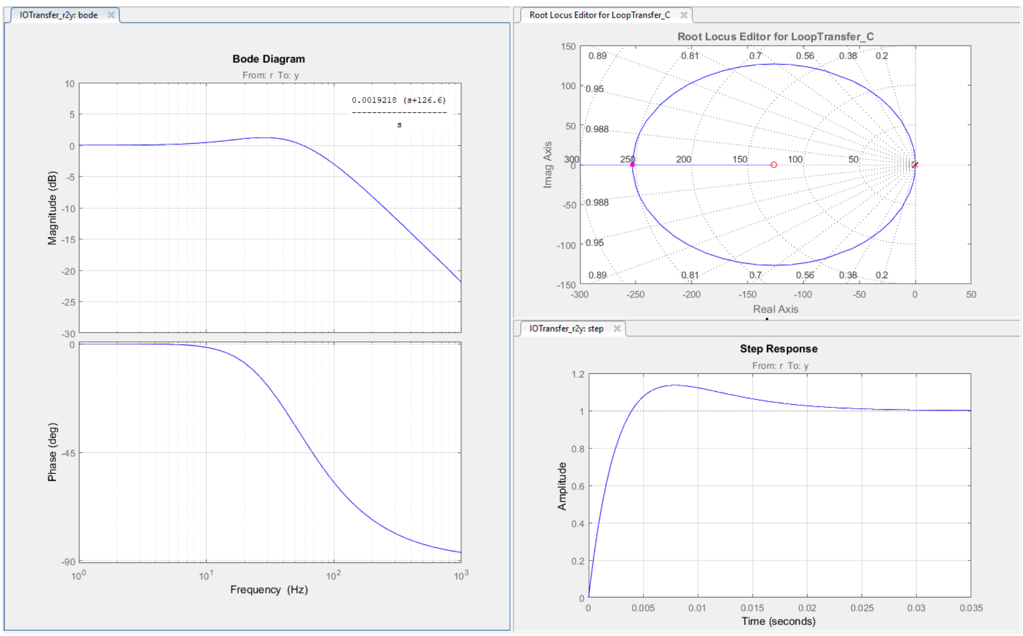

Figure 6.6: 2LVSI dc-link voltage controller: bandwidth = 100 [Hz], damping ratio $\xi = 1.0$.

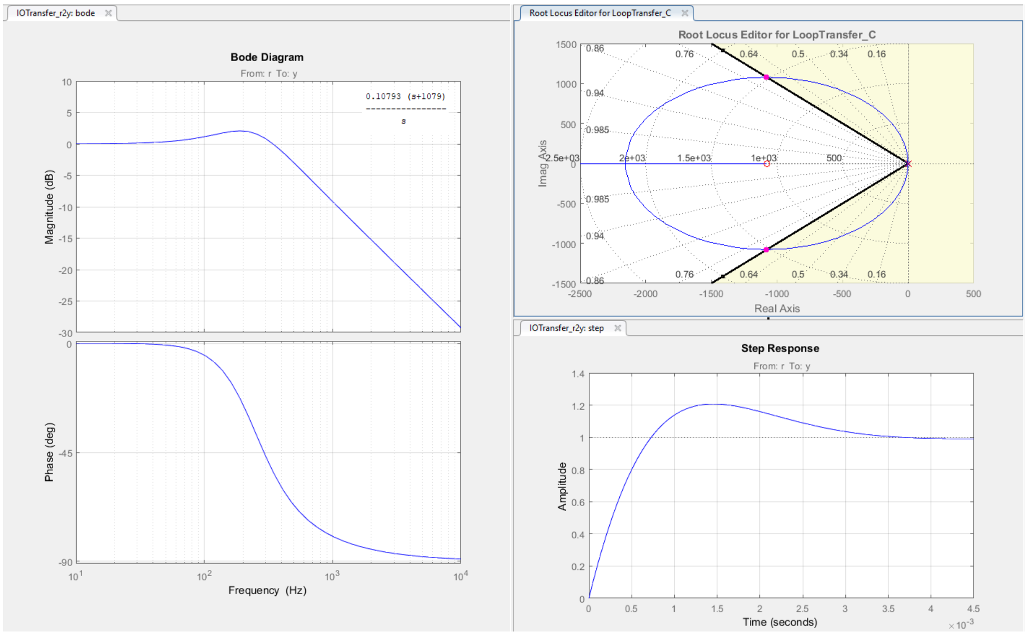

Figure 6.7: 2LVSI d- and q-axis current grid controller: bandwidth = 500 [Hz], damping ratio $\xi = 1/\sqrt{2}$.

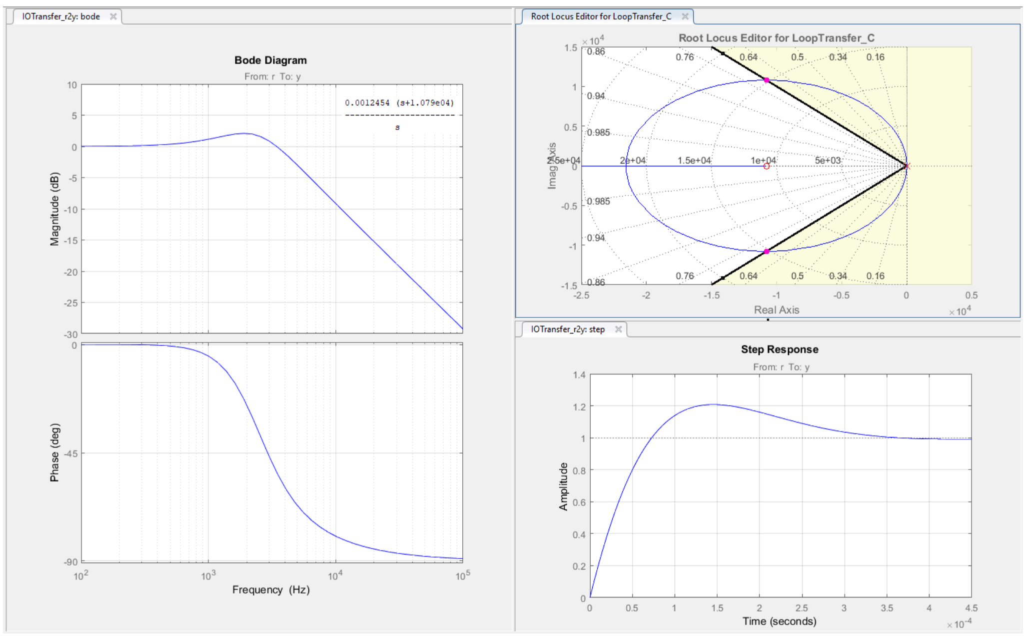

Figure 6.8: IBBC current loop controller: bandwidth = 5 [kHz], damping ratio $\xi = 1/\sqrt{2}$.

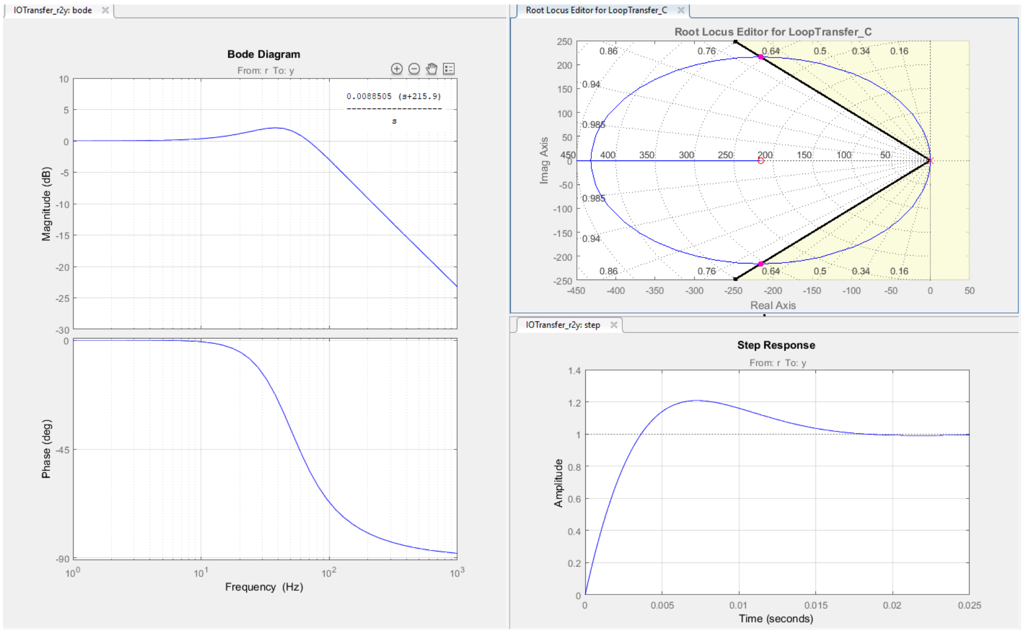

Figure 6.9: IBBC voltage loop controller: bandwidth = 100 [Hz], damping ratio $\xi = 1/\sqrt{2}$.

6.2.3 ESS connection at PV side

The second alternative selected to allow the PV/ESS to provide Global MPPT while complying with the maximum power RR regulation is presented in Fig. 6.10. The PV/ESS shown in Fig. 6.10 is composed of two parts. The first part is formed by a PV array connected to the grid through a 2LVSI and the second is formed of an SC bank connected to the PV array through eight interleaved IBBCs.

The control scheme to manage the power flow from/towards the SC bank is shown in Fig. 6.10. The SC bank power reference (P^*_{sc}) depends on the operating mode of the MPPT. When the MPPT is performing in Global MPPT mode, the SC bank power reference (P^*_{sc}) is given by $P^*_{\mathrm{sc}} = \bar{P}_{\mathrm{pv}} - P_{\mathrm{pv}}$, where $\bar{P}_{pv}$ and P_{pv} are the moving average of the power generated by the PV plant and the instantaneous power generated by the PV plant respectively. Conversely, when the MPPT is performing in P&O mode, the SC bank power reference (P^*_{sc}) is given by the SC charging curve presented in Fig. 6.5 and the parameters from Table 6.1. Hence, allowing the SC bank to be kept within operational range.

The SC bank reference power (P^*_{sc}) is divided by the SC bank voltage v_{sc} generating the total current reference for all the IBBCs. Afterwards the current reference is multiplied by λ=1/8 to even out the current flow through each interleaved IBBC. The current control loop generates the modulation index m for each IBBC. In order to generate a symmetrical signal for the transformer the modulation index must be adapted, generating $\tilde{m}$. This new modulation index is fed to the PWM modulation block.

The parameters of this PV/ESS configuration and the controller's design, applied in this

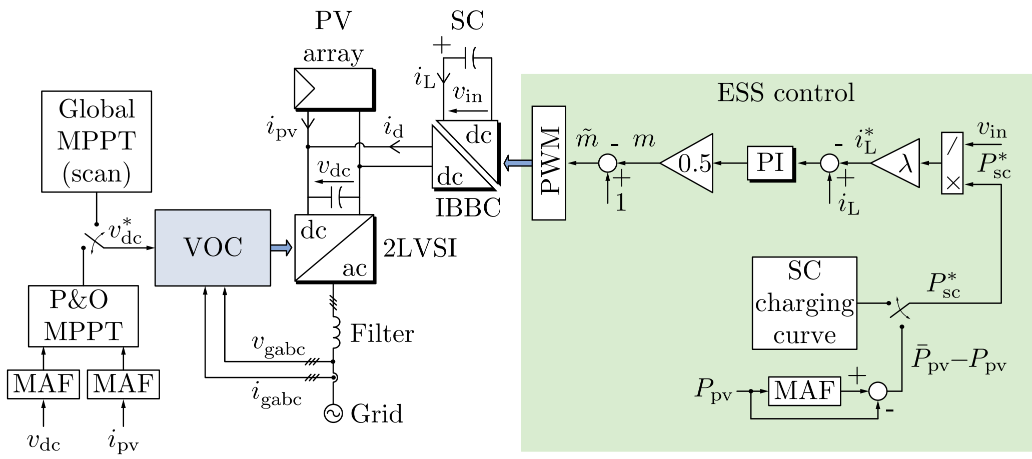

Figure 6.10: Control diagram of a PV/ESS, with ESS connection at PV side, to provide maximum power RR regulation during Global MPPT.

simulation, are the same as those presented in section 6.2.2 (Tables 6.2 and 6.3 and Figs. 6.6 to 6.8). Note that in this PV/ESS configuration the IBBC is connected directly to the dc-link of the 2LVSI of the PV plant.

6.3 Peak Shaving: ESS connection at PV side

The PV/ESS configuration implemented to perform Peak Shaving is displayed in Fig. 6.11. The configuration consists of a PV system and an ESS connected at the PV side. The PV system is composed of a 2LVSI and a PV array, while the ESS is formed by a battery bank connected to the PV array through eight interleaved full bridge based PPCs.

The configuration and complete control scheme of the PV/ESS configuration implemented to perform Peak Shaving is shown in Fig. 6.12. The right side of Fig. 6.12 shows the ESS control scheme, where the PPC Bypass Current Reference block generates the bypass current reference (i^*_{bp}) for each interleaved PPC. A PI controller processes the error between i^*_{bp} and the measurement of the bypass current in each PPC (i_{bp}), generating the modulation index, which is later passed to the PWM modulation block generating the gate signals.

The PPC Bypass Current Reference block shown in Fig. 6.12, operates according to the graph shown in Fig. 6.13, where P_{load}, P_{pv}, λ, v_{dc}, v_{in}, $\check{v}_{\text{in}}$, $\hat{v}_{\text{in}}$ correspond respectively to power demanded by the grid operator, PV plant power, one over the number of interleaved PPCs, dc-link voltage, battery bank current voltage, battery bank minimum safety voltage (80% Depth of Discharge) and battery bank maximum safety voltage (99% of maximum battery pack voltage). When the quotient between $\xi = \lambda \cdot (P_{\text{load}} - P_{\text{pv}})/v_{\text{dc}}$ is greater or equal to i_3 and $\check{v}_{\text{in}} < v_{\text{in}}$, the reference i^*_{bp} is given according to the purple curve (top right). If $\xi \geq i_3$, but $v_{\text{in}} < \check{v}_{\text{in}}$, then $i^*_{\text{bp}} = 0$. Conversely, when ξ is lower than i_4 and $v_{\text{in}} < \hat{v}_{\text{in}}$, the reference is given by the pink curve (bottom left). If $\xi < i_4$ but $\hat{v}_{\text{in}} < v_{\text{in}}$, then the reference i^*_{bp} is 0. In order to keep the battery bank voltage (v_{in}) within a certain range, a charging strategy was added to the bypass current reference generation algorithm, $i^*_{\text{bp}} = i_{\text{bp}\beta}$ when $i_6 \leq \xi < i_5$ and $v_{\text{in}} < \hat{v}_{\text{in}}$. The values of the parameter used in Fig. 6.13 are shown in table 6.4.

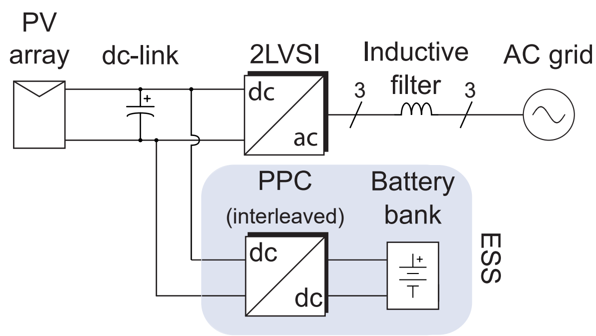

Figure 6.11: PV/ESS configurations for Peak Shaving: PV-side connection.

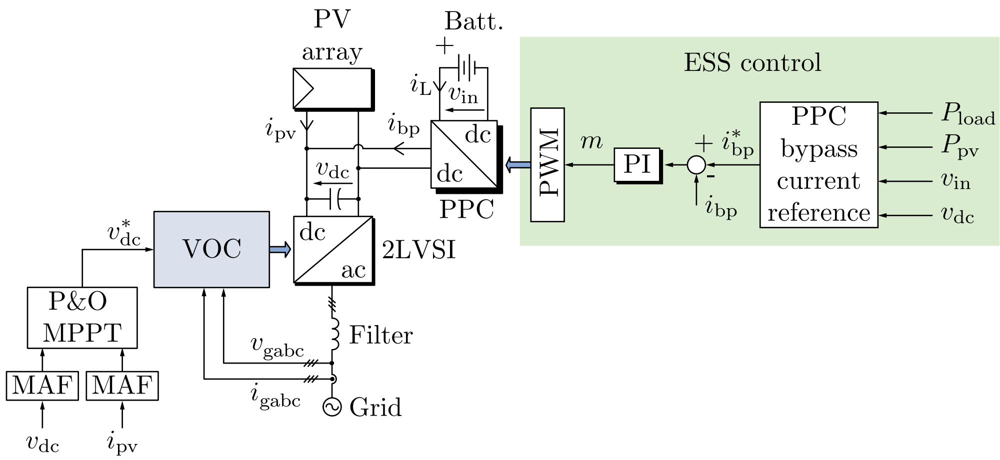

Figure 6.12: Control diagram of a PV/ESS, with ESS connection at the PV side, to provide Peak Shaving.

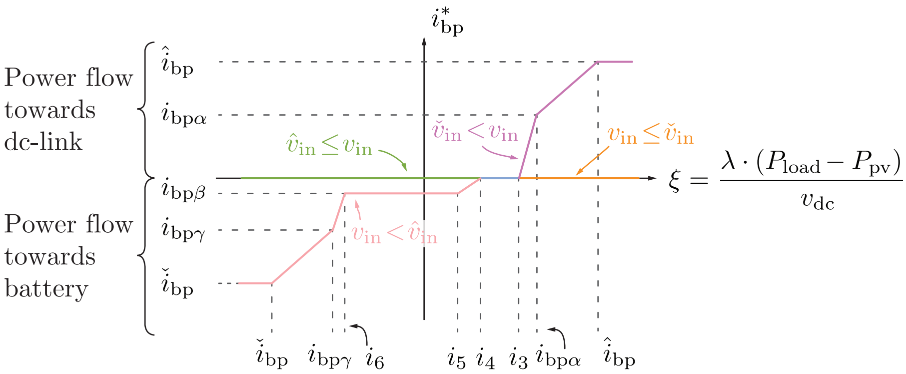

Figure 6.13: PPC bypass current reference

Symbol	Value	Symbol	Value	Symbol	Value
$\hat{i}_{bp}$	$100\ A$	$i_{bp\gamma}$	$-4\ A$	i_4	$2\ A$
$i_{bp\alpha}$	$4\ A$	$\check{i}_{bp}$	$-100\ A$	i_5	$1\ A$
$i_{bp\beta}$	$-1\ A$	i_3	$3\ A$	i_6	$-3\ A$

Table 6.4: EST current reference values

The parameters of the PV array and 2LVSI are the same as those presented in section 6.2.2 (Table 6.2), consequently the design of the controllers (for the VOC scheme) is also the same (table 6.3 and Figs. 6.6 and 6.7).

The parameter of the PPC with the inductor in the input side (PPC ISL) and the battery bank are presented in Table 6.5.

PPC - Input side inductor		
PPC power	P_{ppc}	50.0 [kW]
PPC inductance	L	0.075 [mH]
PPC inductor resistance	R_{L}	0.167 [mH]
PPC transformer ratio	$n_1 : n_2$	1:1
PPC switching frequency	f_{ibbc}	50 [kHz]
Number of interleaved PPCs	N_{ppc}	8 [-]
Battery		
Single cell capacity	C_{cell}	6 [Ah]
Maximum cell charge rate	$C_{\text{rate out}}$	19C
Maximum cell discharge rate	$C_{\text{rate in}}$	20C
Number of cells	n_{cells}	660
Battery bank maximum safety voltage	$\hat{v}_{\text{in}}$	300 [V]
Battery bank minimum safety voltage	$\check{v}_{\text{in}}$	220 [V]

Table 6.5: Configuration parameters: Peak Shaving in a PV/ESS configuration with the ESS connection at PV side.

Converter (loop)	Design details	Plant ($G_{\text{o}}(s)$)	PI controller Continuous-time ($C(s)$)	PI controller Discrete-time ($C[k]$)
PPC ISL (Current)	$T_{\text{s}} = 0.02$[ms] $f_{\text{bw}} = 1$[kHz] $\xi = 1/\sqrt{2}$	$\left(\dfrac{N_2 \cdot v_{\text{oQ}}}{s \cdot L + R_{\text{L}}}\right)$	$\dfrac{0.0004982 \cdot s + 1.075}{s}$	$\dfrac{0.0005089 \cdot z - 0.0004874}{z-1}$

Table 6.6: PI controllers design for the PPC with the inductor in the input side.

The design parameters of the current loop controller of the PPC with the inductor in the input side are presented in Table 6.6. Figure 6.14 shows the bode plots, root locus and step response of this controller design.

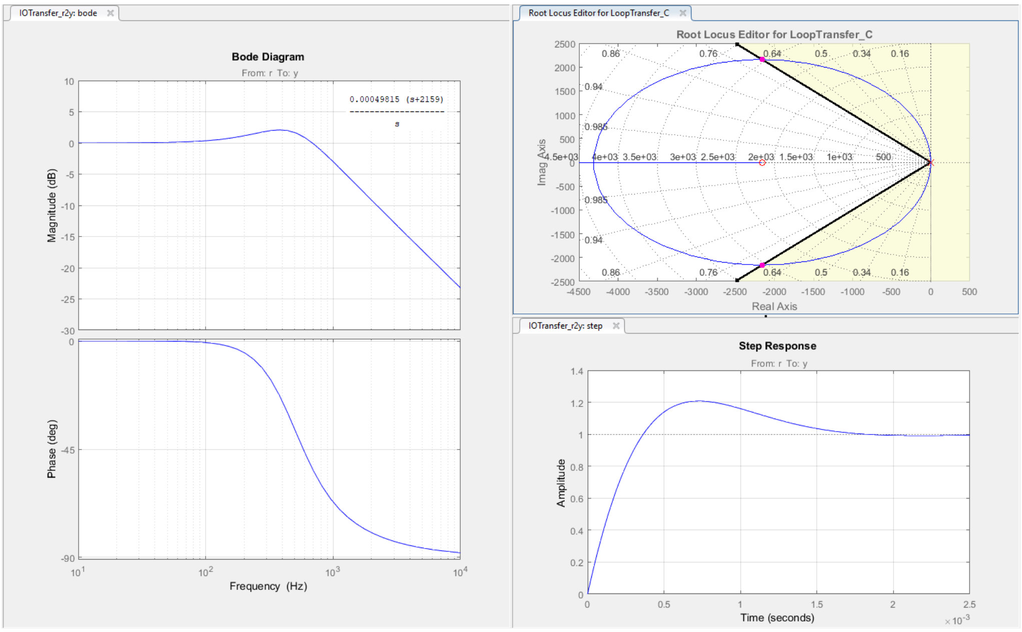

Figure 6.14: PPC input side inductor current loop controller: bandwidth = 1 [kHz], damping ratio $\xi = 1/\sqrt{2}$.

6.4 Power Clipping: ESS connection at PV side

A central inverter PV configuration, operating under power clipping conditions, was considered. The PV/ESS configuration, shown in Fig. 6.15, consists of a PV system formed by a PV array and a 2LVSI, and an ESS formed by a battery bank and an IBBC. In this application, the 2LVSI of the PV system is controlled through a standard VOC strategy with P&O MPPT reference, as depicted in Fig. 6.16.

One of the main objectives in this application is to retrofit an existing PV system. For this purpose an ESS is added at the PV side (DC side) of the inverter, however, the PV system and its control strategy remain unmodified. It must be noted that the addition of an ESS at the AC grid side will not allow harnessing of the loss of power generation caused by power clipping, since the inverter power limitation will remain an issue (reducing the energy yield). This is not the situation in other similar cases, as power curtailment is where the power limitation is imposed by the control strategy and not by the rating of the converter.

Retrofitting forces the ESS control strategy to extract or inject power to the dc-link without modifying the existing P&O MPPT strategy in the PV inverter. A tailored algorithm to generate the ESS current reference (i^*_{ess}), shown the flow chart in Fig. 6.17, was designed for this purpose. P_{pv}, P_{inv}, P_{ess}, P_{mpp}, P_{clip} and P_{pre} correspond respectively to PV plant output power ($P_{\mathrm{pv}} = i_{\mathrm{pv}} \cdot v_{\mathrm{dc}}$), inverter input power ($P_{\mathrm{inv}} = i_{\mathrm{inv}} \cdot v_{\mathrm{dc}}$), ESS power ($P_{\mathrm{ess}} = i_{\mathrm{ess}} \cdot v_{\mathrm{dc}}$), estimated MPP according to eq. (3.14) (Chapter 3), clipping level, and pre-clipping level. This latter parameter is used as a margin to keep the inverter operating below the clipping level thus enabling the ESS to perform power injection or subtraction to/from the dc-link ($P^*_{\mathrm{ess\ aux}} = P_{\mathrm{pre}} - P_{\mathrm{mpp}}$). $\check{P}_{\mathrm{ess}}$ (< 0) and $\hat{P}_{\mathrm{ess}}$ (> 0) corresponds to the minimum and maximum ESS power. This control strategy can be adapted to handle any EST, however the estimation of the ESS SoC value (SoC) in the control

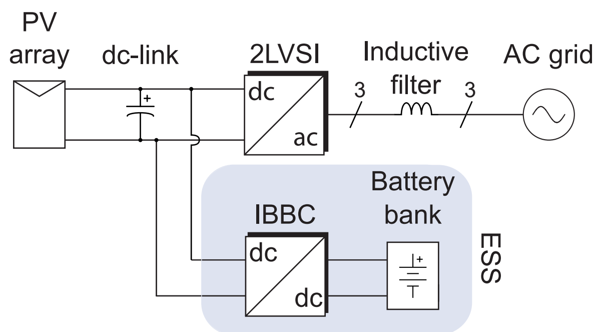

Figure 6.15: PV/ESS configurations for Power Clipping: PV-side connection.

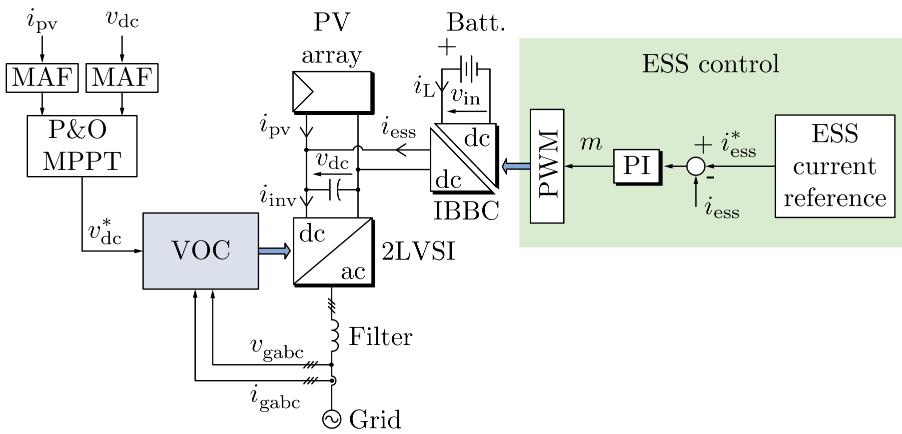

Figure 6.16: Control diagram of a PV/ESS, with the ESS connection at the PV side, to provide Power Clipping: (left side) Perturb and Observe MPPT and Voltage Oriented Control (VOC) scheme applied to the central inverter and (right side) CC charging mode controller scheme applied to the ESS.

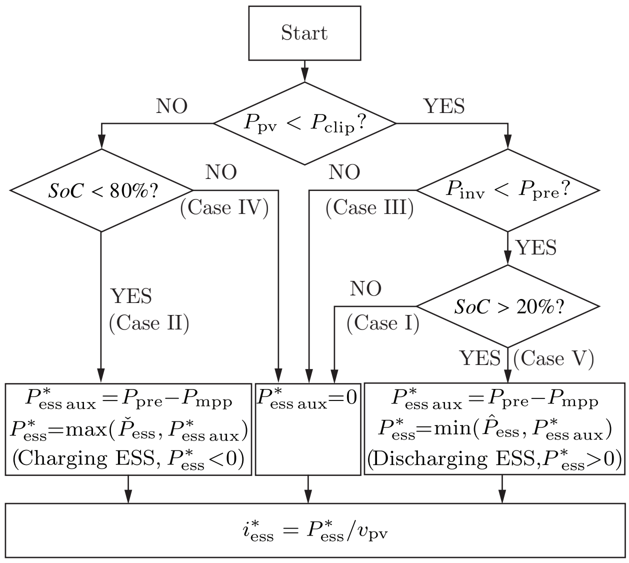

Figure 6.17: ESS current reference flow chart.

scheme of Fig. 6.17 must be replaced by an estimation of the available energy in the selected EST. The ESS output current reference (i^*_{ess}) is provided to a standard PI controller, generating the modulation index and switching pattern. The SoC estimation was performed through standard Coulomb Counting method [134]. Note that Cases I to V were added to simplify the understanding of the result presented in Fig. 7.13.

The parameters of the PV array and 2LVSI are the same as those presented in section 6.2.2

PV plant (Under STC)		
Maximum power point	P_{mpp}	1.029 [MW]
Maximum Power point voltage	$v_{\mathrm{dc\ mpp}}$	1.18 [kV]
Maximum Power point current	$i_{\mathrm{pv\ mpp}}$	870 [A]
Open circuit voltage	$v_{\mathrm{dc\ oc}}$	1.46 [kV]
Short circuit current	$i_{\mathrm{pv\ sc}}$	994 [kA]
Modules connected in series	N_{ms}	36
String connected in parallel	N_{sp}	106
Clipping level (inverter rated power)	P_{clip}	735 [kW]
Battery bank		
Battery bank equivalent capacitance	C_{sc}	29 [F]
Battery bank maximum safety voltage (80% SoC)	$\hat{v}_{\mathrm{in}}$	200 [V]
Battery bank minimum safety voltage (20% SoC)	$\check{v}_{\mathrm{in}}$	120 [V]

Table 6.7: Configuration parameters: Power Clipping in a PV/ESS configuration with the ESS connection at the PV side.

(Table 6.2), consequently the design of the controllers (for the VOC scheme) is also the same (table 6.3 and Figs. 6.6 and 6.7). The parameters of the IBBC and controller's design, applied in this simulation, are the same as those presented in section 6.2.2 (Tables 6.2, 6.3 and Fig. 6.8). However, in the case of this simulation the number of interleaved IBBCs (N_{ibbc}) is 6. Table 6.7 presents the parameters of the battery bank implemented in the simulation.

6.4.1 Perturb and Observe

A standard P&O strategy operating at MPP is shown in Fig. 6.18, where P_{pv} is the PV power, v_{dc} is the dc-link voltage and i_{inv} corresponds to the inverter current. The standard P&O strategy consists of comparing the current power level ($P_{\mathrm{pv}}[k]$) generated by a certain voltage ($v_{\mathrm{dc}}[k]$) and comparing it to the previous power level ($P_{pv}[k-1]$) generated by the previous voltage ($v_{\mathrm{dc}}[k-1]$). If the current power level is greater than the previous power level then the next voltage level will be the the current voltage level plus a constant (Δv), otherwise, the next voltage level will be the current voltage level minus Δv.

Once the MPP is reached, the maximum power output is obtained when the DC-link voltage is in the mid-level, while both higher and lower voltage levels will generate lower power output. A dc-link voltage step up is obtained by instantaneously decreasing the current (i_{inv}) towards the inverter, while a dc-link voltage step down is accomplished by instantaneously increasing the current towards the inverter.

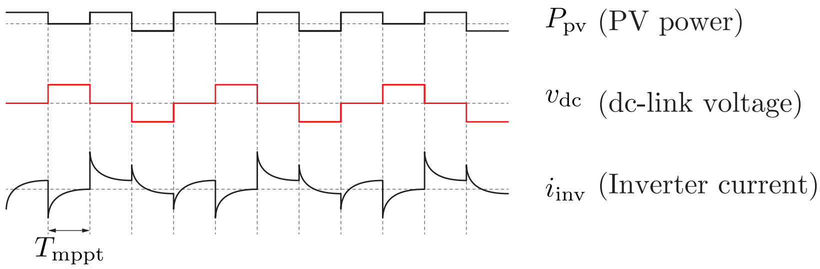

Figure 6.18: Standard P&O MPPT strategy

When the system is clipping the inverter is producing its maximum AC current (and power) output, hence is not capable of tracking the MPP, specifically since dc-link step down in voltage cannot be performed (it will require an instantaneous inverter current level higher than the rated maximum).

Standard P&O MPPT strategy operates at sampling period ($T_{\rm mppt}$) of a few seconds, if the time interval in which the ESS current reference is updated ($T_{\rm iess}$) is greater than several MPPT sampling periods ($T_{\rm mppt}$), then the MPPT algorithm will not detect the effects caused by the ESS injecting/withdrawing a constant current to/from the dc-link. Therefore a smart handling of ESS current ($i_{\rm ess}$) can set the inverter power level below the clipping level, hence enabling MPPT while storing power exceeding (beyond) the clipping level.

6.5 General strategy: ESS connection at PV side

This section presents the simulation results obtained from a PV/ESS configuration with the ESS connection at PV side, that will be contrasted with the experimental results (presented in Chapter 8).

The configurations implemented to perform maximum power RR regulation (with the ESS connection at PV side), peak shaving and power clipping are based on the same PV/ESS configuration. The PV system is composed of a 2LVSI and a PV array, while the ESS is formed of an SC bank or a battery bank connected to the dc-link of the 2LVSI through interleaved dc-dc converters. The control schemes implemented on each one of the aforementioned complementary services include a VOC scheme that regulates the 2LVSI. Additionally, all of the ESS control schemes have an external power reference stage, that is particular to each complementary service, and an inner current loop. This inner current loop allows to generate the desired power profile according to the complementary service. For these reasons a PV/ESS configuration formed of a PV array, a 2LVSI and an ESS was selected to be implemented experimentally. The ESS in this configuration is composed of a bidirectional PPC with the inductor in the partial side (presented in Chapter 5) and an SC bank. Figure 6.19 shows a diagram of the PV/ESS configuration.

Figure 6.20 shows the selected control strategy, where a VOC scheme regulates the 2LVSI and a current control loop that manages the ESS. The output of the ESS current loop's PI controller processes the error between i^*_{bp} and the measurement of the bypass current in each PPC (i_{bp}), generating the phase shifting that is applied over the carriers in the modulation scheme (PWM phase shifted carrier). Note that the use of an external ESS power-profile reference was avoided in order to keep the simulation (and experimental validation) valid for all of the complementary services.

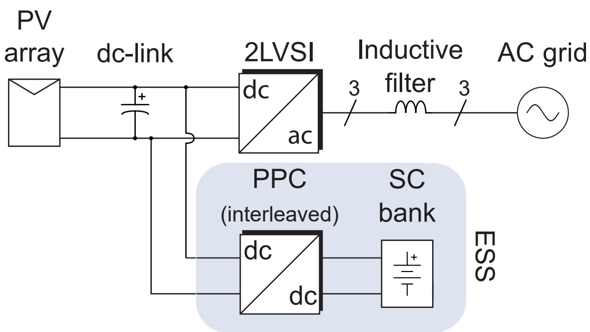

Figure 6.19: PV/ESS configurations for PV-side connection.

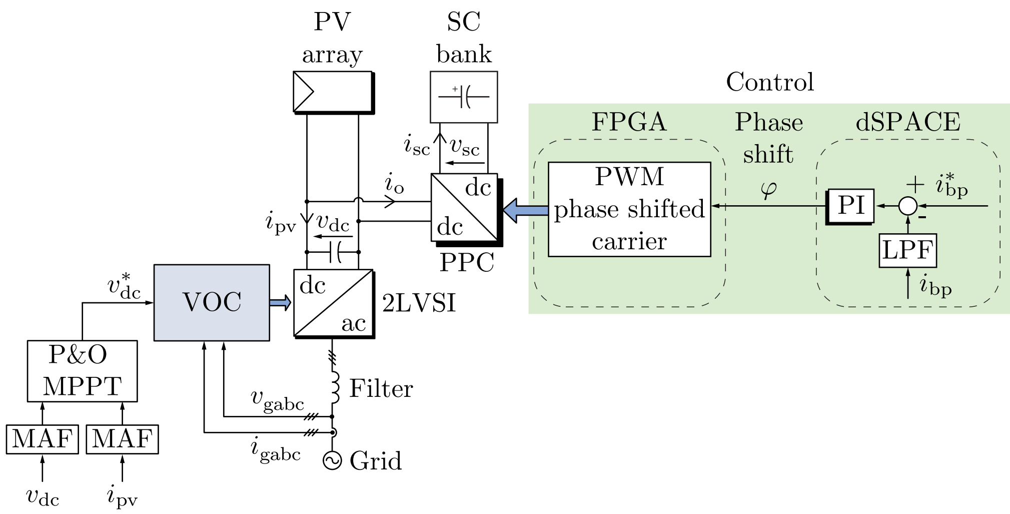

Figure 6.20: Control diagram PV/ESS configuration with PV side connection and full bridge based PPC with inductor at partial side.

The parameters of the PV/ESS configuration are presented in Table 6.8. Note that the value of the resistances, inductances and capacitances were obtained from scaling up (through the PU system) the parameters in the experimental setup. The design of the controllers for the VOC scheme and the PPC with inductor in the partial side are presented in table 6.3 and Figs. 6.6 and 6.7.

The base values applied to scale up the parameters are shown in table 6.9. The definition of the per unit bases in the DC side are based on [135]. Note that the per unit values associated with the ESS voltage and current are based on the power rating of a single dc-dc converter.

The design parameters of the 2LVSI's VOC scheme and PPC's current loop controller are presented in Table 6.10. Figures 6.21, 6.22, 6.23 and 6.24 show the bode plots, root locus and step response of these controllers.

Note that the reconfiguration of the PPC with the inductor in the partial side results in a different power converter for each operation mode (boosting and bucking). This is reflected in a different transfer function for each operation mode (as seen in Chapter 5). For this reason two different PI controller were designed, one for each operating mode (boosting and bucking). The details of both PI controllers are presented in Table 6.10 and Figs. 6.23 and 6.24.

PV plant (Under STC)		
Maximum power point	P_{mpp}	735 [kW]
Maximum Power point voltage	$v_{\text{dc mpp}}$	1.18 [kV]
Maximum Power point current	$i_{\text{pv mpp}}$	622 [A]
Open circuit voltage	$v_{\text{dc oc}}$	1.46 [kV]
Short circuit current	$i_{\text{pv sc}}$	710 [A]
Modules connected in series	N_{ms}	36
String connected in parallel	N_{sp}	76
2LVSI & Grid		
dc-link capacitance	C_{dc}	17.3 [mF]
dc-link voltage	v_{dc}	0.72-1.3 [kV]
Grid voltage (line-line RMS)	$v_{\text{ac RMS}}$	440 [V]
Grid phase voltage (peak)	v_{g}	360 [V]
Grid filter inductance	L_{g}	0.88 [mH]
Grid filter resistance	R_{g}	8.8 [mΩ]
Grid frequency	f_{g}	50 [Hz]
2LVSI switching frequency	f_{sw}	5 [kHz]
SC bank & PPC		
PPC power	P_{ibbc}	50.0 [kW]
PPC inductance	L	2.9 [mH]
PPC inductor's resistance	R_{L}	0.197 [mΩ]
PPC transformer ratio	$n_1 : n_2$	1:8
PPC switching frequency	f_{ibbc}	50 [kHz]
Number of interleaved PPCs	N_{ppc}	8 [-]
SC bank capacitance	C_{sc}	9.4 [F]
SC bank maximum voltage	$\hat{v}_{\text{in}}$	750 [V]

Table 6.8: PV/ESS configuration with ESS connection at the PV side: configuration parameters.

Parameter	Symbol	Value	Per Unit
Power	P_{base}	$735[kW]$	$1[pu]$
AC voltage	$V_{\text{ac base}} = 440 \cdot \sqrt{2/3}$	$360[V]$	$1[pu]$
AC current	$I_{\text{ac base}} = P_{\text{base}} \cdot 2/(3 \cdot V_{\text{ac base}})$	$1.36[kA]$	$1[pu]$
Frequency	ω_{base}	$100 \cdot \pi[rad/s]$	$1[pu]$
Impedance	$Z_{\text{ac base}}$	$0.26[\Omega]$	$1[pu]$
Inductance	$L_{\text{ac base}} = Z_{\text{ac base}}/\omega_{\text{base}}$	$0.84[mH]$	$1[pu]$
Capacitance	$C_{\text{ac base}} = 1/(Z_{\text{ac base}} \cdot \omega_{\text{base}})$	$12[mF]$	$1[pu]$
DC-DC power	$P_{\text{dcdc base}}$	$50[kW]$	$1[pu]$
DC-DC voltage	$V_{\text{dcdc base}} = 2 \cdot V_{\text{ac base}}$	$720[V]$	$1[pu]$
DC-DC current	$I_{\text{dcdc base}} = P_{\text{dcdc base}}/V_{\text{dcdc base}}$	$69.44[A]$	$1[pu]$
Impedance	$R_{\text{dc base}}$	$10.38[\Omega]$	$1[pu]$
Inductance	$L_{\text{dc base}} = R_{\text{dc base}}/\omega_{\text{base}}$	$33[mH]$	$1[pu]$
Capacitance	$C_{\text{dc base}} = 1/(Z_{\text{dc base}} \cdot \omega_{\text{base}})$	$0.3[mF]$	$1[pu]$

Table 6.9: PV/ESS configuration with the ESS connection at the PV side: Base values applied in the per unit system.

Converter (loop)	Design details	Plant ($G_o(s)$)	PI controller Continuous-time ($C(s)$)	Discrete-time ($C[k]$)
2LVSI (Current)	$T_s = 0.2$[ms] $f_{bw} = 250$[Hz] $\xi = 1/\sqrt{2}$	$\frac{1}{L_g \cdot s + R_g}$	$\frac{0.9523 \cdot s + 513.9}{s}$	$\frac{1.004 \cdot z - 0.901}{z - 1}$
2LVSI (Voltage)	$T_s = 0.2$[ms] $f_{bw} = 10$[Hz] $\xi = 1.0$	$-\frac{3}{2} \cdot \frac{v_{gd}}{C_{dc} \cdot s}$	$\frac{0.001626 \cdot s + 0.02057}{s}$	$\frac{0.001628 \cdot z - 0.001623}{z - 1}$
PPC-PSL Bucking (Current)	$T_s = 20[\mu s]$ $f_{bw} = 10$[kHz] $\xi = 0.9$	$\frac{2 \cdot (v_{oQ} - v_{inQ})}{s \cdot L + R_L} \cdot \left(\frac{n_2}{n_1}\right)^2$	$\frac{0.002003 \cdot s + 30.02}{s}$	$\frac{0.002303 \cdot z - 0.001703}{z - 1}$
PPC-PSL Boosting (Current)	$T_s = 20[\mu s]$ $f_{bw} = 10$[kHz] $\xi = 0.9$	$\frac{2 \cdot (v_{oQ})}{s \cdot L + R_L} \cdot \left(\frac{n_2}{n_1}\right)^2$	$\frac{0.0007838 \cdot s + 11.75}{s}$	$\frac{0.0009013 \cdot z - 0.0006663}{z - 1}$

Table 6.10: PI controllers design for the 2LVSI and PPC with the inductor in the partial side (PSL).

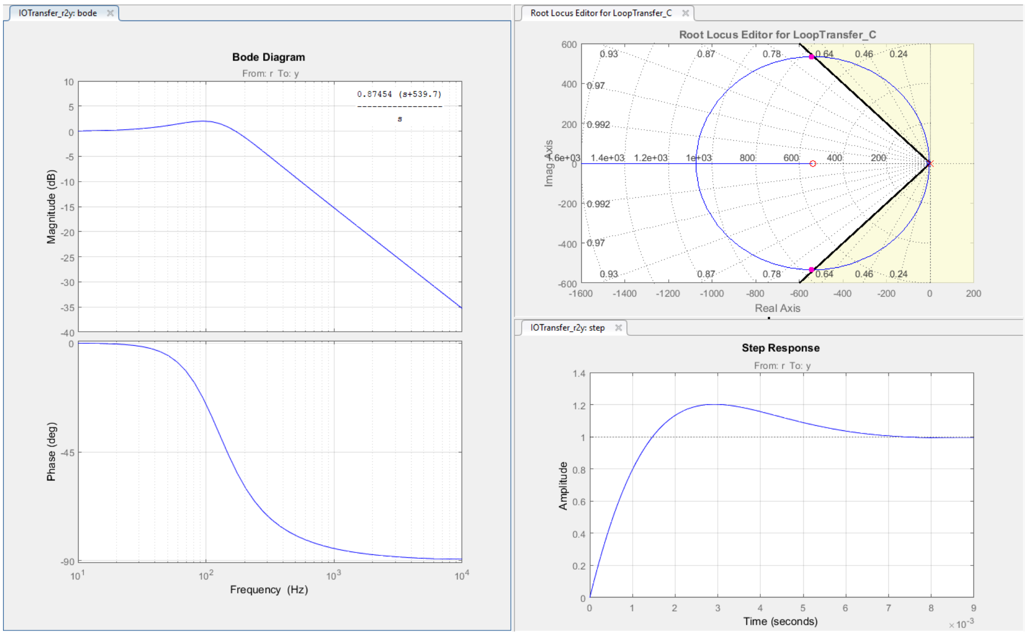

Figure 6.21: 2LVSI d-axis and q-axis current loop controller: bandwidth = 250 [Hz], damping ratio $\xi = 1/\sqrt{2}$.

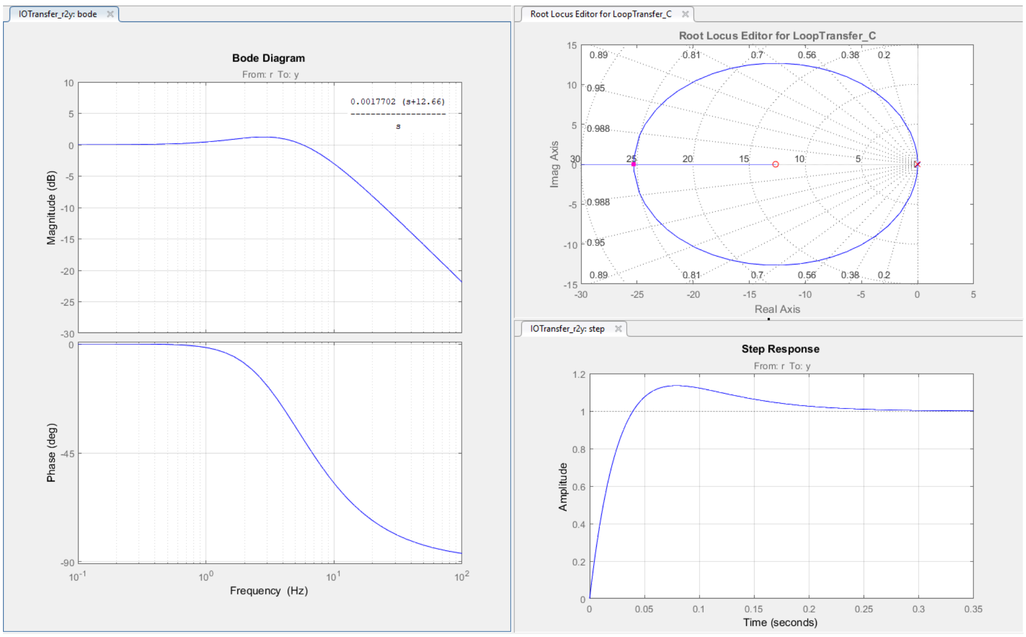

Figure 6.22: 2LVSI dc-link voltage loop controller: bandwidth = 10 [Hz], damping ratio $\xi = 1.0$.

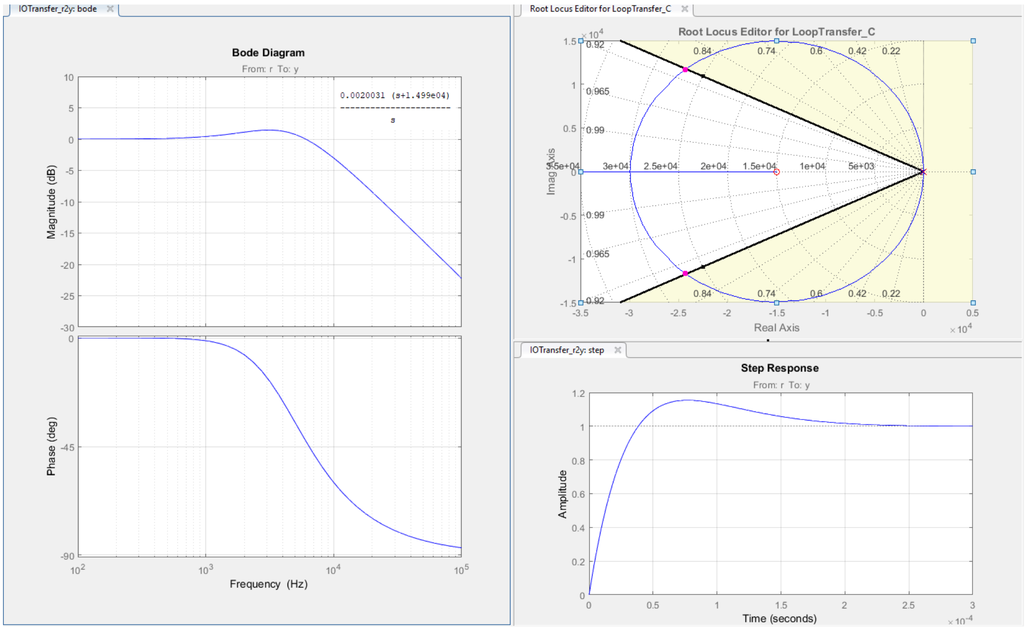

Figure 6.23: PPC partial side inductor current loop controller (bucking mode): bandwidth = 10 [kHz], damping ratio $\xi = 0.9$.

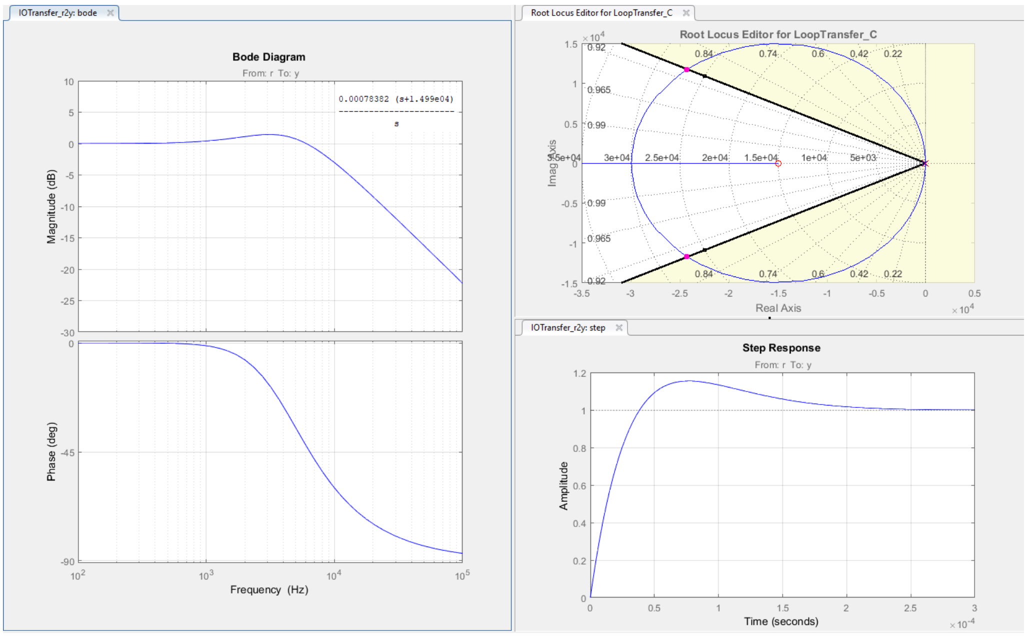

Figure 6.24: PPC partial side inductor current loop controller (boosting mode): bandwidth = 10 [kHz], damping ratio $\xi = 0.9$.

6.6 Summary

In this chapter four different control schemes, that allow the provision of three different complementary services, are presented. The designs of the PI controller, required in each control scheme, are also presented in this chapter.

The first two control strategies presented correspond to two alternative (PV/ESS configurations and control schemes) the performance of the Global MPPT. These alternatives allow to perform global MPPT while complying with the Maximum power RR regulation. Each control scheme was applied over a different PV/ESS configuration (ESS connection at the AC-side or PV-side, allowing for comparison and selection (in the following chapter) of the best fitting alternative to enable a central inverter PV plant to perform Global MPPT.

The third control strategy targets peak shaving in the central inverter PV systems. The ESS connection to the PV system is performed at the PV side. The PPC By Pass Current Reference block allows the regulation of the power generation (performing peak shaving) while keeping the battery bank within operational range. The results obtained from the application of this control scheme will be presented in the following chapter.

A novel control strategy to retrofit central inverter PV plants, in order to reduce the loss of generation caused by power clipping was implemented. This strategy exploits an inherent characteristic of traditional P&O MPPT algorithms, thus allowing the central inverter to keep tracking the MPP despite the PV array surpassing the 2LVSI power rating. The results obtained from the application of this new control strategy will be presented in the following chapter.

All the strategies presented in this chapter allow retrofit of existing PV plants, enabling them to provide a selected complementary service. Nevertheless, both Global MPPT strategies have an extra requirement. This service requires that the central inverter allows the dc-link voltage reference to be set externally.

Additionally, a general control strategy was presented in this chapter. This strategy has as purpose to offer a point of comparison between part of the simulation results presented in the next chapter (Chapter 7) and the experimental results presented in chapter 8.

Chapter 7

Simulation results

7.1 Introduction

This chapter is composed of 4 main sections which present the simulation results associated to each one of the complementary services and PV/ESS configurations addressed in chapter 6. The parameters of each ESS/PC configuration, control scheme and PI controller design can be found in chapter 6.

Section 7.2 presents the simulation results for two PV/ESS configurations that allow the performance at the maximum power RR regulation during a Global MPPT strategy, each PV/ESS configuration presents a different connection point for the ESS (ESS connected at the AC-grid side in section 7.2.1 and ESS merged at the PV side in section 7.2.2). The simulation results of a PV/ESS configuration performing Peak shaving are presented in section 7.3, where the ESS connection is performed at the PV side. The simulation results of a PV/ESS configuration under power clipping operation are presented in section 7.4, in this configuration the ESS is connected at the PV side. Finally, a PV/ESS configuration with the ESS connection at PV side and based on a PPC with inductor at the partial side is presented in section 7.5. The simulation results obtained from this simulation will be contrasted with the experimental results presented in Chapter 8.

7.2 Maximum power RR regulation

The simulation results of two different PV/ESS configurations for maximum power RR regulation under a Global MPPT strategy are presented in this section. The first set of simulation results correspond to a configuration with the ESS connection at the AC-grid side, while the second set of simulation results correspond to a configuration with the ESS connection at the PV side.

7.2.1 ESS connection at AC-grid side

The PV/ESS configuration and control strategy applied in this section were introduced in section 6.2.2. As previously stated, the PV/ESS configuration is formed of a PV array connected to the AC grid through a 2LVSI acting as a central inverter (PV-2LVSI). The ESS is formed of an SC bank connected to a dc-dc converter (IBBC), the output of the dc-dc converter is connected to a 2LVSI (SC-2LVSI) and merges with the PV system at the AC-grid side. Note that the parameters of the PV/ESS configuration and the parameters of the controllers were previously presented in chapter 6 (section 6.2.2).

This simulation tests the capability of the PV/ESS configuration to limit the maximum power RR during the performance of a Global MPPT strategy. Under standard operation the PV/ESS configuration operates in P&O mode, i.e. the PV inverter performs P&O while the ESS charges the SC bank. The PV/ESS operation mode will change to a Global MPPT mode if one of the following conditions take place: if a certain time elapses since the last time the Global MPPT mode was applied (time-triggered) or if the PV array output power experiences a variation greater than a predefined value (power-triggered). Each condition targets different PV power dynamics that may cause several local maxima in the power vs voltage PV curve, the former condition targets slow dynamics, while the latter condition targets fast dynamics. During the Global MPPT mode, the PV inverter performs a Global MPPT (scan of the power vs voltage PV curve) while the ESS provides power support to limit the variation of the power injected into the grid.

The base values applied to transform these simulation results into the per unit system ([pu]) are shown in table 7.1. Note that the per unit values in the SC-bank side considered the power rating of one interleaved dc-dc power converter.

The simulation results are presented in Figs. 7.1 to 7.5. The PV/ESS configuration starts performing in the P&O mode until 0.3 [s], when the configuration changes to the Global MPPT mode (time-triggered), after performing the Global MPPT the PV/ESS configuration returns to the P&O mode. Later, at 1.4 [s], a step-down in solar irradiance from 1000 to 200 [W/m^2] is performed over 5 PV modules in 12 strings (60 PV modules in total), while the rest of the PV array operates under constant irradiance (at 1000 [W/m^2]). This condition emulates a partial shading scenario with two local maxima. This step-down in irradiance generates a variation in the PV array output power that exceeds the predefined power variation triggering value, hence changing the operation mode of the PV/ESS to Global MPPT mode (power-triggered). Once the Global MPPT strategy has ended, the PV/ESS configuration returns to P&O mode. During the simulation the temperature over the PV array was kept constant at 25 [°C].

Figure 7.1 shows the PV system waveforms. Graph a) shows that irradiance is kept constant at 1000 [W/m^2] until 1.4 [s], when a step-down on the irradiance (to 200 [W/m^2]) over 60 PV modules is experienced. The PV array power variation is presented in graph b), here the variation at 0.3 [s] is caused by the PV/ESS configuration performing a time-triggered Global MPPT. The second variation (at 1.4 [s]) is caused by the step-down in solar irradiance, which is reflected on an instantaneous decrease in PV array power, triggering the second performance of the Global MPPT strategy. After the global MPPT, the PV array power settles around to the new MPP. The regulation of the dc-link voltage (and PV array voltage) is/are shown in graph c), where the operation mode of the PV-2LVSI (P&O or Global MPPT) is clearly visible. Graph d) shows the control of the direct (i_{gd1}) and quadrature (i_{gq1}) grid currents. Due to the standard VOC scheme, the control of the dc-link voltage is accomplished through the regulation of i_{gd1}. Note that i^*_{gq1} is kept constant at 0 [A]. Finally, the amplitude of grid currents, shown in Graph e), reflects the behaviour of the PV array output power (P_{pv}).

Figure 7.2 shows the behaviour of the ESS inverter. The PV array output power (P_{pv}) and SC bank power (P_{sc}) are presented in graph a). When the PV/ESS configuration is operating in the Global MPPT mode, the ESS provides the required power to limit the output power variation. This action is reflected in the positive values of P_{sc} (from 0.3 to 0.68 [s] and from 1.4 to 1.8 [s]). On the other hand when the PV/ESS configuration is in the P&O mode, the SC bank is being charged, thus P_{sc} takes negative values. The direct axis grid current and its reference are shown in graph b). Note that assuming the grid voltage amplitude and SC-bank voltage as constants, a linear relationship can be found between i^*_{gd2} and P_{sc}, this explains the identical waveform (graphs a) and b)). During the complete simulation i^*_{gq2} was equal to zero. The control of the quadrature grid current (i_{gq2}) is shown in graph c). Thus setting the regulation of the reactive power to 0

Parameter	Symbol	Value
Power	P_{base}	$735[kW]$
AC voltage	$V_{\text{ac base}} = 440 \cdot \sqrt{2/3}$	$360[V]$
AC current	$I_{\text{ac base}} = P_{\text{base}} \cdot 2/(3 \cdot V_{\text{ac base}})$	$1.36[kA]$
DC-link voltage	$V_{\text{dc base}} = 2 \cdot V_{\text{ac base}}$	$720[V]$
DC-DC power	$P_{\text{dcdc base}}$	$50[kW]$
DC-DC voltage	$V_{\text{dcdc base}}$	$320[V]$
DC-DC current	$I_{\text{dcdc base}} = P_{\text{dcdc base}}/V_{\text{dcdc base}}$	$156.25[A]$

Table 7.1: Maximum power RR regulation in a PV/ESS configuration with the ESS connection at the AC-grid side: Base values applied in the per unit system.

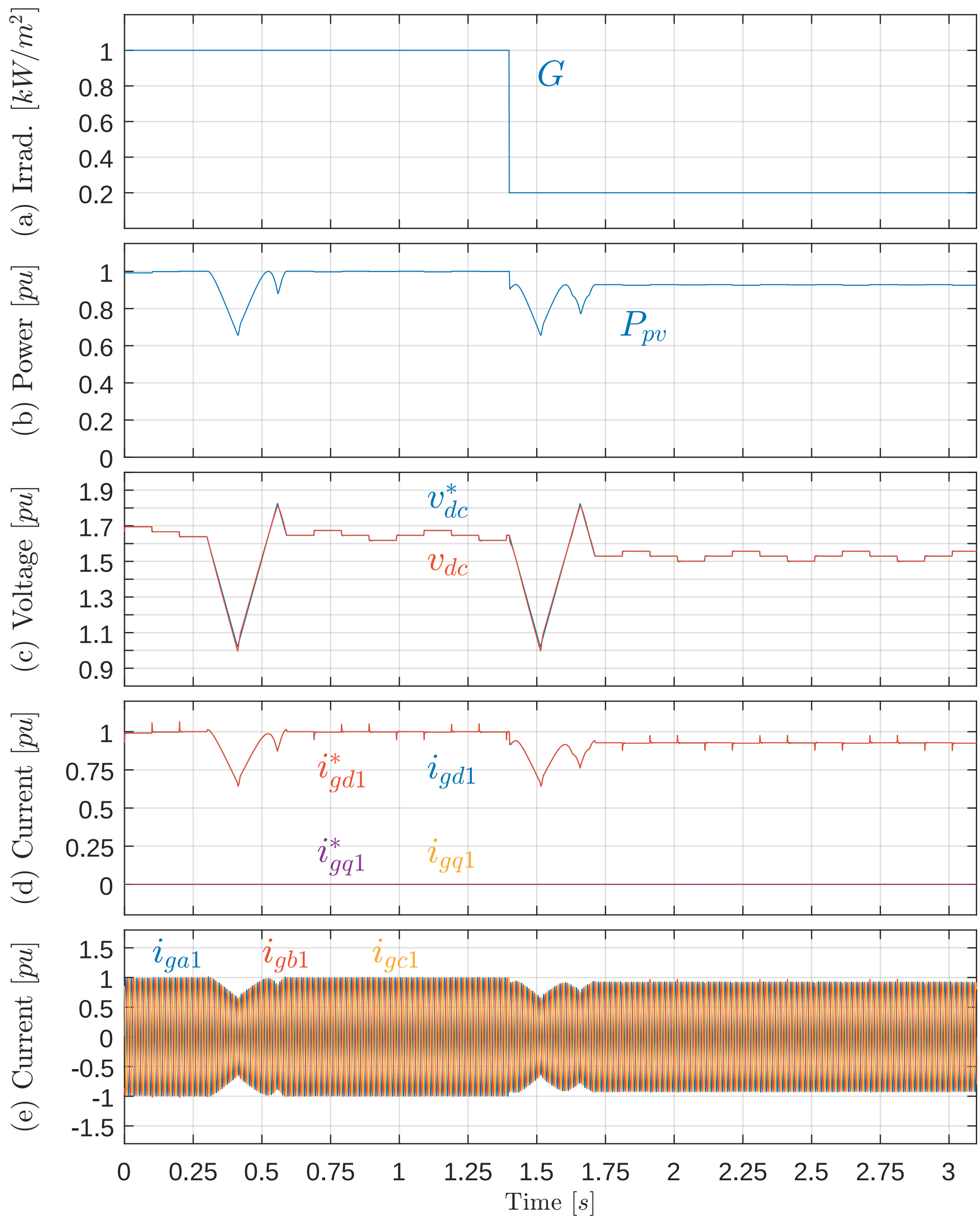

Figure 7.1: Simulation of maximum power RR regulation with the ESS connection at the AC side under a Global MPPT strategy, PV array and PV inverter (PV-2LVSI): a) Solar irradiance (G), b) PV array output power ($P_{\rm pv}$), c) PV array voltage ($v_{\rm dc}$) and reference ($v^*_{\rm dc}$), d) d-axis grid current ($i_{\rm gd1}$), d-axis grid current reference ($i^*_{\rm gd1}$), q-axis grid current ($i_{\rm gq1}$) and q-axis grid current reference ($i^*_{\rm gq1}$) and e) grid currents ($i_{\rm ga1}$, $i_{\rm gb1}$ and $i_{\rm gc1}$).

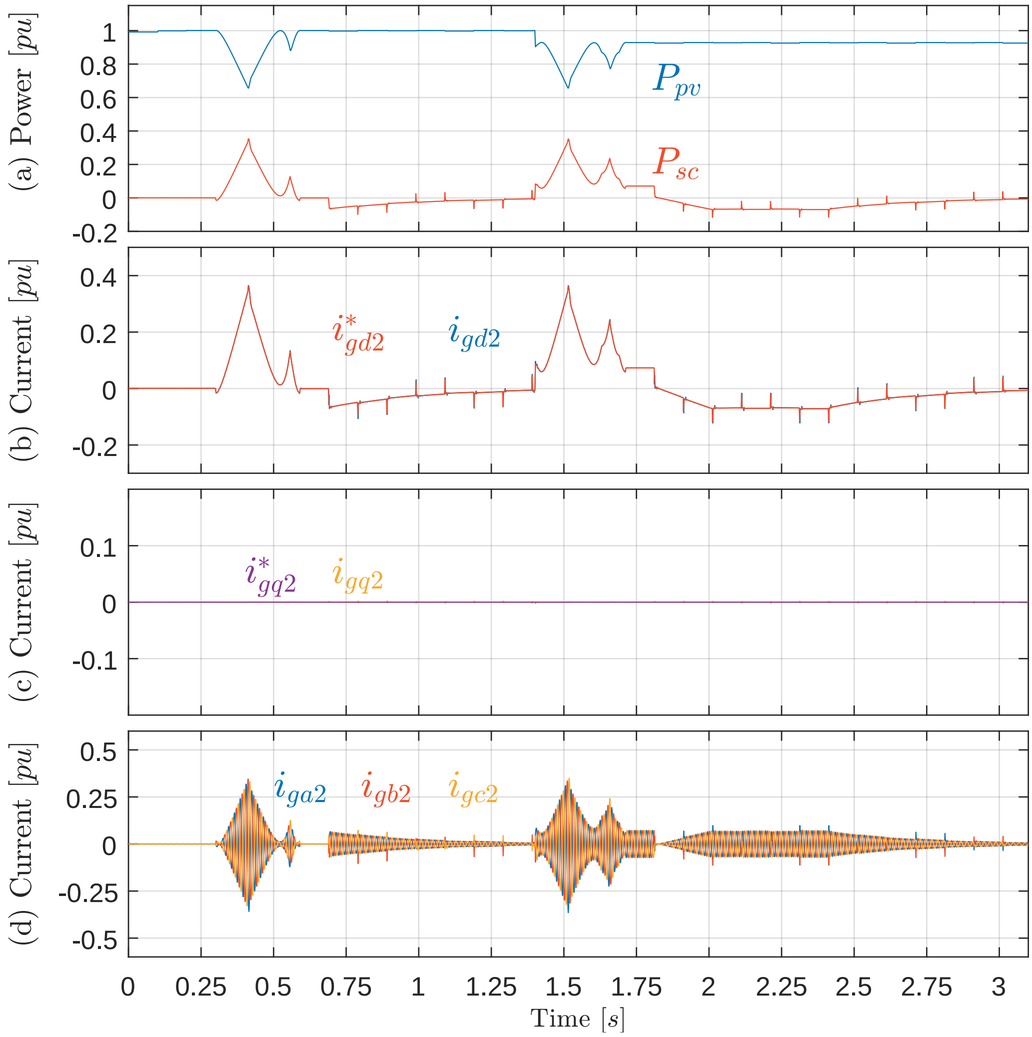

Figure 7.2: Simulation of maximum power RR regulation with the ESS connection at the AC side under a Global MPPT strategy, ESS inverter (SC-2LVSI): a) PV array power (P_{pv}) and SC bank power reference (P^*_{sc}), b) d-axis grid current (i_{gd2}) and d-axis grid current reference (i^*_{gd2}), c) q-axis grid current (i_{gq2}) and q-axis grid current reference (i^*_{gq2}) and d) grid currents (i_{ga2}, i_{gb2} and i_{gc2}).

$[VAR]$. The resulting grid currents are shown in graph d), where the amplitude of the currents reflect the ESS active power flow.

Figure 7.3 presents the simulation results of the dc-dc converter (IBBC) and SC bank. Graph a) shows the output voltage of the IBBC (v_{o}) and its reference (v^*_{o}). Note that the v^*_{o} is constant and equal to 1100 $[V]$ (1.53 [pu]). The output of the PI controller of the output voltage, provides the inductor current reference for all of the interleaved dc-dc converters (i^*_{L}). Graph b) presents inductor current in one interleaved IBBC (i_{L1}) and the reference (i^*_{L}). Note that all other IBBCs

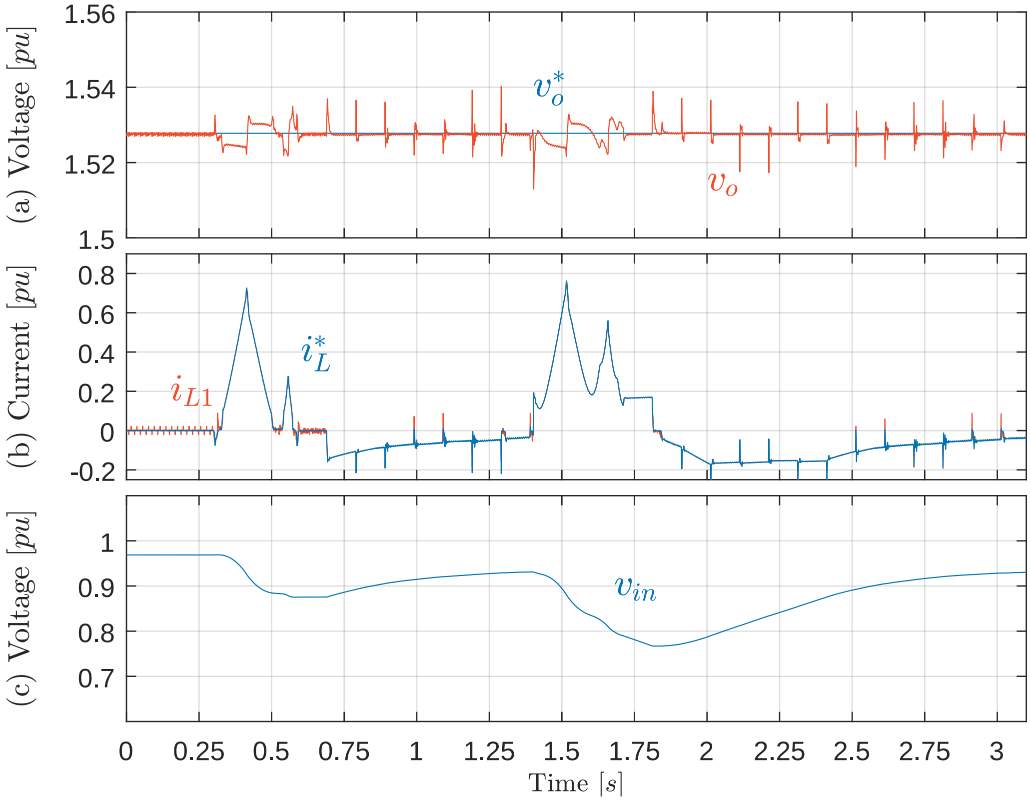

Figure 7.3: Simulation of maximum power RR regulation with the ESS connection at the AC side under a Global MPPT strategy, dc-dc converter (IBBC) and SC bank: a) SC-2LVSI dc-link capacitor voltage (v_o) and reference (v_o^*), b) IBBC inductance current (i_L1) and reference (i_L^*) and c) SC bank voltage (v_in).

perform in exactly the same manner. The significant increase in i_L^* (from 0.3 to 0.68 [s] and from 1.4 to 1.8[s]) is caused by the respective variation of v_o during the operation of the PV/ESS configuration in the Global MPPT mode. On the other hand, the negative values of i_L^* (from 0.7 to 1.4 [s] and from 1.85 to 3.1 [s]) correspond to the charging of the SC bank during P&O. The voltage of the SC bank is presented in graph c), where the decrease in voltage (from 0.3 to 0.68 [s] and from 1.4 to 1.8 [s]) reflects the discharge of the ESS during the Global MPPT mode. The charging of the SC bank is also reflected in the smooth voltage increase from 0.7 to 1.4 and from 1.85 to 3.1 [s].

Figure 7.4 presents a summary of the PV, ESS and combined power and grid current injection. Graph a) presents the total PV/ESS configuration output power (P_t), the PV array output power (P_pv) and the ESS output power (P_sc). The total PV/ESS configuration output power variation does not exceed 10% of the nominal power (74 kW), despite the power variation of the PV system

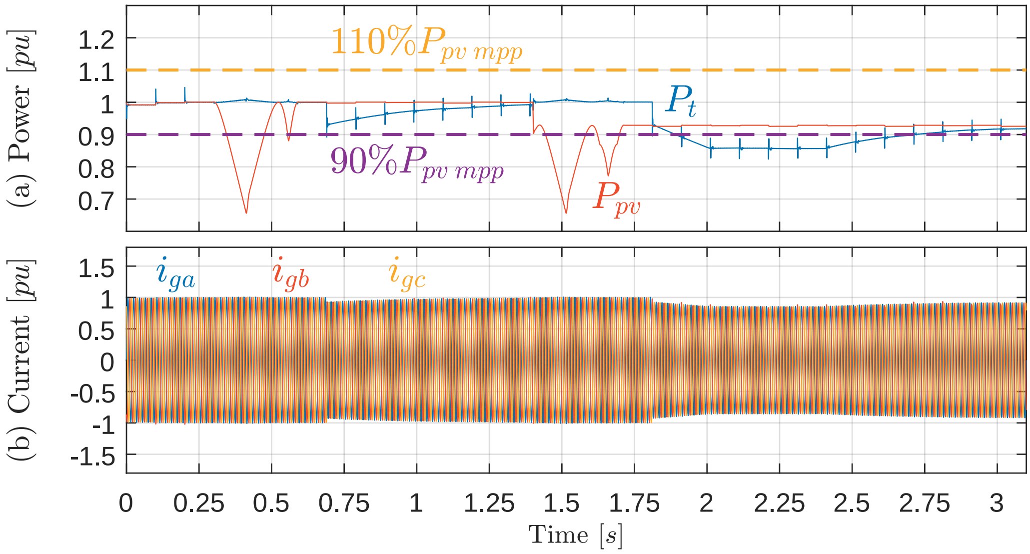

Figure 7.4: Simulation of maximum power RR regulation with the ESS connection at the AC side under a Global MPPT strategy, power and grid currents: a) PV/ESS configuration output power (P_{t}), PV array output power (P_{pv}) and SC bank output power (P_{sc}) and b) PV/ESS configuration grid currents (i_{ga}, i_{gb} and i_{gc}).

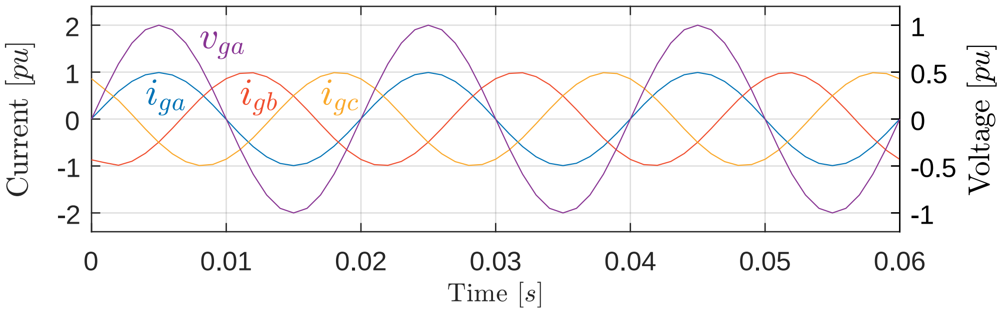

Figure 7.5: Simulation of maximum power RR regulation with the ESS connection at the AC side under a Global MPPT strategy: zoom of the grid currents (i_{ga}, i_{gb} and i_{gc}) and phase a grid voltage (v_{ga}).

during the application of the Global MPPT strategy. It must be noticed that due to simulation purposes a fast charging of the SC bank was chosen. A slower charge will allow a better output power performance. Graph b) shows the grid currents (i_{ga}, i_{gb} and i_{gc}) at the point of common coupling, where the grid current reflects the behaviour of P_{t}. A zoom to the grid currents and phase a grid voltage is presented in Fig. 7.5. The unitary power factor is reflected in the phase delay ($0[rad/s]$) between the 'phase a' grid current and 'phase a' grid voltage.

7.2.2 ESS connection at PV side

The PV/ESS configuration applied in this simulation, introduced in section 6.2.3, consists of a PV system (PV array and 2LVSI) and an ESS (eight interleaved IBBC and an SC bank) interconnected at the PV side (dc-link of the 2LVSI). The parameters of the PV/ESS configuration, the control strategy and the parameters of the corresponding controllers, applied in this simulation, were presented in section 6.2.3.

This simulation shows the performance of the PV/ESS configuration under a Global MPPT strategy. In order to validate the proposed strategy a step-down in solar irradiance from 1000 to 200 [W/m^2] was applied over 60 PV modules (five modules per string over twelve strings) at 1.4 [s]. The step-down over part of the PV array changes the operation of the PV array from a uniform condition (with a single local maximum) to a partial shading scenario (with two local maxima). The simulation results of this validation are presented in Figures 7.6 to 7.9.

The base values applied to transform these simulation results into the per unit system ([pu]) are the same as those presented in table 7.1.

Figure 7.6 shows the PV system initially operating in P&O mode. At 0.3 [s] the configuration switches to Global MPPT mode (0.3 to 0.68 [s]), this transition is time-triggered, i.e. a certain time has elapsed since the last time the Global MPPT mode was performed. After the performance of the Global MPPT the PV/ESS configuration returns to P&O mode. The step-down in solar irradiance at 1.4 [s], generates an instantaneous decrease of the PV power output, switching the operation to Global MPPT mode (1.4 to 1.8 [s]). Finally, after performing the Global MPPT, the configuration returns to P&O mode. Graph a) shows that the solar irradiance (G) is kept constant (at 1000 [W/m^2]) until 1.4 [s], when the step-down (to 200 [W/m^2]) is performed. The behaviour of the PV array power (P_{pv}) is shown in graph b). Here the main variation take place between 0.3 to 0.68 [s] and 1.4 to 1.8 [s], both cases corresponding to the times when the configuration is performing Global MPPT. Note that the difference in PV power level before 1.4 [s] and after 1.8 [s], reflect the step down in solar irradiance. The dc-link voltage (v_{dc}) and its reference (v_{dc}^*) are shown in graph c), during normal operation when classic P&O is performed. When performing Global MPPT the dc-link voltage is swapped in order to cover the PV power vs voltage curve, as seen from 0.3 to 0.68 [s] and from 1.4 to 1.8 [s]. Graph d) shows the control of the direct (i_{gd}) and quadrature (i_{gq}) grid currents. Due to the injection of power from the ESS to the dc-link the variation in d-axis current is smaller than the variation experienced in the d-axis grid current (PV-2LVSI) in the previous simulation (Fig. 7.1). On the other hand, the quadrature grid current reference (i_{gd}^*) is kept constant at 0 [A], thus, regulating the injection of reactive power to zero [VAR]. Finally, the grid currents are shown in graph d), where the output power variation of the

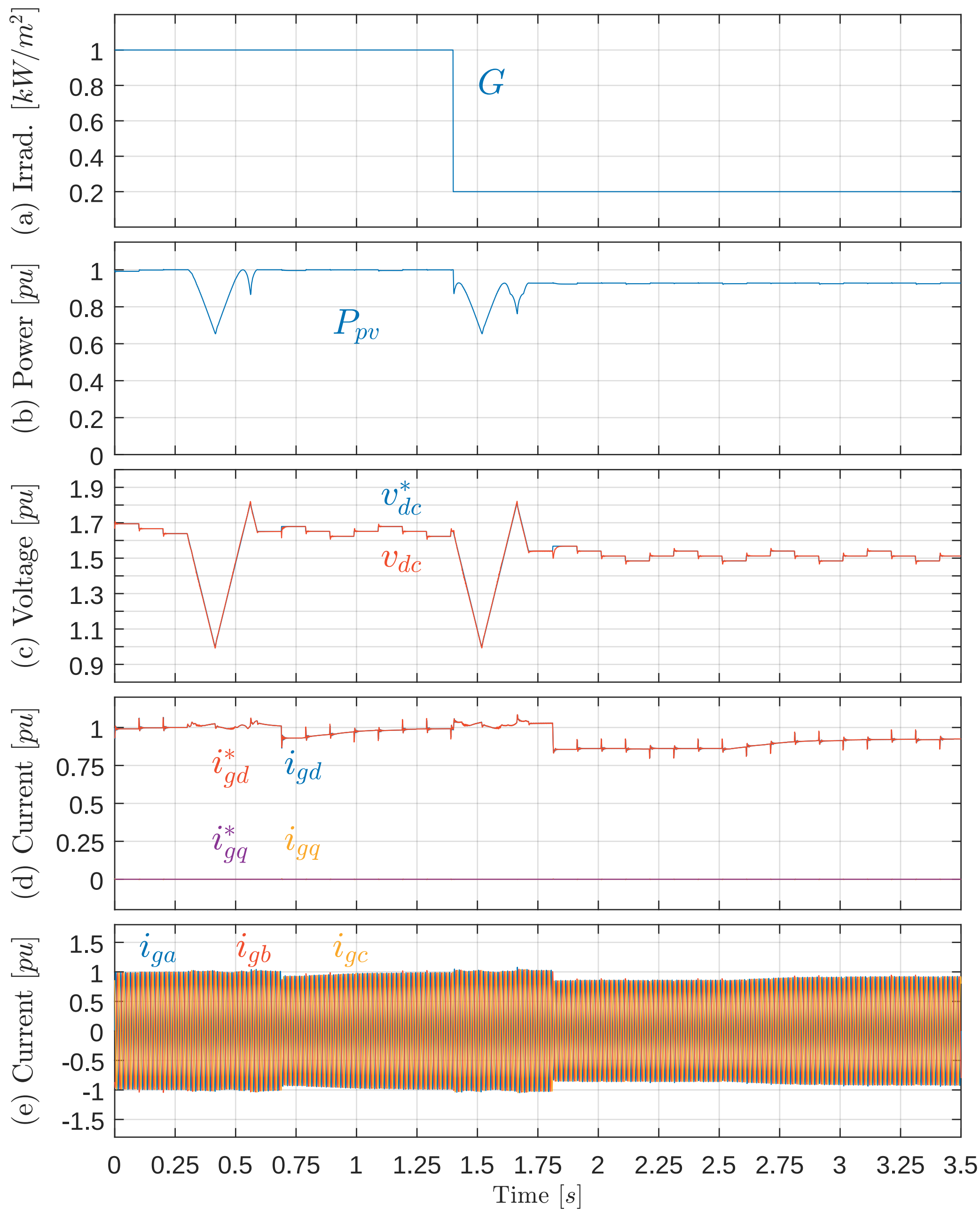

Figure 7.6: Simulation of maximum power RR regulation with the ESS connection at the PV side under a Global MPPT strategy, PV array and PV inverter (PV-2LVSI): a) Solar irradiance (G), b) PV array output power (P_{pv}), c) PV array voltage (v_{dc}) and reference (v_{dc}^*), d) d-axis grid current (i_{gd}), d-axis grid current reference (i_{gd}^*), q-axis grid current (i_{gq}) and q-axis grid current reference (i_{gq}^*) and e) PV/ESS configuration grid currents (i_{ga}, i_{gb} and i_{gc}).

PV/ESS configuration is reflected in the amplitude of the grid currents.

Figure 7.7 presents the waveforms associated with the operation of the ESS during simulation. Graph a) presents the PV array output power ($P_{\rm pv}$). During the operation in P&O mode (from 0.3 to 0.68 [s] and from 1.4 to 1.8 [s]), the variation of $P_{\rm pv}$ exceeds the lower limit imposed by the maximum power RR regulation ($\Delta P_{\rm pv} < -10\%\ P_{\rm mpp}$). The control of the ESS power ($P_{\rm sc}$) is shown in graph b), the main variations (from 0.3 to 0.68 [s] and from 1.4 to 1.8 [s]) reflect the operation in Global MPPT mode. The charge of the SC bank is performed from 0.7 to 1.4 [s] and from 1.85 to 2.3 [s]. The control of the current through the inductance in one (of the eight) interleaved dc-dc converters (IBBC) is presented in graph c), which reflect the behaviour of $P_{\rm sc}$. Graph d) shows the SC bank voltage variation ($v_{\rm in}$).

Figure 7.8 shows the power injected to the grid ($P_{\rm t}$) by the PV/ESS configuration, the power provided by the PV array ($P_{\rm pv}$) and in dashed lines the upper and lower limits to keep power variations within maximum power RR regulation (10% per minute of the nominal PV plant output power). It must be noted that the decrease in power injected to the grid after 1.4 [s] is caused by the step down in solar irradiance. The small peaks in $P_{\rm t}$ during P&O are required to generate the dc-link voltage steps and are caused by the VOC scheme regulating the DC-link voltage. Without the ESS, the Global MPPT through the proposed PV curve voltage scan, will generate power variations greater than those allowed by the maximum power RR regulation, as seen in the power curve $P_{\rm pv}$.

Grid currents ($i_{\rm ga}$, $i_{\rm gb}$ and $i_{\rm gc}$) and grid phase voltage a ($v_{\rm ga}$) under steady state operation are shown in Fig. 7.9. The synchronization between $i_{\rm ga}$ and $v_{\rm ga}$ shows the operation with a power factor equal to one.

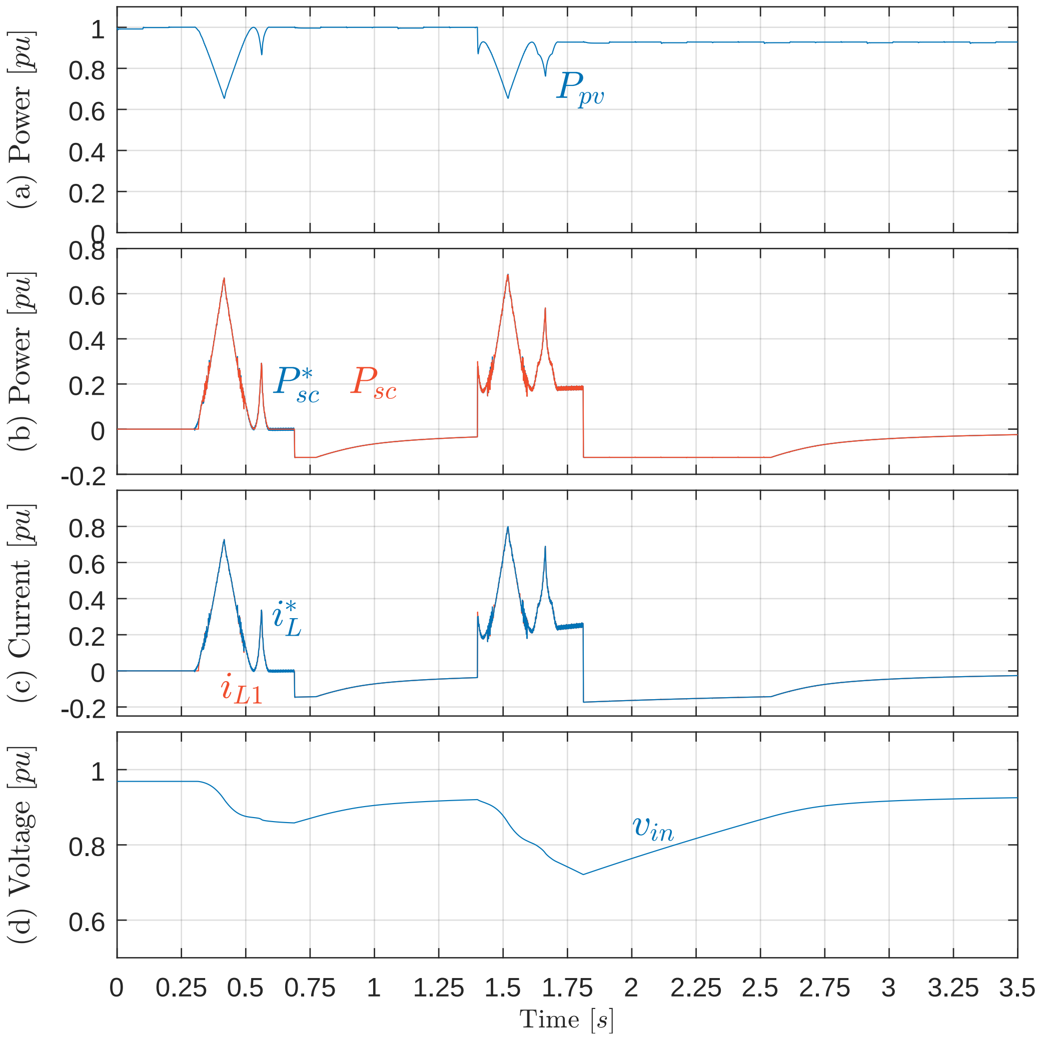

Figure 7.7: Simulation of maximum power RR regulation with the ESS connection at the PV side under a Global MPPT strategy, dc-dc converter (IBBC) and SC bank: a) PV array output power (P_{pv}), b) SC bank output power (P_{sc}) and reference (P_{sc}^*), c) single IBBC inductance current (i_{L1}) and reference (i_{L}^*) and d) SC bank voltage (v_{sc}).

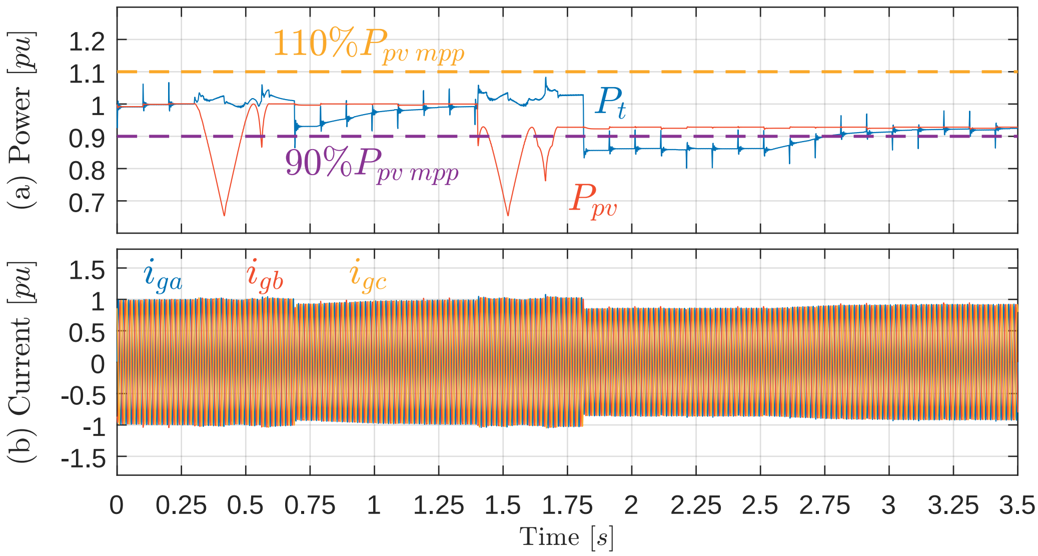

Figure 7.8: Simulation of maximum power RR regulation with the ESS connection at the PV side under a Global MPPT strategy: Full PV/ESS configuration output power (P_{t}), PV plant output power (P_{pv}), maximum power variation per minute (110% $P_{\mathrm{pv\ mpp}}$) and minimum power variation per minute (90% $P_{\mathrm{pv\ mpp}}$).

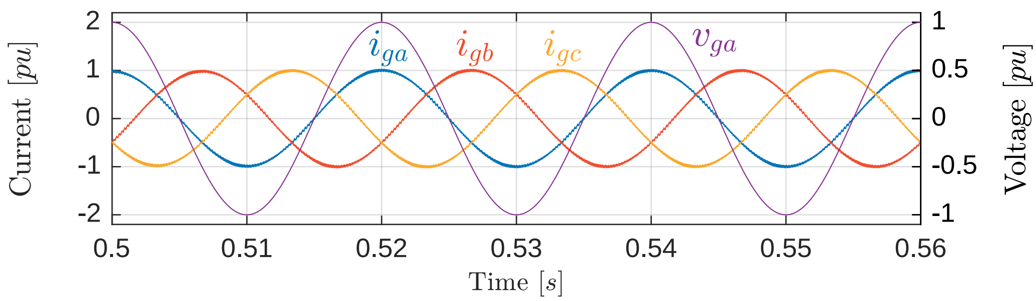

Figure 7.9: Simulation of maximum power RR regulation with ESS connection at PV side under a Global MPPT strategy: Line currents (i_{ga}, i_{gb} and i_{gc}) and grid phase voltage (v_{ga}) during steady state.

7.3 Peak Shaving: ESS connection at PV side

This section presents the simulation results of a PV/ESS configuration under a peak shaving scenario. The PV part of the PV/ESS configuration is composed of a PV array connected to the grid through a single 2LVSI. On the other hand, the ESS part is formed of a battery bank connected to eight interleaved PPCs. The PV system and ESS are merged at the PV side (dc-link of the 2LVSI), as shown in section 6.3 (Fig. 6.12). Note that the parameter of the PV/ESS configuration and control scheme were previously presented in chapter 6 (section 6.3).

The base values applied to transform these simulation results into the per unit system ([pu]) are shown in table 7.2. Note that the per unit values associated with the ESS voltage and current are based on the power rating of a single dc-dc converter.

Peak shaving requires knowing the power demanded by the grid, for this purpose an external signal (P_{load}), that informs the power required by the grid operator, was added to the simulation. In order to validate the configuration and control scheme three different conditions were applied over P_{load}, while keeping solar irradiance and temperature constant at 800 [W/m^2] and 25 [$°C$]. In the first condition the grid operator requires that the PV plant injects (to the grid) the maximum available PV power (from 0 to 0.55 [s], from 1.15 to 1.75 [s] and from 2.35 to 3.0 [s]). The second condition considers that the power demanded by the grid is lower than the available PV power (from 0.55 to 1.15 [s]), and the third condition considers that the grid operator demands more power than the available PV power (from 1.75 to 2.35 [s]).

The simulation results showing the operation of the PV/ESS configuration under the the aforementioned conditions are presented in Figs. 7.10 to 7.12. Figure 7.10 shows the signals

Parameter	Symbol	Value
Power	P_{base}	$735[kW]$
AC voltage	$V_{\text{ac base}} = 440 \cdot \sqrt{2/3}$	$360[V]$
AC current	$I_{\text{ac base}} = P_{\text{base}} \cdot 2/(3 \cdot V_{\text{ac base}})$	$1.36[kA]$
DC-link voltage	$V_{\text{dc base}} = 2 \cdot V_{\text{ac base}}$	$720[V]$
DC-DC power	$P_{\text{dcdc base}}$	$50[kW]$
DC-DC voltage	$V_{\text{dcdc base}}$	$300[V]$
DC-DC current	$I_{\text{dcdc base}} = P_{\text{dcdc base}}/V_{\text{dcdc base}}$	$167[A]$

Table 7.2: Peak Shaving in a PV/ESS configuration with the ESS connection at the PV side: Base values applied in the per unit system.

associated with the control of the PV system. Graph (a) shows the PV array output power (P_{pv}) and the 2LVSI output power (P_{ac}). Graph (b) shows the dc-link voltage (v_{dc}) and its reference (v_{dc}^{*}). Graph (c) presents the control of the direct (i_{gd}) and quadrature (i_{gq}) grid currents. The resulting grid currents, in stationary reference frame (i_{ga}, i_{gb} and i_{gc}), are displayed in graph (d). Figure 7.11 shows the simulation results associated with the ESS. Graph (a) shows the PV array output power (P_{pv}) and the external power reference (P_{load}) provided by the grid operator. Graph (b) shows the power provided by the ESS (P_{BESS}). The PPC's inductor current reference of the Full-Bridge based PPC (i_{L}^{*}) and the inductor current of one of the PPCs (i_{L1}) are shown in graph (c). Graph (d) presents the voltage of the battery bank (v_{in}).

The simulation results show the PV/ESS configuration initially operating with a grid power demand equal to the PV power generation (0 to 0.55 [s]). During this period, the 2LVSI is controlling the power injection to the grid, the tracking of the MPP is visible through the stepped waveform of the dc-link voltage (v_{dc}). At the same time, the ESS is operating in idle mode (not storing nor releasing power), therefore power provided by the ESS (P_{BESS}) and the PPC's inductor current (i_{L}^{*}) are equal to zero and the voltage of the battery bank remains constant. At 0.55 [s] a step-down in grid power demand (P_{load}), generates a drop in the power being injected into the grid (P_{ac}). This reduction is reflected in a decrease of the direct axis grid current (i_{gd}) and a decrease of the amplitude of the grid currents. Despite the reduction of i_{gd}, P_{pv} remains at the same power level as it was before the step-down in P_{load} (v_{dc} remains around 0.95 [pu]). This is due to the action of the ESS, which starts drawing the exceeding PV power (beyond P_{load}) into the battery bank. This action is reflected in the negative value of the ESS power (P_{BESS}), negative value of the PPC's inductor current reference (i_{L}^{*}) and the increase of the battery bank voltage (v_{in}). At 1.15 [s], a step-up in P_{load} equals the power required by the grid (P_{load}) to the available in the PV power (P_{pv}), causing an increase of both the d-axis current and the amplitude of the grid currents. The ESS reacts accordingly, decreasing the power injected to the battery bank to 0 [W], which is reflected in an increase in i_{L}^{*} from -1.0 to 0 [A]. Between 1.15 and 1.75 [s] the power to/from the ESS is equal to 0 [W], thus, keeping v_{in} constant.

At 1.75 [s], a step-up in P_{load} causes an increase in the power being injected to the grid (P_{ac}), despite the available PV power (P_{pv}) remaining constant. The increase of P_{ac} is achieved by increasing the direct axis grid current i_{d}. The extra power (beyond P_{pv}) is provided by the ESS, which is reflected in the positive ESS power (P_{BESS}), a positive current reference i_{L}^{*} and the discharge of the battery bank (decrease of v_{in}). At 2.35 [s], a step-down in P_{load}, equals P_{load} to P_{pv}, thus returning the ESS to idle mode operation. The negative steps in P_{load} causes an increase in P_{BESS}, that is reflected in v_{dc} as an instantaneous decrease in voltage, which is compensated by the increase of i_{gd}. The inverse behaviour takes place over v_{dc} during the positive steps of P_{load}.

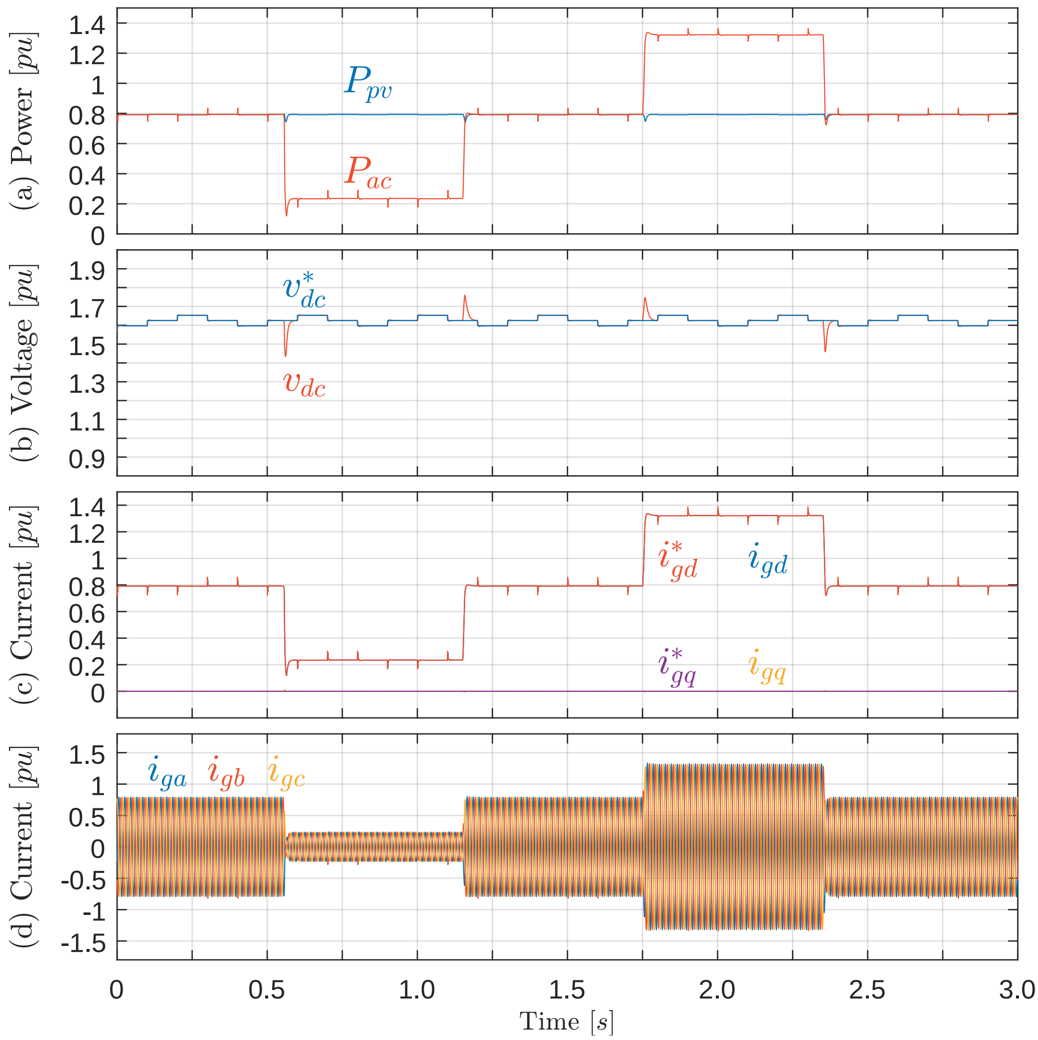

Figure 7.10: Simulation of Peak Shaving with the ESS connection at the PV side, PV array and PV inverter (PV-2LVSI): (a) PV array output power (P_{pv}) and inverter output power (P_{ac}), (b) dc-link voltage (v_{dc}) and its reference (v^*_{dc}), (c) direct axis grid current reference (i^*_{gd}), direct axis grid current measurement (i_{gd}), quadrature axis grid current reference (i^*_{gq}) and quadrature axis grid current measurement (i_{gq}) and (d) grid currents in stationary reference frame (i_{ga}, i_{gb} and i_{gc}).

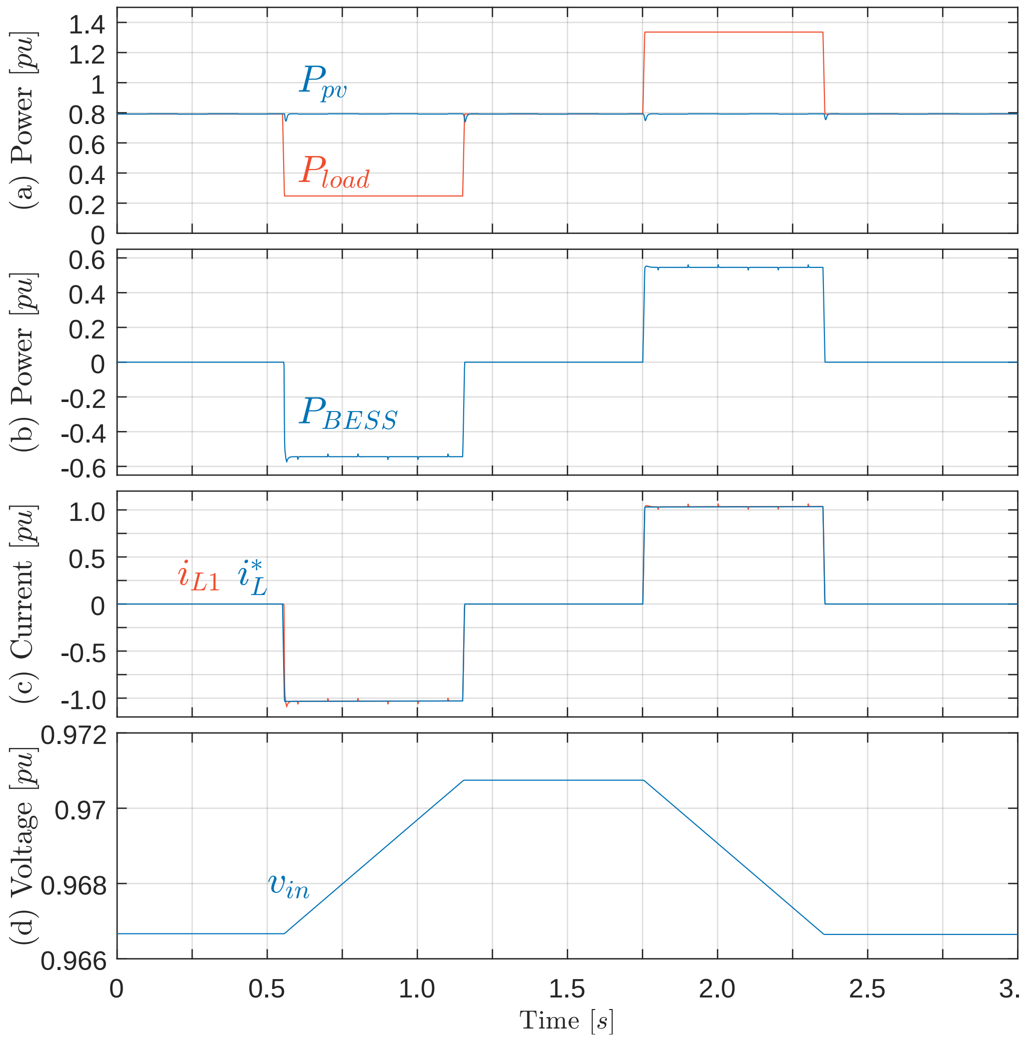

Figure 7.11: Simulation of Peak Shaving with the ESS connection at the PV side, dc-dc converter (PPC) and battery bank: (a) power generated by the PV array (P_{pv}) and power demanded by the grid operator (P_{load}), (b) ESS power (P_{BESS}), (c) Full-Bridge based PPC output current reference (i_{L}^*) and Full-Bridge based PPC output current measurements (i_{L1}) and (d) battery bank voltage (v_{in}).

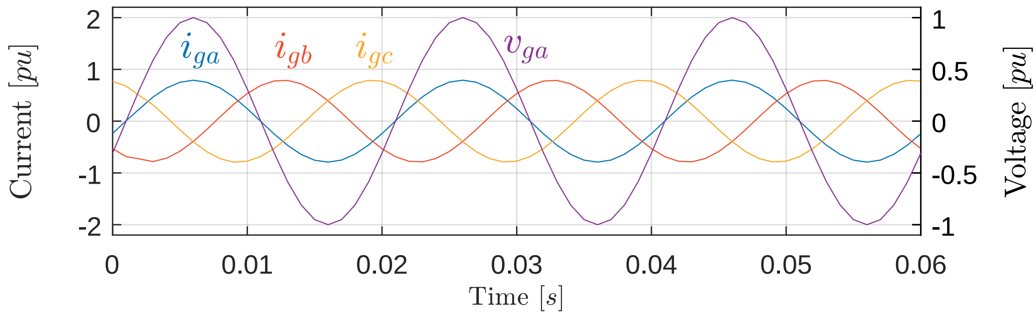

Figure 7.12: Simulation of Peak Shaving with the ESS connection at the PV side: grid currents (i_{ga}, i_{gb} and i_{gc}) and phase a grid voltage (v_{ga}).

7.4 Power Clipping: ESS connection at PV side

This section presents a PV/ESS configuration operating under a power clipping scenario. The idea is to retrofit an existing PV system (PV array and a 2LVSI), adding an ESS formed of a battery bank and a dc-dc power converter (IBBC). Both systems (PV and ESS) are merged at the dc-link of the 2LVSI. This configuration allows storage of the power beyond clipping level (PV inverter rating) and releasing it. This action is performed according to the system requirements and limitations. The PV/ESS configuration and control strategy were previously introduced in section 6.4. The parameters of the PV/ESS configuration and PI controllers, implemented in this simulation, were previously presented in chapter 6 (section 6.4).

The base values applied to transform these simulation results into the per unit system ([pu]) are shown in table 7.3.

Note that the operational range of the ESS is limited by its State of Charge (SoC). This operational range considers a minimum SoC of 20% (120 [V]) and a maximum SoC of 80% (200 [V]).

Figure 7.13 presents the simulation results of the proposed PV/ESS configuration operating under power clipping conditions. The respective case numbers from the control strategy introduced in section 6.4 (Fig. 6.17) were added to the explanation of the simulation results in order to simplify their understanding. From 0 to 0.5 [s] (Case I) the PV array is operates at a power level below clipping level ($P_{\text{clip}} = 735$ [kW]) and the inverter output power is lower than the pre clipping power level ($P_{\text{pre}} = 700$ [kW]), while the SoC of the battery bank equals 20%, hence the ESS power reference (P^*_{ess}) is set to zero. From 0.5 to 1.3 [s] (Case II) a step-up in solar irradiance causes the PV array power (P_{pv}) to surpass P_{clip}, since SoC <80%, P^*_{ess} is set to $P_{\text{pre}} - P_{\text{mpp}}$ (and $i^*_{\text{ess}} = P^*_{\text{ess}}/v_{\text{dc}}$), reducing the power flowing through the inverter (P_{inv}) thus enabling the performance of MPPT. From 1.3 to 1.8 [s] (Case III) a step-down in solar irradiance makes P_{pv} lower than P_{clip} however, since $P_{\text{pre}} < P_{\text{pv}} < P_{\text{clip}}$, thus the ESS power reference (P^*_{ess}) is set to

Parameter	Symbol	Value
Power	P_{base}	$735[kW]$
AC voltage	$V_{\text{ac base}} = 440 \cdot \sqrt{2/3}$	$360[V]$
AC current	$I_{\text{ac base}} = P_{\text{base}} \cdot 2/(3 \cdot V_{\text{ac base}})$	$1.36[kA]$
DC-link voltage	$V_{\text{dc base}} = 2 \cdot V_{\text{ac base}}$	$720[V]$

Table 7.3: Power Clipping in a PV/ESS configuration with ESS connection at PV side: Base values applied in the per unit system.

zero. From 1.8 to 2.07 [s] (Case II) a second step-up in irradiance causes the PV array power to surpass P_{clip}, the system behaves exactly as it did from 0.5 to 1.3 [s]. Once the ESS reaches 80% of the SoC the ESS stops drawing power and the inverter losses momentarily the capability to track the MPP (Case IV, from 2.07 to 2.3 [s]). From 2.3 to 3.5 [s] (Case V) a step-down in solar irradiance causes the PV power to be lower than pre clipping level ($P_{\text{pv}} < P_{\text{pre}} < P_{\text{clip}}$). Additionally, the battery bank SoC is greater than 20%, thus the control strategy generates a positive ESS power reference ($P^*_{\text{ess}} = P_{\text{pre}} - P_{\text{mpp}} > 0$), which is reflected on the releases of power from the ESS towards the dc-link and through the inverter into the grid. From 3.5 to 4.0 [s] the ESS already reached the 20% of the SoC, hence power flow from ESS towards the dc-link was stopped and the system went back to operating in Case I. Note that the ESS was undersized, to show the behaviour of the system when reaching its maximum and minimum permitted SoC.

Figure 7.14 shows the grid currents (i_{ga}, i_{gb} and i_{gc}) and phase a voltage (v_{ga}) of the simulation of power clipping with the ESS connection at the PV side. Note that the unitary power factor is reflected in the phase delay ($0\ [rad]$) between the phase a grid voltage (v_{ga}) and current (i_{ga}).

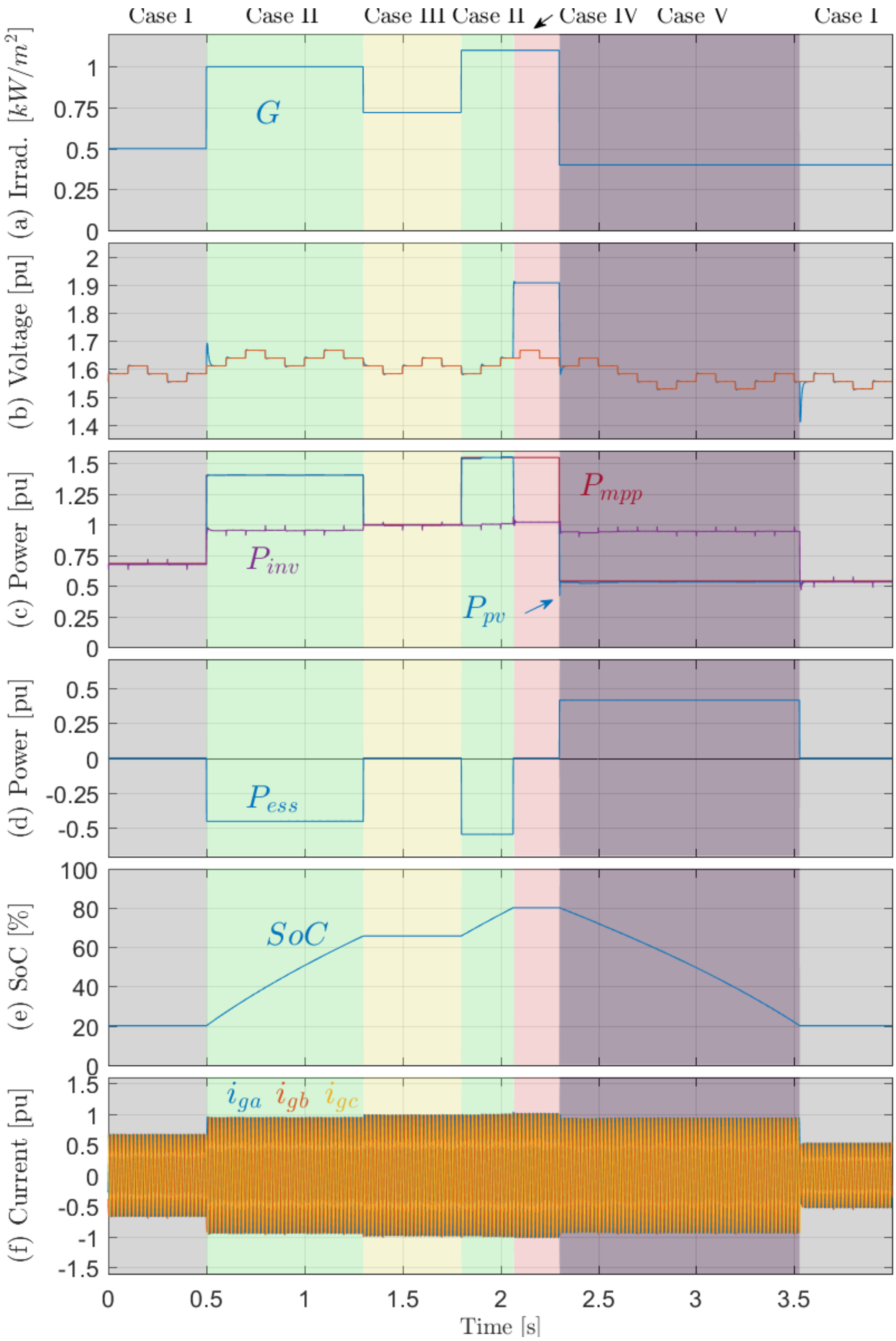

Figure 7.13: Simulation of Power Clipping with the ESS connection at the PV side: a) Irradiance in kW/m^2, b) DC-link voltage and reference, c) Generated PV power (P_{pv}), available PV power without considering clipping limitation (P_{mpp} (available PV power)) and inverter power (P_{inv} (inverter)), d) ESS power (P_{ess}), e) ESS SoC (SoC) and f) grid currents (i_{ga}, i_{gb} and i_{gc}).

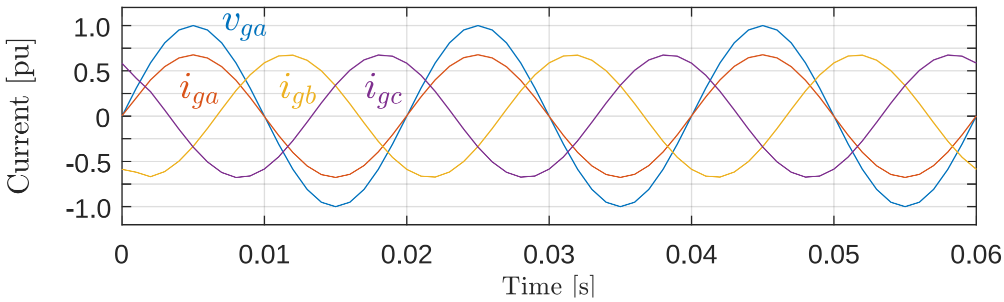

Figure 7.14: Simulation of Power Clipping with ESS connection at PV side: Grid currents (i_{ga}, i_{gb} and i_{gc}) and phase a voltage (v_{ga}).

7.5 Current reference: ESS connection at PV side

This section presents the simulation results of a PV/ESS configuration that will be compared with the experimental results presented in Chapter 8. The PV system is composed of a PV array connected to the grid through a single 2LVSI. The ESS corresponds to an SC bank connected to the dc-link of the 2LVSI through eight interleaved PPCs. These PPCs correspond to the topology with the inductor in the partial side, introduced in section 5.5 (Chapter 5). The PV system and ESS are connected at the PV side (dc-link of the 2LVSI), as previously shown in Chapter 6 (section 6.5). The parameter of the PV/ESS configuration and control scheme were presented in chapter 6 (section 6.5). Note that this simulation is not based on a particular complementary service, but instead analyses the common part of the control strategies, i.e. VOC and ESS current loop. Thus, providing a general validation of the strategies that allow to perform a complementary service.

The base values applied to transform these simulation results into the per unit system ([pu]) are shown in table 7.4. Note that the per unit values associated with the ESS voltage and current are based on the power rating of a single dc-dc converter.

In order to test the PV/ESS configuration and control scheme three different operation modes were applied, while keeping solar irradiance and temperature constant at 800 [W/m^2] and 25 [$^\circ C$]. The first mode consists of the operation of the PV system without power being drawn (or injected) by the ESS. This action takes place from 0 to 0.5[s], from 1.2 to 2.1 and from 2.8 to 3.2[s]. The characteristic waveforms associated with a 2LVSI performing P&O MPPT can be seen, in Fig 7.15, during these periods.

The second operation mode (bucking mode) takes place between 0.5 and 1.2[s]. This can be seen in Figs. 7.15 and 7.16. The operation in bucking mode is caused by a positive bypass current

Parameter	Symbol	Value
Power	P_{base}	$735[kW]$
AC voltage	$V_{\text{ac base}} = 440 \cdot \sqrt{2/3}$	$360[V]$
AC current	$I_{\text{ac base}} = P_{\text{base}} \cdot 2/(3 \cdot V_{\text{ac base}})$	$1.36[kA]$
DC-DC power	$P_{\text{dcdc base}}$	$50[kW]$
DC-DC voltage	$V_{\text{dcdc base}} = 2 \cdot V_{\text{ac base}}$	$720[V]$
DC-DC current	$I_{\text{dcdc base}} = P_{\text{dcdc base}}/V_{\text{dcdc base}}$	$69.44[A]$

Table 7.4: PV/ESS configuration with the ESS connection at the PV side: Base values applied in the per unit system.

reference (i^*_{bp}). During bucking mode operation, power is drawn from the dc-link and injected into the ESS (increasing the SC bank voltage). This causes a decrease of the power being injected into the grid (P_{ac}), despite the PV power remaining constant. This is also reflected in the decrease of the d-axis grid current (i_{gd}) and grid current amplitudes (i_{ga}, i_{gb} and i_{gc}). The bucking mode operation is ended when the bypass current reference (i^*_{bp}) returns to 0 [A] (at 1.2[s]).

The third operation mode corresponds to boosting mode, here the power flows from the ESS into the dc-link (causing a decrease of the SC bank voltage). This operation mode can be seen in Figs. 7.15 and 7.16 from 2.1 to 2.8 [s]. This operation mode is cased by a negative bypass current reference (i^*_{bp}) and is reflected in the negative values of P_{ess}. During boosting mode operation the power injected to the grid (P_{ac}) is increased, thus, increasing the d-axis grid current (i_{gd}) and grid current amplitudes (i_{ga}, i_{gb} and i_{gc}). The boosting mode operation is ended at 2.8[s] when the bypass current reference returns to zero.

The simulation results showing the operation of the PV/ESS configuration under the the aforementioned conditions are presented in Figs. 7.15 to 7.17. Figure 7.15 shows the signals associated with the control of the PV system. Graph (a) shows the PV array output power (P_{pv}) and the 2LVSI output power (P_{ac}). Graph (b) shows the dc-link voltage (v_{dc}) and its reference (v^*_{dc}). Graph (c) presents the control of the direct (i_{gd}) and quadrature (i_{gq}) grid currents. The resulting grid currents, in stationary reference frame (i_{ga}, i_{gb} and i_{gc}), are displayed in graph (d). Figure 7.16 shows the simulation results associated with the ESS. Graph (a) shows the power injected (positive) or drawn (negative) by a single PPC into the ESS (P_{ESS}). The PPC's bypass current reference of the Full-Bridge based PPC (i^*_{bp}) and the inductor current of one of the PPCs (i_{bp1}) are shown in graph (b). Graph (c) presents the current injected (¿ 0) or drawn (¡ 0) to the SC bank by a single PPC. Graph (d) presents the voltage of the SC bank (v_{sc}).

Note that during the simulation the 2LVSI was able to keep tracking of the MPP, despite power being injected or drawn from the dc-link. Additionally, note that the operation in bucking and boosting mode is not symmetrical. This is due to the reconfiguration of the PPC to operate in bucking or boosting mode.

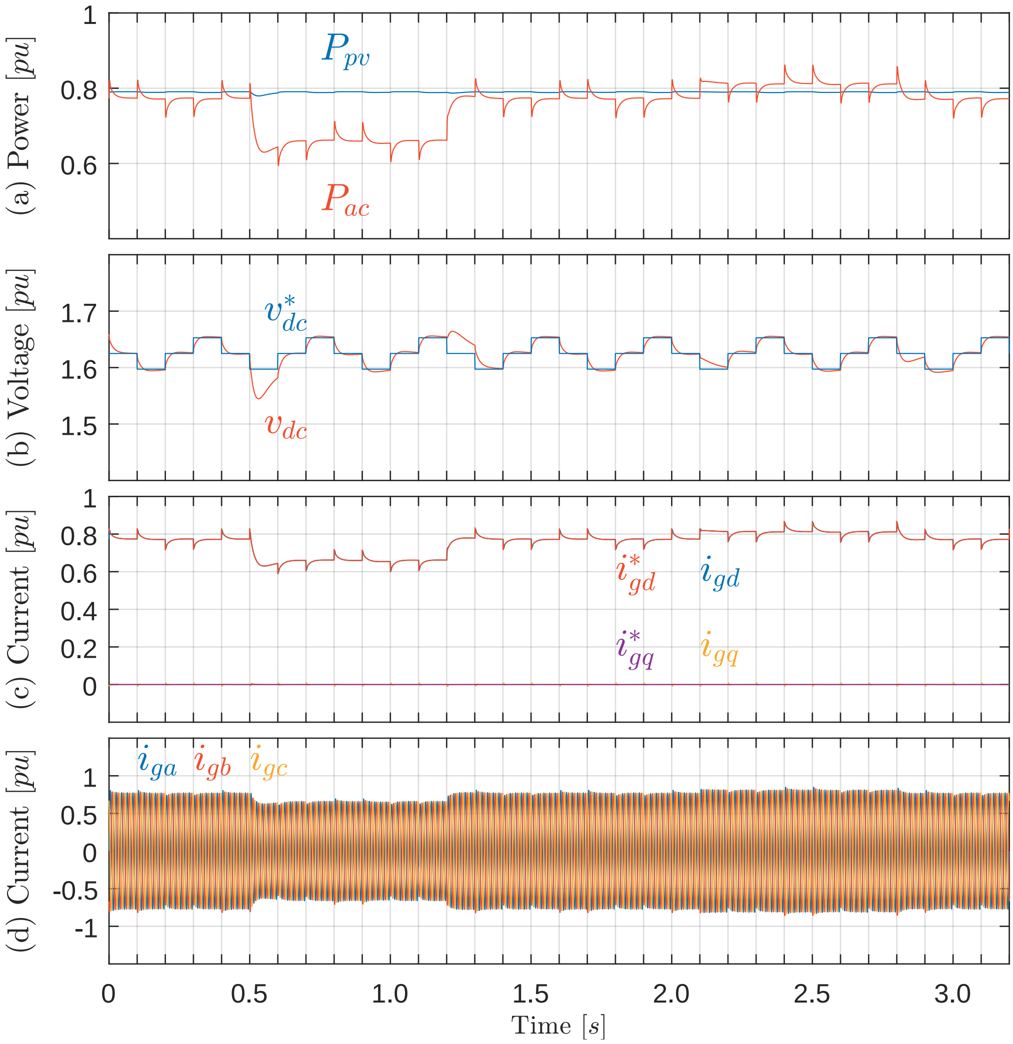

Figure 7.15: Simulation of a PV/ESS configuration with the ESS connection at the PV side, PV array and PV inverter (PV-2LVSI): (a) PV array output power (P_{pv}) and inverter output power (P_{ac}), (b) dc-link voltage (v_{dc}) and its reference (v^*_{dc}), (c) direct axis grid current reference (i^*_{gd}), direct axis grid current measurement (i_{gd}), quadrature axis grid current reference (i^*_{gq}) and quadrature axis grid current measurement (i_{gq}) and (d) grid currents in stationary reference frame (i_{ga}, i_{gb} and i_{gc}).

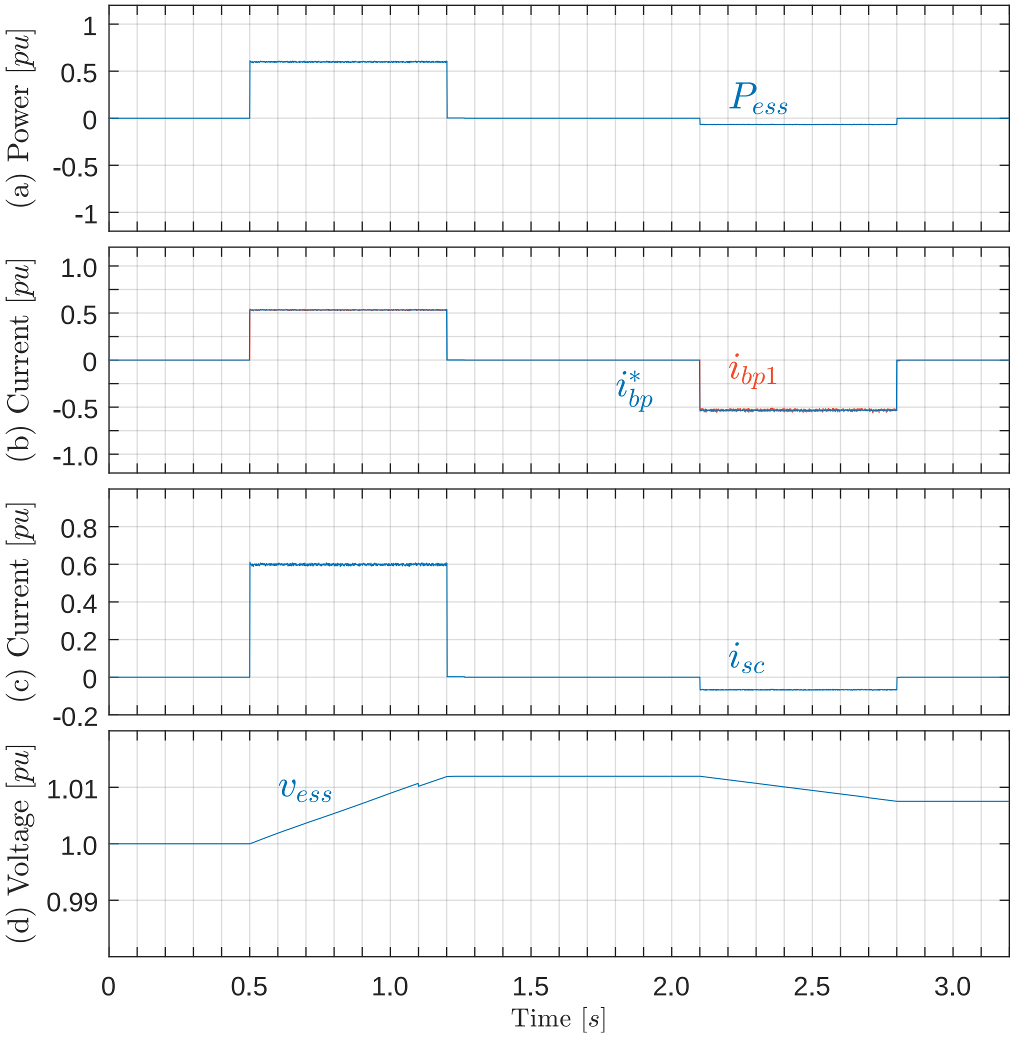

Figure 7.16: Simulation of a PV/ESS configuration with the ESS connection at the PV side, dc-dc converter (PPC) and SC bank: (a) single PPC power at ESS side (P_{ESS}), (b) PPC bypass current reference (i^{*}_{bp}) and single PPC bypass current measurements (i_{bp1}) and (c) SC bank current (i_{sc}) and (d) SC bank voltage (v_{ess}).

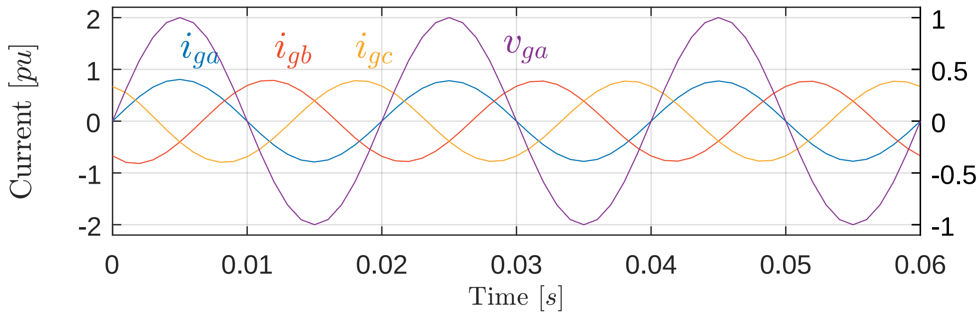

Figure 7.17: Simulation of a PV/ESS configuration with the ESS connection at the PV side: grid currents (i_{ga}, i_{gb} and i_{gc}) and phase a grid voltage (v_{ga}).

7.6 Summary

This chapter presents four simulations associated with three different complementary services. Note that the P&O time step was reduced to $0.1[s]$, instead of the industrial practice ($\approx 5[s]$), due to the computational limitations associated with the maximum step size of the simulations ($T_\mathrm{s} = (1/50[kHz])/100$). Moreover the same PV array was considered in all of the simulations except in the Power Clipping scenario, where the number of strings was increased by 40%. The design of the 2LVSI, VOC scheme and PI controller design for all the simulations was the same.

The first two simulations show two different PV/ESS configurations performing maximum power RR regulation under a Global MPPT scenario. In the first simulation the ESS was merged to the PV system at the AC-grid side. In the second simulation the connection between ESS and PV system was performed at the PV side. In both cases the ESS/PV configuration is capable of limiting the output power variation and remaining within power RR regulation ($< 10\% \cdot P_{\mathrm{pv\ mpp}}$). Additionally, in both cases the 2LVSI continues tracking the MPP during P&O mode, despite part of the PV power being injected to the SC-bank (charging). Note that the ESS/PV configuration with the ESS connected at the PV side presents higher power variation than the ESS connected at the AC side. However, the ESS/PV configuration with the ESS connected at the PV side requires one power converter fewer, thus eliminating the energy losses associated with the ESS inverter (increasing the overall efficiency of the ESS, while eliminating the necessity to acquire an additional inverter). On the other hand, the PV/ESS configuration with the AC-grid-side connection can be beneficial in larger scale PV plants, where several central inverters are connected at the AC side. Here, the Global MPPT can be performed one central inverter at a time (sequentially), thus minimising the output power PV variation, reducing the ESS size and cost. Note, that this strategy will require charging of the ESS between Global MPPTs.

The third simulation shows a PV/ESS configuration performing peak shaving, the ESS and PV system are connected at the PV side. This simulation was performed keeping the irradiance and temperature constant, thus keeping the MPP constant. This is reflected in the tracking of the MPP, where the dc-link voltage is kept around the MPP despite part of the PV power being injected to/from the BESS. Note that this strategy relies on an external power reference provided by the GO. This same strategy could also be applied to other complementary services as frequency regulation. A simplification of this strategy was experimentally implemented and is presented in the following chapter.

The fourth simulation presents a PV/ESS configuration performing power clipping. In this simulation the ESS is merged to the PV system at the PV side. Note that in power clipping the power limitation is imposed by the rating of the 2LVSI instead of the PV array power rating, thus, the only alternative for recovering this loss of generation is to connect the ESS at the PV side. The results show that the proposed configuration keeps the tracking of the MPP despite the ESS power flowing from/towards the dc-link, thus allowing deceiving of the P&O MPPT strategy and enabling retrofitting of existing PV plants without further intervention than connecting the ESS to the dc-link of the PV inverter. Moreover, the storing capability offers an alternative to performing other complementary services when injecting the stored energy into the grid.

The fifth simulation presented a PV/ESS configuration based on a PPC with the inductor in the partial side. This simulation was performed keeping the irradiance and temperature constant. The results show that the PV systems is capable of tracking the MPP, despite of power being injected or drawn from the dc-link. The PPC shows a good tracking of the current reference. However, the reconfiguration of the PPC, to operate in bucking or boosting mode, generates an asymmetric operation.

Chapter 8

Experimental results

8.1 Introduction

This chapter presents the experimental results of a PV/ESS configuration with the connection of an ESS at the PV side (dc-link). The bidirectional dc-dc power converter, presented in section 5.5 was considered for this purpose. Due to hardware availability and time constraints, the PV/ESS configuration was partially tested. The PV system (PV emulator and 2LVSI connected to the grid) was fully implemented, however, the PPC that was built was not reconfigurable. This limited the operation of the PPC to unidirectional power flow. Thus, the power flow between the dc-link and the SC bank was tested only in bucking mode operation (storing energy in the SC bank).

The chapter is composed of two main sections. The first section presents the PPC in standalone operation under steady state and dynamic tests. This section includes a description of the set-up implemented to test the PPC, the control scheme implemented over the PPC and the design of the PI controller that regulates the PPC. The second section shows the operation of the PV/ESS configuration in bucking mode operation (storing energy in the SC bank) under dynamic tests. This section corresponds to the experimental validation of the PV/ESS configuration, control strategy and simulation presented in Chapter 5 (section 6.5) and Chapter 7 (7.5). This section includes a description on the PV/ESS configuration's set-up and the control schemes of the PV system and ESS.

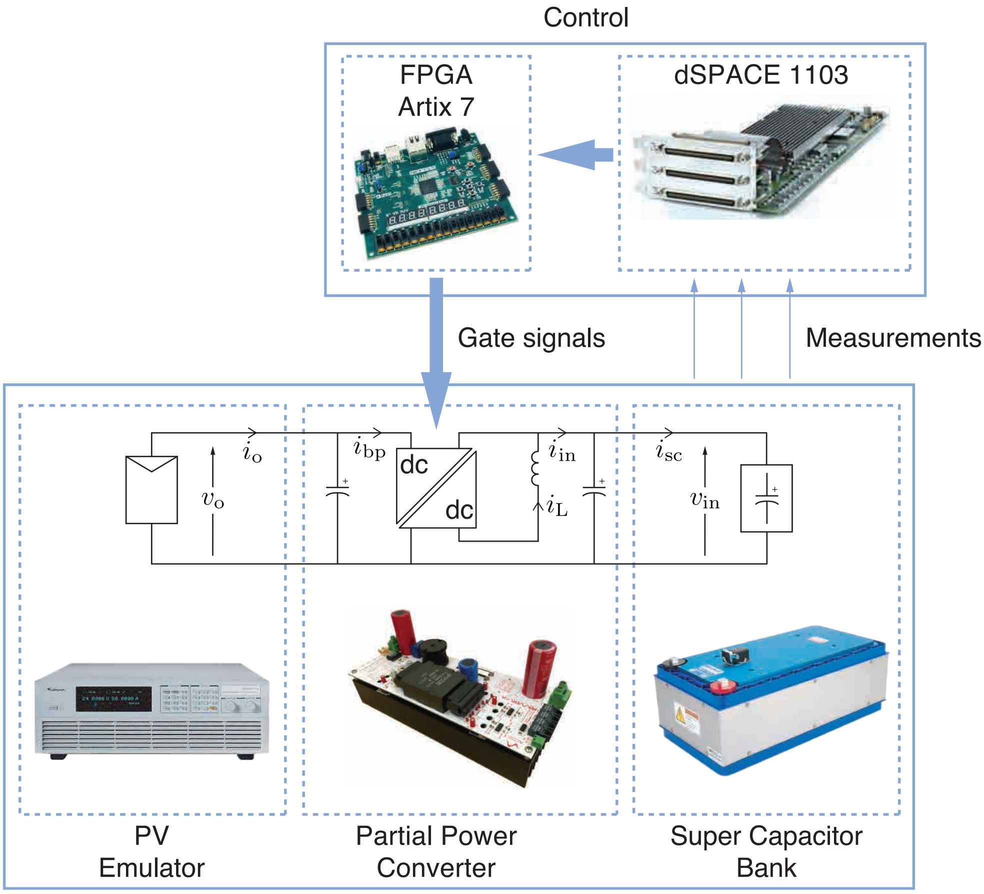

Figure 8.1: Full bridge based PPC topology with inductor in the partial side: configuration of the experimental setup.

8.2 PPC with inductor at partial side: Standalone Operation

8.2.1 Configuration description

The configuration implemented to validate the operation of the PPC in standalone operation consists of a PV emulator, operating as a dc voltage source and an SC bank acting as load. Figure 8.1 shows a simplified diagram of the configuration. The parameters of the standalone set-up are presented in Table 8.1. The base values applied to calculate the per unit equivalent of the parameters presented in Table 8.3 are: $P_{\text{base}} = 450$[W], $v_{\text{dc base}} = 60$[V], $i_{\text{dc base}} = 7.5$[A], $\omega_{\text{dc base}} = 50$[Hz], $R_{\text{dc base}} = 8[\Omega]$, $L_{\text{dc base}} = 25.5[H]$ and , $C_{\text{dc base}} = 0.398[mF]$. These values were calculated applying the definition from [135].

SC bank and PPC			
dc-link voltage	v_{dc}	100-150 [V]	0.83-1.25 [pu]
SC bank capacitance	C_{sc}	94 [F]	-
SC bank maximum voltage	$\hat{v}_{sc}$	75 [V]	0.625 [pu]
SC maximum current	$\hat{i}_{sc}$	5 [A]	1.33 [pu]
PPC inductance	L	2.2 [mH]	0.0864 [pu]
PPC transformer ratio	$n_1 : n_2$	1:8	-
PPC switching frequency	f_{ppc}	50 [kHz]	-

Table 8.1: Full bridge based PPC with inductor at partial side: configuration parameters of the experimental setup.

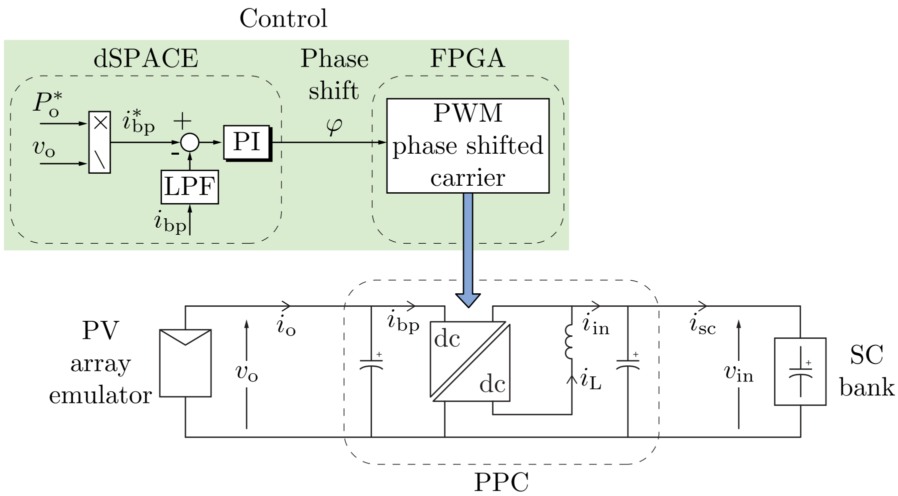

Figure 8.2: PPC with the inductor in the partial side, standalone configuration: Control diagram.

8.2.2 Controller

Figure 8.2 presents the control strategy applied to control the power flow from the dc source (PV emulator) towards the load (SC bank). Note that the low pass filter (LPF) applied over i_{bp} allows control of the mean value of i_{bp}, instead of trying to control its chopped waveform (see Fig. 5.10 in section 5.5.3).

Table 8.2 shows the criteria applied to design the partial side inductor - PPC's current loop controller, the PPC's plant and the gains of the PI controller that were implemented in the experimental tests. Note that the PPC's plant model was presented in chapter 5. Figure 8.3 shows the bode plots, root locus and step response of this controller design.

Converter (loop)	Design details	Plant ($G_o(s)$)	PI controller Continuous-time ($C(s)$)	PI controller Discrete-time ($C[k]$)
PPC PSL (Current)	$T_s = 20[\mu s]$ $f_{bw} = 10[kHz]$ $\xi = 1/\sqrt{2}$	$\frac{2\cdot(v_{oQ}-v_{inQ})}{s\cdot L+R_L}\cdot\left(\frac{n_2}{n_1}\right)^2$	$\frac{0.01142\cdot s+246.4}{s}$	$\frac{0.01388\cdot z-0.008952}{z-1}$

Table 8.2: PI controllers design for the PPC with the inductor in the partial side (PSL): bucking mode operation.

8.2.3 Experimental results

Steady State Operation

The configuration was tested operating at 375 [W] (flowing from the PV emulator towards the SC bank). Figure 8.4 shows the PV emulator voltage (v_o), SC bank voltage (v_{in}), current from the PV emulator (i_o) and current through the SC bank (i_{sc}). Note that the slight increment on v_{in}, caused by the constant current injection, is not appreciable due to the time scale of the figure.

Dynamic Tests

Two dynamic tests were performed to validate the operation of the PPC in standalone operation.

Step down

The first test consisted of a step down in P_o^* ($= i_o \cdot v_o$) from 450 to 150 [W] at time $t = 0$ [s]. Due to the control scheme this step down in power reference is reflected in a step down in the bypass current reference (i_{bp}^*). Figure 8.5 shows the PV emulator voltage (v_o), SC bank voltage (v_{in}), current from the PV emulator (i_o) and current through the SC bank (i_{sc}) waveforms obtained from the scope. The step down in power reference is reflected in a step down in both currents (i_o and i_{sc}).

Figure 8.6 shows the measurements obtained from the dSPACE platform, where the step down in P_o^*, causes the step down in i_{bp}^* and consequently the decrease of i_{sc} ($\approx i_L + i_{bp}$). Note that the PV emulator voltage (v_o) remains constant, while the voltage over the SC bank (v_{in}) experiences a decrease in its charging rate (not visible due to the time frame).

Note that the configuration is capable of reaching its new reference value within 1 [μs].

Step up

The second test consisted of applying a step up in power reference (P_o^*) from 150 to 450 [W] at time $t = 0$ [s]. This step is reflected in the currents from the PV emulator (i_o) and towards the

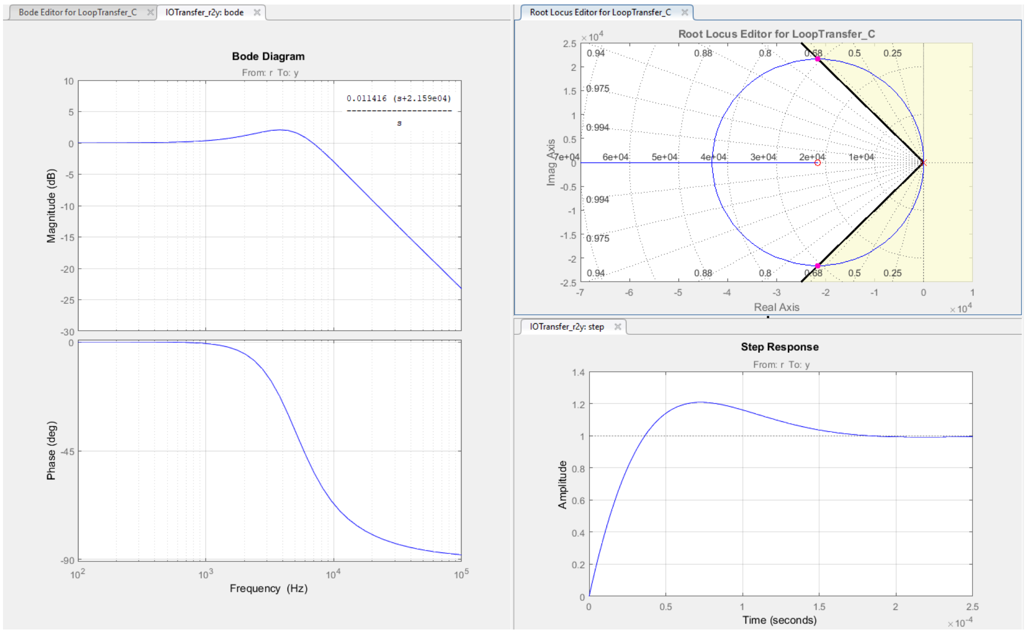

Figure 8.3: PPC input side inductor current loop controller: bandwidth = 10 [kHz], damping ratio $\xi = 1/\sqrt{2}$.

SC bank (i_{sc}), while the PV emulator voltage (v_{o}) remains constant. Due to the time frame, the increase in the charging slope of the voltage of the SC bank is not appreciable.

The measurements obtained from the control platform (dSPACE) are displayed in Fig. 8.8, where the step up in P_{o}^{*} causes the step up in i_{bp}^{*}. This causes the current towards the SC bank (i_{sc}) to increase in value. As shown in Fig. 8.7 the voltage of the PV emulator remains constant while the voltage on the SC bank experiences an increase in the charging rate (not visible due to the time frame).

Note that the configuration is capable of reaching its new reference value within 1 [μs].

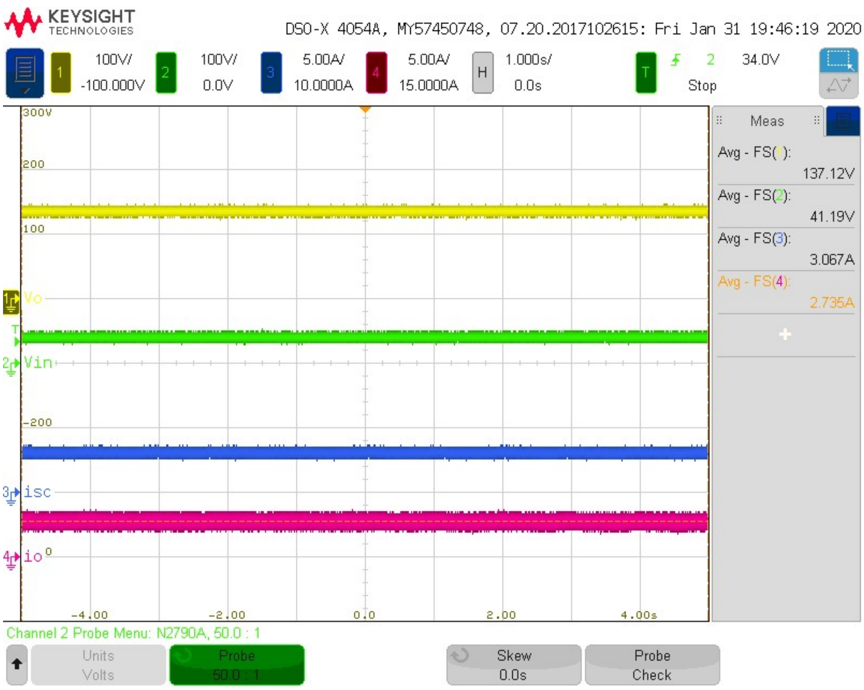

Figure 8.4: PPC with constant dc-link voltage (constant voltage source) and SC bank load, steady state operation: dc-link capacitor voltage (v_o), SC bank voltage (v_{in}), dc-link current towards PPC (i_o) and SC bank current (i_{sc}).

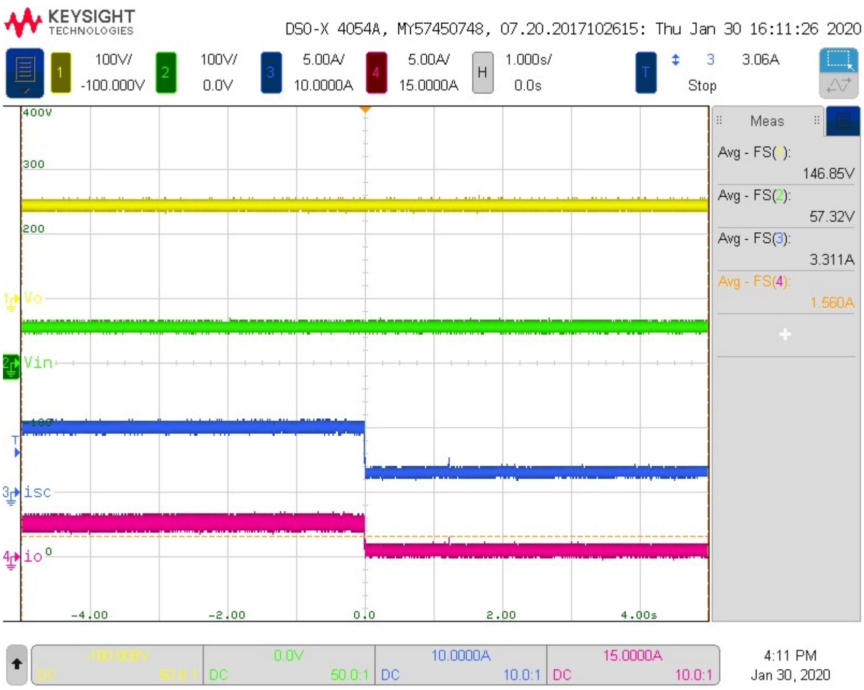

Figure 8.5: PPC with constant dc-link voltage (constant voltage source) and SC bank load, step down in SC bank power reference (P_{o}^{*} from 450 to 150 [W]): dc-link capacitor voltage (v_{o}), SC bank voltage (v_{in}), dc-link current towards PPC (i_{o}) and SC bank current (i_{sc}).

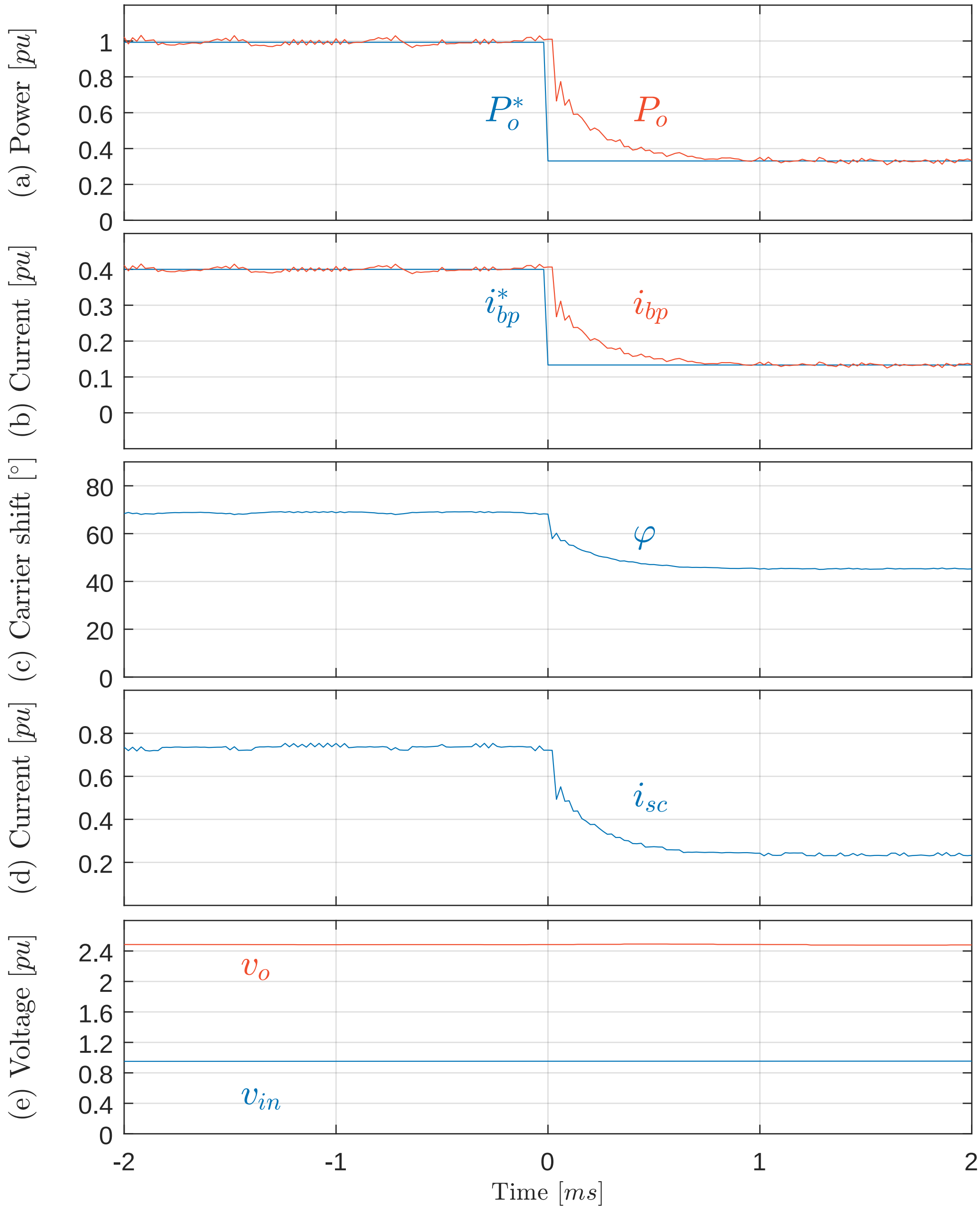

Figure 8.6: PPC with constant dc-link voltage (constant voltage source) and SC bank load, step down in SC bank power reference (P_o^* from 450 to 150 [W]): a) SC bank power and its reference (P_o and P_o^*), b) bypass current and its reference (i_bp and i_bp^*), c) carrier shift (φ), d) current towards the SC bank (i_sc) and e) dc-link voltage and SC bank voltage (v_o and v_in).

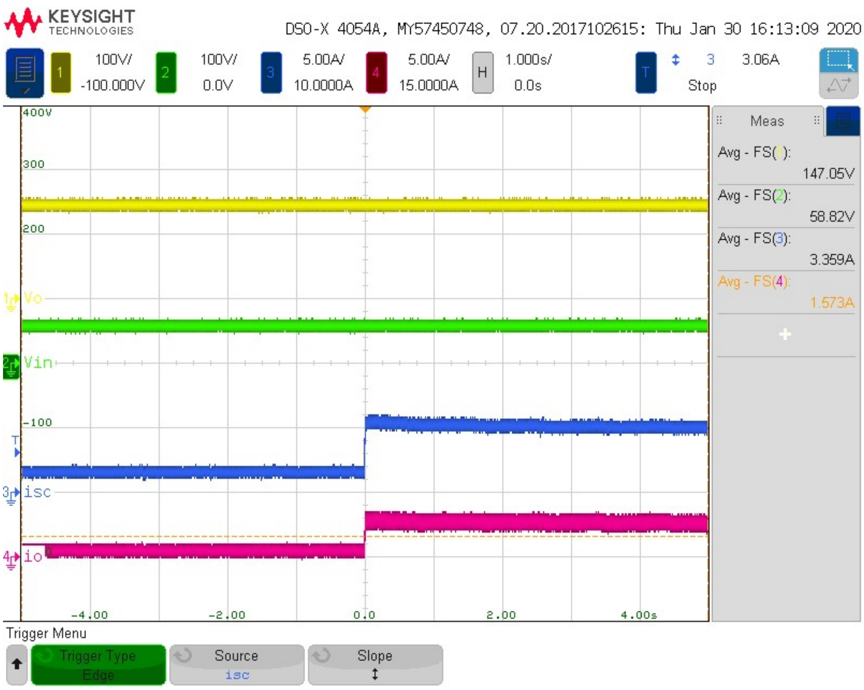

Figure 8.7: PPC with constant dc-link voltage (constant voltage source) and SC bank load, step up in SC bank power reference (P_o^* from 150 to 450 [W]): dc-link capacitor voltage (v_o), SC bank voltage (v_{in}), dc-link current towards PPC (i_o) and SC bank current (i_{sc}).

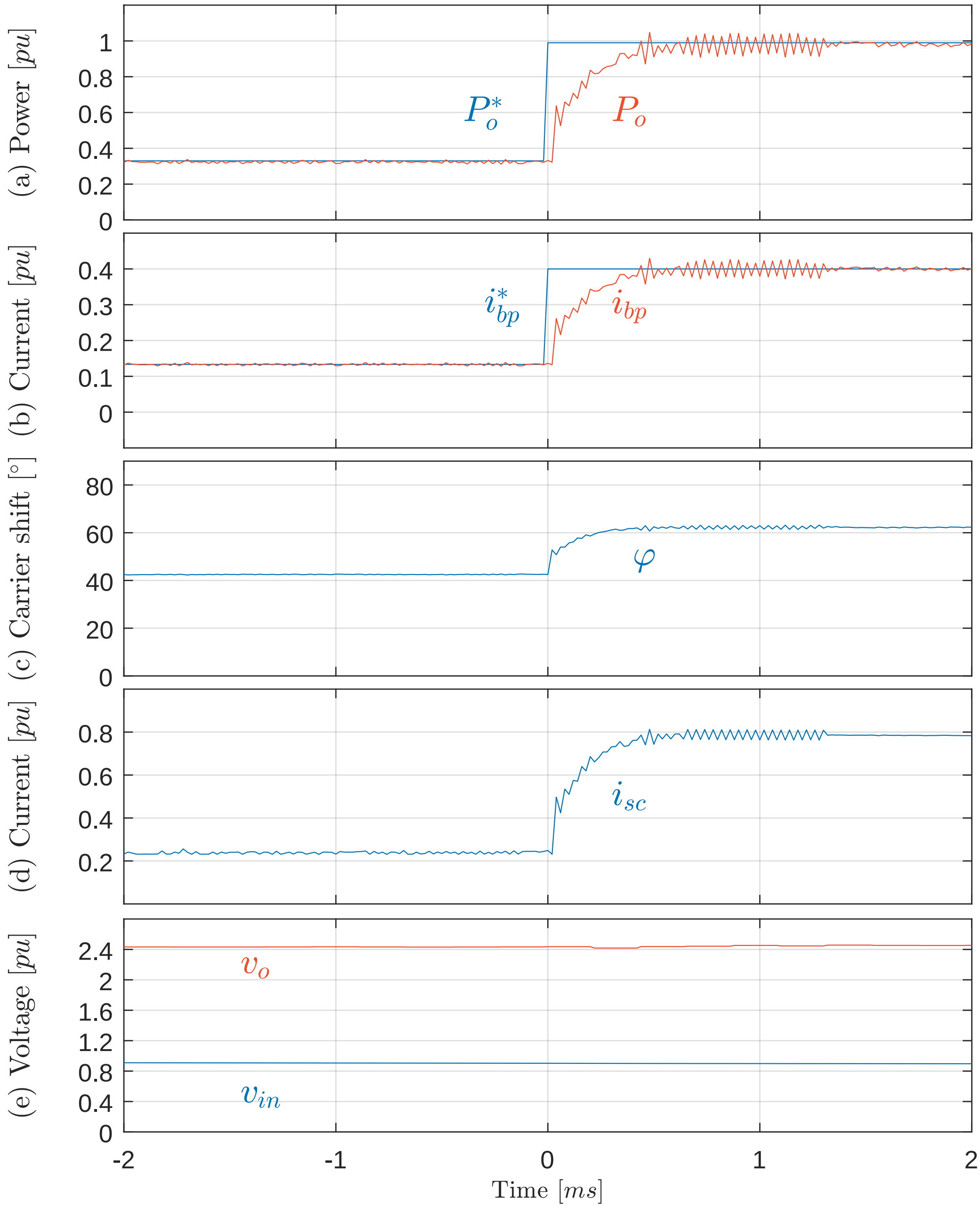

Figure 8.8: PPC with constant dc-link voltage (constant voltage source) and SC bank load, step up in SC bank power reference (P^*_{ESS} from 150 to 450 [W]): a) SC bank power and its reference (P_{ESS} and P^*_{ESS}), b) bypass current and its reference (i_{bp} and i^*_{bp}), c) carrier shift (φ), d) current towards the SC bank (i_{sc}) and e) dc-link voltage and SC bank voltage (v_{o} and v_{in}).

8.3 PV/ESS Configuration with PV side connection

This section presents the experimental validation of a PV/ESS Configuration with its connection at the PV side.

8.3.1 Configuration description

A simplified diagram of the implemented configuration, applied to validate the PV/ESS configuration with the connection at the PV side, is shown in Fig. 8.9. The configuration consists of a PV emulator connected to the grid through a standard 2LVSI, additionally a full bridge based PPC with inductor at the partial side is connected between the dc-link of the 2LVSI and the SC bank. Note that the full PV/ESS configuration was scaled down in order to match the parameters of the SC bank and PPC ratings. The parameters of the PV emulator and 2LVSI are presented in Table 8.3. The base values applied to calculate the per unit equivalent of the parameters presented in Table 8.3 are: $P_{\text{base}} = 450$[W], $v_{\text{dc base}} = 60$[V], $i_{\text{dc base}} = 7.5$[A], $v_{\text{ac base}} = 30$[V], $i_{\text{ac base}} = 10$[A], $Z_{\text{base}} = 3[\Omega]$, $f_{\text{base}} = 50$[Hz], $L_{\text{base}} = 9.5$[mH] and $C_{\text{base}} = 1.1$[mF].

Note that the parameters of the SC bank and PPC with the inductor in the partial side were presented in Table 8.1.

PV plant (Under STC)			
Maximum power point	P_{mpp}	450 [W]	1.0 [pu]
Maximum Power point voltage	$v_{\text{dc mpp}}$	120 [V]	2.0 [pu]
Maximum Power point current	$i_{\text{pv mpp}}$	3.75 [A]	0.5 [pu]
Open circuit voltage	$v_{\text{dc oc}}$	154.6 [V]	2.58 [pu]
Short circuit current	$i_{\text{pv sc}}$	5.1 [A]	0.68 [pu]
2LVSI & Grid			
PV-2LVSI dc-link capacitance	C_{dc}	1530 [μF]	1.44 [pu]
PV-2LVSI dc-link voltage	v_{dc}	90-130 [V]	1.5-2.17 [pu]
Grid maximum voltage	v_{gd}	30 [V]	1.0 [pu]
Grid filter inductance	L_{g}	10 [mH]	1.0472 [pu]
Grid filter resistance	R_{g}	0.1 [Ω]	0.0333 [pu]
Grid frequency	f_{g}	50 [Hz]	1.0 [pu]
Switching frequency	f_{2LVSI}	5 [kHz]	–

Table 8.3: PV/ESS configuration with PV side connection and full bridge based PPC with the inductor at partial side: configuration parameters of the experimental setup.

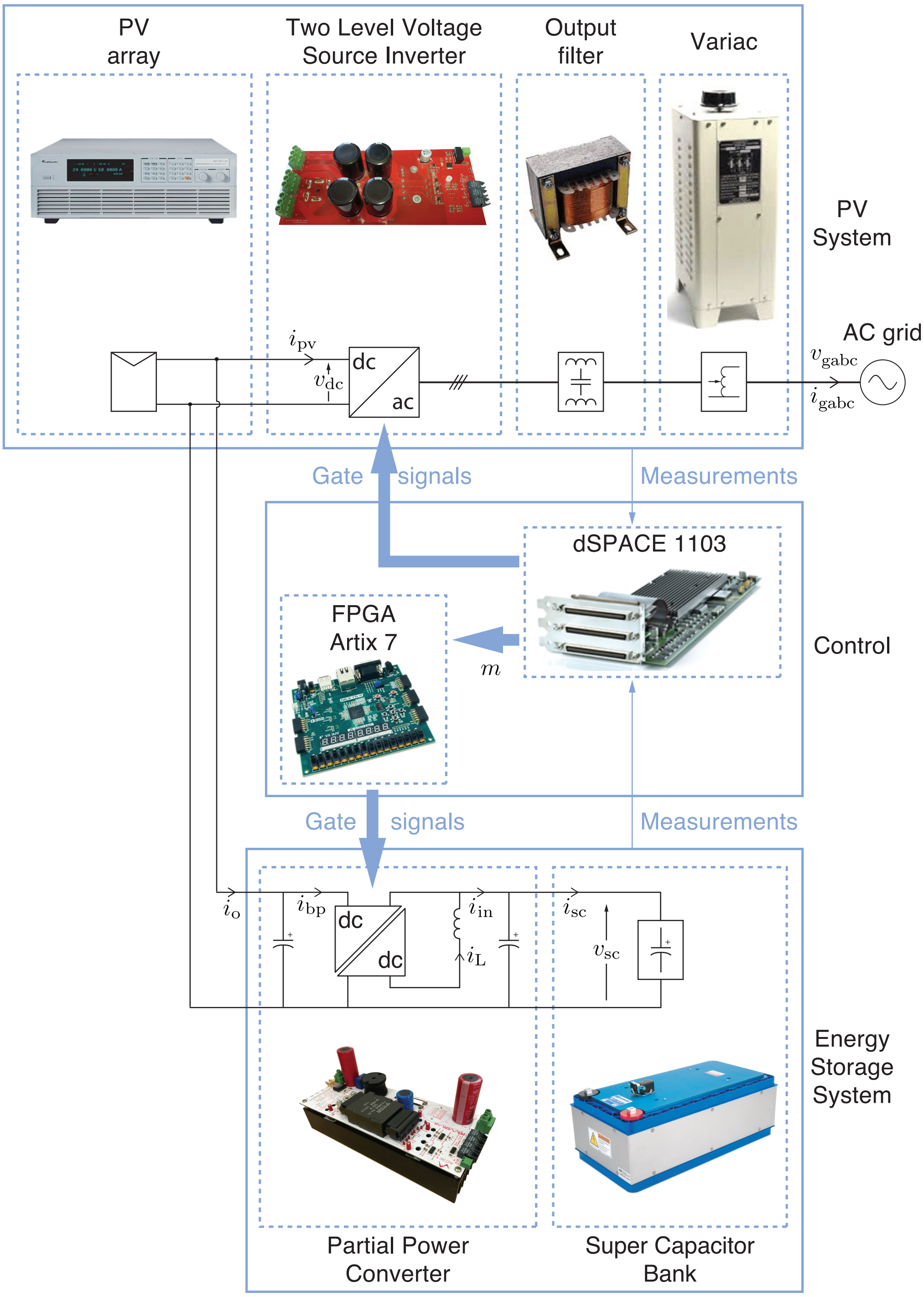

Figure 8.9: PV/ESS configuration with PV side connection and full bridge based PPC with inductor at partial side: configuration of the experimental setup.

Converter (loop)	Design details	Plant ($G_o(s)$)	PI controller Continuous-time ($C(s)$)	Discrete-time ($C[k]$)
2LVSI (Current)	$T_s = 0.2$[ms] $f_{bw} = 250$[Hz] $\xi = 1/\sqrt{2}$	$\dfrac{1}{L_g \cdot s + R_g}$	$\dfrac{10.79 \cdot s + 5825}{s}$	$\dfrac{11.38 \cdot z - 10.21}{z - 1}$
2LVSI (Voltage)	$T_s = 0.2$[ms] $f_{bw} = 10$[Hz] $\xi = 1.0$	$-\dfrac{3}{2} \cdot \dfrac{v_{gd}}{C_{dc} \cdot s}$	$\dfrac{0.001721 \cdot s + 0.021782}{s}$	$\dfrac{0.001723 \cdot z - 0.001719}{z - 1}$

Table 8.4: PI controllers design for the 2LVSI: current and voltage loops.

8.3.2 Controller

The control scheme of the full PV/ESS system is shown in Fig. 8.10, where two independent control loops controlling the 2LVSI and SC bank are illustrated. The first control scheme (2LVSI) consists of a standard VOC scheme (as the one shown in Fig. 6.2), which allows management of the dc-link voltage and injection of current to the grid, while tracking the MPP. The second control scheme controls the current flow towards the SC bank and corresponds to a single PI controller applied over the error between the bypass current of the PPC (i_{bp}) and its reference (i^*_{bp}).

The design parameters of the dc-link voltage and d- and q- axis current loop controllers of the 2LVSI are presented in Table 8.4. Figures 8.11 and 8.12 show the bode plots, root locus and step response of these controllers.

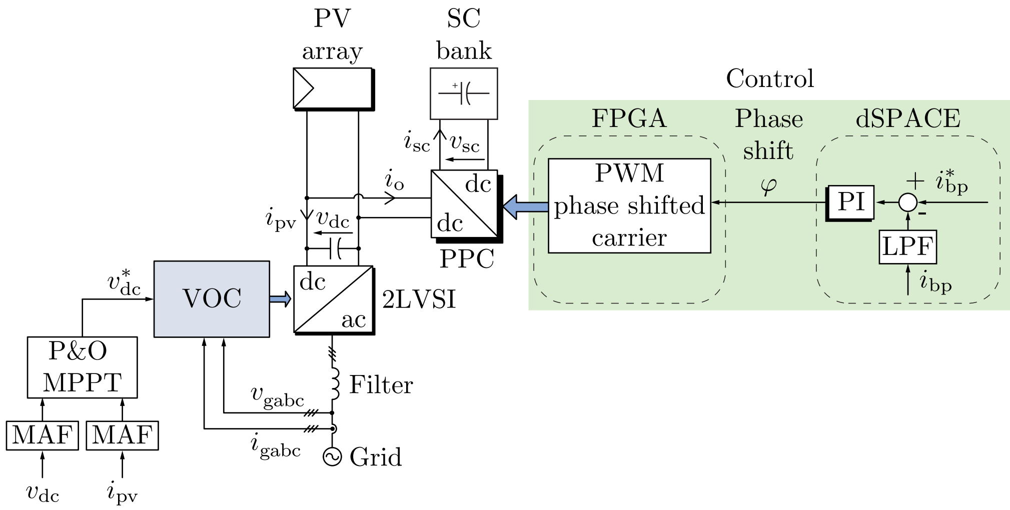

Figure 8.10: Control diagram PV/ESS configuration with PV side connection and full bridge based PPC with inductor at partial side.

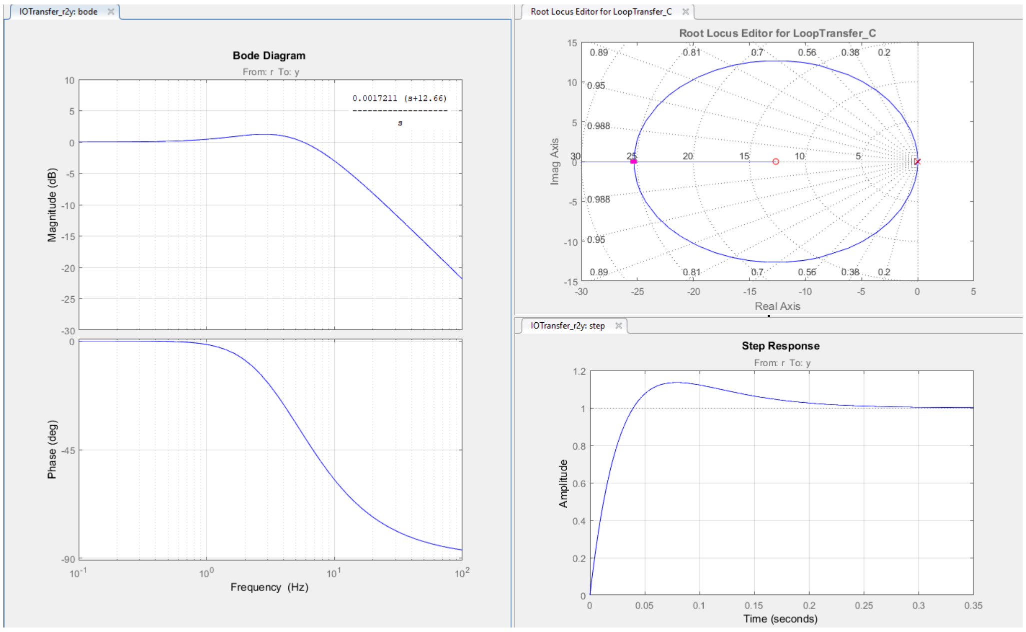

Figure 8.11: 2LVSI dc-link voltage loop controller: bandwidth = 10 [Hz], damping ratio $\xi = 1.0$.

8.3.3 Experimental results

Two dynamic tests were performed to validate the operation of the full PV/ESS configuration with PV side connection. The tests consist of keeping the PV array operating with constant irradiance and temperature conditions (for a predefined current versus voltage PV curve) and applying a step variation to the reference of the current being extracted from the dc-link towards the SC bank (i^*_{bp}).

Step up in bypass current

The first test consists of applying a step up in the bypass current reference (i^*_{bp}) from 0 to 2 [A] at time $t = 0$ [s], this step is reflected over the current towards the SC bank (i_{sc}). Since part of the current being generated by the PV emulator goes into the SC bank, a decrease in the current passing towards the 2LVSI (i_{pv}) is observed. On the other hand, the dc-link voltage remains performing the standard P&O stepped waveform. Due to the time frame, the increase in the charging slope of the voltage of the SC bank is not visible.

Figure 8.14 presents the measurements of the 2LVSI obtained from the control platform (dSPACE), where the step up in bypass current (i_{bp}) at t = 0 [s], generates a step down in current towards the 2LVSI (i_{pv}) and thus a reduction in the currents towards the grid. Additionally, the step up in i_{bp} causes a perturbation on the dc-link voltage (v_{dc}), which is compensated by the 2LVSI control scheme (VOC).

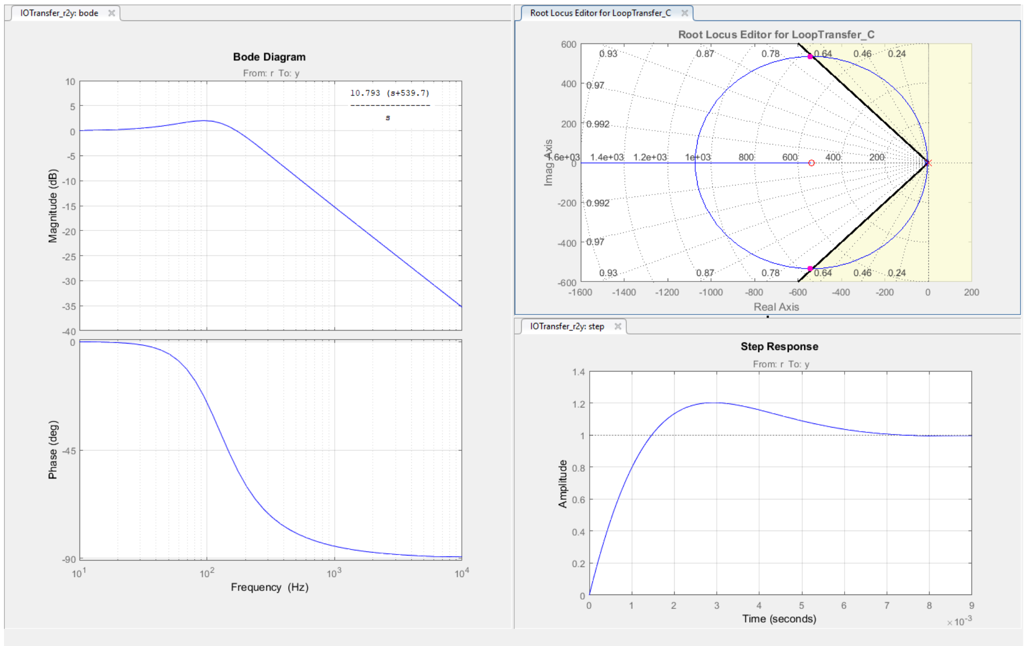

Figure 8.12: 2LVSI d-axis and q-axis current loop controller: bandwidth = 250 [Hz], damping ratio $\xi = 1/\sqrt{2}$.

The results associated with the PPC and the SC bank, obtained from the dSPACE platform, are presented in Fig. 8.15. Here, the step up in bypass current (i_{bp}) generates a step up of the power and current towards the SC bank (P_{sc} and i_{sc}). Additionally the injection of current (i_{sc}) towards the SC bank causes an increase of the voltage in the SC bank (v_{sc}).

Step down in bypass current

A step down in the bypass current reference (i^*_{bp}) from 2.0 to 0 [A] was applied at 0 [s]. Since the current towards the SC bank is extracted from the dc-link, the step down in i^*_{bp} causes an increase in i_{pv} as shown in Fig. 8.16. Note that the dc-link voltage keeps tracking the MPP, despite the step down in i_{bp}.

The measurements taken from the 2LVSI through the dSPACE platform are shown in Fig. 8.17, where the power towards the 2LVSI (P_{pv}) experiences an increase (caused by the decrease in power towards the SC bank), which is reflected in an increase in the direct axis grid current (i_{gd}) and consequently in the grid currents (i_{ga}, i_{bg} and i_{gc}). Additionally, the perturbation in the dc-link voltage (v_{dc}) at 0 [s] is caused by the step up in the current towards the 2LVSI (i_{pv}), which is regulated by the 2LVSI control scheme.

The results obtained from the PPC and the SC bank, through thee control platform (dSPACE),

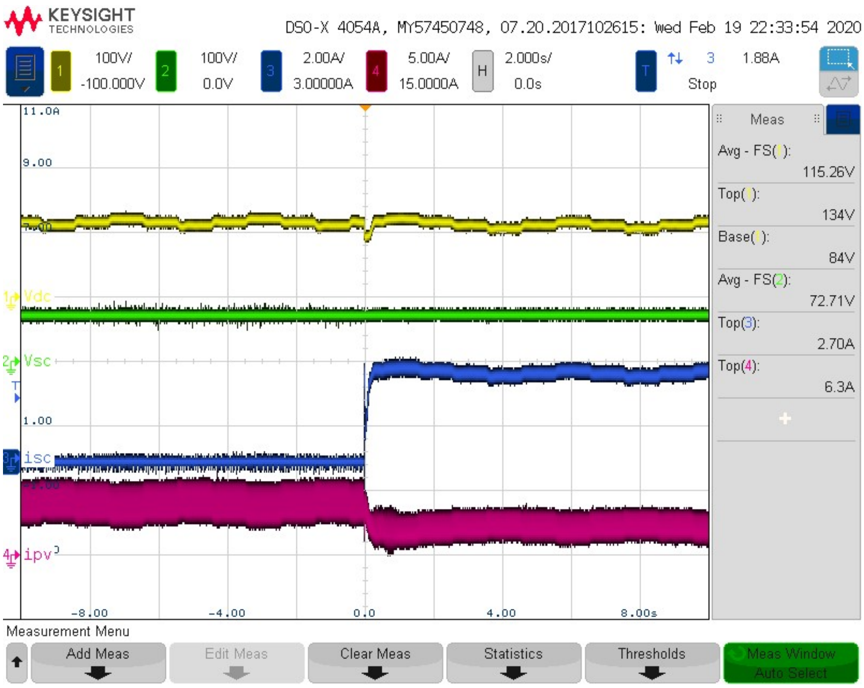

Figure 8.13: PV/ESS configuration with PV side connection and full bridge based PPC with inductor at the partial side, step up in bypass current reference reference (i^*_{bp}) from 0 to 2.0 [A] at 0 [s]: dc-link capacitor voltage (v_{dc}), SC bank voltage (v_{in}), SC bank current (i_{sc}) and current towards the 2LVSI (i_{pv}).

are shown in Fig. 8.18, where the step down in i_{bp} is reflected over the power and current towards the SC bank (P_{sc} and i_{sc}). Additionally, when i_{bp} reaches 0 [A], the charging of the SC bank is stopped. Note that the drop in v_{sc} voltage at 0 [s] shows the effect of the equivalent series resistance (ESR) of the SC bank.

The results show a good match between the simulation results presented in Chapter 7 (section 7.5 and the experimental results. It must be noted that the PV/ESS configuration that was simulated corresponds to an scaled-up version of the experimental setup, where the parameters where scaled applying the per unit values presented in Tables 8.1 and 8.3.

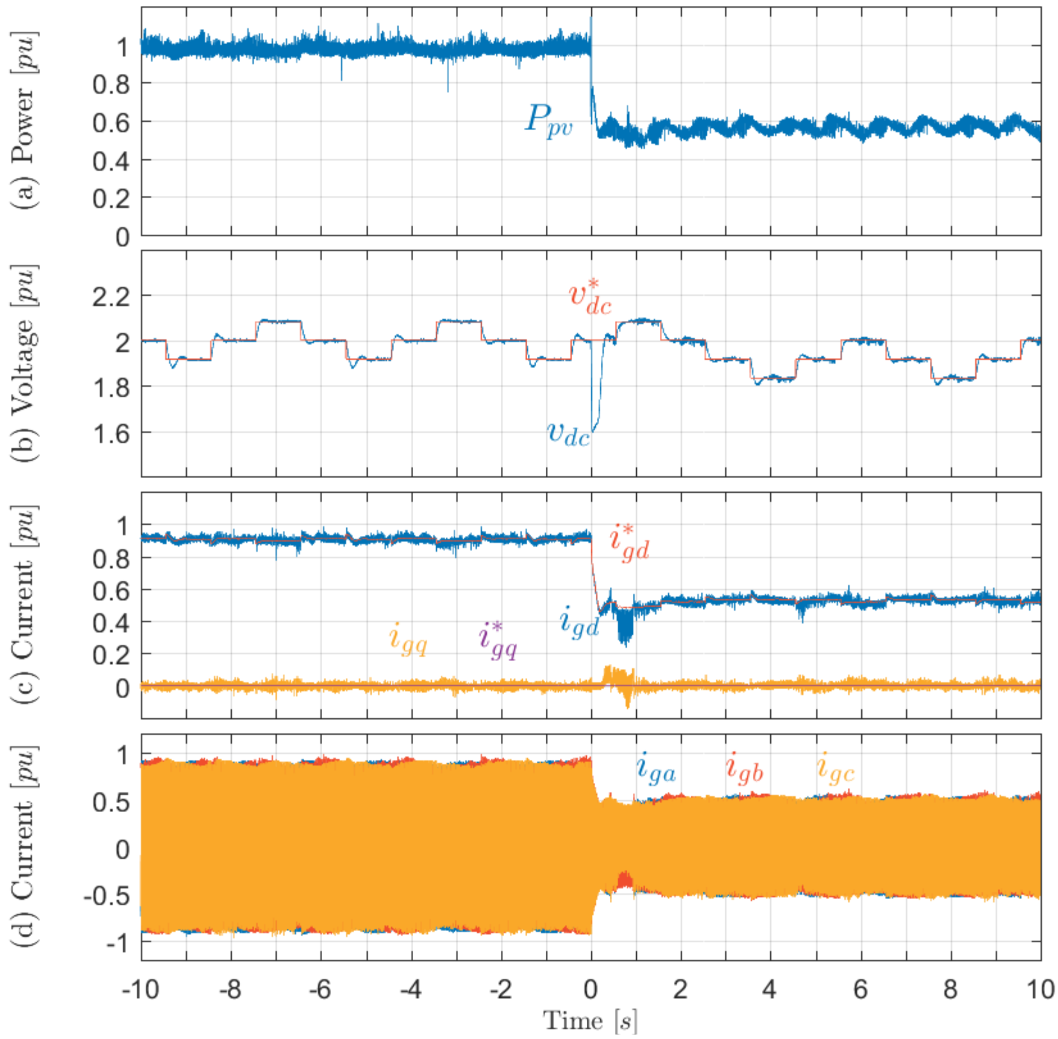

Figure 8.14: PV/ESS configuration with PV side connection and full bridge based PPC with inductor at the partial side, step up in bypass current reference (i_{bp}^*) from 0 to 2.0 [A] at 0 [s]: a) power towards the 2LVSI ($P_{\mathrm{pv}} = i_{\mathrm{pv}} \cdot v_{\mathrm{dc}}$), b) dc-link voltage and its reference (v_{dc} and v_{dc}^*), c) direct and quadrature grid currents and its reference (i_{gd}, i_{gq}, i_{gd}^* and i_{gq}^*) and d) grid currents (i_{ga}, i_{gb} and i_{gc}).

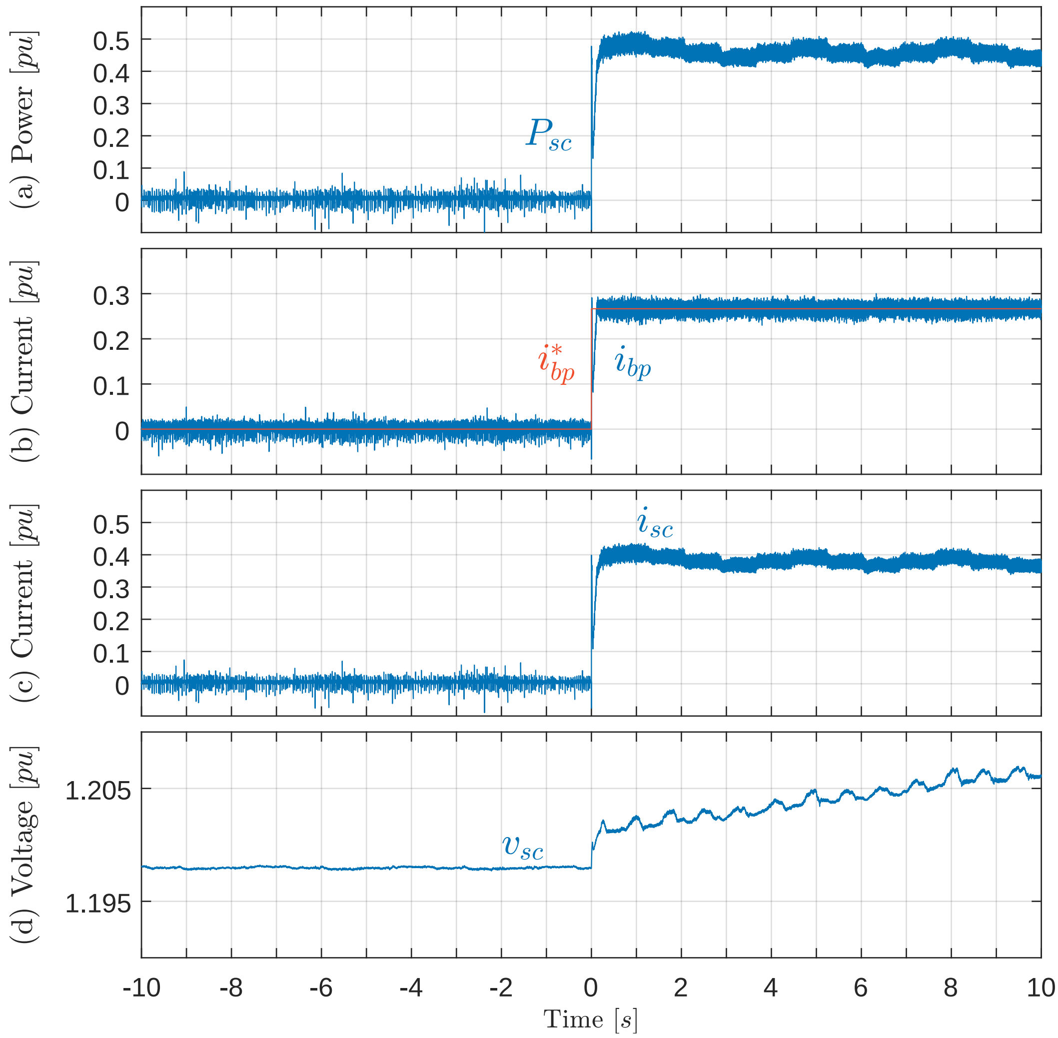

Figure 8.15: PV/ESS configuration with PV side connection and full bridge based PPC with inductor at the partial side, step up in bypass current reference reference (i^*_{bp}) from 0 to 2.0 [A] at 0 [s]: a) power towards the SC bank (P_{sc}), b) bypass current and its reference (i_{bp} and i^*_{bp}), c) current through the SC bank (i_{sc}) and d) SC bank voltage (v_{sc}).

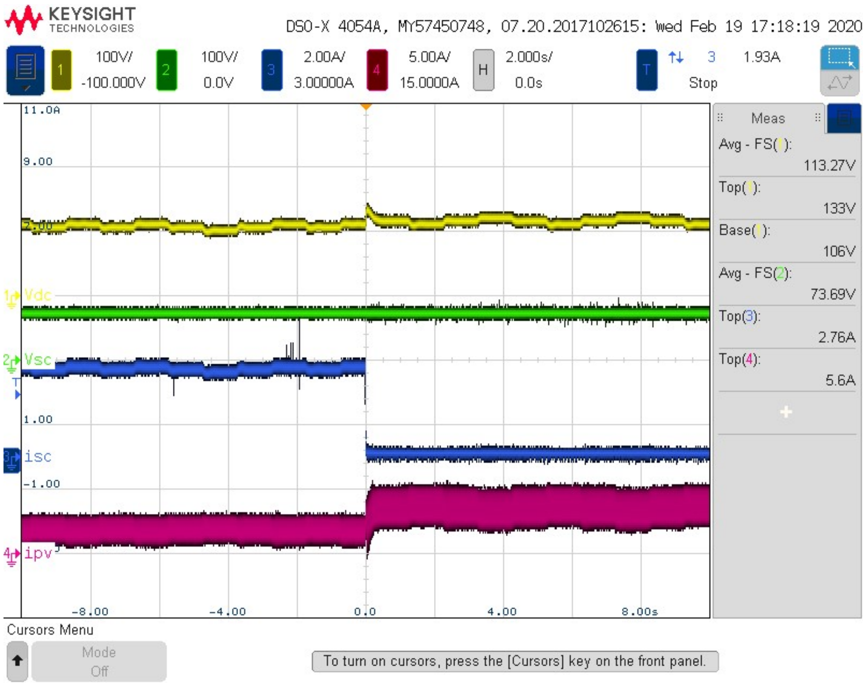

Figure 8.16: PV/ESS configuration with PV side connection and full bridge based PPC with inductor at the partial side, step down in bypass current reference reference (i^*_{bp}) from 2.0 to 0 [A] at 0 [s]: dc-link capacitor voltage (v_{dc}), SC bank voltage (v_{in}), SC bank current (i_{sc}) and current towards the 2LVSI (i_{pv}).

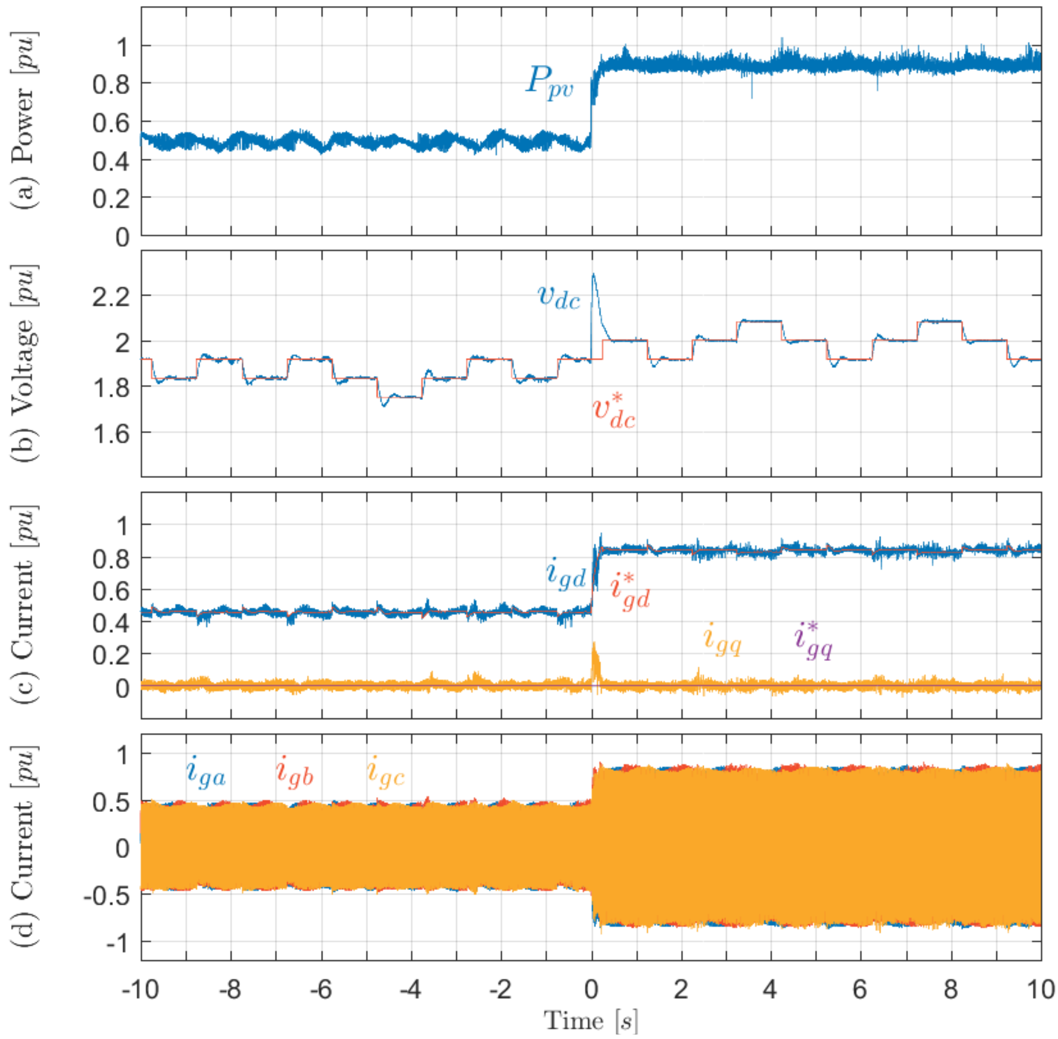

Figure 8.17: PV/ESS configuration with PV side connection and full bridge based PPC with inductor at the partial side, step down in bypass current reference (i^*_{bp}) from 2.0 to 0 [A] at 0 [s]: a) power towards the 2LVSI ($P_{\mathrm{pv}} = i_{\mathrm{pv}} \cdot v_{\mathrm{dc}}$), b) dc-link voltage and its reference (v_{dc} and v^*_{dc}), c) direct and quadrature grid currents and its reference (i_{gd}, i_{gq}, i^*_{gd} and i^*_{gq}) and d) grid currents (i_{ga}, i_{gb} and i_{gc}).

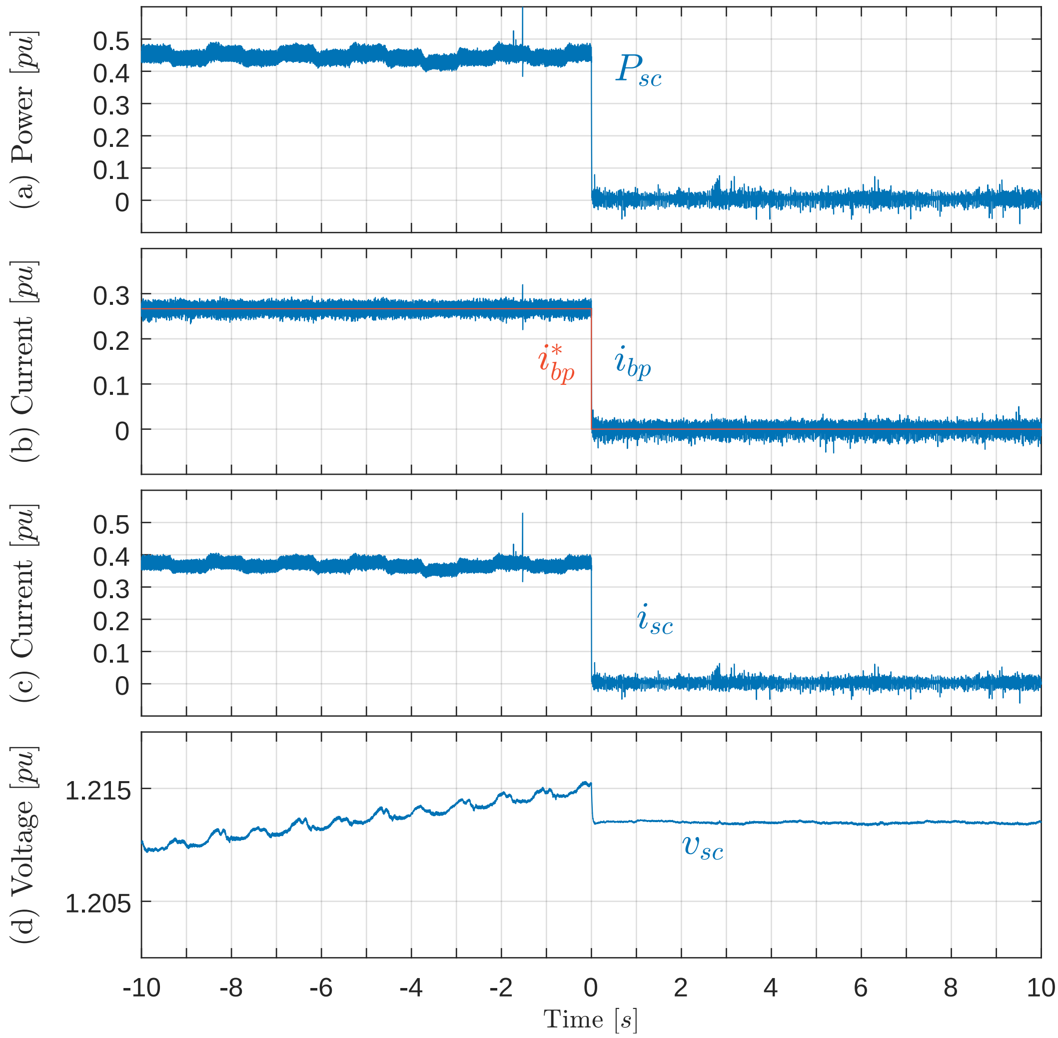

Figure 8.18: PV/ESS configuration with PV side connection and full bridge based PPC with inductor at the partial side, step down in bypass current reference reference (i^*_{bp}) from 2.0 to 0 [A] at 0 [s]: a) power towards the SC bank (P_{sc}), b) bypass current and its reference (i_{bp} and i^*_{bp}), c) current through the SC bank (i_{sc}) and d) SC bank voltage (v_{sc}).

8.4 Summary

This chapter presents the experimental validation of a full bridge based PPC topology with the inductor at the partial side and the experimental validation of a PV/ESS configuration. The first part of this chapter presented the validation of a unidirectional full bridge based PPC operating in bucking mode. This section includes the configuration diagram, configuration parameters and control scheme applied over the PPC in standalone operation. The configuration implemented for this purpose included a unidirectional full bridge based PPC, a PV emulator operating as a constant voltage source and an SC bank operating as load.

The second part of this chapter presented the validation of a PV/ESS configuration with the connection at the PV side. This section includes the configuration diagram, configuration parameters and control scheme applied over the PV/ESS configuration. Two dynamic tests were performed to validate the operation of the PV/ESS configuration.

The simulation results presented in Chapter 7 match the experimental results obtained from the PV/ESS configuration operating in bucking mode. Both results show a good performance of the PV/ESS configuration, where the ESS is capable of storing the energy injected from the dc-link. Additionally both results show that the PV system is keeps performing P&O MPPT despite power being drawn from the dc-link. It must be noted that the VOC scheme in both cases is capable of regulating the dc-link voltage perturbations caused by the PPC (when the bucking mode starts or stops its operation).

Chapter 9

Conclusions

The main objectives of the work presented in this document were to develop an ESS sizing strategy and to propose, simulate and validate a power converter interface, capable of merging ESS into PV plants, while enabling them to provide an specific complementary service. Both objectives where achieved and the results obtained are commented on below.

PV modelling

The first step towards developing an ESS sizing strategy was for selecting the best performing PV model, capable of estimating (from irradiance, temperature and PV plant parameters) the available PV power. Single diode circuital model, ANN and analytical models were tested for this purpose. The estimated PV power, obtained from all models, was contrasted against empirical data from a PV plant located in Cambridge. This comparison showed that all models have a good correlation between measurement and prediction. In addition to its simplicity, the analytical model was selected as the best performing PV model, since it presented a low error, the lowest execution time, the lowest complexity and no requirement of an optimisation stage. This model was applied to estimate a year of PV power generation (sampled every minute) in two locations, Atacama (Chile) and Cambridgeshire (UK). The data obtained from both annual estimations allowed a deeper understanding to develop on how PV power generation varies over a year, especially in terms of daily behaviour and seasonality.

ESS sizing strategy

Two novel ESS sizing strategies were developed, targeting different complementary services. The first of those strategies aimed towards providing smoothed PV power, compliant with maximum power ramp rate regulations. For this purpose the annual energy loss, caused by complying several RR restrictions, was estimated (from the annual PV power prediction). The predicted PV power was used as the input to the DWT-based ESS sizing strategy, which calculates the ESS power reference required to comply with a certain maximum power Ramp Rate regulation. Finally, a combined power and energy analysis, that allows sizing of the ESS (daily) energy as a function of the ESS power, is performed. The proposed ESS sizing strategy for RR regulation presents a better performance than the best-performing previously-available ESS sizing strategy.

The second ESS sizing strategy was focused on how to reduce the loss of generation caused by oversizing a PV array with respect to the power rating of its converter (power clipping). This ESS sizing strategy was based on a combined power and energy approach, which used statistical data to select the best fitting (power and energy) ESS ratings, thus, allowing the ESS energy sizing to be obtain as a function of the percentage of clipped power to be recovered. Additionally, a second analysis allowed obtaining of the ESS power rating as a function of the previously obtained ESS energy rating. In fact this work showed that with only a 13% of the central inverter rated power the ESS was able to handle 80% of the loss of generation (clipping) needs of the PV plant during a year. This means that for a 1[MW] central inverter a 130 [kW] ESS would suffice. To the best knowledge of the author, there is no other ESS sizing strategy available in literature targeting a reduction of loss of generation in power clipping scenarios.

With the proper model and data available, both ESS sizing strategies can be extended to other renewable energy sources, as such as wind and marine energy conversion systems.

Most ESS sizing strategies neglect the relationship between power and energy, thus providing an oversized solution. Both ESS sizing strategies presented in this work, apply a power-energy analysis, leading to a more cost-effective sizing.

Additionally, combining the annual PV power generation profile with the power requirements for an specific complementary service, allows identification of the probability of ESS idle operation (per hour) for that specific complementary service, thus, enabling the use of the ESS to offer other complementary services during its idle operation time. As an example, power clipping hours during a day can be easily predicted, hence idle hours of the ESS can be used to provide Peak Shaving.

Configuration and topologies

Two power converter configurations were analysed as possible alternatives to interface an ESS into PV systems, i.e. the AC grid side connection and the PV array side connection. In general terms, the first alternative allows a concentrated solution requiring, due to aggregation (low pass filtering effect), a lower ESS sizing. On the other hand, the PV-array-side configuration offers a distributed, modular and scalable solution.

All the PV systems configurations presented along this thesis, correspond to PV arrays connected to the grid through central inverter configuration based on 2LVSI. Three different bidirectional dc-dc converters were considered to handle the bidirectional power flow to the ESS. These power converters are the Isolated Bidirectional Boost Converter (IBBC) and Bidirectional Partial Power Converter (PPC), with the inductor at the input side and the Bidirectional Partial Power Converter (PPC) with the inductor at the partial side. Due to the power rating of each complementary service, the dc-dc conversion stage in each application considered one of the aforementioned dc-dc power converters in interleaved configuration.

Despite the asymmetry in the operation (different H-bridges being triggered) caused by power flowing in one or the opposite direction, the IBBC and PPC with the inductor at the input side can be modelled through a single mathematical model. Nonetheless, the differences in terms of operation, caused by the power flowing in one direction or the other, are reflected in the modulation stage.

The proposed bidirectional PPC with the inductor in the input side corresponds to a new power converter. Meanwhile the bidirectional PPC with the inductor in the partial side, corresponds to a new reconfigurable connection that merges into one power converter.

Controllers

Regarding the control strategies implemented in the PV/ESS configurations, all PV systems in the configurations were operated with traditional P&O MPPT and VOC (cascaded external dc-link voltage loop and internal current loop). On the other hand, the control strategies implemented on the ESS had an external algorithm, generating the power reference and ESS charging schedule, and an internal current loop regulating the current flow from or towards the energy storage device. Additionally, each complementary service has an specific power profile, thus the algorithms implemented to generate the power reference for each complementary service are different from other services.

In order to deceive the P&O MPPT strategy, in the power clipping application, an ESS charging/discharging strategy with an update period larger than the P&O update period was applied. This allowed an injection/withdrawal current from the dc-link without it being noticed by the P&O MPPT strategy. Note that this strategy corresponds to new knowledge and enables retrofitting existing Central PV inverters with an ESS without affecting or need to intervene its MPPT or control algorithm. .

Simulation results

Three different complementary services were tested during the development of this thesis, namely maximum power ramp rate regulation for global MPPT, peak shaving and power clipping. It must be noted that all results obtained considered a PV system formed by a grid-tied central inverter with 2LVSI topology and a VOC scheme.

In the case of maximum power ramp rate regulation, two PV/ESS configurations were tested (AC-grid-side connection and PV-array-side connection) showing good and equivalent performance, while complying with the imposed RR regulation (10% of the nominal power per minute). The proposed PV/ESS configuration with ESS connection at the PV side requires a 2LVSI less than the PV/ESS configuration with the ESS connection at the AC grid side. This allows an increase of the reliability and efficiency of the system, and while reducing losses and cost (per ESS unit). On the other hand, the PV/ESS configuration with AC-grid-side connection can be thought at larger scale or plant level, employing a single ESS for several central inverter configurations. This can be achieved by sequentially performing the global MPPT (among central inverter configurations), thus reducing ESS size and cost.

The results associated with Peak Shaving show a good performance of the PV/ESS configuration (with the ESS connected at the PV side). In this complementary service, the external power reference (provided by the grid operator) is required to regulate the power injected into the grid by the central inverter grid-tied PV system (with VOC scheme). This power reference was also used by the ESS control scheme, allowing to reduce or increase the power injected to the grid, despite the PV power being generated. The proposed ESS and control scheme were designed to be a plug-in solution for existing grid-tied PV plants, lacking peak shaving capability. Moreover, a small modification in the control strategy will allow ESS to reduce (avoid) the PV plant power curtailment, required by grid operators to compensate grid frequency variations.

The last complementary service tested was power clipping, where the PV array was operated at a power rating beyond the inverter nominal rating. This was achieved by injecting/withdrawing continuous current to/from the dc-link (from/to the energy storage device), thus allowing deceiving of the P&O MPPT strategy and enabling existing PV plants to be retrofitted without further intervention other than connecting the ESS to the dc-link of the PV inverter.

Experimental results

Full bridge based PPCs are a viable solution to merge PV systems into ESS at the dc-link side. The experimental tests showed that the full bridge based PPC with the inductor at the partial side, is capable of handling the power flow control between the PV emulator and the ESS, without modifying the 2LVSI standard control loop.

The fast response of the power control in both dynamic tests (step up and down), show that the PPC is capable of managing power under circumstances similar to peak shaving and other ancillary services as such as frequency regulation. Moreover, the response obtained from the configuration surpasses the required response speed of all frequency regulation services (fast, primary, secondary and tertiary), allowing a better chance to diminish variability and intermittency related concerns and increasing renewables penetration into the electric markets.

The tests over the PV/ESS configuration with the ESS connection at PV side show that retrofitting PV plants is an alternative to enhancing (existing) PV systems, without further modifications.

Future Work

Many ideas arose during the development of this thesis, however, the finiteness of time forces focussing on some of them leaving the others to further research. Some of these topics are:

- One of the novel PPCs (with the inductor in the partial side) was preliminary tested through simulation and experimental results. The available PPC's PCB was not reconfigurable, thus only half of the PPC operation was tested (ESS charging). The building the reconfigurable PPC and testing the other operation mode (ESS discharging) remains a future work to be performed. Moreover the experimental validation of the second PPC (with the inductor in the input side) is also a future task to be performed.

- ESS in PV applications are sized and operated to fulfil a specific complementary service, however the amount of idle operation hours has not been addressed to explore idle operation services opportunities. Additionally, some complementary services have a higher probability of occurring during specific hours of the day, while other services could be required during other hours. Therefore, a probabilistic analysis of the requirement of each complementary service, during each hour of the day, would allow the finding of compatible complementary services which minimise the probability of time overlapping, thus allowing an increase in both the amount of complementary service offered by a single ESS and the revenue generated by the PV/ESS configuration.

- Retrofitting existing PV systems requires to intervene in an operational PV plant, while minimising the intervention on the original system. Interfacing the ESS at the PV array level, requires provision of a power injection/removal strategy that allows the PV system to keep operating with its original MPPT strategy. In standard P&O MPPT strategies, the current and voltage measurements are averaged, thus making the algorithm unable to detect injection/removal of constant current to/from the dc-link. This strategy was tested against P&O, however, its validation over different MPPT strategies has not been performed, and allows a new line of investigation towards retrofitting of PV plants.

- Bidirectional partial power converters offer two different power flow paths, depending on the power flow direction (boosting or bucking). For this reason a deeper analysis on how each element in the topology contributes to the efficiency in each power flow direction remains a non-explored topic.

Bibliography

[1] REN21, *Renewbles 2019: Global Status Report.* REN21, 2019.

[2] M. Bragard, N. Soltau, S. Thomas, and R. W. De Doncker, "The balance of renewable sources and user demands in grids: Power electronics for modular battery energy storage systems," *IEEE Trans. Power Electron.*, vol. 25, no. 12, pp. 3049–3056, 2010.

[3] E. Romero-Cadaval, B. Francois, M. Malinowski, and Q. C. Zhong, "Grid-connected photovoltaic plants: An alternative energy source, replacing conventional sources," *IEEE Ind. Electron. Mag.*, vol. 9, no. 1, pp. 18–32, 2015.

[4] S. Vazquez, S. M. Lukic, E. Galvan, L. G. Franquelo, and J. M. Carrasco, "Energy Storage Systems for Transport and Grid Applications," *IEEE Trans. Ind. Electron.*, vol. 57, no. 12, pp. 3881–3895, 2010.

[5] M. Lei, Z. Yang, Y. Wang, H. Xu, L. Meng, J. C. Vasquez, and J. M. Guerrero, "An MPC-Based ESS Control Method for PV Power Smoothing Applications," *IEEE Trans. Power Electron.*, vol. 33, no. 3, pp. 2136–2144, 2018.

[6] J. Lhermenault, C. Zakhour, C. Ducharme, E. Radvanyi, S. Ruiz, B. Deneuville, and G. Lancel, "Energy storage systems (ESS) and microgrids in Brittany islands," *CIRED - Open Access Proc. J.*, vol. 2017, no. 1, pp. 1741–1744, 2017.

[7] H. G. Lee, G. G. Kim, B. G. Bhang, D. K. Kim, N. Park, and H. K. Ahn, "Design Algorithm for Optimum Capacity of ESS Connected with PVs under the RPS Program," *IEEE Access*, vol. 6, pp. 45899–45906, 2018.

[8] Q. Cheng, "Energy management system of a smart railway station considering stochastic behaviour of ESS and PV generation," in *Proc. - 2018 Int. Symp. Comput. Consum. Control. IS3C 2018*, pp. 457–460, IEEE, 2019.

[9] SMA Solar Technology, "Solar Inverters."

[10] A. Tani, M. B. Camara, and B. Dakyo, “Energy Management in the Decentralized Generation Systems Based on Renewable Energy - Ultracapacitors and Battery to Compensate the Wind/Load Power Fluctuations,” *IEEE Trans. Ind. Appl.*, vol. 51, no. 2, pp. 1817–1827, 2015.

[11] H. Renaudineau, *Hybrid Renewable Energy Sourced System Energy Management & Self-Diagnosis*. PhD thesis, Université de Lorraine, 2013.

[12] P. Thounthong, S. Sikkabut, P. Mungporn, L. Piegari, B. Nahid-Mobarakeh, S. Pierfederici, and B. Davat, “DC Bus Stabilization of Li-Ion Battery Based Energy Storage for a Hydrogen/Solar Power Plant for Autonomous Network Applications,” *IEEE Trans. Ind. Appl.*, vol. 51, no. 4, pp. 2717–2725, 2015.

[13] P. Thounthong, “Model based-energy control of a solar power plant with a supercapacitor for grid-independent applications,” *IEEE Trans. Energy Convers.*, vol. 26, no. 4, pp. 1210–1218, 2011.

[14] M. Datta, T. Senjyu, A. Yona, T. Funabashi, and Chul-Hwan Kim, “A Frequency-Control Approach by Photovoltaic Generator in a PV–Diesel Hybrid Power System,” *IEEE Trans. Energy Convers.*, vol. 26, pp. 559–571, jun 2011.

[15] D. J. Won, Y. S. Noh, M. Y. Ryu, C. Y. Won, and H. W. Lim, “A study of grid-connected PV-AC module with active power decoupling and ESS,” in *Proc. IEEE Int. Conf. Ind. Technol.*, pp. 491–496, IEEE, 2014.

[16] N. Müller, S. Kouro, P. Zanchetta, P. Wheeler, G. Bittner, and F. Girardi, “Energy storage sizing strategy for grid-tied PV plants under power clipping limitations,” *Energies*, vol. 12, no. 9, pp. 1–17, 2019.

[17] SBC Energy Institute, “Electricity Storage Factbook,” 2013.

[18] D. D. Rastler, EPRI, D. D. Rastler, EPRI, D. D. Rastler, EPRI, and D. D. Rastler, “Electric Energy Storage Technology Options: A White Paper Primer on Applications, Costs and Benefits,” *Epri*, p. 170, 2010.

[19] A. R. Jordehi, “Parameter estimation of solar photovoltaic (PV) cells: A review,” *Renew. Sustain. Energy Rev.*, vol. 61, pp. 354–371, 2016.

[20] G. Graditi, S. Ferlito, and G. Adinol, “Comparison of Photovoltaic plant power production prediction methods using a large measured dataset,” vol. 90, pp. 513–519, 2016.

[21] J. M. Lopez-Guede, J. A. Ramos-Hernanz, E. Zulueta, U. Fernadez-Gamiz, and F. Oterino, "Systematic modeling of photovoltaic modules based on artificial neural networks," *Int. J. Hydrogen Energy*, vol. 41, no. 29, pp. 12672–12687, 2016.

[22] A. Mellit, S. Saglam, and S. Kalogirou, "Artificial neural network-based model for estimating the produced power of a photovoltaic module," *Renew. Energy*, vol. 60, pp. 71–78, dec 2013.

[23] Q. Jiang and H. Hong, "Wavelet-Based Capacity Configuration and Coordinated Control of Hybrid Energy Storage System for Smoothing Out Wind Power Fluctuations," *IEEE Trans. Power Syst.*, vol. 28, no. 2, pp. 1363–1372, 2013.

[24] S. Kouro, J. I. Leon, D. Vinnikov, and L. G. Franquelo, "Grid-connected photovoltaic systems: An overview of recent research and emerging PV converter technology," *IEEE Ind. Electron. Mag.*, vol. 9, no. 1, pp. 47–61, 2015.

[25] I. Enphase Energy, "Enphase Microinverter," 2020.

[26] Huawei, "PV inverters," 2020.

[27] Firmer, "PV inverters."

[28] CanadianSolar, "PV inverters."

[29] Siemens, "SINACON PV Central Inverter," 2020.

[30] A. A. Khodadoost Arani, G. B. Gharehpetian, and M. Abedi, "Review on Energy Storage Systems Control Methods in Microgrids," *Int. J. Electr. Power Energy Syst.*, vol. 107, no. December 2018, pp. 745–757, 2019.

[31] L. A. Wong, V. K. Ramachandaramurthy, P. Taylor, J. B. Ekanayake, S. L. Walker, and S. Padmanaban, "Review on the optimal placement, sizing and control of an energy storage system in the distribution network," *J. Energy Storage*, vol. 21, no. December 2018, pp. 489–504, 2019.

[32] F. Nadeem, S. M. Hussain, P. K. Tiwari, A. K. Goswami, and T. S. Ustun, "Comparative review of energy storage systems, their roles, and impacts on future power systems," *IEEE Access*, vol. 7, pp. 4555–4585, 2019.

[33] International Electrotechnical Commission and others, *Grid Integration of Large-capacity Renewable Energy Sources and Use of Large-capacity Electrical Energy Storage: White Paper*. International Electrotechnical Commission, 2012.

[34] REN21, "The First Decade: 2004 – 2014," tech. rep., REN21, 2015.

[35] P. Castillo, S. Kouro, C. A. Rojas, and N. Muller, "Photovoltaic DC-DC converter for direct power interface to copper electrorefining process," *IECON 2015 - 41st Annu. Conf. IEEE Ind. Electron. Soc.*, pp. 4388–4393, 2015.

[36] CanadianSolar, "HiDM-Black PV module."

[37] JinkoSolar, "Cheetah Plus HC 78M," 2020.

[38] N. M.-A. J. M. Carrasco, L. G. Franquelo, J. T. Bialasiewicz, E. Galvan, R. C. Portillo-Guisado, M. A. M. Prats, J. I. Leon, "Power-Electronic Systems for the Grid Integration of Renewable Energy Sources: A Survey," *1002 IEEE Trans. Ind. Electron.*, vol. 53, no. 4, pp. 1002–1016, 2006.

[39] A. Camacho, M. Castilla, J. Miret, R. Guzman, and A. Borrell, "Reactive power control for distributed generation power plants to comply with voltage limits during grid faults," *IEEE Trans. Power Electron.*, vol. 29, no. 11, pp. 6224–6234, 2014.

[40] S. Chen, T. Zhang, H. B. Gooi, R. D. Masiello, and W. Katzenstein, "Penetration rate and effectiveness studies of aggregated BESS for frequency regulation," *IEEE Trans. Smart Grid*, vol. 7, no. 1, pp. 167–177, 2016.

[41] J. H. Enslin, "Integration of photovoltaic solar power - The quest towards dispatchability," *IEEE Instrum. Meas. Mag.*, vol. 17, no. 2, pp. 21–26, 2014.

[42] C. nacional de energía, "NORMA TÉCNICA DE SEGURIDAD Y CALIDAD DE SERVICIO," 2018.

[43] E. Perez, H. Beltran, N. Aparicio, and P. Rodriguez, "Predictive power control for PV plants with energy storage," *IEEE Trans. Sustain. Energy*, vol. 4, no. 2, pp. 482–490, 2013.

[44] Q. Zhao, K. Wu, and A. M. Khambadkone, "Optimal sizing of energy storage for PV power ramp rate regulation," in *ECCE 2016 - IEEE Energy Convers. Congr. Expo. Proc.*, pp. 1–6, IEEE, 2016.

[45] J. Galtieri and P. Krein, "Solar Variability Reduction Using Off-Maximum Power Tracking and Battery Storage," *2017 IEEE 44th Photovolt. Spec. Conf. PVSC 2017*, pp. 1–4, 2017.

[46] A. Aichhorn, M. Greenleaf, H. Li, and J. Zheng, "A cost effective battery sizing strategy based on a detailed battery lifetime model and an economic energy management strategy," *IEEE Power Energy Soc. Gen. Meet.*, pp. 1–8, 2012.

[47] B.-R. Ke, T.-T. Ku, Y.-L. Ke, C.-Y. Chung, and H.-Z. Chen, "Sizing the Battery Energy Storage System on a University CampusWith Prediction of Load and Photovoltaic Generation," *IEEE Trans. Ind. Appl.*, vol. 52, no. 2, pp. 1136–1147, 2016.

[48] V. Rallabandi, O. M. Akeyo, N. Jewell, and D. M. Ionel, "Incorporating battery energy storage systems into multi-MW grid connected PV systems," *IEEE Trans. Ind. Appl.*, vol. 55, no. 1, pp. 638–647, 2019.

[49] H. Nazaripouya, Y. Wang, P. Chu, H. R. Pota, and R. G. Members, "Optimal Sizing and Placement of Battery Energy Storage in Distribution System Based on Solar Size for Voltage Regulation," in *2015 IEEE Power Energy Soc. Gen. Meet.*, (Denver, USA), 2015.

[50] A. Arabali, M. Ghofrani, M. Etezadi-Amoli, and M. S. Fadali, "Stochastic performance assessment and sizing for a hybrid power system of Solar/Wind/Energy Storage," *IEEE Trans. Sustain. Energy*, vol. 5, no. 2, pp. 363–371, 2014.

[51] Q. Li, S. S. Choi, Y. Yuan, and D. L. Yao, "On the determination of battery energy storage capacity and short-term power dispatch of a wind farm," *IEEE Trans. Sustain. Energy*, vol. 2, no. 2, pp. 148–158, 2011.

[52] P. Pinson, G. Papaefthymiou, B. Klöckl, and J. Verboomen, "Dynamic sizing of energy storage for hedging wind power forecast uncertainty," *2009 IEEE Power Energy Soc. Gen. Meet. PES '09*, pp. 1–8, 2009.

[53] Y. V. Makarov, P. Du, M. C. W. Kintner-Meyer, C. Jin, and H. F. Illian, "Sizing energy storage to accommodate high penetration of variable energy resources," *IEEE Trans. Sustain. Energy*, vol. 3, no. 1, pp. 34–40, 2012.

[54] H. Renaudineau, A. Houari, J. P. Martin, S. Pierfederici, F. Meibody-Tabar, and B. Gerardin, "A new approach in tracking maximum power under partially shaded conditions with consideration of converter losses," *Sol. Energy*, vol. 85, no. 11, pp. 2580–2588, 2011.

[55] Q. Duan, J. Leng, P. Duan, B. Hu, and M. Mao, "An improved variable step PO and global scanning MPPT method for PV systems under partial shading condition," in *Proc. - 2015 7th Int. Conf. Intell. Human-Machine Syst. Cybern. IHMSC 2015*, vol. 1, pp. 382–386, IEEE, 2015.

[56] B. N. Alajmi, K. H. Ahmed, S. J. Finney, and B. W. Williams, "A maximum power point tracking technique for partially shaded photovoltaic systems in microgrids," *IEEE Trans. Ind. Electron.*, vol. 60, no. 4, pp. 1596–1606, 2013.

[57] K. Itako, "PCS with scanning-type MPPT control for industrial grid-connected PV power generation system," in *2014 Int. Power Electron. Conf. IPEC-Hiroshima - ECCE Asia 2014*, pp. 3244–3248, IEEE, 2014.

[58] H. Renaudineau, F. Donatantonio, J. Fontchastagner, G. Petrone, G. Spagnuolo, J. P. Martin, and S. Pierfederici, "A PSO-based global MPPT technique for distributed PV power generation," *IEEE Trans. Ind. Electron.*, vol. 62, no. 2, pp. 1047–1058, 2015.

[59] R. Kot, S. Stynski, and M. Malinowski, "Simple scanning methods for a Global-MPP determination in a PV string," *2015 Sel. Probl. Electr. Eng. Electron. WZEE 2015*, pp. 1–6, 2015.

[60] K. Chen, S. Tian, Y. Cheng, and L. Bai, "An improved MPPT controller for photovoltaic system under partial shading condition," *IEEE Trans. Sustain. Energy*, vol. 5, no. 3, pp. 978–985, 2014.

[61] M. Boztepe, F. Guinjoan, G. Velasco-Quesada, S. Silvestre, A. Chouder, and E. Karatepe, "Global MPPT scheme for photovoltaic string inverters based on restricted voltage window search algorithm," *IEEE Trans. Ind. Electron.*, vol. 61, no. 7, pp. 3302–3312, 2014.

[62] E. Koutroulis and F. Blaabjerg, "A new technique for tracking the global maximum power point of PV arrays operating under partial-shading conditions," *IEEE J. Photovoltaics*, vol. 2, no. 2, pp. 184–190, 2012.

[63] K. Ishaque and Z. Salam, "A deterministic particle swarm optimization maximum power point tracker for photovoltaic system under partial shading condition," *IEEE Trans. Ind. Electron.*, vol. 60, no. 8, pp. 3195–3206, 2013.

[64] N. Muller, S. Kouro, P. Zanchetta, P. Wheeler, and A. Marzo, "Wavelet-based ESS sizing strategy to enable power peak-shaving in PV systems," in *2019 IEEE 28th Int. Symp. Ind. Electron.*, pp. 2458–2463, 2019.

[65] J. Marcos, O. Storkël, L. Marroyo, M. Garcia, and E. Lorenzo, "Storage requirements for PV power ramp-rate control in a PV fleet," *Sol. Energy*, vol. 169, pp. 28–35, 2014.

[66] National Renewable Energy Laboratory (NREL), "Review of PREPA Technical Requirements for Interconnecting Wind and Solar Generation," 2013.

[67] BEIS, "Digest of United Kingdom Energy Statistics 2018," *Dig. UK Energy Stat.*, no. July, p. 260, 2018.

[68] F. Serdio Fernández, M. A. Muñoz-García, and S. Saminger-Platz, "Detecting clipping in photovoltaic solar plants using fuzzy systems on the feature space," *Sol. Energy*, vol. 132, pp. 345–356, 2016.

[69] J. Good and J. X. Johnson, "Impact of inverter loading ratio on solar photovoltaic system performance," *Appl. Energy*, vol. 177, pp. 475–486, 2016.

[70] N. Muller, S. Kouro, H. Renaudineau, and P. Wheeler, "Energy storage system for global maximum power point tracking on central inverter PV plants," in *2016 IEEE 2nd Annu. South. Power Electron. Conf. SPEC 2016*, 2016.

[71] J. Dong, F. Gao, X. Guan, Q. Zhai, and J. Wu, "Storage Sizing With Peak-Shaving Policy for Wind Farm Based on Cyclic Markov Chain Model," *IEEE Trans. Sustain. Energy*, vol. 8, pp. 978–989, jul 2017.

[72] ABB, "Solar Inverters," 2019.

[73] J. W. Zapata, S. Kouro, G. Carrasco, H. Renaudineau, and T. A. Meynard, "Analysis of Partial Power DC-DC Converters for Two-Stage Photovoltaic Systems," *IEEE J. Emerg. Sel. Top. Power Electron.*, vol. 7, no. 1, pp. 591–603, 2019.

[74] S.-u. D. Voltage, R. Range, J. Rafael, R. Zientarski, S. Member, and S. Martins, "Series-Connected Partial-Power Converters Applied to PV Systems : A Design Approach Based on," *IEEE Trans. POWER Electron.*, vol. 33, no. 9, pp. 7622–7633, 2018.

[75] J. Rafael, R. Zientarski, S. Member, M. Lúcio, J. R. Pinheiro, and H. L. Hey, "Evaluation of Power Processing in Series-Connected Partial-Power Converters," *IEEE J. Emerg. Sel. Top. POWER Electron.*, vol. 7, no. 1, pp. 343–352, 2019.

[76] Energy UK, "Ancillary services report 2017," Tech. Rep. April, Energy UK, 2017.

[77] Coordinador Electrico Nacional, "Informe de Servicios Complementarios Año 2020," tech. rep., Coordinador Eléctrico Nacional, 2019.

[78] Australian Energy Market Operator (AEMO), "Ancillary Service Reportfor the WEM 2018-19," Tech. Rep. June, Australian Energy Market Operator (AEMO), 2018.

[79] Electric Power Research Institute (EPRI), "Ancillary Services Measurement Handbook," 2001.

[80] GE Energy Management, "Ancillary Services Definitions and Capability Study," Tech. Rep. December, GE Energy Consulting, 2012.

[81] E. S. D. A. N. Laboratory, "Survey of U.S. Ancillary Services Markets," 2016.

[82] M. Dabbagh, A. Rayes, B. Hamdaoui, and M. Guizani, "Peak shaving through optimal energy storage control for data centers," in *2016 IEEE Int. Conf. Commun. ICC 2016*, pp. 1–6, IEEE, 2016.

[83] S. Nykamp, A. Molderink, J. L. Hurink, and G. J. Smit, "Storage operation for peak shaving of distributed PV and wind generation," in *2013 IEEE PES Innov. Smart Grid Technol. Conf. ISGT 2013*, pp. 1–6, IEEE, 2013.

[84] A. Marinopoulos and P. Bakas, "Evaluation of a very large scale PV power system with energy storage for capacity firming," in *2015 IEEE Eindhoven PowerTech, PowerTech 2015*, pp. 1–6, IEEE, 2015.

[85] J. Sardi, N. Mithulananthan, D. Q. Hung, and K. Bhumkittipich, "Load levelling and loss reduction by ES in a primary distribution system with PV units," in *Proc. 2015 IEEE Innov. Smart Grid Technol. - Asia, ISGT ASIA 2015*, pp. 1–6, IEEE, 2015.

[86] Hydrostor, "A-CAES technology," 2018.

[87] S. A. Abdelrazek and S. Kamalasadan, "Integrated PV Capacity Firming and Energy Time Shift Battery Energy Storage Management Using Energy-Oriented Optimization," *IEEE Trans. Ind. Appl.*, vol. 52, no. 3, pp. 2607–2617, 2016.

[88] J. Muñoz-Cruzado-Alba, C. A. Rojas, S. Kouro, and E. G. Díez, "Power production losses study by frequency regulation in weak-grid-connected utility-scale photovoltaic plants," *Energies*, vol. 9, no. 5, pp. 1–21, 2016.

[89] E. Abierta, "Generación Bruta Horaria Sen," 2020.

[90] U. E. I. Administration, "Today in Energy," 2020.

[91] P. J. Grbovic, *Ultra-capacitors in Power Conversion Systems: Applications, Analysis, and Design from Theory to Practice.* John Wiley & Sons, 2013.

[92] H. Chen, T. N. Cong, W. Yang, C. Tan, Y. Li, and Y. Ding, "Progress in electrical energy storage system: A critical review," *Prog. Nat. Sci.*, vol. 19, no. 3, pp. 291–312, 2009.

[93] A. G. Ter-Gazarian, *Energy storage for power systems.* Iet, 1994.

[94] S. Sabihuddin, A. E. Kiprakis, and M. Mueller, "A numerical and graphical review of energy storage technologies," *Energies*, vol. 8, no. 1, pp. 172–216, 2015.

[95] E. Chemali, M. Preindl, P. Malysz, and A. Emadi, "Electrochemical and Electrostatic Energy Storage and Management Systems for Electric Drive Vehicles: State-of-the-Art Review and Future Trends," *IEEE J. Emerg. Sel. Top. Power Electron.*, vol. 4, no. 3, pp. 1117–1134, 2016.

[96] M. K. Kazimierczuk, *Pulse-width Modulated DC-DC Power Converters.* John Wiley and Sons, Ltd, 2008.

[97] J. W. Zapata, H. Renaudineau, S. Kouro, M. A. Perez, and T. A. Meynard, "Partial Power DC-DC Converter for Photovoltaic Microinverters," in *IECON 2016 - 42nd Annu. Conf. IEEE Ind. Electron. Soc.*, pp. 6740–6745, IEEE, 2016.

[98] J. W. Zapata, T. A. Meynard, and S. Kouro, "Partial Power DC-DC Converter for Large-Scale Photovoltaic Systems," in *2016 IEEE 2nd Annu. South. Power Electron. Conf.*, pp. 1–6, IEEE, 2016.

[99] A. Morrison, J. W. Zapata, S. Kouro, M. A. Perez, T. A. Meynard, and H. Renaudineau, "Partial Power DC-DC Converter for Photovoltaic Two-Stage String Inverters," in *2016 IEEE Energy Convers. Congr. Expo.*, (Milwaukee, WI, USA), pp. 1–6, IEEE, 2016.

[100] J. W. Zapata, T. A. Meynard, and S. Kouro, "Multi-channel partial power DC-DC converter for current balancing of LED strings," *IEEE Int. Symp. Ind. Electron.*, pp. 775–780, 2017.

[101] J. Rojas, H. Renaudineau, S. Kouro, and S. Rivera, "Partial Power DC-DC Converter for Electric Vehicle Fast Charging Stations," in *43rd Annu. Conf. IEEE Ind. Electron. Soc. IECON 2017*, 2017.

[102] K. Ding, X. Bian, H. Liu, and T. Peng, "A MATLAB-simulink-based PV module model and its application under conditions of nonuniform irradiance," *IEEE Trans. Energy Convers.*, vol. 27, no. 4, pp. 864–872, 2012.

[103] R. Abbassi, A. Abbassi, M. Jemli, and S. Chebbi, "Identification of unknown parameters of solar cell models: A comprehensive overview of available approaches," *Renew. Sustain. Energy Rev.*, vol. 90, no. March, pp. 453–474, 2018.

[104] J. M. Lopez-Guede, J. A. Ramos-Hernanz, E. Zulueta, U. Fernadez-Gamiz, and F. Oterino, "Systematic modeling of photovoltaic modules based on artificial neural networks," *Int. J. Hydrogen Energy*, vol. 41, no. 29, pp. 12672–12687, 2016.

[105] M. Karamirad, M. Omid, R. Alimardani, and H. Mousazadeh, “ANN based simulation and experimental verification of analytical four- and five-parameters models of PV modules,” *Simul. Model. Pract. Theory*, vol. 34, pp. 86–98, 2013.

[106] A. Abbassi, R. Gammoudi, M. Ali, O. Hasnaoui, and M. Jemli, “An improved single-diode model parameters extraction at different operating conditions with a view to modeling a photovoltaic generator : A comparative study,” *Sol. Energy*, vol. 155, pp. 478–489, 2017.

[107] D. Sera, R. Teodorescu, and P. Rodriguez, “PV panel model based on datasheet values,” in *IEEE Int. Symp. Ind. Electron.*, no. 4, pp. 2392–2396, IEEE, 2007.

[108] B. K. Nayak, A. Mohapatra, and K. B. Mohanty, “Parameters estimation of photovoltaic module using nonlinear least square algorithm: A comparative study,” *2013 Annu. IEEE India Conf. INDICON 2013*, pp. 1–6, 2013.

[109] L. M. Elobaid, A. K. Abdelsalam, and E. E. Zakzouk, “Artificial neural network-based photovoltaic maximum power point tracking techniques: a survey,” *IET Renew. Power Gener.*, vol. 9, no. 8, pp. 1043–1063, 2015.

[110] J. M. Lopez-Guede, J. A. Ramos-Hernanz, E. Zulueta, U. Fernadez-Gamiz, and F. Oterino, “Systematic modeling of photovoltaic modules based on artificial neural networks,” *Int. J. Hydrogen Energy*, vol. 41, no. 29, pp. 12672–12687, 2016.

[111] M. Khosravi, S. Heshmatian, D. A. Khaburi, C. Garcia, and J. Rodriguez, “A novel hybrid model-based MPPT algorithm based on artificial neural networks for photovoltaic applications,” in *2017 IEEE South. Power Electron. Conf.*, pp. 1–6, 2017.

[112] JinkoSolar, “PV module JKM260PP datasheet,” 2008.

[113] B. Pakkiraiah and G. D. Sukumar, “Research Survey on Various MPPT Performance Issues to Improve the Solar PV System Efficiency,” *J. Sol. Energy*, vol. 2016, pp. 1–20, 2016.

[114] I. Vernica, H. Wang, and F. Blaabjerg, “Impact of Long-Term Mission Profile Sampling Rate on the Reliability Evaluation of Power Electronics in Photovoltaic Applications,” *2018 IEEE Energy Convers. Congr. Expo. ECCE 2018*, pp. 4078–4085, 2018.

[115] S. Armstrong and W. G. Hurley, “A thermal model for photovoltaic panels under varying atmospheric conditions,” *Appl. Therm. Eng.*, vol. 30, no. 11-12, pp. 1488–1495, 2010.

[116] Y. Xie and M. Sengupta, “Toward Improved Modeling of Spectral Solar Irradiance for Solar Energy Applications,” No. October, pp. 2079–2081, 2017.

[117] W. Ma, W. Wang, X. Wu, R. Hu, F. Tang, W. Zhang, X. Han, and L. Ding, “Optimal Allocation of Hybrid Energy Storage Systems for Smoothing Photovoltaic Power Fluctuations Considering the Active Power Curtailment of Photovoltaic,” *IEEE Access*, vol. 7, pp. 74787–74799, 2019.

[118] R. Luthander, D. Lingfors, and J. Widén, “Large-scale integration of photovoltaic power in a distribution grid using power curtailment and energy storage,” *Sol. Energy*, vol. 155, pp. 1319–1325, 2017.

[119] G. Vahan and S. Booth, “Review of PREPA technical requirements for interconnecting wind and solar generation,” 2013.

[120] I. de la Parra, J. Marcos, M. García, and L. Marroyo, “Storage requirements for PV power ramp-rate control in a PV fleet,” *Sol. Energy*, vol. 118, pp. 426–440, 2015.

[121] Australian Government, “Australian Standard Grid connection of energy systems via inverters Part 2 : Inverter requirements,” *As 4777.2*, 2015.

[122] Comisión Nacional de Energía. Gobierno de Chile, “Norma Técnica de Seguridad y Calidad de Servicio,” 2013.

[123] LG Chem, “Product, ESS,” 2019.

[124] Toshiba, “SCiB,” 2019.

[125] Samsung SDI, “Energy Storage System Aplication,” 2016.

[126] J. R. R. Zientarski, M. L. Da Silva Martins, J. R. Pinheiro, and H. L. Hey, “Evaluation of Power Processing in Series-Connected Partial-Power Converters,” *IEEE J. Emerg. Sel. Top. Power Electron.*, vol. 7, no. 1, pp. 343–352, 2019.

[127] F. Flores-Bahamonde, J. Rojas, S. Kouro, A. M. Llor, C. A. Rojas, and M. A. Perez, “Sub-modular Power Optimizers Based on Partial Power Converters for Utility Scale PV Plants,” *IECON 2019 - 45th Annu. Conf. IEEE Ind. Electron. Soc.*, vol. 1, pp. 4423–4428, 2019.

[128] B. Arif, L. Tarisciotti, P. Zanchetta, J. Clare, and M. Degano, “Integrated grid inductance estimation technique for finite control set model predictive control in grid connected converters,” *2014 IEEE Energy Convers. Congr. Expo. ECCE 2014*, pp. 5797–5804, 2014.

[129] L. Guo, Y. Huangfu, and Y. Zhang, “A Smooth Sliding Mode Control for a High-Conversion-Ratio Bidirectional DC-DC Converter,” in *2019 IEEE Int. Conf. Ind. Technol.*, pp. 1669–1674, IEEE, 2019.

[130] D. Sera, L. Mathe, T. Kerekes, S. V. Spataru, S. Member, and R. Teodorescu, "On the Perturb-and-Observe and Incremental Conductance MPPT Methods for PV Systems," *IEEE J. Photovoltaics*, vol. 3, no. 3, pp. 1070–1078, 2013.

[131] C. Sola, "Canadian Solar, solar panels, CS6X-P-FG," 2016.

[132] G. power conversion, "GE power conversion, ProSolar Central Solar Inverter," 2012.

[133] Maxwel, "Products, Ultracapacitors," 2019.

[134] W.-Y. Chang, "The State of Charge Estimating Methods for Battery: A Review," *ISRN Appl. Math.*, vol. 2013, no. 1, pp. 1–7, 2013.

[135] A. Yazdani and R. Iravani, *Voltage-Sourced Converters in Power Systems: Modeling, Control, and Applications.* 2010.

[136] B. Wu, Y. Lang, N. Zargari, and S. Kouro, *Power conversion and control of wind energy systems.* John Wiley \& Sons, 2011.

[137] Standex Electronics, "Planar Transformers - Product Line Brochure," 2021.

[138] F. Blaabjerg, *Control of Power Electronic Converters and Systems.* Elsevier Inc., 2018.

[139] G. Goodwin, S. Graebe, and M. Salgado, *Control System Design.* Upper Saddle River, NJ: Prentice Hall, 2001.

[140] S. Mallat, "A theory for multiresolution signal decomposition: the waveletr epresentation," *PATTERN Anal. Mach. Intell. IEEE Trans.*, vol. 11, no. 7, pp. 674–693, 1989.

[141] K. Tapan and C. Su, "A Tutorial on Wavelets from an Electrical Engineering Perspective, Part 1: Discrete Wavelet Techniques," *IEEE Antennas Propag. Mag.*, vol. 40, no. 6, pp. 36–49, 1998.

[142] S. Mallat, *A Wavelet tour of signal processing.* Burlington, MA, United States: Elsevier Inc., third ed., 2009.

Appendix A

Two Level Voltage Source Inverter

A standard two Level Voltage Source Inverter (2LVSI) converter, with IGBT semiconductors is shown in Fig. A.1. The mathematical averaged model of the 2LVSI in the Laplace domain is presented through eqs. (A.1) to (A.3), where v_{gx}, i_{gx}, v_{dc}, v_{rx}, L_{g}, R_{g}, v_{Nn} correspond respectively to the phase-neutral grid voltage in phase x in [V], grid current in phase x in [A], dc-linkvoltage in [V], inverter voltage in phase x in [V], inductance of the grid filter in [H], resistance of the grid filter in [Ω] and N-n (Negative bar-neutral) voltage in [V]. Note that $\mathrm{x} \in \{\mathrm{a, b, c}\}$.

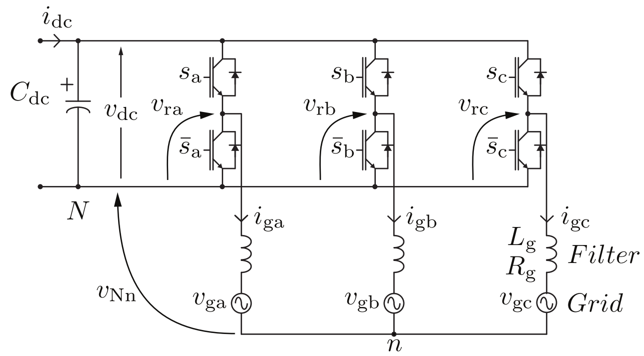

Figure A.1: Two Level Voltage Source Inverter (2LVSI) circuit.

$$i_{\mathrm{ga}} = \left(\frac{1}{L_{\mathrm{g}} \cdot s + R_{\mathrm{g}}}\right) \cdot (v_{\mathrm{ra}} - v_{\mathrm{ga}} + v_{\mathrm{Nn}}) \tag{A.1}$$

$$i_{\mathrm{gb}} = \left(\frac{1}{L_{\mathrm{g}} \cdot s + R_{\mathrm{g}}}\right) \cdot (v_{\mathrm{rb}} - v_{\mathrm{gb}} + v_{\mathrm{Nn}}) \tag{A.2}$$

$$i_{\mathrm{gc}} = \left(\frac{1}{L_{\mathrm{g}} \cdot s + R_{\mathrm{g}}}\right) \cdot (v_{\mathrm{rc}} - v_{\mathrm{gc}} + v_{\mathrm{Nn}}) \tag{A.3}$$

To simplify the control strategy, eqs. (A.1) to (A.3) were transformed into a rotational reference frame oriented with the grid voltage, through Clarke and Park transformations. This results in eqs (A.4) and (A.5), where ω, i_{gd}, i_{gq}, v_{rd}, v_{rq}, v_{gd} and v_{gq} are the angular frequency of the grid in [rad/s], d-axis axis grid current in [A], q-axis grid current in [A], d-axis inverter voltage in [V], q-axis inverter voltage in [V], d-axis grid voltage in [V] and q-axis grid voltage in [V].

$$i_{\mathrm{gd}} = \left(\frac{1}{L_{\mathrm{g}} \cdot s + R_{\mathrm{g}}}\right) \cdot (v_{\mathrm{rd}} + L_{\mathrm{g}} \cdot \omega \cdot i_{\mathrm{gq}} - v_{\mathrm{gd}}) \tag{A.4}$$

$$i_{\mathrm{gq}} = \left(\frac{1}{L_{\mathrm{g}} \cdot s + R_{\mathrm{g}}}\right) \cdot (v_{\mathrm{rq}} - L_{\mathrm{g}} \cdot \omega \cdot i_{\mathrm{gd}} - v_{\mathrm{gq}}) \tag{A.5}$$

The resulting transfer function between the input (v_{rx}) and the output (i_{gx}), with $x \in \{d, q\}$, is

$$TF_{i_{\mathrm{gx}} v_{\mathrm{rx}}} = \frac{i_{\mathrm{gx}}}{v_{\mathrm{rx}}} = \left(\frac{1}{L_{\mathrm{g}} \cdot s + R_{\mathrm{g}}}\right) \tag{A.6}$$

The transfer function between i_{gd} and the square of the voltage in the dc-link capacitor (v_{dc}^2) in the Laplace domain is shown in equation (A.7), where v_{gdQ} and C_{dc} are the amplitude of the grid voltage in the operation point Q and the capacitance of the dc-link.

$$TF_{v_{\mathrm{dc}} i_{\mathrm{gd}}} = \frac{v_{\mathrm{dc}}^2}{i_{\mathrm{gd}}} = -\frac{3}{2} \cdot \frac{v_{\mathrm{gdQ}}}{s \cdot C_{\mathrm{dc}}} \tag{A.7}$$

Note that all the variables in the previous analysis correspond to averaged values.

Appendix B

Power Converters Design

The elements of the power converter were designed considering the operation in steady state. The following sections present the design criteria for the 2LVSI and dc-dc power converters.

B.1 Two Level Voltage Source Inverter

The design of the 2LVSI grid filter inductor and capacitive dc-link is based on the per unit system described below [136].

The three phase (3ϕ) base power is defined as

$$P_{3\phi \text{ base}} = \frac{3}{2} \cdot v_{\text{base}} \cdot i_{\text{base}} \tag{B.1}$$

where v_{base} and i_{base}, are the base voltage in [V] ($v_{\text{base}} = v_{1\phi \text{ rms}} \cdot \sqrt{2}$, i.e. peak grid voltage) and the base current in [A] ($i_{\text{base}} = i_{\text{rms}} \cdot \sqrt{2}$, i.e. peak grid current). Note that this definition is based on the active power definition for voltage oriented control.

The base impedance (Z_{base}), base inductance (L_{base}) and base capacitance (Z_{base}) are defined according to

$$Z_{\text{base}} = \frac{v_{\text{base}}}{i_{\text{base}}}, \qquad L_{\text{base}} = \frac{Z_{\text{base}}}{\omega_{\text{base}}} \qquad \textit{and} \qquad C_{\text{base}} = \frac{1}{\omega_{\text{base}} \cdot Z_{\text{base}}} \tag{B.2}$$

, where ω_{base} is the base angular frequency in [rad/s] ($\omega_{\text{base}} = 2\pi \cdot f_{\text{base}}, \quad f_{\text{base}} = 50[\text{Hz}]$).

Parameter	symbol	value	per unit
Base power	$P_{3\phi \text{ base}}$	800 [kW]	1.0 [pu]
Base voltage	v_{base}	360 [V]	1.0 [pu]
Base current	i_{base}	1481 [A]	1.0 [pu]
Base frequency	ω_{base}	$100 \cdot \pi$ [rad/s]	1.0 [pu]
Base impedance	Z_{base}	242 [mΩ]	1.0 [pu]
Base inductance	L_{base}	0.77 [mH]	1.0 [pu]
Base capacitance	C_{base}	13.153 [mF]	1.0 [pu]
Selected inductance	L_{g}	0.05 [mH]	0.065 [pu]
Selected capacitance	C_{dc}	2.05 [mF]	0.156 [pu]

Table B.1: Design considerations: 2LVSI.

The inductive grid filter was selected, according to the criteria defined in [136], within 0.05 to 0.10 [pu] of the base inductance (L_{base}). The selected inductor corresponds to $L = 0.05[mH]$.

DC-link capacitor was arbitrarily chosen to be within 0.10 to 0.20 [pu] of the base capacitance (C_{base}). The selected DC-link capacitance corresponds to $C = 2050[\mu F]$.

B.2 DC-DC power converters design

The following design strategy shows the algorithm implemented to calculate the minimum inductance (L_{min}) for the inductors in the dc-dc power converters presented in chapter 5. The first step consists of defining a general expression to find the minimum inductance (L_{min}) of the inductor in the dc-dc power converters, based on the parameters of each converter during steady state operation.

Let us consider a switching frequency $f_{\text{sw}} = 1/T$, the switching period $T = t_{\text{on}} + t_{\text{off}}$ and the duty cycle $d = t_{\text{on}}/T$. During $t \in [0, t_{\text{on}}]$ the voltage in the inductor is $v_{\text{L on}}$ and during $t \in [t_{\text{on}}, T]$ the voltage in the inductor is $v_{\text{L off}}$.

Note that in steady state operation, the variation of the inductor current ($\Delta i_{\text{L on}}$) in $t \in [0, t_{\text{on}}]$ and in $t \in [t_{\text{on}}, T]$ ($\Delta i_{\text{L off}}$) must comply with $\Delta i_{\text{L on}} = \Delta i_{\text{L off}}$, thus

$$L \cdot \Delta i_{\text{L on}} = \int_0^{t_{\text{on}}} v_{\text{L on}} \, d\tau = -\int_{t_{\text{on}}}^{T} v_{\text{L off}} \, d\tau = -L \cdot \Delta i_{\text{L off}} \tag{B.3}$$

Assuming that the time-variation of both voltage values in the inductor ($v_{\text{L on}}$ and $v_{\text{L off}}$) is small, i.e. within one switching period $v_{\mathrm{L\ on}} \approx constant$ and $v_{\mathrm{L\ off}} \approx constant$, then eq. (B.3) results in:

$$t_{\mathrm{on}} \cdot v_{\mathrm{L\ on}} = -(T - t_{\mathrm{on}}) \cdot v_{\mathrm{L\ off}} \tag{B.4}$$

Dividing eq (B.4) by the switching period (T) and clearing d gives

$$d = \frac{v_{\mathrm{L\ off}}}{(v_{\mathrm{L\ off}} - v_{\mathrm{L\ on}})} \tag{B.5}$$

Let us now consider the inductor's element equation during $t \in [0, t_{\mathrm{on}}]$, then

$$\Delta i_{\mathrm{L\ on}} = \frac{1}{L}\int_0^{t_{\mathrm{on}}} v_{\mathrm{L\ on}}\, d\tau = \frac{v_{\mathrm{L\ on}} \cdot d}{L \cdot f_{\mathrm{sw}}} \tag{B.6}$$

, where t_{on} has been replaced by its equivalent d/f_{sw}.

Clearing L in eq. (B.6) results in

$$L = \frac{v_{\mathrm{L\ on}} \cdot d}{\Delta i_{\mathrm{L\ on}} \cdot f_{\mathrm{sw}}} \tag{B.7}$$

Considering that to achieve a certain inductor current variation ($\Delta i_{\mathrm{L\ on}}$) or lower, the inductor must be greater than or equal to a certain value (L_{min}) and replacing eq. (B.5) into eq. (B.7) results in

$$L_{\mathrm{min}} \geq \frac{v_{\mathrm{L\ on}}}{\Delta i_{\mathrm{L\ on}} \cdot f_{\mathrm{sw}}} \cdot \frac{v_{\mathrm{L\ off}}}{(v_{\mathrm{L\ off}} - v_{\mathrm{L\ on}})} \tag{B.8}$$

Equation (B.8) presents a general expression to calculate the minimum inductance (L_{min}) capable of achieving a given current variation ($\Delta i_{\mathrm{L\ on}}$).

The parameters considered to design the dc-dc power converters (IBBC, PPC with the inductor on the input side and PPC with the inductor on the partial side) are shown in table B.2. Note that all the dc-dc power converters were designed for 50[kW], however, the simulated applications considered interleaving these power converters to achieve higher power ratings.

Table B.3 shows a summary of the calculation of the minimum inductance for each dc-dc power converter. For all dc-dc power converters the selected inductance value was $0.075[mH]$.

Note that these designs consider implementing Standex (strong series) planar transformers [137] and Rhom semiconductors (model BSM600C12P3G201: $1200[V]$, $600[A]$ at $50[kHz]$).

Parameter	symbol	value
Power	P_{o}	$50[kW]$
Input Voltage	v_{in}	$100[V]$
Input Current	i_{in}	$500[A]$
Current variation	$\Delta i_{\mathrm{L\ on}}$	$5\% \cdot i_{\mathrm{in}}$
Output voltage	v_{o}	$1300[V]$
Switching frequency	f_{sw}	$50[kHz]$
Transformer turns ratio	$n_1 : n_2$	$1 : 1$

Table B.2: Design parameters for the dc-dc power converters.

Converter	Inductor voltage		Duty cycle (d)	Minimum inductance	
	$v_{\mathrm{L\ on}}$	$v_{\mathrm{L\ off}}$		expression	value
IBBC	$v_{\mathrm{in}} - v_{\mathrm{on}} \cdot \left(\frac{n_1}{n_2}\right)$	v_{in}	$\left(\frac{n_2}{n_1}\right) \cdot \left(\frac{v_{\mathrm{in}}}{v_{\mathrm{o}}}\right)$	$\frac{\left[\left(\frac{v_{\mathrm{in}}^2}{v_{\mathrm{o}}}\right) \cdot \left(\frac{n_2}{n_1}\right) - v_{\mathrm{in}}\right]}{\Delta i_{\mathrm{L}} \cdot f_{\mathrm{sw}}}$	$0.074[mH]$
PPC Input Side Inductor	$\left(\frac{n_2}{n_1+n_2}\right) \cdot v_{\mathrm{o}} - v_{\mathrm{in}}$	$-v_{\mathrm{in}}$	$\left(\frac{n_1+n_2}{n_2}\right) \cdot \frac{v_{\mathrm{in}}}{v_{\mathrm{o}}}$	$\frac{\left[v_{\mathrm{in}} - \left(\frac{n_1+n_2}{n_2}\right) \cdot \left(\frac{v_{\mathrm{in}}^2}{v_{\mathrm{o}}}\right)\right]}{\Delta i_{\mathrm{L}} \cdot f_{\mathrm{sw}}}$	$0.068[mH]$
PPC Partial Side Inductor Bucking	$\left(\frac{n_2}{n_1}\right) \cdot (v_{\mathrm{o}} - v_{\mathrm{in}}) - v_{\mathrm{in}}$	$-v_{\mathrm{in}}$	$\left(\frac{n_1}{n_2}\right) \cdot \left(\frac{v_{\mathrm{in}}}{v_{\mathrm{o}} - v_{\mathrm{in}}}\right)$	$\frac{\left[v_{\mathrm{in}} - \left(\frac{n_1}{n_2}\right) \cdot \left(\frac{v_{\mathrm{in}}^2}{v_{\mathrm{o}} - v_{\mathrm{in}}}\right)\right]}{\Delta i_{\mathrm{L}} \cdot f_{\mathrm{sw}}}$	$0.073[mH]$
PPC Partial Side Inductor Boosting	$(v_{\mathrm{in}} - v_{\mathrm{o}}) + \left(\frac{n_2}{n_1}\right) \cdot v_{\mathrm{o}}$	$(v_{\mathrm{in}} - v_{\mathrm{o}})$	$\left(\frac{n_1}{n_2}\right) \cdot \left(\frac{v_{\mathrm{o}} - v_{\mathrm{in}}}{v_{\mathrm{o}}}\right)$	$\frac{\left[(v_{\mathrm{o}} - v_{\mathrm{in}}) - \left(\frac{(v_{\mathrm{o}} - v_{\mathrm{in}})^2}{v_{\mathrm{o}}}\right) \cdot \left(\frac{n_1}{n_2}\right)\right]}{\Delta i_{\mathrm{L}} \cdot f_{\mathrm{sw}}}$	$0.074[mH]$

Table B.3: DC-DC power converter's inductor design summary

Appendix C

Controllers design procedure

This section presents the procedure to design the PI controllers applied in the thesis.

The aim of the controllers' design procedure is to find the gains (k_{p} and k_{i}) for the PI controller(s) of each power converter. These gains were obtained by applying the root locus tool over the continuous-time transfer function of the power converters, presented in Chap. 5 (and Appendix A), and considering PI controllers of the form $C(s) = (k_{\mathrm{p}} \cdot s + k_{\mathrm{i}})/s$. Note that the design of the inductor and capacitor of the power converters can be found in Appendix B.

A given bandwidth frequency and damping ratio ($\xi = 1/\sqrt(2)$) were used as design criterion for the design of most of the PI controllers. The standard value $\xi = 1/\sqrt(2)$ was implemented in all the designs, in order to minimise the resonance peak (visible in the Bode's magnitude plot). Nevertheless, in the case of the dc-link voltage loop, the damping ratio was increased to $\xi = 1.0$ in order to decrease oscillations [138].

The simulation and experimental results were performed applying digital controllers, where a PWM-based single update symmetry sampling was implemented [138].

In order to avoid the compensation of the modulation [138], the bandwidths of the dc-dc converter's closed loop systems were limited to a maximum value of one tenth of the sampling frequency (f_{sw}). This limitation was also applied over the (inner) current loop in the cascaded VOC scheme of the 2LVSI. Additionally, the (outer) voltage loop's bandwidth (of the closed loop) of the 2LVSI was limited to a maximum value of one fifth of the (inner) current loop's bandwidth (of the closed loop).

The previously described procedure, results in continuous-time PI controllers, which were later discretised applying the Tusting discretisation method:

$$s = \frac{2}{T} \cdot \left(\frac{z-1}{z+1} \right) \tag{C.1}$$

Note that the implementation of the discrete PI controllers included the saturation and anti-wind-up schemes based on the scheme presented in [139].

Appendix D

State Space Models

This chapter presents the state space models of the three bidirectional power converters presented in chapter 5.

The standard state space model of a system is given by

$$\dot{X} = A \cdot X + B \cdot U + E \cdot P \tag{D.1}$$

$$Y = C \cdot X + D \cdot U + F \cdot P \tag{D.2}$$

where X, U, P and Y are respectively the matrices containing the state variables, actuation, perturbations and outputs. Transforming this system of equations into Laplace domain and clearing X from eq. (D.1) gives:

$$X = (sI - A)^{-1} \cdot (B \cdot U + E \cdot P) \tag{D.3}$$

where s and I are the Laplace variable (complex frequency $j \cdot \omega$) and identity matrix.

Replacing eq. (D.3) into eq. (D.2),

$$Y = C \cdot [(sI - A)^{-1} \cdot (B \cdot U + E \cdot P)] + D \cdot U + F \cdot P \tag{D.4}$$

Reordering eq. (D.4),

$$Y = [C \cdot (sI - A)^{-1} \cdot B + D] \cdot U + [C \cdot (sI - A)^{-1} \cdot E + F] \cdot P \tag{D.5}$$

The transfer functions actuation-to-output (G_{yu}) and perturbation-to-output (G_{yp}) are:

$$G_{\mathrm{yu}} = \frac{Y}{U} = C \cdot (sI - A)^{-1} \cdot B + D \tag{D.6}$$

$$G_{\mathrm{yp}} = \frac{Y}{P} = C \cdot (sI - A)^{-1} \cdot E + F \tag{D.7}$$

D.1 Isolated Bidirectional Boost Converter

The linear state space model model of the IBBC is generated by linearising and rearranging the system of equations presented in eqs. (5.20), (5.21) and (5.23).

$$\begin{bmatrix} \frac{di_{\mathrm{L}}}{dt} \\ \\ \frac{dv_{\mathrm{o}}}{dt} \end{bmatrix} = \begin{bmatrix} \frac{-R_{\mathrm{L}}}{L} & \left(\frac{n_1}{n_2}\right) \cdot \frac{-M_{\mathrm{Q}}}{L} \\ \\ \left(\frac{n_1}{n_2}\right) \cdot \frac{M_{\mathrm{Q}}}{C_{\mathrm{o}}} & 0 \end{bmatrix} \cdot \begin{bmatrix} i_{\mathrm{L}} \\ \\ v_{\mathrm{o}} \end{bmatrix} + \begin{bmatrix} \left(\frac{n_1}{n_2}\right) \cdot \frac{-v_{\mathrm{oQ}}}{L} \\ \\ \left(\frac{n_1}{n_2}\right) \cdot \frac{i_{\mathrm{LQ}}}{C_{\mathrm{o}}} \end{bmatrix} \cdot \begin{bmatrix} M \end{bmatrix} + \begin{bmatrix} \frac{1}{L} & 0 \\ \\ 0 & \frac{-1}{C_{\mathrm{o}}} \end{bmatrix} \cdot \begin{bmatrix} v_{\mathrm{in}} \\ \\ i_{\mathrm{o}} \end{bmatrix} \tag{D.8}$$

$$\begin{bmatrix} i_{\mathrm{L}} \\ \\ i_{\mathrm{d}} \end{bmatrix} = \begin{bmatrix} 1 & 0 \\ \\ \left(\frac{n_1}{n_2}\right) \cdot M_{\mathrm{Q}} & 0 \end{bmatrix} \cdot \begin{bmatrix} i_{\mathrm{L}} \\ \\ v_{\mathrm{o}} \end{bmatrix} + \begin{bmatrix} 0 \\ \\ \left(\frac{n_1}{n_2}\right) \cdot i_{\mathrm{LQ}} \end{bmatrix} \cdot \begin{bmatrix} M \end{bmatrix} + \begin{bmatrix} 0 & 0 \\ \\ 0 & 0 \end{bmatrix} \cdot \begin{bmatrix} v_{\mathrm{in}} \\ \\ i_{\mathrm{o}} \end{bmatrix} \tag{D.9}$$

In the state space model presented in eqs. (D.8) and (D.9), i_{L} and v_{o} correspond to the state variables, M corresponds to the actuation, v_{in} and i_{o} are perturbations and i_{L} and i_{d} are the outputs of the state space model. Sub-index $_{\mathrm{Q}}$ indicates a variable in its equilibrium point value.

The output of the state space model can be rewritten as a function of the actuation and perturbations. Note that F can be neglected from eq. (D.7) since it is a (2 by 2) zero matrix.

Finally, replacing the values of matrices A, B, C, D, E and F in equations (D.6) and (D.6) results in:

$$G_{\mathrm{yu}} = \begin{bmatrix} \dfrac{-s \cdot N_{\mathrm{o}} \cdot C_{\mathrm{o}} \cdot V_{\mathrm{oQ}} - N_{\mathrm{o}}^2 \cdot i_{\mathrm{LQ}} \cdot M_{\mathrm{Q}}}{s \cdot C_{\mathrm{o}} \cdot (s \cdot L + R_{\mathrm{L}}) - N_{\mathrm{o}}^2 \cdot M_{\mathrm{Q}}^2} \\ \\ \dfrac{N_{\mathrm{o}} \left(s \cdot C_{\mathrm{o}} \cdot i_{\mathrm{LQ}} \cdot (s \cdot L + R_{\mathrm{L}}) - s \cdot N_{\mathrm{o}} \cdot C_{\mathrm{o}} \cdot M_{\mathrm{Q}} \cdot V_{\mathrm{oQ}} - 2 \cdot N_{\mathrm{o}} \cdot i_{\mathrm{LQ}} \cdot M_{\mathrm{Q}}^2\right)}{s \cdot C_{\mathrm{o}} \cdot (s \cdot L + R_{\mathrm{L}}) - N_{\mathrm{o}}^2 \cdot M_{\mathrm{Q}}^2} \end{bmatrix} \tag{D.10}$$

$$G_{\mathrm{yp}} = \begin{bmatrix} \dfrac{-s \cdot C_{\mathrm{o}}}{s \cdot C_{\mathrm{o}} \cdot (s \cdot L + R_{\mathrm{L}}) - N_{\mathrm{o}}^2 \cdot M_{\mathrm{Q}}^2} & \dfrac{-N_{\mathrm{o}} \cdot M_{\mathrm{Q}}}{s \cdot C_{\mathrm{o}} \cdot (s \cdot L + R_{\mathrm{L}}) - N_{\mathrm{o}}^2 \cdot M_{\mathrm{Q}}^2} \\ \\ \dfrac{-s \cdot N_{\mathrm{o}} \cdot C_{\mathrm{o}} \cdot M_{\mathrm{Q}}}{s \cdot C_{\mathrm{o}} \cdot (s \cdot L + R_{\mathrm{L}}) - N_{\mathrm{o}}^2 \cdot M_{\mathrm{Q}}^2} & \dfrac{-N_{\mathrm{o}}^2 \cdot M_{\mathrm{Q}}^2}{s \cdot C_{\mathrm{o}} \cdot (s \cdot L + R_{\mathrm{L}}) - N_{\mathrm{o}}^2 \cdot M_{\mathrm{Q}}^2} \end{bmatrix} \tag{D.11}$$

Where N_{o} is n_1/n_2.

D.2 Bidirectional Partial Power Converter - Input Side Inductor

The state space model of the full bridge based PPC with an input side inductor is presented in eqs. (D.12) and (D.13). Where i_{L} and v_{o} correspond to the state variables, M corresponds to the actuation, v_{in} and i_{o} are perturbations and i_{L} and i_{bp} are the outputs of the state space model. The variable in its equilibrium point value where indicated by the sub-index $_{\mathrm{Q}}$.

$$\begin{bmatrix} \dfrac{di_{\mathrm{L}}}{dt} \\ \\ \dfrac{dv_{\mathrm{o}}}{dt} \end{bmatrix} = \begin{bmatrix} \dfrac{-R_{\mathrm{L}}}{L} & N_2 \cdot \dfrac{M_{\mathrm{Q}}}{L} \\ \\ N_2 \cdot \dfrac{-M_{\mathrm{Q}}}{C_{\mathrm{o}}} & \dfrac{-1}{R_{\mathrm{o}}} \end{bmatrix} \cdot \begin{bmatrix} i_{\mathrm{L}} \\ \\ v_{\mathrm{o}} \end{bmatrix} + \begin{bmatrix} N_2 \cdot \dfrac{v_{\mathrm{oQ}}}{L} \\ \\ N_2 \cdot \dfrac{-i_{\mathrm{LQ}}}{C_{\mathrm{o}}} \end{bmatrix} \cdot \begin{bmatrix} M \end{bmatrix} + \begin{bmatrix} \dfrac{-1}{L} & 0 \\ \\ 0 & \dfrac{1}{C_{\mathrm{o}}} \end{bmatrix} \cdot \begin{bmatrix} v_{\mathrm{in}} \\ \\ i_{\mathrm{o}} \end{bmatrix} \tag{D.12}$$

$$\begin{bmatrix} i_{\mathrm{L}} \\ \\ i_{\mathrm{bp}} \end{bmatrix} = \begin{bmatrix} 1 & 0 \\ \\ N_2 \cdot M_{\mathrm{Q}} & 0 \end{bmatrix} \cdot \begin{bmatrix} i_{\mathrm{L}} \\ \\ v_{\mathrm{o}} \end{bmatrix} + \begin{bmatrix} 0 \\ \\ N_2 \cdot i_{\mathrm{LQ}} \end{bmatrix} \cdot \begin{bmatrix} M \end{bmatrix} + \begin{bmatrix} 0 & 0 \\ \\ 0 & 0 \end{bmatrix} \cdot \begin{bmatrix} v_{\mathrm{in}} \\ \\ i_{\mathrm{o}} \end{bmatrix} \tag{D.13}$$

The transfer functions of the state space model can be obtained by applying eq. (D.5) into eqs. (D.12) and (D.13),

$$G_{\mathrm{yu}} = \frac{Y}{U} = \begin{bmatrix} \dfrac{N_2 \cdot (C_{\mathrm{o}} \cdot v_{\mathrm{oQ}} \cdot (s \cdot R_{\mathrm{o}} + 1) - N_2 \cdot M_{\mathrm{Q}} \cdot R_{\mathrm{o}} \cdot i_{\mathrm{LQ}})}{C_{\mathrm{o}} \cdot (s \cdot R_{\mathrm{o}} + 1) \cdot (s \cdot L + R_{\mathrm{L}}) + N_2^2 \cdot M_{\mathrm{Q}}^2 \cdot R_{\mathrm{o}}} \\ \\ \dfrac{N_2 \cdot C_{\mathrm{o}} \cdot (s \cdot R_{\mathrm{o}} + 1) \cdot (i_{\mathrm{LQ}} \cdot (s \cdot L + R_{\mathrm{L}}) + N_2 \cdot M_{\mathrm{Q}} \cdot v_{\mathrm{oQ}})}{C_{\mathrm{o}} \cdot (s \cdot R_{\mathrm{o}} + 1) \cdot (s \cdot L + R_{\mathrm{L}}) + N_2^2 \cdot M_{\mathrm{Q}}^2 \cdot R_{\mathrm{o}}} \end{bmatrix} \tag{D.14}$$

$$G_{\mathrm{yp}} = \frac{Y}{P} = \frac{1}{C_{\mathrm{o}} \cdot (s \cdot R_{\mathrm{o}} + 1) \cdot (s \cdot L + R_{\mathrm{L}}) + N_2^2 \cdot M_{\mathrm{Q}}^2 \cdot R_{\mathrm{o}}} \cdot \begin{bmatrix} -C_{\mathrm{o}} \cdot (s \cdot R_{\mathrm{o}} + 1) & N_2 \cdot M_{\mathrm{Q}} \cdot R_{\mathrm{o}} \\ \\ -N_2 \cdot C_{\mathrm{o}} \cdot M_{\mathrm{Q}}(s \cdot R_{\mathrm{o}} + 1) & N_2^2 \cdot M_{\mathrm{Q}}^2 \cdot R_{\mathrm{o}} \end{bmatrix} \tag{D.15}$$

D.3 Bidirectional Partial Power Converter - Partial Side Inductor

The relays in this configuration allow restructuring of the resulting topology, thus enabling handling of the power flow in each direction (bucking or boosting). However, this reconfiguration produces a different equivalent circuit, thus requiring a different model for bucking or boosting. The following analyses show the resulting state space model for each operation mode.

D.3.1 Bucking mode

The state space model of the bidirectional PPC with the inductor in the partial side operating in bucking mode is obtained by linearising the averaged model from eqs. (5.89) to (5.92).

$$\begin{bmatrix} \frac{di_{\mathrm{L}}}{dt} \\ \frac{dv_{\mathrm{o}}}{dt} \end{bmatrix} = \begin{bmatrix} \frac{-R_{\mathrm{L}}}{L} & \left(\frac{n_2}{n_1}\right) \cdot \frac{M_{\mathrm{tQ}}}{L} \\ -\left(\frac{n_2}{n_1}\right) \cdot \frac{M_{\mathrm{tQ}}}{C_{\mathrm{o}}} & \frac{-1}{R_{\mathrm{o}} \cdot C_{\mathrm{o}}} \end{bmatrix} \cdot \begin{bmatrix} i_{\mathrm{L}} \\ v_{\mathrm{o}} \end{bmatrix} + \begin{bmatrix} \left(\frac{n_2}{n_1}\right) \cdot \frac{(v_{\mathrm{oQ}} - v_{\mathrm{inQ}})}{L} \\ -\left(\frac{n_2}{n_1}\right) \cdot \frac{i_{\mathrm{LQ}}}{C_{\mathrm{o}}} \end{bmatrix} \cdot \begin{bmatrix} M_{\mathrm{t}} \end{bmatrix} \cdots$$

$$\cdots + \begin{bmatrix} -\left(\frac{n_2}{n_1}\right) \cdot \frac{M_{\mathrm{tQ}}}{L} - \frac{1}{L} & 0 \\ 0 & \frac{1}{C_{\mathrm{o}}} \end{bmatrix} \cdot \begin{bmatrix} v_{\mathrm{in}} \\ i_{\mathrm{o}} \end{bmatrix} \tag{D.16}$$

$$\begin{bmatrix} i_{\mathrm{L}} \\ i_{\mathrm{bp}} \\ i_{\mathrm{in}} \end{bmatrix} = \begin{bmatrix} 1 & 0 \\ \left(\frac{n_2}{n_1}\right) \cdot M_{\mathrm{tQ}} & 0 \\ \left(\frac{n_2}{n_1}\right) \cdot M_{\mathrm{tQ}} + 1 & 0 \end{bmatrix} \cdot \begin{bmatrix} i_{\mathrm{L}} \\ v_{\mathrm{o}} \end{bmatrix} + \begin{bmatrix} 0 \\ \left(\frac{n_2}{n_1}\right) \cdot i_{\mathrm{LQ}} \\ \left(\frac{n_2}{n_1}\right) \cdot i_{\mathrm{LQ}} \end{bmatrix} \cdot \begin{bmatrix} M_{\mathrm{t}} \end{bmatrix} + \begin{bmatrix} 0 & 0 \\ 0 & 0 \\ 0 & 0 \end{bmatrix} \cdot \begin{bmatrix} v_{\mathrm{in}} \\ i_{\mathrm{o}} \end{bmatrix} \tag{D.17}$$

where i_{L} and v_{o} are the state variables (X), M_{t} is the actuation (U), v_{in} and i_{o} are the perturbations (P) and i_{L}, i_{bp} and i_{in} are the outputs (Y). The sub index $_{\mathrm{Q}}$ indicates a variable in its operation point.

Considering the standard notation for the state variables model (see eqs. (D.1) and (D.2)), the transfer function between actuation and output and between perturbation and output are respectively given by eqs. (D.18) and (D.19).

$$G_{\mathrm{yu}} = \frac{Y}{U} = C \cdot (sI - A)^{-1} \cdot B + D \tag{D.18}$$

$$G_{\mathrm{yp}} = \frac{Y}{P} = C \cdot (sI - A)^{-1} \cdot E + F \tag{D.19}$$

To simplify the notation let's define Λ as:

$$\Lambda_{\mathrm{t}} = \frac{1}{s^2 + \left(\frac{R_{\mathrm{L}}}{L} + \frac{1}{R_{\mathrm{o}} \cdot C_{\mathrm{o}}}\right) \cdot s + \left(\frac{R_{\mathrm{L}}}{L \cdot R_{\mathrm{o}} \cdot C_{\mathrm{o}}} + \frac{1}{L \cdot C_{\mathrm{o}}} \cdot \left[\left(\frac{n_2}{n_1}\right) \cdot M_{\mathrm{tQ}}\right]^2\right)} \tag{D.20}$$

The transfer functions between actuation and output are given by

$$G_{\mathrm{yu}} = \frac{Y}{U} = \begin{bmatrix} G_{i_{\mathrm{L}} M_{\mathrm{t}}} \\ \\ G_{i_{\mathrm{bp}} M_{\mathrm{t}}} \\ \\ G_{i_{\mathrm{in}} M_{\mathrm{t}}} \end{bmatrix} \tag{D.21}$$

where $G_{i_{\mathrm{L}} M_{\mathrm{t}}}$, $G_{i_{\mathrm{bp}} M_{\mathrm{t}}}$ and $G_{i_{\mathrm{in}} M_{\mathrm{t}}}$ are respectively:

$$G_{i_{\mathrm{L}} M_{\mathrm{t}}} = \frac{i_{\mathrm{L}}}{M_{\mathrm{t}}} = \Lambda_{\mathrm{t}} \cdot \left[\left(s + \frac{1}{R_{\mathrm{o}} \cdot C_{\mathrm{o}}}\right) \cdot \left(\frac{n_2}{n_1}\right) \cdot \left(\frac{v_{\mathrm{oQ}} - v_{\mathrm{inQ}}}{L}\right) - \left(\frac{n_2}{n_1}\right)^2 \cdot \frac{M_{\mathrm{tQ}}}{L} \cdot \frac{i_{\mathrm{LQ}}}{C_{\mathrm{o}}}\right] \tag{D.22}$$

$$G_{i_{\mathrm{bp}} M_{\mathrm{t}}} = \frac{i_{\mathrm{bp}}}{M_{\mathrm{t}}} = \Lambda_{\mathrm{t}} \cdot \left[\left(s + \frac{1}{R_{\mathrm{o}} \cdot C_{\mathrm{o}}}\right) \cdot \left(\frac{n_2}{n_1}\right)^2 \cdot M_{\mathrm{tQ}} \cdot \left(\frac{v_{\mathrm{oQ}} - v_{\mathrm{inQ}}}{L}\right) - \left(\frac{n_2}{n_1}\right)^3 \cdot \frac{M_{\mathrm{tQ}}^2}{L} \cdot \frac{i_{\mathrm{LQ}}}{C_{\mathrm{o}}} + \left(\frac{n_2}{n_1}\right) \cdot i_{\mathrm{LQ}}\right] \tag{D.23}$$

$$\begin{aligned} G_{i_{\mathrm{in}} M_{\mathrm{t}}} = \frac{i_{\mathrm{in}}}{M_{\mathrm{t}}} = \Lambda_{\mathrm{t}} \cdot \Bigg[\left(s + \frac{1}{R_{\mathrm{o}} \cdot C_{\mathrm{o}}}\right) \cdot \left(\left(\frac{n_2}{n_1}\right) \cdot M_{\mathrm{tQ}} + 1\right) \cdot \left(\frac{n_2}{n_1}\right) \cdot \left(\frac{v_{\mathrm{oQ}} - v_{\mathrm{inQ}}}{L}\right) \dots \\ - \left(\frac{n_2}{n_1}\right)^2 \cdot \frac{M_{\mathrm{tQ}}}{L} \cdot \left(\left(\frac{n_2}{n_1}\right) \cdot M_{\mathrm{tQ}} + 1\right) \cdot \frac{i_{\mathrm{LQ}}}{C_{\mathrm{o}}} + \left(\frac{n_2}{n_1}\right) \cdot i_{\mathrm{LQ}}\Bigg] \end{aligned} \tag{D.24}$$

On the other hand, the transfer function between perturbation and output are given by

$$G_{\mathrm{yp}} = \frac{Y}{P} = \begin{bmatrix} G_{i_{\mathrm{L}} v_{\mathrm{in}}} & G_{i_{\mathrm{L}} i_{\mathrm{o}}} \\ \\ G_{i_{\mathrm{bp}} v_{\mathrm{in}}} & G_{i_{\mathrm{bp}} i_{\mathrm{o}}} \\ \\ G_{i_{\mathrm{in}} v_{\mathrm{in}}} & G_{i_{\mathrm{in}} i_{\mathrm{o}}} \end{bmatrix} \tag{D.25}$$

$$G_{i_{\mathrm{L}} v_{\mathrm{in}}} = \Lambda_{\mathrm{t}} \cdot \left(-\frac{1}{L}\right) \cdot \left(s + \frac{1}{R_{\mathrm{o}} \cdot C_{\mathrm{o}}}\right) \cdot \left(\left(\frac{n_2}{n_1}\right) \cdot M_{\mathrm{tQ}} + 1\right) \tag{D.26}$$

$$G_{i_{\mathrm{L}} i_{\mathrm{o}}} = \Lambda_{\mathrm{t}} \cdot \left(\frac{n_2}{n_1}\right) \cdot \frac{M_{\mathrm{tQ}}}{L \cdot C_{\mathrm{o}}} \tag{D.27}$$

$$G_{i_{\mathrm{bp}} v_{\mathrm{in}}} = \Lambda_{\mathrm{t}} \cdot \left(-\frac{1}{L}\right) \cdot \left(s + \frac{1}{R_{\mathrm{o}} \cdot C_{\mathrm{o}}}\right) \cdot \left(\frac{n_2}{n_1}\right) \cdot M_{\mathrm{tQ}} \cdot \left(\left(\frac{n_2}{n_1}\right) \cdot M_{\mathrm{tQ}} + 1\right) \tag{D.28}$$

$$G_{i_{\mathrm{bp}} i_{\mathrm{o}}} = \Lambda_{\mathrm{t}} \cdot \left(\frac{n_2}{n_1}\right)^2 \cdot \frac{M_{\mathrm{tQ}}^2}{L \cdot C_{\mathrm{o}}} \tag{D.29}$$

$$G_{i_{\mathrm{in}} v_{\mathrm{in}}} = \Lambda_{\mathrm{t}} \cdot \left(-\frac{1}{L}\right) \cdot \left(s + \frac{1}{R_{\mathrm{o}} \cdot C_{\mathrm{o}}}\right) \cdot \left(\left(\frac{n_2}{n_1}\right) \cdot M_{\mathrm{tQ}} + 1\right)^2 \tag{D.30}$$

$$G_{i_{\mathrm{in}} i_{\mathrm{o}}} = \Lambda_{\mathrm{t}} \cdot \left(\frac{n_2}{n_1}\right) \cdot \frac{M_{\mathrm{tQ}}}{L \cdot C_{\mathrm{o}}} \cdot \left(\left(\frac{n_2}{n_1}\right) \cdot M_{\mathrm{tQ}} + 1\right) \tag{D.31}$$

D.3.2 Boosting mode

The state space model for the bidirectional PPC with partial side inductor in boosting mode is obtained by linearising eqs. (5.112), (5.113) and (5.114).

$$\begin{bmatrix} \frac{di_{\mathrm{L}}}{dt} \\ \\ \frac{dv_{\mathrm{o}}}{dt} \end{bmatrix} = \begin{bmatrix} \frac{-R_{\mathrm{L}}}{L} & \frac{1}{L}\left[\left(\frac{n_2}{n_1}\right) \cdot M_{\mathrm{bQ}} - 1\right] \\ \\ -\frac{1}{C_{\mathrm{o}}}\left[\left(\frac{n_2}{n_1}\right) \cdot M_{\mathrm{bQ}} - 1\right] & \frac{-1}{R_{\mathrm{o}} \cdot C_{\mathrm{o}}} \end{bmatrix} \cdot \begin{bmatrix} i_{\mathrm{L}} \\ \\ v_{\mathrm{o}} \end{bmatrix} \cdots$$
$$\cdots + \begin{bmatrix} \left(\frac{n_2}{n_1}\right) \cdot \frac{v_{\mathrm{oQ}}}{L} \\ \\ -\left(\frac{n_2}{n_1}\right) \cdot \frac{i_{\mathrm{LQ}}}{C_{\mathrm{o}}} \end{bmatrix} \cdot \begin{bmatrix} M_{\mathrm{b}} \end{bmatrix} + \begin{bmatrix} \frac{1}{L} & 0 \\ \\ 0 & \frac{1}{C_{\mathrm{o}}} \end{bmatrix} \cdot \begin{bmatrix} v_{\mathrm{in}} \\ \\ i_{\mathrm{o}} \end{bmatrix} \tag{D.32}$$

$$\begin{bmatrix} i_{\mathrm{L}} \\ i_{\mathrm{bp}} \\ i_{\mathrm{in}} \end{bmatrix} = \begin{bmatrix} 1 & 0 \\ \left(\frac{n_2}{n_1}\right) \cdot M_{\mathrm{bQ}} & 0 \\ -1 & 0 \end{bmatrix} \cdot \begin{bmatrix} i_{\mathrm{L}} \\ v_{\mathrm{o}} \end{bmatrix} + \begin{bmatrix} 0 \\ \left(\frac{n_2}{n_1}\right) \cdot i_{\mathrm{LQ}} \\ 0 \end{bmatrix} \cdot \begin{bmatrix} M_{\mathrm{b}} \end{bmatrix} + \begin{bmatrix} 0 & 0 \\ 0 & 0 \\ 0 & 0 \end{bmatrix} \cdot \begin{bmatrix} v_{\mathrm{in}} \\ i_{\mathrm{o}} \end{bmatrix} \tag{D.33}$$

In order to simplify the notation of the state space model Λ_{b} is defined as:

$$\Lambda_{\mathrm{b}} = \frac{1}{s^2 + \left(\frac{R_{\mathrm{L}}}{L} + \frac{1}{R_{\mathrm{o}} \cdot C_{\mathrm{o}}}\right) \cdot s + \left(\frac{R_{\mathrm{L}}}{L \cdot R_{\mathrm{o}} \cdot C_{\mathrm{o}}} + \frac{1}{L \cdot C_{\mathrm{o}}} \cdot \left[\left(\frac{n_2}{n_1}\right) \cdot M_{\mathrm{bQ}} - 1\right]^2\right)} \tag{D.34}$$

Equation (D.35) presents the transfer functions between actuation (U) and output (Y)

$$G_{\mathrm{yu}} = \frac{Y}{U} = \begin{bmatrix} G_{i_{\mathrm{L}} M_{\mathrm{b}}} \\ G_{i_{\mathrm{bp}} M_{\mathrm{b}}} \\ G_{i_{\mathrm{in}} M_{\mathrm{b}}} \end{bmatrix} \tag{D.35}$$

where $G_{i_{\mathrm{L}} M_{\mathrm{b}}}$, $G_{i_{\mathrm{bp}} M_{\mathrm{b}}}$ and $G_{i_{\mathrm{in}} M_{\mathrm{b}}}$ are respectively:

$$G_{i_{\mathrm{L}} M_{\mathrm{b}}} = \frac{i_{\mathrm{L}}}{M_{\mathrm{b}}} = \Lambda_{\mathrm{b}} \cdot \frac{1}{L} \cdot \left(\frac{n_2}{n_1}\right) \cdot \left\{\left(s + \frac{1}{R_{\mathrm{o}} \cdot C_{\mathrm{o}}}\right) \cdot v_{\mathrm{oQ}} - \left[\left(\frac{n_2}{n_1}\right) \cdot M_{\mathrm{bQ}} - 1\right] \cdot \frac{i_{\mathrm{LQ}}}{C_{\mathrm{o}}}\right\} \tag{D.36}$$

$$G_{i_{\mathrm{bp}} M_{\mathrm{b}}} = \frac{i_{\mathrm{bp}}}{M_{\mathrm{b}}} = \Lambda_{\mathrm{b}} \cdot \left(\frac{n_2}{n_1}\right) \cdot \left\{\frac{M_{\mathrm{bQ}}}{L} \cdot \left(\frac{n_2}{n_1}\right) \cdot \left[\left(s + \frac{1}{R_{\mathrm{o}} \cdot C_{\mathrm{o}}}\right) \cdot v_{\mathrm{oQ}} - \left[\left(\frac{n_2}{n_1}\right) \cdot M_{\mathrm{bQ}} - 1\right] \cdot \frac{i_{\mathrm{LQ}}}{C_{\mathrm{o}}}\right] + i_{\mathrm{LQ}}\right\} \tag{D.37}$$

$$G_{i_{\mathrm{in}} M_{\mathrm{b}}} = \frac{i_{\mathrm{in}}}{M_{\mathrm{b}}} = -\Lambda_{\mathrm{b}} \cdot \frac{1}{L} \cdot \left(\frac{n_2}{n_1}\right) \cdot \left\{\left(s + \frac{1}{R_{\mathrm{o}} \cdot C_{\mathrm{o}}}\right) \cdot v_{\mathrm{oQ}} - \left[\left(\frac{n_2}{n_1}\right) \cdot M_{\mathrm{bQ}} - 1\right] \cdot \frac{i_{\mathrm{LQ}}}{C_{\mathrm{o}}}\right\} \tag{D.38}$$

The transfer functions between perturbation (P) and output (Y) are given by

$$G_{\mathrm{yp}} = \frac{Y}{P} = \begin{bmatrix} G_{i_{\mathrm{L}} v_{\mathrm{in}}} & G_{i_{\mathrm{L}} i_{\mathrm{o}}} \\ G_{i_{\mathrm{bp}} v_{\mathrm{in}}} & G_{i_{\mathrm{bp}} i_{\mathrm{o}}} \\ G_{i_{\mathrm{in}} v_{\mathrm{in}}} & G_{i_{\mathrm{in}} i_{\mathrm{o}}} \end{bmatrix} \tag{D.39}$$

where $G_{i_\mathrm{L} v_\mathrm{in}}$, $G_{i_\mathrm{L} i_\mathrm{o}}$, $G_{i_\mathrm{bp} v_\mathrm{in}}$, $G_{i_\mathrm{bp} i_\mathrm{o}}$, $G_{i_\mathrm{in} v_\mathrm{in}}$ and $G_{i_\mathrm{in} i_\mathrm{o}}$ are:

$$G_{i_\mathrm{L} v_\mathrm{in}} = \Lambda_\mathrm{b} \cdot \left(\frac{1}{L}\right) \cdot \left(s + \frac{1}{R_\mathrm{o} \cdot C_\mathrm{o}}\right) \tag{D.40}$$

$$G_{i_\mathrm{L} i_\mathrm{o}} = \Lambda_\mathrm{b} \cdot \left(\frac{1}{L \cdot C_\mathrm{o}}\right) \cdot \left[\left(\frac{n_2}{n_1}\right) \cdot M_\mathrm{tQ} - 1\right] \tag{D.41}$$

$$G_{i_\mathrm{bp} v_\mathrm{in}} = \Lambda_\mathrm{b} \cdot \left(\frac{1}{L}\right) \left(\frac{n_2}{n_1}\right) \cdot M_\mathrm{bQ} \cdot \left(s + \frac{1}{R_\mathrm{o} \cdot C_\mathrm{o}}\right) \tag{D.42}$$

$$G_{i_\mathrm{bp} i_\mathrm{o}} = \Lambda_\mathrm{b} \cdot \left(\frac{1}{L \cdot C_\mathrm{o}}\right) \cdot \left(\frac{n_2}{n_1}\right) \cdot M_\mathrm{bQ} \cdot \left[\left(\frac{n_2}{n_1}\right) \cdot M_\mathrm{bQ} - 1\right] \tag{D.43}$$

$$G_{i_\mathrm{in} v_\mathrm{in}} = -\Lambda_\mathrm{b} \cdot \left(\frac{1}{L}\right) \cdot \left(s + \frac{1}{R_\mathrm{o} \cdot C_\mathrm{o}}\right) \tag{D.44}$$

$$G_{i_\mathrm{in} i_\mathrm{o}} = -\Lambda_\mathrm{b} \cdot \left(\frac{1}{L \cdot C_\mathrm{o}}\right) \cdot \left[\left(\frac{n_2}{n_1}\right) \cdot M_\mathrm{bQ} - 1\right] \tag{D.45}$$

Appendix E

Wavelet Transform

Wavelet Transform is a time-frequency signal analysis tool that allows simultaneous decomposition of a time signal ($x(t)$) in time and frequency domains [140–142]. In order to perform the decomposition a wavelet function ($\Psi_{j,n}(t)$) and a scaling function ($\Phi_{j,n}(t)$) are required. The inner product between the scaling function with the signal generates an approximation ($L_x(j = 1, n)$, lower frequencies) of the signal $x(t)$, while the inner product between the wavelet function with the signal $x(t)$ keeps the details ($W_x(j = 1, n)$, higher frequencies); thus working respectively as low-pass and high-pass filters. This decomposition process can be repeated by separating the obtained approximation ($L_x(j = 1, n)$) into the following level of detail ($W_x(j = 2, n)$) and approximation ($L_x(j = 2, n)$), and so on (as shown in eq. (E.1) and (E.2)).

$$L_x(j, n) =< x(t), \Phi_{j,n}(t) >= \int_{-\infty}^{\infty} x(t) \cdot \Phi^*_{j,n}(t)dt \tag{E.1}$$

$$W_x(j, n) =< x(t), \Psi_{j,n}(t) >= \int_{-\infty}^{\infty} x(t) \cdot \Psi^*_{j,n}(t)dt \tag{E.2}$$

The algorithm applied in this work corresponds to a DWT calculated through the Fast Wavelet Transform (FWT) algorithm introduced in [140]. The FWT mathematical procedure is shown in eqs. (E.3) and (E.4) [142], where $a_j[n]$ is decomposed into an approximation ($a_{j+1}[n]$) and details ($d_{j+1}[n]$) by convoluting $a_j[n]$ with low-pass and high-pass conjugate mirror filters (h and g). This procedure can be cascaded generating further decomposition of the approximations obtained. The sub-index $_j$ indicates the level of decomposition.

$$a_{j+1}[t] = \sum_{t=-\infty}^{\infty} h[n - 2t] \cdot a_j[n] \tag{E.3}$$

$$d_{j+1}[t] = \sum_{t=-\infty}^{\infty} g[n-2t] \cdot a_j[n] \tag{E.4}$$

The re-composition of the signal is performed through the Inverse Fast Wavelet Transform (IFWT) [142].

$$a_j[t] = \sum_{n=-\infty}^{\infty} h[t-2n] \cdot a_{j+1}[n] + \sum_{n=-\infty}^{\infty} g[t-2n] \cdot d_{j+1}[n] \tag{E.5}$$